LES of transient premixed flames using a dynamic flame surface density model

by

Ruipengyu (Brandon) Li

A Thesis Submitted in Partial Fulfilment of the
Requirements for the Degree of Doctor of Philosophy at
Loughborough University

Abstract

Transient premixed flames are significant in areas such as spark-ignition engines and gas explosions. However, physical understanding and accurate prediction remain challenging due to the fact that the flame typically transits from early quasi-laminar to fully turbulent, and the interactions with the surrounding solid structures often lead to the continuous stretching of the flame front. This study has considered the large eddy simulation (LES) techniques for the simulations of transient turbulent premixed flames. The LES technique has evolved as a powerful computational tool for the prediction of unsteady flame propagation. The difficulty of applying LES for turbulent premixed combustion is to account for the thin flame front using appropriate methods. This thesis considers a dynamic flame surface density (DFSD) model to close the filtered reaction rate. It automatically computes the model parameter based on the characteristics of the resolved flame front. The model is first validated in a one-dimensional laminar case to ensure the correct behaviours including the filtered flame thickness and laminar burning velocity with the absence of sub-grid turbulence.

The LES-DFSD approach is then applied to study the transient flame propagation past solid obstacles in a small-scale combustion chamber. The present work explores the model capabilities for the three different fuel/air mixtures (propane, methane and hydrogen) and obstacle configurations using a series of experimental test cases. The sensitivity of results to the numerical conditions including the methods of flame initiation, grid resolution, turbulence parameters and the filter width is also investigated. Generally, the approach is found to be successful in capturing the essential flame characteristics during the unsteady flame propagation. Critical parameters such as the maximum overpressure and flame speed are correctly predicted compared with experiments. The evolution of the sub-grid wrinkling factor serves as an indicator of the strength of the flame-turbulence interactions for various test environments. LES has the capability of reproducing the vortex and turbulence structures generated by the obstacles. The impact of the number, location and size of the obstacles is discussed, and combustion characteristics of three fuels are compared.

Keywords: LES, transient premixed flames, dynamic FSD model, flame-obstacle interaction

Publications

Journals:

1. **R. Li**, W. Malalasekera, S. Ibrahim, B. Liu, On the mechanism of pressure rise in vented explosions : A numerical study, *Process Safety and Environmental Protection.* 117 (2018) 551-564.

2. **R. Li**, W. Malalasekera, S. Ibrahim, Numerical study of vented hydrogen explosions in a small scale obstructed chamber, *International Journal of Hydrogen Energy.* 43 (2018) 16667-16683.

Conferences:

1. **R. Li**, W. Malalasekera, S. Ibrahim, Numerical investigation of early flame propagation in vented explosion, in: *Tenth Mediterranean Combustion Symposium (MCS-10)*, Naples, Italy, 2017.

2. **R. Li**, W. Malalasekera, S. Ibrahim, LES-DFSD modelling of turbulent premixed flames past repeated obstacles, in: *Proceedings of the 3rd World Congress on Momentum, Heat and Mass Transfer (MHMT'18)*, Budapest, Hungary, 2018.

Acknowledgements

I would like to express my appreciation to my supervisors Prof Weeratunge Malalasekera and Dr Salah Ibrahim for their invaluable support, comments and guidance throughout the past three years. They provided me with a free research environment and considerably considered my opinions in the path of the project. I would express my gratitude to Dr Bo Liu from the University of Sheffield for the constructive discussion between us when he was at Loughborough. Bo has always been an immensely kind and helpful colleague to work with. His knowledge, experience and enthusiasm of CFD, the physical insights into problems, as well as the working attitude has benefited me from my PhD and beyond. I would also thank Prof Denis Veynante, Prof Arnaud Trouve, and Dr Chathura Ranasinghe for the email communication on various modelling issues. I would appreciate my colleagues including Dr Thomas Beard, Dr Asela Uyanwaththa and Dr Zhixin Cao for the fruitful discussions on a day-to-day basis. I have also benefited from the conversation with the visiting scholars, Dr Satoki Yokoi from Tohoku University and Dr Roberto Moro-Filho from Brazil, in the early stage of my PhD. Special thanks to Fan Yang for the continuous support and encouragement especially during my writing period. Last but not least, my deepest thanks go to my parents, for their endless and unconditional love they give in my life.

Contents

Abstract ii
Publications iii
Acknowledgements iv
Contents iv
List of Figures vii
List of Tables ix
List of Symbols x
1 Introduction 1
1.1 Background and motivation . . . 1
1.1.1 Internal combustion engines . . . 1
1.1.2 Vented flame deflagrations . . . 3
1.1.3 Hydrogen: features and safety . . . 6
1.2 Computational approaches for turbulent combustion . . . 8
1.2.1 DNS . . . 8
1.2.2 RANS . . . 9
1.2.3 LES . . . 10
1.3 Objectives and thesis outline . . . 11
2 Literature Review 13
2.1 Turbulent premixed flames: general features . . . 13
2.1.1 Interactions between flows and flames . . . 13
2.1.2 Regimes of turbulent premixed combustion . . . 15
2.2 Overview of premixed combustion models . . . 18
2.2.1 Difficulties in LES of turbulent premixed combustion . . . 19
2.2.2 "No model" approach . . . 19
2.2.3 Eddy-break-up (EBU) model . . . 20
2.2.4 Level-set (G-equation) . . . 21
2.2.5 Artificially thickened flames . . . 21
2.2.6 Flame surface density . . . 22
2.3 Algebraic flame surface density models . . . 23
2.3.1 Boger's algebraic model . . . 23
2.3.2 Refinement of Boger's model . . . 26
2.3.3 Closure of the sub-grid wrinkling factor . . . 26
2.3.4 Dynamic formalism for the flame surface density . . . 28
2.4 Initialisation of combustion . . . 31
2.4.1 Difficulties of modelling ignition . . . 32
2.4.2 Lagrangian models . . . 32
2.4.3 Autoignition models . . . 33
2.4.4 Energy deposition approach . . . 34
2.4.5 Flame initiation for LES-FSD . . . 34
2.5 Flame propagation with obstructions . . . 36
2.5.1 Experimental studies . . . 36
2.5.2 Numerical studies . . . 37

2.6 Summary . . . 39
3 Governing Equations and Models 40
3.1 Conservation equations for reactive flows . . . 40
3.1.1 Conservation of mass and momentum . . . 40
3.1.2 Conservation of scalars . . . 41
3.2 Filtered governing equations . . . 42
3.2.1 LES filtering . . . 43
3.2.2 Filtered mass and momentum equations . . . 43
3.2.3 Filtered equation for progress variable . . . 45
3.2.4 Filtered energy equation . . . 45
3.3 The dynamic flame surface density model . . . 46
3.4 Methods for flame kernel initiation . . . 47
3.4.1 I1: Flame kernel model . . . 48
3.4.2 I2: Filtered flame kernel from a 1-D solution . . . 50
3.4.3 I3: Pre-filtered burned flame kernel approach . . . 50
3.4.4 I4: Setting a region of "burning" cells . . . 50
3.5 Summary . . . 51
4 Numerical Approach 52
4.1 Discretisation of transport equations . . . 52
4.1.1 Unsteady term . . . 54
4.1.2 Advection term . . . 54
4.1.3 Diffusion term . . . 55
4.1.4 Source term . . . 55
4.1.5 Complete discretised equation . . . 56
4.2 Time advancement . . . 56
4.3 Pressure correction method . . . 57
4.4 Solution of algebraic equations . . . 58
4.5 Boundary conditions . . . 59
4.5.1 Solid boundaries . . . 59
4.5.2 Outflow boundaries . . . 59
4.6 Solution procedure . . . 60
4.7 Implementation of the DFSD model . . . 61
4.8 Implementation of the flame kernel model . . . 64
4.9 1-D planar flame tests . . . 64
4.9.1 Theoretical analysis . . . 64
4.9.2 Numerical consideration . . . 65
4.9.3 Results . . . 67
4.10 Summary . . . 69
5 Test Cases and Numerical Setup 71
5.1 Experimental considerations . . . 71
5.1.1 Combustion chamber specification . . . 72
5.1.2 Experimental procedures . . . 73
5.1.3 Flow configurations . . . 75
5.1.4 Other considerations . . . 75
5.2 Averaging of pressure signals . . . 77
5.3 Computational setup . . . 78
5.4 Summary . . . 80
6 Results and Discussion: Propane 81
6.1 Parametric study . . . 81
6.1.1 Effect of combustion initialisation . . . 82
6.1.2 Grid sensitivity study . . . 85
6.1.3 Influence of Smagorinsky constant . . . 88

6.1.4 Impact of the filter width . . . 90
6.1.5 Other considerations . . . 91
6.2 Phenomenological study . . . 93
6.2.1 Development of propagating flames . . . 93
6.2.2 Mechanisms of pressure rise . . . 95
6.3 Flame-turbulence interactions . . . 98
6.3.1 LES regime of combustion . . . 105
6.4 Comparative study of flow configurations . . . 108
6.4.1 Combustion characteristics: family 1 . . . 108
6.4.2 Combustion characteristics: family 2 . . . 113
7 Results and Discussion: Hydrogen **117**
7.1 Qualitative study . . . 117
7.2 Overview of overpressure prediction . . . 121
7.3 Effect of obstruction arrangements and size . . . 123
7.4 Comparison of three fuels . . . 132
8 Conclusions and Future Perspectives **140**
8.1 Conclusions and present contributions . . . 140
8.2 Recommendations for future work . . . 144
Bibliography **145**
Appendix A Dynamic Smagorinsky Model **155**

List of Figures

1.1 Flame development and propagation in a stratified-charge SI engine. 2
1.2 Schematic of turbulence generation by obstacles in a vented deflagration. . . . 3
1.3 The mechanism of pressure build-up for a vented deflagration. 4
1.4 Gas explosion in the Buncefield incident 5
1.5 Illustration of the quantitative risk assessment tool: HyRAM. 7
1.6 Turbulence energy spectrum as a function of wave number. 9
1.7 An example of the local temperature computed by RANS, LES and DNS. . . . 10

2.1 Illustration of flame wrinkling by turbulence. 14
2.2 Regime diagram of turbulent premixed flames [34] 16
2.3 LES regime diagram of turbulent premixed flames [35] 18
2.4 Numerical difficulty of resolving the thin flame front on an LES mesh 20

4.1 Grid layout in PUFFIN. 53
4.2 A finite volume cell and its neighbours in the xy-plane. 53
4.3 Effect of a Gaussian filter. 61
4.4 Test filter near the computational boundary. 62
4.5 Illustration of filter sizes. 63
4.6 1-D laminar flame tests: illustration 65
4.7 1-D laminar flame tests: computational domain 66
4.8 1-D laminar flame tests: effect of filter width 67
4.9 1-D laminar flame tests: instantaneous flame images 68
4.10 1-D laminar flame tests: influence of flame initiation and mesh resolution . . . 69
4.11 1-D laminar flame tests: temperature profiles 69

5.1 Experimental test cases: schematic of combustion chamber 73
5.2 Experimental test cases: list of studied configurations 76
5.3 Experimental test cases: pressure signal processing 78
5.4 Experimental test cases: computational mesh 79

6.1 Parametric study: flame kernel structure 83
6.2 Parametric study: effect of flame initialisation methods - configuration 000S . . 84
6.3 Parametric study: effect of flame initialisation methods, configuration BBBS . 84
6.4 Parametric study: sensitivity to mesh resolution 86
6.5 Parametric study: resolved TKE for two mesh resolutions 87
6.6 Parametric study: effect of turbulence modelling on combustion 89
6.7 Parametric study: effect of turbulence modelling on wrinkling factor 89
6.8 Parametric study: sensitivity to filter width 91
6.9 Parametric study: wrinkling factor using different filter widths 91
6.10 Phenomenological study: flame images - configuration 000S 94
6.11 Phenomenological study: flame images - configuration BBBS 95
6.12 Phenomenological study: axial pressure profile 96
6.13 Phenomenological study: mechanisms of pressure build-up 97
6.14 Flame/turbulence interactions: vortex structure - configuration 000S 99

6.15 Flame/turbulence interactions: vortex structure - configuration BBBS 100
6.16 Flame/turbulence interactions: overpressure - configurations 000S and BBBS . 102
6.17 Flame/turbulence interactions: $\langle \Xi \rangle_f$ - configurations 000S and BBBS 103
6.18 Flame/turbulence interactions: 3-D LES flame images 104
6.19 Flame/turbulence interactions: LES regime diagram 107
6.20 Effect of flow configurations: studied test cases 109
6.21 Effect of flow configurations: overpressure - family 1 109
6.22 Effect of flow configurations: flame front speed - family 1 111
6.23 Effect of flow configurations: sub-grid wrinkling factor $\langle \Xi \rangle_f$ - family 1 112
6.24 Effect of flow configurations: overpressure - family 2 113
6.25 Effect of flow configurations: flame front speed - family 2 114
6.26 Effect of flow configurations: sub-grid wrinkling factor $\langle \Xi \rangle_f$ - family 2 114
6.27 Effect of flow configurations: pressure peak magnitudes 115
6.28 Effect of flow configurations: time taken to reach pressure peaks 116

7.1 Hydrogen: flame images - configuration B0BS 119
7.2 Hydrogen: spatial variation of overpressure in the axial direction 120
7.3 Hydrogen: numerical flame snapshots with vorticity contours 121
7.4 Hydrogen: overview of pressure prediction for groups 1-6 122
7.5 Hydrogen: overpressure traces - group 1 123
7.6 Hydrogen: flame speed - group 1 124
7.7 Hydrogen: overpressure - group 2 125
7.8 Hydrogen: flame speed - group 2 125
7.9 Hydrogen: overpressure - group 3 126
7.10 Hydrogen: flame front speed - group 2 127
7.11 Hydrogen: overpressure - group 4 128
7.12 Hydrogen: flame front speed - group 4 128
7.13 Hydrogen: effect of the single grid 129
7.14 Hydrogen: overpressure - group 5 130
7.15 Hydrogen: overpressure - group 6 130
7.16 Hydrogen: effect of obstacle size from flame snapshots - group 5 131
7.17 Effect of fuel types: overpressure traces using methane ($\Phi = 1.0$) 134
7.18 Effect of fuel types: overpressure traces using propane ($\Phi = 1.0$) 134
7.19 Effect of fuel types: overpressure traces using hydrogen ($\Phi = 0.7$) 135
7.20 Effect of fuel types: flame/obstacle interactions - methane and hydrogen 136
7.21 Effect of fuel types: flame position and wrinkling factor - configuration BB0S . 138

List of Tables

2.1 List of algebraic formulations for evaluation of Ξ 28

6.1 List of methods for flame initiation. 82
6.2 List of advantages and disadvantages of each flame initiation approach 85
6.3 List of studied computational grids 86
6.4 List of simulations for parametric study 92

7.1 List of grouped obstacle configurations in hydrogen simulations 118
7.2 List of input laminar flame properties for the three fuel/air mixtures. 132

List of Symbols

Roman Symbols

A	Area	m^2
A_m	Mean flame area during flame kernel development	m^2
A_t	Total flame area during flame kernel development	m^2
A_{exit}	Area of chamber exit plane	m^2
b_i	Body force per unit volume in i direction	N/m^3
C	Model coefficient in the Smagorinsky model	–
c	Reaction progress variable	–
C_s	Smagorinsky constant	–
D	Diffusion coefficient	m^2/s
Da	Damköhler number	–
h	Specific enthalpy	J/kg
Ka	Karlovitz number	–
Ka_δ	Second Karlovitz number	–
L	Length of combustion chamber (Chapter 5)	mm
ℓ_0	Integral length scale of turbulence	m
ℓ_δ	Reaction zone thickness	m
ℓ_κ	Kolmogorov length scale of turbulence	m
ℓ_G	Gibson length scale of turbulence	m
M	Molecular weight	g/mol
$\tilde{\mathbf{n}}$	Vector of normal direction	–
n_{res}	Number relating $\Delta = n_{res}\Delta x$	–
p	Pressure	Pa
p_{max}	Maximum overpressure	$mbar$
Pr	Prandtl number	–
Pr_t	Turbulent Prandtl number	–

$\dot{q}'''$	Volumetric heating term in energy equation	$J/(m^3 \cdot s)$
R_0	Universal gas constant	$8.314 J/(mol \cdot K)$
Re	Reynolds number	–
Re_Δ	Sub-grid Reynolds number	–
Re_t	Turbulent Reynolds number	–
s_L	Laminar burning velocity	cm/s
s_L^0	Unstrained laminar burning velocity	cm/s
S_{ij}	Rate of strain tensor	$1/s$
Sc	Schmitt number	–
Sc_t	Turbulent Schmitt number	–
T	Temperature	K
t	Time domain	s
$t_{p,exp}$	Time to reach peak pressure from experiments	ms
$t_{p,LES}$	Time to reach peak pressure from LES	ms
u'	Velocity fluctuations	m/s
u'_Δ	Sub-grid scale velocity fluctuations	m/s
u_p	Apparent flame propagation speed	m/s
u_i	Velocity component	m/s
V	Volume	m^3
$\dot{V}$	Volume flow rate	m^3/s
W	Width of combustion chamber (Chapter 5)	mm
x_i	Cartesian coordinate in computational domain	m
Y_F	Mass fraction of fuel	–
Y_P	Mass fraction of combustion products	–

Greek Symbols

β	Model coefficient in the DFSD model	–
ΔH_F	Heat of combustion	J/kg
Δt	Time step size	s
Δx	Computational mesh size	m
δx	Grid spacing in x-direction	m
δy	Grid spacing in y-direction	m
δz	Grid spacing in z-direction	m

Δ	Combustion filter width	m
δ_c	Inner cut-off scale	mm
δ_L	Laminar flame thickness	mm
δ_L^0	Unstrained laminar flame thickness	mm
Δ_m	Filter width of volume averaging	m
δ_{ij}	Kronecker delta	s
$\dot{\omega}_c$	Reaction rate in terms of c	$kg/(m^3 \cdot s)$
ϵ	Dissipation rate of turbulent kinetic energy	$J/(kg \cdot s)$
Γ	Kinematic diffusion coefficient	$kg/(m \cdot s)$
γ	Constant corresponding to the effective filter size	$-$
Γ_Δ	Efficiency function	$-$
μ	Dynamic viscosity	$Pa \cdot s$
μ_t	Turbulent viscosity	$Pa \cdot s$
ν	Kinematic viscosity	m^2/s
ν_t	Turbulent kinematic viscosity	m^2/s
Ω	Volume of computational domain	m^3
Φ	Equivalence ratio	$-$
ϕ	General scalar or variable (Chapter 4)	$-$
ρ	Density of fluid	kg/m^3
Σ	Flame surface density	$1/m$
τ_κ	Kolmogorov time scale	s
τ_c	Chemistry time scale	s
τ_{ij}	Stress tensor	Pa
τ_{ij}^{sgs}	SGS stress tensor	Pa
Ξ	Sub-grid flame wrinkling factor	$-$
Ξ_{ker}	Wrinkling factor during flame kernel development	$-$
$\overline{\Delta}$	Flow filter width	m
$\widehat{\Delta}$	Combustion test-filter width	m
$\widehat{\overline{\Delta}}$	Test-filter width for dynamic Smagorinsky model	m

Subscripts

δ	Reaction zone
κ	Kolmogorov scale

atm	Atmospheric condition
b	Burned gases
exp	Experiments or explicit (Chapter 4)
$expa$	Gas expansion
i, j, k	Index notation for Cartesian coordinates
L	Laminar
p	Peak pressure
res	Resolved part
sgs	Sub-grid-scale
t	Turbulent
u	Unburned gases
$vent$	Venting

Superscripts

0	Unstrained

Operators

$''$	Favre fluctuation
$\langle ... \rangle$	Volume averaging
$\langle ... \rangle_f$	Volume averaging over flame
$\overline{...}$	Spatial filtering (unweighted)
$\widehat{...}$	Test-filtering
$\widetilde{...}$	Favre filtering

Abbreviations

1-D	One-dimensional
3-D	Three-dimensional
ABR	Area blockage ratio
B1	Baffle plate no. 1
B2	Baffle plate no. 2
B3	Baffle plate no. 3
BML	Bray-Moss-Libby
BRZ	Broken reaction zones
C_3H_8	Propane
CF	Corrugated flamelets

CFD	Computational fluid dynamics
CFL	Courant-Friedrichs-Lewy number
CGT	Counter-gradient transport
CH_4	Methane
CNG	Compressed natural gas
DFSD	Dynamic flame surface density
DNS	Direct numerical simulation
DS	Dynamic Smagorinsky
FDS	Flame Dynamics Simulator
FSD	Flame surface density
H_2	Hydrogen
KH	Kelvin-Helmholtz
KPP	Kolmogorov, Petrovski and Piskunov
L	Large central obstacle
LD	Landau-Darrieus
LES	Large eddy simulation
LHS	Left-hand side of an equation
LIF-OH	Laser-induced fluorescence of OH
LPG	Liquid petroleum gas
PUFFIN	Particles IN Unsteady Fluid Flow
QRA	Quantitative risk assessment
RANS	Reynolds-Averaged Naiver-Stokes
RHS	Right-hand side of an equation
RMS	Root mean square
RT	Rayleigh-Taylor
SGS	Sub-Grid Scale
Sq.Ob	Small square central obstacle
TKE	Turbulent kinetic energy
TRZ	Thin reaction zones
VBR	Volume blockage ratio

Chapter 1

Introduction

1.1 Background and motivation

Combustion has been the primary means of energy utilisation for many decades, and the need for the safe and clean use of oil and gas continues to grow [1]. The benefits of combustion are present in almost every aspect of our daily life. The modern transportation systems often rely on the combustion of hydrocarbon fuels. Electricity generation mainly requires the burning of coal or natural gas. Industrial processes involve the heavy use of combustion devices such as boilers and ovens. While the heat and power accompanying combustion plays a profound role in our society, the downside issues including fire hazards, accidental explosions and pollutant emissions also result from combustion.

Turbulent premixed combustion is a category of combustion processes where the fuel and air are sufficiently mixed before the occurrence of the chemical reaction. Practical devices such as spark-ignition (SI) engines, lean-burn gas turbines and industrial gas burners often involve a considerable amount of premixed burning. On the other side, burning of a premixed gas cloud in buildings or offshore areas may cause a rapid increase of pressure, leading to undesired gas explosions.

1.1.1 Internal combustion engines

A practical example of the application of turbulent premixed combustion is the SI engine. Its profound influence on the overall engine performance such as the brake power and fuel economy motivates the study of flow and combustion in engines. Furthermore, the legislative requirements for emissions also drive the design and optimisation of internal combustion (IC) engines to meet the increasingly stringent emission standards.

The in-cylinder flows in an SI engine are inherently turbulent, and the chaotic nature of

turbulence contributes to cycle-to-cycle variations in the engine operation. Figure 1.1 shows flame images taken through a pent-roof window, indicating the early flame development and its interaction with flows and the cylinder walls. Motions of swirl and tumble may be produced and managed by the geometric configurations of the intake ports and valves, piston crown and the combustion chamber. In a typical automotive engine, their length scales can be of the order of the bore to sub-millimetre. Corresponding time scales can range from a few microseconds to some milliseconds [2], and the flame is highly unsteady due to turbulence effects of various scales and strengths. In-cylinder turbulent eddies may wrinkle the propagating flame front so that the flame surface area increases. However, very high turbulence intensities induce excessive strain and tear apart flame fronts. This process may hinder the flame propagation and lead to flame extinction.

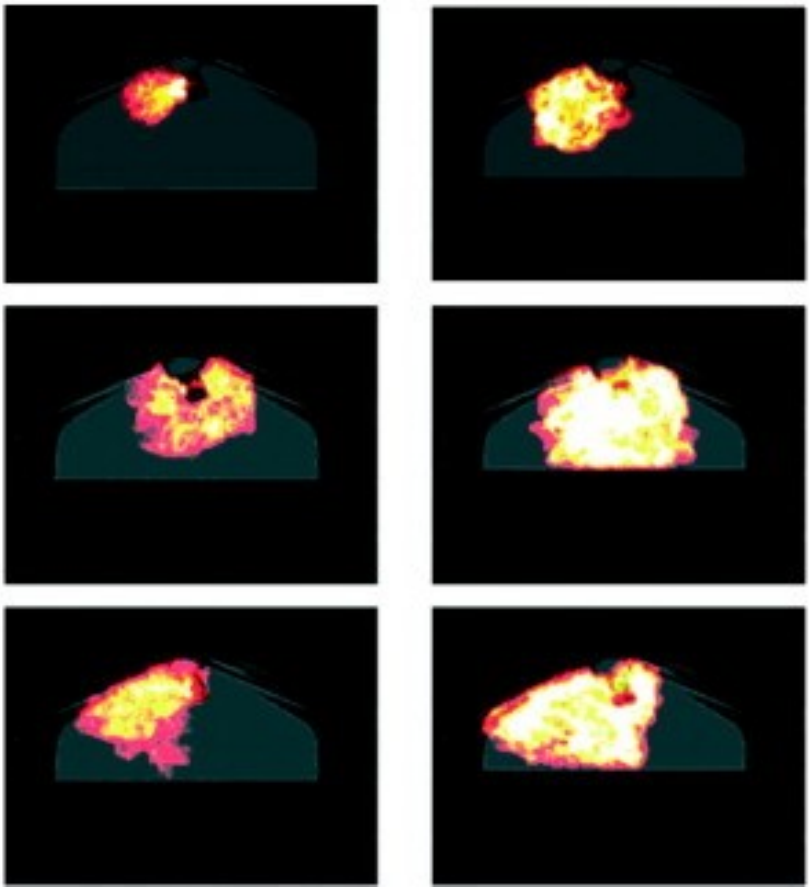

Figure 1.1: Typical images of flame development and propagation in a lean-burn stratified-charge SI engine. Reproduced from Aleiferis et al. [3].

The engine optimisation traditionally follows repetitive hardware modifications, excessive testing and exhaustive analysis of experimental data, and this iterative process is often slow and costly. The use of computational fluid dynamics (CFD) techniques for engine design and

support has become increasingly popular during the last two decades, thanks to the substantial development in numerical methods and computing resources. Compared with experiments, CFD is relatively inexpensive and flexible, and it can potentially shorten the design cycle of the product by minimising the number of experimental tests. Validated 3-D CFD models can couple with 0-D or 1-D system simulation codes to provide high modelling capabilities [4]. There have been well-established CFD codes for analysing in-cylinder flow and combustion of IC engines, for examples: KIVA [5] and STAR-CD [6].

1.1.2 Vented flame deflagrations

Accidental release of flammable gas or vapour into a cloud may produce a combustible fuel-air mixture. In such a situation a combustion wave can be triggered if a suitable ignition source is present. It may subsequently lead to high overpressure in the presence of confinements and obstructions, depending on how much pressure expands away from the burned gases and how fast the flame travels.

Generally, a flame can propagate in two different modes through the flammable gas cloud: *(i)* deflagration and *(ii)* detonation. The most common mode is the deflagration where the flame front travels at subsonic (relative to the speed of sound in the unburned mixture) speed, typically of the order of $1 - 1000\ m/s$ [7]. In contrast, a detonation is a supersonic combustion wave coupled with a shock wave. In this case, the flame velocity can be $1500 - 2000\ m/s$ [7]. The consequences of gaseous explosion hazards often lead to the destruction of buildings, off-shore plants and equipment in process industries, and the damage caused by the initial overpressure is generally more severe than the ensuing fires.

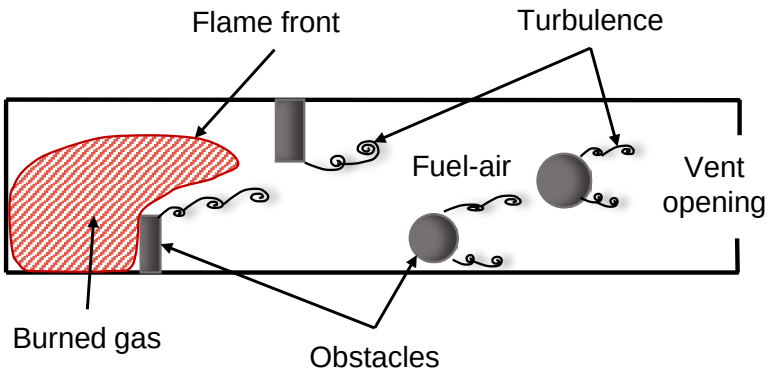

Figure 1.2: Schematic of turbulence generation by obstacles in a vented deflagration.

Figure 1.2 gives an example of how turbulence can be induced by obstacles and confinement

in a vented explosion. The deflagration normally starts out as a slow laminar flame, and it is likely to accelerate in a confined and obstructed (e.g. process equipment) environment. The evolution of flame acceleration due to turbulence generated from obstacles is responsible for many severe damages in real-world explosions.

Figure 1.3 briefly illustrates the mechanism of pressure build-up in partially-confined vented explosions with the presence of obstacles. During the combustion process for a typical hydrocarbon fuel, the burned gases can expand by a factor of up to 9 [7] and induce a turbulent flow field ahead of the flame front. The interaction between the flame and flow leads to an increase in the burning rate and flame velocity, which further strengthens the downstream turbulent flow field. The typical positive feedback mechanism of explosions results in considerable flame acceleration and large pressures and even transition to detonation in certain cases.

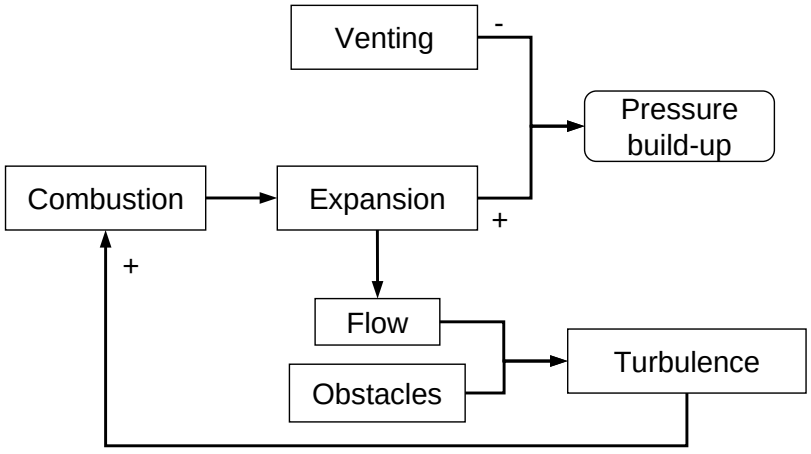

Figure 1.3: The mechanism of pressure build-up for a vented deflagration in the presence of solid obstructions. Promotion (+) or suppression (−).

Explosions in chemical process plants are physically sophisticated, and predicting the produced overpressure for safety guidance could be a challenging task. In the final report of the Buncefield incidence (Figure 1.4) [8], for example, the investigation board estimated that $700-1000$ *mbar* of overpressure would have been generated in the Northgate and Fuji car parks of the site, based on the degree of damage to the adjacent buildings. However, overpressure calculation using available simple models substantially underestimated the case, giving only up to about 50 *mbar* in a similar environment. It indicates the uncertainties in the overpressure predictions and the complex mechanisms involved in the explosion at the Buncefield scenario.

Parameters such as maximum explosion overpressure and its time of incidence are vital for design engineers and safety managers. Hence, there is a growing need for prediction and risk assessment tools for the safe design of many industrial structures and processes. Thus,

Figure 1.4: The gas explosion of the Buncefield incident. Image from [8].

accurate prediction and assessment of explosion is a challenging task. There have been several early attempts to use simple correlations and formulas for predictions of explosion pressures in compartments [7]. However, the typical weakness with such formulas is that they do not take into account turbulence generation and flame acceleration, therefore, the results can be an order of magnitude different from experiments [7]. The main advantage of such numerical calculations is the much cheaper computational cost compared to 3-D numerical simulations, and they also account for simple flame shapes and geometries. However, as a typical explosion in process industries often involves obstacles such as pipe racks or congested plants, such zero-dimensional models are generally unable to consider the effects of obstacle-generated turbulence and flame stretch. Applying CFD in chemical process plants safety is a relatively new research field. Thanks to the improvements in computational technology and resources, CFD is becoming a more attractive and reliable tool as an alternative to experiments in process industries. Commercial and open-source CFD codes such as FLACS [9] and Fire Dynamics Simulator (FDS) [10] were mainly developed for fire and explosions. Robust and efficient engineering design in process industries can also benefit from the combination of CFD and advanced statistical methods to optimise product performance by understanding the effects of various design factors. For example, it is possible to combine CFD and mathematical correlations to efficiently predict the explosion overpressure in a wide range of operating scenarios [11]. Compared with the conventional empirical approaches for design and decision making, new correlations proposed based on CFD are attractive to designers and engineers [12].

1.1.3 Hydrogen: features and safety

Hydrogen (H_2) as an alternative fuel and an energy carrier has many benefits due to its high heat value, renewable capability and the absence of harmful emissions [13]. The utilisation of hydrogen lies in hydrogen fuel cell electric vehicles [14, 15], hydrogen-fuelled internal combustion engines [16] and heating in buildings and industry [17]. However, some of its properties require additional engineering controls and considerations to ensure the safe use [18, 19]. As hydrogen is much lighter than air and rapidly dissipates when released, a leak often leads to fast mixing with surrounding air. Also, it has a wide range of flammability limits and relatively low ignition energy, making burning and accidental explosion of hydrogen-air mixtures more likely. The situation may be less severe in an open space since H_2 rises quickly into the atmosphere, but it can be a dangerous gas in confined or partially-confined regions involved in its production, storage, transport and end-user application [20].

Explosion hazards and safety issues while working with hydrogen has been a significant concern in its related storage, buildings and processing plants [19–22]. Compared with other common fuels such as methane (CH_4) and propane (C_3H_8), hydrogen explosions are potentially more dangerous due to its high combustion speed and excessively generated overpressure. The possibility of hydrogen leaks and subsequent explosions in situations such as tunnels and refuelling stations [19, 23] necessitates an improved understanding of the features and behaviours of hydrogen explosions. Yanez et al. [24] reported the production, discharge, accumulation and explosion of hydrogen during the Fukushima-Daiichi accident (March 11, 2011) and estimated the amount of hydrogen involved to be 130 kg. Based on the consequence of the explosion, they concluded that even with the a considerably smaller amount of H_2, a destructive explosion would have occurred.

Quantitative risk assessment (QRA) is becoming essential for the future safe design and operation of hydrogen-related systems including fuel tanks and stations. For the first time, the Sandia National Laboratories (SNL) has been developing a comprehensive software toolkit, namely the Hydrogen Risk Assessment Models (HyRAM), to provide QRA combining probability methods, physical models and consequence analysis (failure and risk metrics) [25]. Figure 1.5 is a methodology flowchart [25] showing modules for the two main hazards: jet fires and deflagrations combined with the models for hydrogen release. As illustrated by SNL [25], CFD-based physical models play an essential role in predicting the overpressure and impulse signals into the HyRAM interface. Furthermore, methods for protecting structures from in-

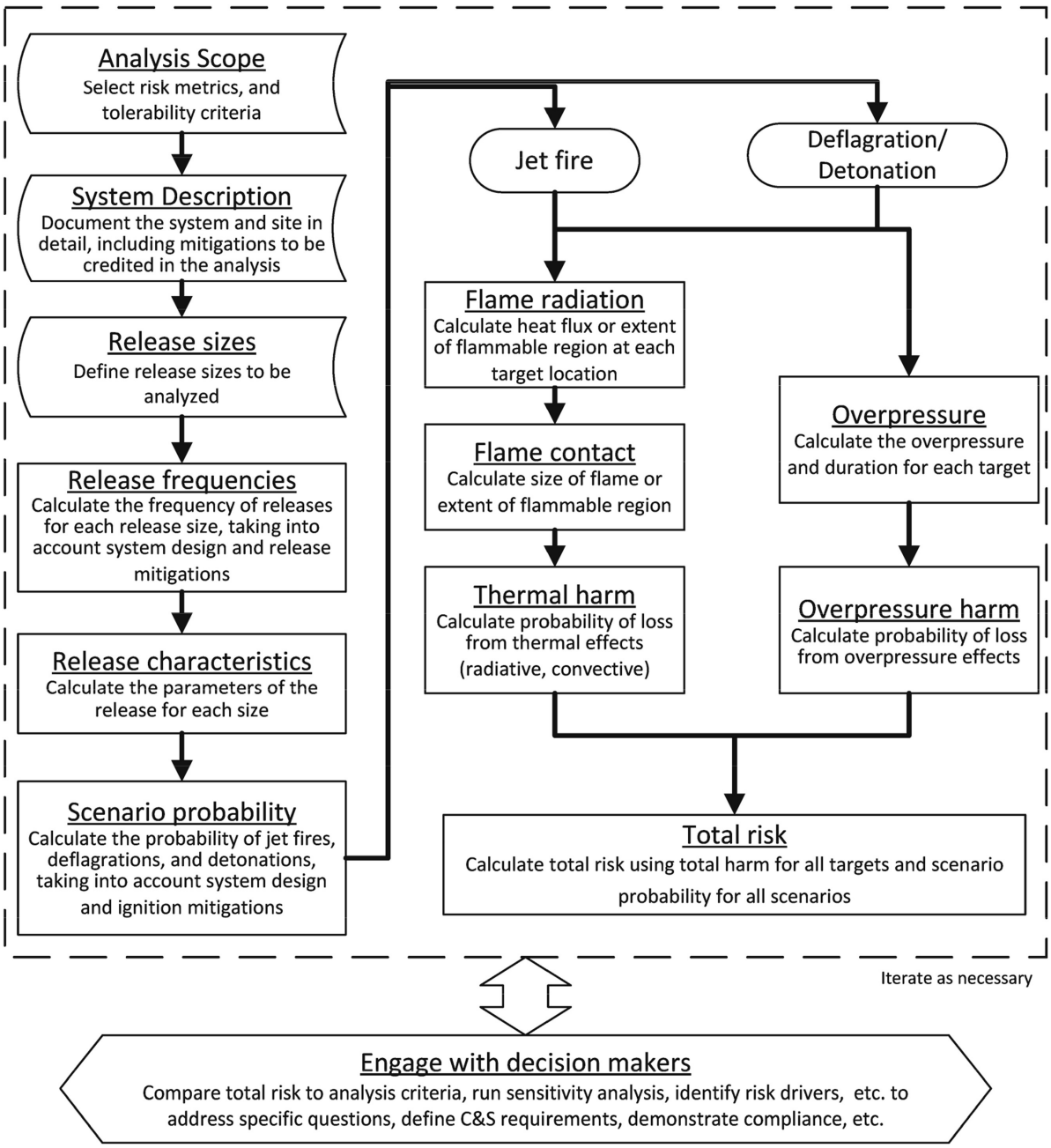

Figure 1.5: Illustration of the quantitative risk assessment tool: HyRAM. Reproduced from [25].

ternal explosions including venting and suppression require the knowledge of the explosion characteristics, and there is a demand for developing accurate and efficient CFD models in the hydrogen community. Overpressure and flame acceleration involved in a hydrogen explosion can be dependent on various conditions such as the hydrogen mass fraction in the flammable mixture, size of surrounding obstructions and the initial atmospheric condition. Therefore, it is necessary to study a range of scales and conditions for the estimation of hydrogen explosion hazards.

1.2 Computational approaches for turbulent combustion

The description of turbulent combustion using CFD may be divided into three categories: direct numerical simulation (DNS), Models for Reynolds-averaged Navier-Stokes (RANS) equations and large eddy simulation (LES) [26]. Figure 1.6 summarises the properties of the three methods using an energy spectrum. DNS resolves the whole of the turbulence spectrum, as shown in Figure 1.6. It is expected to give the most accurate results but is limited only for academic flows (e.g. combustion in a small cubic domain) due to the excessive computational cost. The use of RANS based models is commonly accepted in industries due to their relatively low computational cost and moderate accuracy, e.g. the KIVA code for engine simulation [5] and the FLACS software for gas explosions in buildings and off-shore process plants [27]. LES, in general, is accepted as the next generation tool for turbulence modelling. It has been able to bridge the gap between classical RANS modelling and expensive DNS to a certain extent. The use of LES has become increasingly popular as a more reliable prediction tool than RANS for simulating complex flow phenomena encountered in various engineering applications, e.g. the commercial code FDS [10] applies LES to study fire and explosions. Figure 1.7 gives an example of computed temperature signals at one point of the computational domain from DNS, RANS and LES for a stationary flame.

1.2.1 DNS

On a DNS mesh, the three-dimensional instantaneous Navier-Stokes equations are directly solved, providing that all the turbulence scales, as well as their effects on combustion, are explicitly determined. In principle, a DNS grid must be fine enough to resolve the smallest eddies which are of the size of the Kolmogorov length scale $\ell_\kappa = \left(\nu^3/\epsilon\right)^{1/4}$ [29], where ν and ϵ are the kinematic viscosity and dissipation rate of turbulent kinetic energy, respectively. Also, the Kolmogorov time scale $\tau_k = (\nu/\epsilon)^{1/2}$ limits the time step Δt used in the simulation [29].

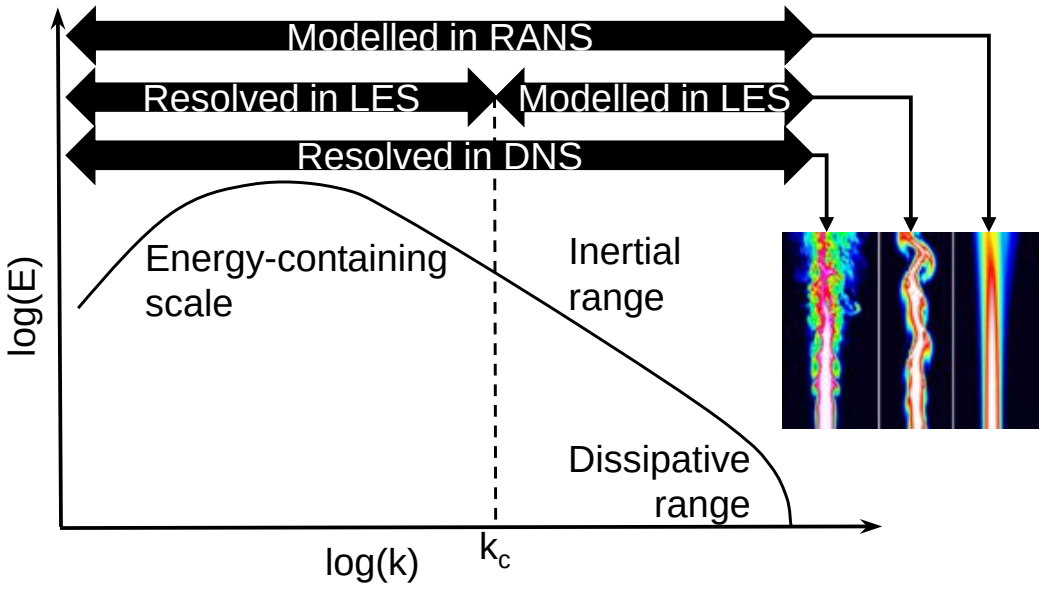

Figure 1.6: Turbulence energy (E) spectrum as a function of wave number (k). k_c is the cut-off scale for LES. Characteristic results are also shown from the computations of a turbulent jet using DNS, LES and RANS, respectively [28].

On top of that, as the inner flame structure (for premixed flames) has also to be resolved, a sufficient number of grid points (at least 20 with simple chemistry [26]) are required in the flame front. Hence, the demanding computation makes DNS constrained to flows with low Reynolds numbers and simplified geometries. For a stationary flame given in Figure 1.7, DNS based simulations would produce all the time variations of temperature, similar to a high-resolution experimental probe.

1.2.2 RANS

RANS based computation requires solving for a Reynolds averaged set of conservation equations, modelling all turbulent motions in the energy spectrum. Since it only calculates mean quantities, a RANS mesh is significantly coarser than DNS, allowing for faster computations. Typically, the unclosed Reynolds stress terms require a turbulence model such as the famous $k-\epsilon$ model [29], and the mean reaction rate needs closing with a combustion model. Figure 1.7 shows a constant temperature computed by (steady-state) RANS in a stationary system, referring to the mean value at the point. Compared with DNS results, the mean flow characteristics captured in RANS appears to be smoother.

Transient solutions are available with the inclusion of the unsteady terms in the RANS equations, and this may be referred to as (unsteady) RANS (URANS). This technique is still the industry standard for applications such as gas turbines, piston engines and explosions. Due to the nature of the time-averaged approximation to the conservation equations of fluid

dynamics, RANS models give the smoothed appearance of the results even in highly resolved simulations, e.g. Figure 1.6. Consequently, the evolution of large eddy structures of flames and the local transient events are lost.

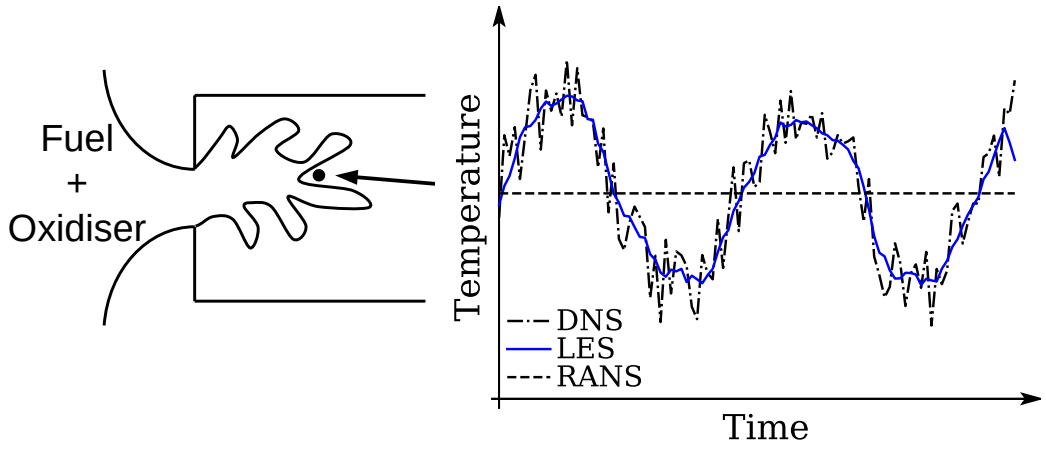

Figure 1.7: An example of the local temperature computed by RANS, LES and DNS.

1.2.3 LES

Applying the LES technique to combustion aims to achieve greater spatial and temporal fidelity on finer grids by faster computers. It lies between DNS and RANS where large scales of turbulent motions are explicitly calculated while the effects of smaller eddies are modelled. This approach involves solving for a set of filtered governing equations derived by applying a low-pass filter. Sub-grid models for turbulence and combustion are required to account for the scales lost in the filtering process. As shown in Figure 1.7, LES captures low-frequency temperature variations compared to DNS.

LES is now accepted as an accurate computational tool in predicting critical characteristics of turbulent combustion. It has a clear advantage over the classical RANS based methods in the capability of accounting for time-varying nature of the flow in situations such as combustion instabilities and cycle-to-cycle variations in IC engines. This feature is particularly useful in transient processes such as propagating premixed flames described in Sections 1.1.1 and 1.1.2. As the majority of industrial combustion processes are highly sophisticated, developing new and improving existing combustion sub-models for LES is essential.

1.3 Objectives and thesis outline

Reliable LES simulations are often limited by the accurate sub-models to account for various time and length scales of turbulence and their interaction with the flame. Among currently available models for turbulent premixed combustion, the flame surface density (FSD) based models are attractive due to the simplicity and robustness.

The objective of the present study is twofold: (*i*) to assess the capability of a newly implemented dynamic flame surface density (DFSD) model in predicting transient premixed combustion; (*ii*) to investigate the underlying physics and mechanisms of propagating flames with the presence of obstructions. Specific objectives and efforts of this thesis are described as follows.

Chapter 2 outlines the fundamental features of turbulent premixed flames and the various sub-grid models available. A brief list of formalism for calculating FSD and wrinkling factor is included, and the dynamic modelling of FSD is discussed. Next, different methods for initialising combustion are reviewed. Then, the literature about hydrogen simulation and propagating flames with obstacles is reviewed.

Chapter 3 presents the governing equations and the combustion model used for the present study. A brief introduction to the conservation equations for reacting flows and the LES filtering approach is given, followed by the description of the DFSD model. Methods of flame initiation investigated in this work are also included.

Chapter 4 describes the numerical methods adopted in this work. The main elements of the in-house code PUFFIN including spatial discretisation, pressure correction algorithm and boundary conditions are introduced. Then, the implementation of the current combustion and ignition models is outlined. The computational set-up is first tested in a series of 1-D laminar cases, and the results are presented to justify the correct model behaviour when the turbulence effect vanishes.

Chapter 5 includes the experimental test cases considered for model validation. A wide range of flow configurations is used to investigate the influence of obstacles and the model performance. Averaging of pressure signals and the uncertainties in experiments are discussed.

Chapter 6 presents the results using the stoichiometric propane/air mixture. A comprehensive parametric study is conducted to investigate the sensitivity to model factors including ignition modelling, filter width, Smagorinsky constant and mesh resolution. The flame propagation and pressure rise are investigated phenomenologically, and two families of flow configu-

rations are used to illustrate the effect of obstructions. Another focus is the flame-turbulence interactions interpreted by the sub-grid wrinkling factor and the LES regime of combustion.

In Chapter 7, the results of lean hydrogen/air mixtures are presented. The effect of location, number and size of the obstacles is discussed. Lastly, a comparison is given among the three fuels (propane, methane and hydrogen) regarding the combustion characteristics and model performance.

Finally, Chapter 8 summarises the conclusions from the present work with critical contributions towards the prediction capabilities, understanding transient flame propagation. Suggestions are given for further extensions of the in-house code and future direction of research.

Chapter 2

Literature Review

This chapter reviews the essential elements needed to describe and model turbulent premixed combustion and lays the theoretical foundation for the work conducted in this thesis. Section 2.1 outlines the features and mathematical descriptions of turbulent premixed flames. Section 2.2 includes an overview of the available modelling approaches for the filtered chemical source term in LES. The algebraic flame surface density models and the dynamic formalisms are specifically discussed in Section 2.3. Section 2.4 explores the methods of initialising combustion, and the suitable options for the present study are identified. Finally, some of the previous experimental and numerical work regarding flame propagation with obstacles are described in Section 2.5.

2.1 Turbulent premixed flames: general features

Premixed combustion takes places when the fuel and oxidiser are mixed prior to ignition. A propagating flame front travelling towards the turbulent unburned flows, and their interactions can greatly alter the characteristics of the flame. Rather than reviewing the vast and complex subjects of chemical kinetics and turbulence, the focus of this section is on the features of flame-turbulence interactions and the resulting regime diagrams of turbulent premix combustion.

2.1.1 Interactions between flows and flames

Turbulence and flames have a two-way interaction. On the one hand, turbulence is altered by combustion due to the strong flow acceleration through the flame front. It is induced by the heat release generated from the chemical process. On the other hand, the flame structure can be modified by turbulent eddies of different sizes. The approach to study turbulent flames is greatly based on the understanding of laminar flames. There are two important properties for an unstrained laminar flame: the burning velocity (s_L^0) and the flame thickness (δ_L^0), respectively. Recall that the laminar premixed combustion manifests itself as the propagation of a thin (δ_L^0

of the order of 0.1 mm) flame front in a mixture of fresh reactants, the burning velocity s_L^0 for a usual hydrocarbon/air flame at standard condition is of the order of $0.2 - 1\ m/s$. In turbulent premixed combustion, the flame front can travel at a speed of tens to hundreds of meters per second due to the influence of turbulent eddies, and the interaction may strongly increase the overall flame speed and thickness.

2.1.1.1 The influence of flames on flows

The flame front in premixed combustion separates the cold unburned and hot burned gases. The flow pattern may be changed in certain scenarios because of the thermal expansion. For a turbulent flame, the strong flow acceleration across the flame front resulting from the density ratio of the unburned and burned gases ($\rho_u/\rho_b \approx 8$ for a common hydrocarbon fuel/air mixture) may subsequently modify the vorticity and turbulent flow field. On the other hand, as the temperature considerably changes from the unburned to the burned side ($300 - 2000\ K$), the kinematic viscosity ν increases significantly, resulting in a much smaller local Reynolds number in the burned gases compared with the fresh mixture. This phenomenon may lead to relaminarisation of a turbulent flow after ignition [26].

2.1.1.2 The influence of turbulence on flames: wrinkling

The main mechanism controlling the turbulent premixed flame is wrinkling. As illustrated in Figure 2.1, the flame surface can be distorted by the incoming turbulent eddies of various length scales. It results in an increase in the flame surface and an overall enhancement of the mass consumption rate. The increase of the turbulent flame speed s_T due to the growth in the total flame surface A_T is $s_T \propto A_T s_L^0$.

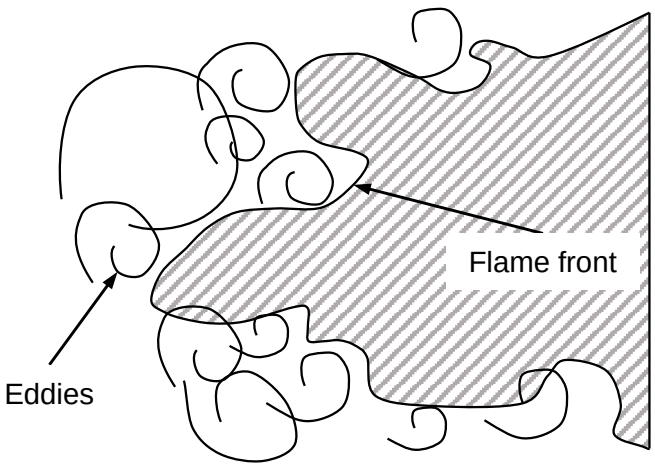

Figure 2.1: Illustration of flame wrinkling by turbulence. The flame surface is distorted by turbulent eddies of various scales. The dark area denotes the burned gases. The flame front propagates from right to left.

2.1.2 Regimes of turbulent premixed combustion

Turbulent premixed combustion is often described as the interaction between a flame front and eddies of various sizes, from Kolmogorov (ℓ_κ) to integral (ℓ_0) scales. Combustion regimes diagrams identified by various velocity and length scales are important to justify the turbulence influences on flames and validity of turbulent combustion models. Diagrams have been proposed by Borghi [30], Peters [31], Abdel-Gayed et al. [32], and Poinsot et al. [33]. They indicate essential information whether the flows contain flamelets, pockets or distributed reaction zones. In this section, an updated regime diagram by Peters [34] and an LES version by Pitsch and De La Geneste [35] are presented. The three non-dimensional numbers, namely the turbulent Reynolds (Re_t), Damköhler (Da) and Karlovitz (Ka) numbers [36] are used to differentiate various regimes of combustion. The turbulent Reynolds number based on integral length scale characteristics is defined as

$$Re_t = \frac{u'\ell_0}{\nu} = \frac{u'\ell_0}{s_L\delta_L} \tag{2.1}$$

where u' is the root-mean-square (RMS) velocity. Note that in Eq. (2.1), the flame thickness is defined as $\delta_L = D/s_L$ [36] and the Schmidt number $Sc = \nu/D$ is taken as unity. The Damköhler number is expressed as the ratio of the integral time scale (τ_0) of turbulence and chemical or flame (τ_c) time scale:

$$Da = \frac{\tau_0}{\tau_c} = \frac{s_L\ell_0}{u'\delta_L} \tag{2.2}$$

The chemical reaction process is much slower than the turbulent mixing rate when $Da \ll 1$, and this condition corresponds to a well-stirred reactor where nearly all of the turbulent eddies are embedded in the reaction zone. In contrast, if $Da \gg 1$, it defines a fast-chemistry regime, and the flame may be seen as 'flamelets'. The Karlovitz number is defined as the ratio between the flame time scale ($\tau_c = \delta_L/s_L$) and Kolmogorov time scale τ_κ,

$$Ka = \frac{\tau_c}{\tau_\kappa} = \frac{\delta_L^2}{\ell_\kappa^2} \tag{2.3}$$

It is useful to define a second Karlovitz number based on the inner reaction zone thickness ℓ_δ as

$$Ka_\delta = \frac{\ell_\delta^2}{\ell_\kappa^2} \approx 0.01Ka \tag{2.4}$$

assuming the inner layer thickness $\ell_\delta \approx 0.1\delta_L$ [36, see Eq. (1.100)].

The classical Peters regime diagram [34] is shown in Figure 2.2. Two flamelet regimes are of practical interest: corrugated flamelets (CF) and thin reaction zones (TRZ). In the former regime, the Kolmogorov scale is still larger than the laminar flame thickness ($\delta_L < \ell_\kappa$), meaning that the entire flame structure is not disturbed by turbulence. While in the thin reaction zone, the smallest eddies of the Kolmogorov length scale can enter into the flame structure since $\ell_\kappa < \delta_L$. However, they are still larger than the inner layer thickness ℓ_δ, therefore, cannot penetrate into the reaction zone ($Ka_\delta < 1$). The smallest eddies enter the preheat zone and enhance scalar mixing but do not penetrate the inner layer. The broken reaction zone (BRZ) corresponds to the region beyond the line $Ka_\delta = 1$ when mixing is faster than chemistry and Kolmogorov eddies are smaller than the inner layer thickness. The BRZ regime is usually avoided in fully premixed combustion systems, as the small eddies may enter the inner layer and perturb it with the possibility of local extinction [36].

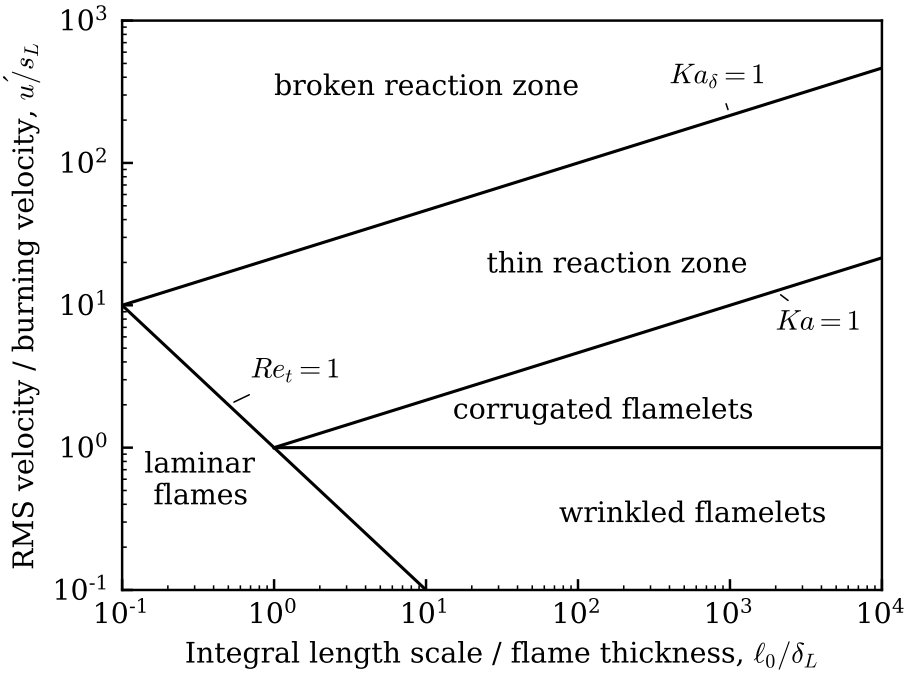

Figure 2.2: Regime diagram of Peters [34] for turbulent premixed flames (reproduced from [34])

The Peters diagram requires physical quantities such as u' and ℓ_0 which are not available in an LES simulation. Since the focus of this work is on combustion modelling in the LES context, the regime diagram for LES constructed by Pitsch [37] is presented below, which uses the filter width as a unique parameter. In the LES diagram, the non-dimensional groups are defined in terms of the filter width Δ and the characteristic sub-grid velocity fluctuation u'_Δ

as

$$Re_\Delta = \frac{u'_\Delta \Delta}{s_L \delta_L}, \qquad Da_\Delta = \frac{s_L \Delta}{u'_\Delta \delta_L} \tag{2.5}$$

To evaluate the Karlovitz number in Eq. (2.3), an estimation of the dissipation rate ϵ is required. From dimensional arguments

$$\epsilon = \frac{\nu^3}{\ell_\kappa^4} \tag{2.6}$$

and the following scaling relation can be obtained with the assumption of constant Schmidt number $\nu = D = s_L \delta_L$ [35]:

$$\epsilon = \frac{u'^3}{\ell_0} = \frac{u'^3_\Delta}{\Delta} = \frac{(s_L \delta_L)^3}{\ell_\kappa^4} \tag{2.7}$$

Finally, the Karlovitz number Ka (Eq. (2.3)) in the diagram can be rewritten as [35]

$$Ka = \sqrt{\frac{\delta_L}{s_L^3}\epsilon} = \sqrt{\left(\frac{u'_\Delta}{s_L}\right)^3 \frac{\delta_L}{\Delta}} \tag{2.8}$$

A second Karlovitz number, Ka_δ, can be defined similarly based on the thickness of the inner layer of the reaction zone (Eq. (2.4)). The important point is that the Karlovitz number is independent of Δ and is based entirely on the physical quantities. Eq. (2.8) implies how u'_Δ is influenced by the variations in the filter width as a result of constant Karlovitz number, but practically, as u'_Δ is a modelled quantity in LES, the changes may not match the variation in Δ to maintain a constant Ka. The Gibson scale $\ell_G = s_L^3/\epsilon$ is also introduced to divide the diagram further.

Figure 2.3 contains the information on LES regime diagram and gives some insights into combustion modelling. Moving horizontally in the diagram alters turbulence/chemistry interaction with constant Δ, while the effect of filter width with the same physical parameters can be investigated by moving vertically. Reducing Δ would result in a decrease in u'_Δ, as can be seen from Eq. (2.8). A change in Δ does not alter the combustion regime across $Ka = 1$ and $Ka_\delta = 1$, i.e. between any of CF, TRZ and BRZ regimes. In order to illustrate the implications of this diagram, the modelled part of the combustion process is assumed to be in the CF regime, for example, $\Delta/\delta_L = 500$ and $Ka = 0.2$. When Δ is reduced below ℓ_G, u'_Δ would be less than s_L. Then, the modelled part of combustion will enter into the wrinkled

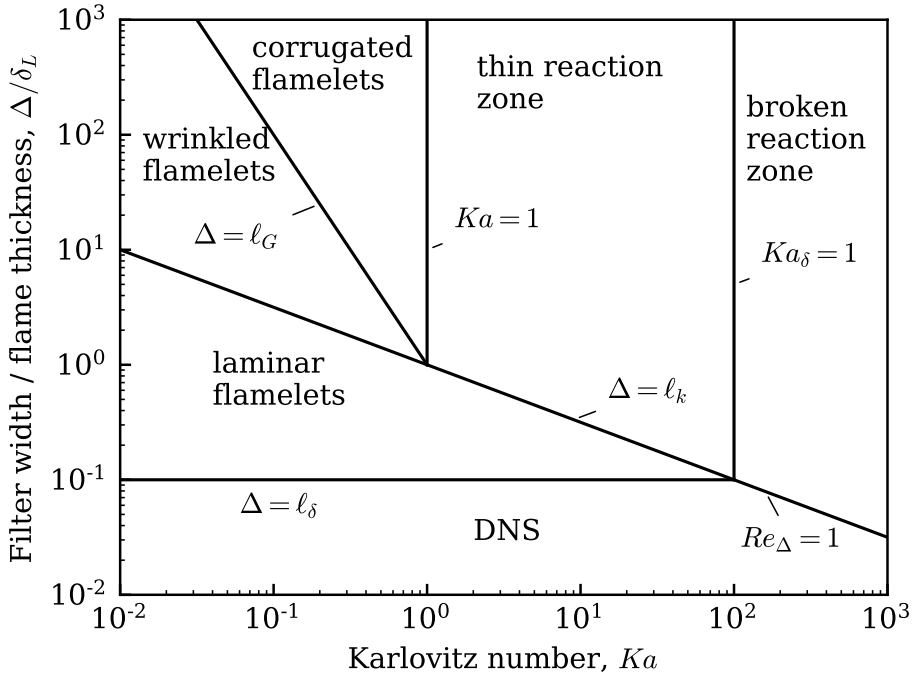

Figure 2.3: Regime diagram of Pitsch and De La Geneste [35] for LES of turbulent premixed flames (reproduced from [35]).

flamelets regime. Since a smaller filter width accompanies with a more substantial resolved part of the flame, the corrugated flamelets are now at resolved scales.

Decreasing the filter width further when $\Delta < \ell_\kappa$, all the turbulence is resolved in this laminar flamelets regime. However, the filter width is still larger than the reaction zone thickness ($\Delta > \ell_\delta$), meaning that not all of the flame is resolved. When $\Delta < \ell_\delta$, the length scale of the reaction zone is resolved, and the simulation essentially reaches the DNS limit. Clearly, the regime diagram for LES (Figure 2.3) illustrates the turbulence-chemistry interaction of the modelled part of the combustion and the influence of the characteristic sub-grid length scale Δ.

2.2 Overview of premixed combustion models

Models of premixed combustion for RANS have been used for a few decades, while the development of LES combustion models is still at an early stage. As a direct numerical simulation for the 3-D unsteady turbulent premixed flame would be too expensive to perform under the present computational power, models have been proposed to provide a prediction of essential characteristics of the problem. Sub-models based on the flamelet concept are cases where physical insights have been used to simplify the problem. It regards a turbulent premixed flame as laminar flamelets embedded in a turbulent flow field and was initially proposed in the

RANS context. It is typically applicable in situations of large Da with turbulent eddy scales larger than the flame thickness. Flamelet modelling often uses a reaction progress variable c to describe the progress of the chemical reaction in the flame front, and it may be defined as the non-dimensional fuel mass fraction or temperature between the unburned and burned gases. While a complete set of governing equations will be presented in Chapter 3, the transport equation for filtered $\widetilde{c}$ in LES is described here to facilitate the subsequent discussions:

$$\frac{\partial \overline{\rho}\widetilde{c}}{\partial t} + \frac{\partial (\overline{\rho}\widetilde{u}_i\widetilde{c})}{\partial x_i} + \frac{\partial}{\partial x_i}\overline{\rho}\left(\widetilde{u_i c} - \widetilde{u}_i\widetilde{c}\right) = \overline{\frac{\partial}{\partial x_i}\left(\rho D \frac{\partial c}{\partial x_i}\right)} + \overline{\dot{\omega}}_c \tag{2.9}$$

where $\overline{\dot{\omega}}_c$ represents the filtered reaction rate, and it is the main challenge of modelling the turbulent premixed combustion. The following sections provide an overview of the various approaches for modelling turbulent premixed flames. The statistical methods [38] such as probability density function and conditional moment closure are of less relevance to the present work and are thus not included.

2.2.1 Difficulties in LES of turbulent premixed combustion

Figure 2.4 shows a difficulty of applying LES in premixed combustion: the thickness of the flame (δ_L^0) is usually only a fraction of 1 mm, and it is generally much smaller than a typical LES mesh size Δx. It means that typically no portion of the filtered chemical source term can be resolved in LES [39]. Therefore, the modelling effort comes to the representation of the filtered reaction rate in the governing equations, for example, the source term $\overline{\dot{\omega}}_c$ in Eq. (2.9). When the flame is thinner than the LES grid size, solving for the progress variable c is fairly stiff in space and can lead to numerical issues [26]. Three main techniques have been proposed to overcome the issue: (*i*) use a flame-tracking method such as the G-equation [35, 37, 40]; (*ii*) compute an artificially thickened flame instead [41–44]; (*iii*) solve for a filtered flame instead, with a filter larger than the mesh size [45–49].

It is worth noting the distinction between modelling turbulence and combustion. In momentum transport, most of the turbulence energy lies in large or resolved scale motions, leaving the small scales modelled. However, combustion is mostly a sub-grid scale (SGS) phenomenon, and this implies the difficulty of treating it properly.

2.2.2 "No model" approach

This most straightforward approach in RANS is to completely neglect the effects of turbulence on combustion and express the mean reaction rate only in terms of the mean temperature

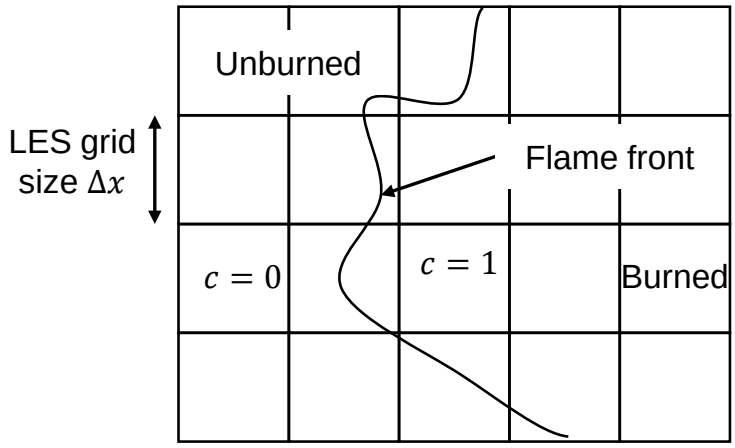

Figure 2.4: Issue of resolving the flame front on an LES mesh: the flame is thinner than the mesh grid.

or mass fraction [26]. In LES, this corresponds to computing the filtered reaction rate only as a function of resolved quantities (e.g. $\widetilde{c}$), neglecting the sub-grid contributions. Assuming single-step chemistry with the Arrhenius form, the filtered reaction rate can be expressed as

$$\begin{aligned}\overline{\dot{\omega}}_c \approx \dot{\omega}(\widetilde{c}) &= -A_c\overline{\rho}\,(1-\widetilde{c})\exp\left(\frac{-T_a}{\widetilde{T}}\right)\\ &= -A_c\overline{\rho}\,(1-\widetilde{c})\exp\left[\frac{-T_a}{T_u+\widetilde{c}(T_b-T_u)}\right]\end{aligned} \tag{2.10}$$

where A_c is the pre-exponential constant and T_a is the activation temperature. This method is only relevant when the chemistry has a much larger time scale than turbulence (i.e. low Damköhler number limit), e.g. Nieuwstadt and Meeder [50] have simulated the chemical reactions in atmospheric boundary layers using this approach. However, the approach is inadequate in most of the cases for turbulent combustion [26]. Nevertheless, this highlights the importance of accounting for the sub-grid effect of the turbulence on combustion.

2.2.3 Eddy-break-up (EBU) model

The classical RANS closures such as the EBU model, first proposed by Spalding [51], can be extended to the LES context as [52]

$$\overline{\dot{\omega}}_c \approx C_{EBU}\frac{\Delta}{\sqrt{k_{sgs}}}\overline{\rho}\widetilde{c}(1-\widetilde{c}) \tag{2.11}$$

where C_{EBU} is flow-dependent model constant, and the sub-grid turbulent kinetic energy k_{sgs} may be estimated from an algebraic expression or a balance equation. A typical drawback of

this method is that the model constant C_{EBU} requires adjustment from case to case.

2.2.4 Level-set (G-equation)

The G-equation formalism may be seen as a numerical technique rather than a model. It avoids resolving a too thin flame front by treating the flame thickness as zero, and the flame front is indicated by a tracking field variable G [26]

$$\frac{\partial \overline{\rho}\widetilde{G}}{\partial t} + \frac{\partial \overline{\rho}\widetilde{u}_i\widetilde{G}}{\partial x_i} = \rho_u \overline{s}_T |\nabla \overline{G}| \tag{2.12}$$

where $\overline{s}_T$ is the SGS turbulent burning velocity requiring closure, and it is generally based on [26]:

$$\frac{\overline{s}_T}{s_L} = 1 + \alpha_g \left(\frac{u'_\Delta}{s_L} \right)^n \tag{2.13}$$

where u'_Δ is the SGS turbulence level. The constants α_g and n in Eq. (2.13) are specified by the user. The variable G usually identifies a signed distance from the flame front, and it can be smoothed out to be resolved on the LES mesh [39]. The level-set approach provides information only on the flame front but not on the structure, and the coupling with the flow equations is still challenging [40].

2.2.5 Artificially thickened flames

The artificially thickened flame model for LES (TFLES) was directly derived from RANS and has been used by many researchers [41, 42, 53, 54]. The key idea of the thickened flame model is to thicken the flame so that it can be well resolved numerically but keep the same laminar burning velocity [41, 42, 44]. The following relation can be obtained from the laminar flame theory [55]:

$$s_L \propto \sqrt{D\overline{\dot{\omega}}} \qquad \text{and} \qquad \delta_L \propto \frac{D}{s_L}.$$

Thickening can be achieved practically by replacing thermal and molecular diffusivity D with FD, and the reaction rate $\overline{\dot{\omega}}$ by $\overline{\dot{\omega}}/F$ where F is the thickening factor. Consequently, the flame is thickened from δ_L to $F\delta_L$ while s_L is kept constant. For sufficiently large F, the flame can be resolved on the LES grid. The thickened flame approach is attractive from the numerical point of view. The actual flame is replaced by a thicker laminar one without filtering hence sub-grid-scale models may not be required [41]. The chemical reactions described by Arrhenius

law can be maintained, and various phenomena such as ignition and flame/wall interactions may be directly accounted for without ad-hoc sub-models [26].

However, the interaction between turbulence and chemistry is modified as the flame is thickened from δ_L to $F\delta_L$ due to the change in Damköhler number. Da is decreased by a factor of F to D/F, therefore, the flame and turbulence interaction may be modified. This means that the thickened flame becomes less sensitive to the wrinkling induced by turbulent eddies, and consequently, less flame surface area is generated compared to that of the un-thickened flame. An efficiency function Γ_Δ or an effective wrinkling factor Ξ is derived and added to the diffusion and reaction rate terms to tackle this drawback [41, 56]. For practical implementation, for example, in the context of a progress variable (or fuel mass fraction), the transport equation may take the form [41, 52, 56]:

$$\frac{\partial\widetilde{\rho c}}{\partial t}+\frac{\partial(\widetilde{\rho u_i c})}{\partial x_i}=\frac{\partial}{\partial x_i}\left(\rho DF\Gamma_\Delta\frac{\partial\widetilde{c}}{\partial x_i}\right)+\frac{A}{F}\overline{\rho}\Gamma_\Delta(1-\widetilde{c})exp\left(-\frac{T_a}{\widetilde{T}}\right) \tag{2.14}$$

The central problem of applying TFLES is to evaluate the efficiency function Γ_Δ in Eq. (2.14) and comprehensive discussions have been given by Colin et al. [41] and Charlette et al. [56].

2.2.6 Flame surface density

Flame surface density methods have been extensively used for RANS simulations [38] and were first introduced to LES by Boger et al. [45]. Their argument is that even though the flame front (i.e. the gradient of c) is too thin to be resolved on an LES grid, the filtered progress variable $\widetilde{c}$ may be resolved using a spatial filter with the size Δ greater than the mesh size Δx. The flame surface density Σ is defined as the available flame area per unit volume [38]. It can either be modelled by solving for an additional transport equation [56–60] or using an algebraic formalism [42, 45, 46, 61, 62]. For example, the unclosed Σ transport equation derived by Hawkes and Cant [57] has the form:

$$\frac{\partial\Sigma}{\partial t}+\frac{\partial\widetilde{u}_i\Sigma}{\partial x_i}=-\frac{\partial(\overline{(u_i)}_s-\widetilde{u}_i)\Sigma}{\partial x_i}+\overline{(a_T)}_s\Sigma-\frac{\partial\overline{(wN_i)}_s\Sigma}{\partial x_i}+\overline{\left(w\frac{\partial N_i}{\partial x_i}\right)}_s\Sigma \tag{2.15}$$

where N_i is the local normal direction, a_T denotes the surface strain due to the fluid flow, $\overline{(...)}_s$ represents averaging over the flame surface, and w is the local relative propagation speed. The RHS terms of Eq. (2.15) require closure.

On the other hand, the algebraic models generally relate Σ with a sub-grid wrinkling factor Ξ, i.e. $\Sigma=f(\widetilde{c},\Xi)$. Ξ can be assumed to be a constant depending on the flow condition

[48], solved from a transport equation [63] or determined dynamically from the resolved flame information [47] As the algebraic FSD approach is adopted for the present study, it is further discussed in Section 2.3.

2.3 Algebraic flame surface density models

The purpose of applying algebraic FSD models is to avoid solving for a transport equation for Σ where more unclosed terms would appear. Algebraic models are generally efficient and relatively easy to implement. They can also benefit from a dynamic procedure where model constant may be determined on-the-fly. In this section, some of the available algebraic models are reviewed, with the focus of Boger et al. [45] based models and their refinement in the past few years. In LES, the filtered equation for c is recast here as

$$\underbrace{\frac{\partial \overline{\rho}\widetilde{c}}{\partial t}}_{\text{temperal}} + \underbrace{\frac{\partial}{\partial x_i}\left(\overline{\rho}\widetilde{u}_i\widetilde{c}\right)}_{\text{convection}} = -\underbrace{\frac{\partial}{\partial x_i}\left(\overline{\rho u_i c} - \overline{\rho}\widetilde{u}_i\widetilde{c}\right)}_{\text{unresolved flux}} + \underbrace{\overline{\frac{\partial}{\partial x_i}\left(\rho D \frac{\partial c}{\partial x_i}\right)}}_{\text{molecular diffusion}} + \underbrace{\overline{\dot{\omega}}_c}_{\text{reaction rate}} \tag{2.16}$$

The RHS terms of Eq. (2.16) require modelling. The filtered molecular diffusion and reaction rate terms can be combined as a single flame-front displacement term [38, 45, 64]

$$\overline{\nabla \cdot (\rho D \nabla c)} + \overline{\dot{\omega}}_c = \overline{\rho w |\nabla c|} \tag{2.17}$$

with w being the displacement speed of the iso-c surface. As a first step, Boger et al. [45] proposed an algebraic expression to close the displacement term.

2.3.1 Boger's algebraic model

Most of FSD based methods for LES originate from the study of Boger et al. [45], which is discussed in this section. By defining a sub-grid-scale flame surface density (flame surface per unit volume) $\Sigma = \overline{|\nabla c|}$, the flame front displacement term in Eq. (2.17) can be written as

$$\overline{\rho w |\nabla c|} = \langle \rho w \rangle_s \, \Sigma = \langle \rho w \rangle_s \, \Xi |\nabla \overline{c}| \tag{2.18}$$

where $\langle ... \rangle_s$ represents the surface average. Ξ is the sub-grid-scale flame wrinkling factor (i.e. the sub-grid flame surface divided by the projected surface in the propagating direction) defined as

$$\Xi = \overline{|\nabla c|} / |\nabla \overline{c}| \tag{2.19}$$

such that

$$\Sigma = \Xi|\nabla\overline{c}| \tag{2.20}$$

and $\Xi = 1$ for a plane flame front. Assuming laminar flame elements the surface average term can be defined as

$$\langle \rho w \rangle_s \approx \rho_u s_L \tag{2.21}$$

where ρ_u and s_L are unburned gas density and laminar flame speed, respectively. This derivation leads to the expression for the displacement term in Eq. (2.17):

$$\overline{\rho w|\nabla c|} \approx \rho_u s_L \Sigma = \rho_u s_L \Xi|\nabla\overline{c}| \tag{2.22}$$

It is important to mention that not only Ξ requires modelling but $|\nabla\overline{c}|$ also needs closure as $\overline{c}$ is an unknown quantity from the transport equation of $\widetilde{c}$. Boger et al. [45] proposed a simple algebraic expression by filtering the DNS data:

$$\Sigma = 4\sqrt{\frac{6}{\pi}}\Xi\frac{\overline{c}\,(1-\overline{c})}{\Delta} \tag{2.23a}$$

or simply expressed as

$$\Sigma = 4\alpha\frac{\overline{c}\,(1-\overline{c})}{\Delta} \tag{2.23b}$$

where Δ is the filter width and $\alpha = \sqrt{\frac{6}{\pi}}\Xi$ is a model coefficient. Eq. (2.23b) approximates the flame surface density as a parabolic function of $\widetilde{c}$. In Eq. (2.23b), Δ/α represents the degree of flame wrinkling [65] and is subject to change based on mesh resolution, etc. [66].

2.3.1.1 Practical considerations

Two possibilities arise for calculating Σ in LES: (i) use Eq. (2.20) with an additional closure for Ξ [67, 68]; (ii) use Eq. (2.23b) and specify α prior to the simulation. In fact, the majority of Σ models have the formulation of Eq. (2.20) and only differ due to the evaluation for Ξ. Hence, the expression of Eq. (2.23b) essentially approximates the term $\Xi|\nabla\overline{c}|$ using a parabolic function which assembles the classical Bray-Moss-Libby (BML) formula in RANS [69, 70]. However, there is a concern that the un-weighted filtered progress variable $\overline{c}$ in Eq. (2.20) is not

directly available from LES. A relation between the un-weighted $\overline{c}$ and mass-weighted $\widetilde{c}$ needs to be provided, and this may be obtained using an expression similar to the BML formulation [70] or an extended version for LES proposed by Chakraborty and Cant [71]. The formalism of Eq. (2.20) has been used to study transient premixed flames by Di Sarli et al. [72] and Di Sarli et al. [73, 74].

The unresolved scalar flux term in Eq. (2.16) is usually modelled using a simple gradient expression

$$\overline{\rho}(\widetilde{u_i c} - \widetilde{u}_i \widetilde{c}) = -\frac{\mu_t}{Sc_t} \tag{2.24}$$

with the turbulent viscosity and Schmitt number denoted as μ_t and Sc_t, respectively. However, it also contains a contribution from the counter-gradient transport (CGT) (i.e. with a sign opposite to the prediction using Eq. (2.24)) [45, 61], and it is promoted with higher heat release factor [45]. Some researchers (such as Ma et al. [62]) recommended the use of a simple explicit CGT model to avoid unintended flame thickening occurring in their work. The CGT can also be accounted for implicitly by replacing $\overline{c}$ with $\widetilde{c}$ in Eqs. (2.20) and (2.23b) [46, 61], and this treatment is also mentioned recently by Allauddin et al. [75]. The present study uses the implicit method for the CGT.

On the other hand, when applying Eq. (2.23b) in LES, the choice of the LES filter width Δ may not be trivial. It is worth noting that Boger et al. [45] applied a spatial Gaussian filter of various sizes $\Delta > \Delta x$ on the DNS data to obtain a filtered flame front. In LES, the effect of introducing a filter for the $\widetilde{c}$ equation is to numerically resolve the filtered flame front on an LES grid. For a general LES solver applying implicit filtering, this may be naturally set to $\Delta = \overline{\Delta}$, consistent with the filter width of the momentum equations. Note that it is the Δ/α, not the filter width alone that plays the role of evaluating Σ as the model coefficient α in Eq. (2.23b) also requires adjustment. The successful work of Kirkpatrick et al. [76] and Gubba et al. [77] have demonstrated the ability of this formulation in calculating transient flame propagation though they included the resolved molecular diffusion term [see 76, Equation 24] in the $\widetilde{c}$ equation. As illustrated by Mercier et al. [78], the filter width Δ is regarded as a dedicated parameter for the flame and may be referred to as a "combustion" filter. Note that the original Boger et al. [45] model has been subsequently refined by researchers to recover the laminar behaviour of the flame when turbulence vanishes [46], and to introduce a dynamic formalism to evaluate Ξ [47].

2.3.2 Refinement of Boger's model

The Boger et al. [45] algebraic model has been refined by Boger and Veynante [46] considering the counter-gradient scalar transport (replacing $\overline{c}$ in Eq. (2.23b) by $\widetilde{c}$) and recovering laminar propagation (modifying diffusion term). The modified $\widetilde{c}$ equation is

$$\frac{\partial \overline{\rho}\widetilde{c}}{\partial t} + \frac{\partial}{\partial x_i}\left(\overline{\rho}\widetilde{u}_i\widetilde{c}\right) = \frac{\partial}{\partial x_i}\left[\left(\frac{\rho_u s_L^0 \Delta}{16\sqrt{6/\pi}} + \frac{\mu_t}{Sc_t}\right)\frac{\partial \widetilde{c}}{\partial x_i}\right] + 4\rho_u s_L^0 \sqrt{\frac{6}{\pi}}\Xi\frac{\widetilde{c}\left(1-\widetilde{c}\right)}{\Delta} \tag{2.25}$$

Eq. (2.25) was slightly modified later [47, 79] where the modelled turbulent flux term is dropped from Eq. (2.25) and is replaced by Ξ in the diffusion term. Based on that, the $\widetilde{c}$-transport equation adopted for the present study is written as [47]

$$\frac{\partial \overline{\rho}\widetilde{c}}{\partial t} + \frac{\partial}{\partial x_i}\left(\overline{\rho}\widetilde{u}_i\widetilde{c}\right) = \frac{\partial}{\partial x_i}\left(\frac{\rho_u \Xi s_L^0 \Delta}{16\sqrt{6/\pi}}\frac{\partial \widetilde{c}}{\partial x_i}\right) + 4\rho_u s_L^0 \sqrt{\frac{6}{\pi}}\Xi\frac{\widetilde{c}\left(1-\widetilde{c}\right)}{\Delta} \tag{2.26}$$

For the present study, both Eq. (2.25) and Eq. (2.26) have been tested and the difference between the solution is negligible. Hence, Eq. (2.26) is adopted for this work.

Note that the filtered flame thickness would be uncontrolled when Eq. (2.22) is used in conjunction with Eq. (2.16). Ma et al. [62] reported that this issue is particularly applicable to the gradient-type $|\nabla\overline{c}|$ models. In contrast, computation using Eq. (2.26) is free from the issue, and the flame thickness is controlled by Δ.

Klein and Chakraborty [80] provided a new definition of wrinkling factor as $\Xi = \overline{|\nabla c|}/|\nabla\widetilde{c}|$ but maintain the original form of the $\widetilde{c}$ equation (Eqs. (2.16) and (2.17)) to gain the control of the flame thickness. However, Ma et al. [62] viewed the lack of flame thickness control is of limited influence in practical cases.

Another critical improvement regarding Eq. (2.25) is that the laminar burning velocity is ensured when turbulence vanishes. This is essential for reducing errors in simulating transient propagating flames where a laminar phase could be present. It can be said that the filter Δ is a dedicated parameter to resolve the flame front on the LES grid, and a rigorous explanation of the consistency between flow and flame filter scales is given by Mercier et al. [78]. The control of resolved flame thickness and the reproduction of laminar propagation for the current model setup have been addressed using a one-dimensional test (see Section 4.9).

2.3.3 Closure of the sub-grid wrinkling factor

The sub-grid-scale flame wrinkling factor Ξ defined by Eq. (2.19) may be evaluated using an algebraic formalism or calculated dynamically based on the resolved flame characteristics. The

filtered reaction rate is written under the generic form [47, 68, 81, 82] as

$$\overline{\dot{\omega}}_c = \Xi \frac{W(\widetilde{c})}{\Delta} \tag{2.27}$$

where $W(\widetilde{c})/\Delta$ corresponds to the resolved (filtered) reaction rate without sub-grid wrinkling ($\Delta = 1$). The sub-grid-scale wrinkling factor Ξ represents the ratio of total to resolved flame surfaces in the filtering volume [81]. It has been shown by Veynante and Moureau [81] that Eq. (2.27) can be used to generalise some of the classical turbulent combustion models such as level-set, thickened flame and FSD. For example, in Boger et al. [45] algebraic model, $W(\widetilde{c}) = 4\rho_u s_L^0 \sqrt{\frac{6}{\pi}} \widetilde{c}(1-\widetilde{c})$ using Eq. (2.27). As a demonstration, the flame surface density Σ [45] can be split into the resolved and unresolved parts:

$$\Sigma = \underbrace{4\sqrt{\frac{6}{\pi}} \frac{\widetilde{c}(1-\widetilde{c})}{\Delta}}_{\text{resolved}} + \underbrace{4\sqrt{\frac{6}{\pi}} (\Xi - 1) \frac{\widetilde{c}(1-\widetilde{c})}{\Delta}}_{\text{unresolved (SGS)}} \tag{2.28}$$

2.3.3.1 Algebraic models for flame wrinkling factor

The algebraic FSD model requires an expression for the sub-grid wrinkling factor Ξ. Table 2.1 summarises the formulations of selected algebraic models for Ξ in the literature. Note that the derivation for these expressions can vary. For example, Colin et al. [41] derived their models according to a DNS study of vortex flame interactions, while Fureby [67] considered Ξ using a fractal-based approach. Most of the models in Table 2.1 require evaluating an efficiency function Γ_Δ. It may have various forms based on their derivation, e.g. Colin et al. [41] provides

$$\Gamma_\Delta = 0.75 \exp\left[\frac{-1.2}{\left(u'_\Delta / s_L^0\right)^{0.3}}\right] \left(\frac{\Delta}{\delta_L^0}\right)^{2/3} \tag{2.29}$$

and Charlette et al. [56] proposed a general fitting function for Γ [see 56, Equation 30]. A realistic evaluation of Γ_Δ is of central importance for using models such as Colin et al. [41] and Charlette et al. [56] formulations.

Most of the models for Ξ require the sub-grid-scale velocity fluctuations u'_Δ as an input. It is typically estimated using the Smagorinsky model [83] from the computed SGS turbulent viscosity [62] or using a scale-similarity approach [41, 84]. The evaluation of u'_Δ is not trivial as it provides the information of turbulence at SGS level that interacts with the flame. One may expect the algebraic FSD closures to be influenced by the evaluation of u'_Δ since its modelling

Table 2.1: List of some available algebraic formulations for Ξ

Publications	Formulation	Description
Angelberger et al. [42]	$\Xi = 1 + \alpha_1 \Gamma_\Delta \frac{u'_\Delta}{s_L^0}$	α_1: model constant
Charlette et al. [56]	$\Xi = 1 + min\left[\frac{\Delta}{\delta_L^0}, \Gamma_\Delta \frac{u'_\Delta}{s_L^0}\right]^{\beta_1}$	$\beta_1 = 0.5$
Colin et al. [41]	$\Xi = 1 + \alpha_1 \frac{2\ln(2)}{3c_{ms}(Re_t^{1/2} - 1)} \Gamma_\Delta \frac{u'_\Delta}{s_L^0}$	Re_t: turbulent Reynolds number $c_{ms} = 0.28$
Fureby [67]	$\Xi = \left(\Gamma_\Delta \frac{u'_\Delta}{s_L}\right)^{D_f - 2}$	D_f: fractal dimension
Weller et al. [63]	$1 + 2\widetilde{c}(\Xi^* - 1)$	$\Xi^* = 1 + 0.62\left(\frac{u'_\Delta l_\kappa}{\nu}\right)\sqrt{\frac{u'_\Delta}{s_L^0}}$ l_κ: Kolmogorov length scale

remains an open question. Langella et al. [85] have recently studied the piloted stoichiometric methane-air Bunsen flame using an algebraic closure for the filtered scalar dissipation rate of the progress variable. They found that the LES results have some sensitivity to the u'_Δ model [85]. However, the influence of u'_Δ on the Ξ formulations is generally not sufficiently investigated in the literature. This is part of the motivation of applying a dynamic formalism where Ξ is not solely computed based on the SGS turbulence information.

2.3.4 Dynamic formalism for the flame surface density

Dynamic combustion models are mostly inspired by the successful modelling of the SGS turbulence in the momentum transport, first proposed by Germano et al. [86]. The basic idea is to take advantage of the known instantaneous resolved large scales to adjust the model parameters automatically. This is typically realised by comparing the LES resolved field at the filter scale and this field at the test-filter scale.

Dynamic modelling of flame surface density Σ, or more generally, the wrinkling factor Ξ, intends to evaluate the sub-grid reaction rate based on the resolved flame features (by test filtering). In this way, the model parameter is self-adjusted to account for various levels of flame wrinkling by turbulence. It has several advantages over the algebraic closure: (i) it extracts information from the filtered flame front, thus avoid evaluating the SGS turbulence quantities such as u'_Δ in Table 2.1; (ii) most of the algebraic closures are derived assuming equilibrium between flame and turbulence [53]. However, the model parameter constants (e.g. β_1 in Table 2.1) would not be valid for cases where the flame is initially laminar and progressively

stretched by turbulent eddies, and it typically occurs in the development of a deflagrating flame.

2.3.4.1 Knikker et al. [61] dynamic model

One of the first dynamic models was proposed by Knikker et al. [61] and Knikker et al. [87] from a priori test on experimental data. Recall that the flame surface density Σ can be separated into

$$\Sigma = \overline{|\nabla c|} = \Xi_\Delta \, |\nabla \overline{c}| = \underbrace{|\nabla \overline{c}|}_{\text{resolved}} + \underbrace{\left(\overline{|\nabla c|} - |\nabla \overline{c}| \right)}_{\text{unresolved}} \tag{2.30}$$

Knikker et al. [61] assume the unresolved FSD to be similar (proportional) to the resolved part between the grid and test-filter scales:

$$\Sigma = \overline{|\nabla c|} = \Xi_\Delta \, |\nabla \overline{c}| = |\nabla \overline{c}| + K_s \left(\widehat{|\nabla \overline{c}|} - |\nabla \widehat{\overline{c}}| \right) \tag{2.31}$$

where $\widehat{...}$ denotes the test-filter operation. The model coefficient K_s is determined by identifying the sub-grid scale flame surface as a fractal surface:

$$K_s = \frac{1}{1 - (\widehat{\Delta}/\Delta)^{2-D}} \left[\left(\frac{\Delta}{\delta_c} \right)^{D-2} - 1 \right] \tag{2.32}$$

The inner cut-off scale δ_c is generally a function of the laminar flame thickness. The fractal dimension D may be evaluated algebraically [66] or dynamically [87]. The gradient type $|\nabla \overline{c}|$ may be replaced by the parabolic expression of Boger et al. [45] in the dynamic formalism.

The derivation of Knikker et al. [87] similarity model was primarily motivated to build a link between the resolved and unresolved flame surface density. It avoids the possible deficiencies of directly estimating the wrinkling factor by sub-grid-scale turbulent properties [81]. This model was subsequently implemented numerically by Gubba et al. [88] for turbulent deflagration problems with satisfactory results.

2.3.4.2 Wang et al. [47] dynamic model

The dynamic model used in this thesis is primarily based on the work of Wang et al. [47]. Following the work of Charlette et al. [68], Wang et al. [47] proposed a simple fractal-like dynamic formalism

$$\Xi = \left(\frac{\Delta}{\delta_c} \right)^\beta \tag{2.33}$$

where $\beta = D - 2$ is the model parameter. Eq. (2.33) ensures that $\beta = 0$ for planar laminar flames ($\Xi = 1$). β can be determined dynamically equating flame surfaces when computed at filtered and test-filtered level [47, 81, 82]:

$$\left(\frac{\Delta}{\delta_c}\right)^{\beta} \left\langle |\widehat{\nabla \overline{c}}| \right\rangle = \left(\frac{\gamma\Delta}{\delta_c}\right)^{\beta} \left\langle |\nabla \widehat{\overline{c}}| \right\rangle \tag{2.34}$$

where $\langle\cdot\rangle$ represents the volume averaging introduced to eliminate un-physical fluctuations, and it should be larger than the test filter. Eq. (2.34) uses a "Germano-like" identity [68] and assumes that the two wrinkling factors (at filtered and test-filtered scales) are uniform over the averaging volume. Then, the model parameter β is

$$\beta = \frac{\ln\left(\left\langle |\widehat{\nabla \overline{c}}| \right\rangle / \left\langle |\nabla \widehat{\overline{c}}| \right\rangle\right)}{\ln(\gamma)} \tag{2.35}$$

The combination of the LES and test filter operators gives an effective filter width $\gamma\Delta$:

$$\gamma\Delta = \sqrt{\Delta^2 + \widehat{\Delta}^2} \tag{2.36}$$

where $\widehat{\Delta}$ is the test-filter width and is typically larger than Δ. Eq. (2.35) provides a dynamic formalism for determining β. By construction, γ is greater than unity ($\ln(\gamma) > 0$), and $|\widehat{\nabla \overline{c}}| \geq |\nabla \widehat{\overline{c}}|$. In their practical implementation [47, 53], β was updated every 100 LES time steps only, considering the flame evolving time compared with time step limit by their LES solver. As a first step, Wang et al. [47] and Wang et al. [53] assumed a uniform or global model parameter β on the resolved flame surface based on (*i*) flame and turbulence in the test cases have homogeneous behaviours, (*ii*) reduced computational cost compared with a local approach and (*iii*) ease of numerical implementation. It results in the use of the whole computational domain for the volume averaging, and β only evolves with time. When the averaging volume $\langle\cdot\rangle$ is limited to the vicinity of a point at the flame, β is a local parameter varying in both space and time. In the local formalism, volume averaging is later replaced by a Gaussian filter [81, 82] considering the ease of implementation.

However, Eq. (2.36) involves the complexity of evaluating the un-weighted $\overline{c}$. Based on a priori analysis [81, 89], Eq. (2.35) is approximated by

$$\beta \approx \frac{\ln\left(\langle |\widehat{\nabla \overline{c}}| \rangle / \langle |\nabla \widehat{\overline{c}}| \rangle\right)}{\ln(\gamma)} \tag{2.37}$$

Eq. (2.37) has been confirmed by DNS analysis [81]. The unweighted averaging or Gaussian filtering $\langle\cdot\rangle$, larger than the test-filter scale, is performed over the resolved flame front. The size of this Gaussian filter, Δ_m, is implicitly assumed to be $1.5\widehat{\Delta} < \Delta_m < 3\widehat{\Delta}$. The model was proved to recover unity wrinkling factor ($\Xi = 1$ and $\beta = 0$) under the laminar flame conditions or when the flame wrinkling is fully resolved [47, 82]. The dynamic model has been tested for a flame kernel growth problem by Wang et al. [47] (Eq. (2.35)) and for a Bunsen burner configuration by Schmitt et al. [82] (Eq. (2.37)).

As reported by Mouriaux et al. [79] very recently in the context of IC engine simulations, Ξ predicted by Eq. (2.37) could be erroneous close to the computational domain boundaries. Mouriaux et al. [79] showed that for 1-D laminar flames, $\Xi \gg 1$ close to the boundary due to the fact that $\Sigma_1 = |\widehat{\nabla\widetilde{c}}|$ is larger than $\Sigma_2 = |\nabla\widehat{\widetilde{c}}|$ in Eq. (2.37). Mouriaux et al. [79] proposed a modified $\Sigma_{2,mod} = |\widehat{\nabla\widetilde{c}}|$ in Eq. (2.37) to overcome this difficulty. Corrections for computational boundaries are implemented in this work. Un-physical Ξ values may also occur when flame fronts interact at the test-filter scale, and they are also corrected by Mouriaux et al. [79]. However, corrections for flame front interactions are not included in the present study as they do not cause unrealistic numerical issues.

2.4 Initialisation of combustion

The nature of LES computation requires an appropriate method to initialise combustion. It is known that the characteristics of combustion during the early stage of flame kernel formation is fundamentally different from its fully developed phase as the flame has not achieved equilibrium and propagation is mainly influenced by volumetric expansion. Description of ignition and early combustion is often of less importance in simulating statistically stationary flames (e.g. a turbulent swirling flame in an industrial burner [90]) as results are generally processed over a time period after the initial transients [91]. On the other hand, devices such as IC engines are operated with a cyclic variation. In order to predict in-cylinder pressure development and pollutant formation, a correct prediction of the initial combustion stages is of great importance traditionally in engine simulations. As the present study compares transient simulation data including pressure and flame position with the experiments, the initiation and early stages of flame propagation are considered to be of greater effects. This section first outlines the difficulties of modelling an ignition process. Then, some of the techniques for numerical flame initiation are reviewed, and their relevance to the present work is discussed.

2.4.1 Difficulties of modelling ignition

The initiation of ignition is a challenging modelling problem. Firstly, the length and time scales of the initial breakdown phase, energy deposition and kernel formation are generally much smaller than that in the flame propagation phase. Secondly, estimation of initial kernel size and temperature depends largely on energy deposited thus an accurate description of the plasma and breakdown phase is needed. Thirdly, chemical reactions at the electrical discharge phase are highly complex in nature involving high-temperature plasma physics. Consequently, general chemical kinetics of combustion is only applicable when the plasma formation is not significant, and the kernel temperature is sufficiently low [92]. In addition to the sophisticated physical phenomena present during the ignition, local flow conditions such as turbulence are often not negligible and affect the kernel development. The initial flame kernel exhibits a laminar-like behaviour and is often observed to be spherical under general circumstances [93]. The kernel could be subsequently stretched and deformed with the presence of strong turbulence particularly in IC engines [94].

A complete ignition process is physically complex to model. It involves spark channel breakdown, radical formation and recombination, surface chemistry, mixture inhomogeneity, heat dissipation and turbulence-chemistry interactions [95]. In general, standard CFD codes cannot simulate plasma thermodynamics. Thus, simplified approaches have been proposed for most engineering applications. More importantly, the methodology and implementation of an ignition model are strongly linked to the main combustion model to be coupled with.

2.4.2 Lagrangian models

The difficulty of detailed ignition modelling lies on resolving the very short characteristic time (less than 10^{-6} s) and length (of the order of the spark gap size or laser focus point) scales compared with that of the ignition system. Hence, it is often not practical to compute ignition details on a typical numerical grid. To avoid this issue, some researchers [96, 97] proposed methods based on the Lagrangian framework where the flame kernel is tracked as marked particles. The Lagrangian approaches may be advantageous as they are less dependent on the grid and flame kernel sizes.

The first attempt was the discrete particle ignition kernel (DPIK) model proposed by Fan et al. [96] and further extended by Tan and Reitz [97] in SI engine simulations. In their approach, the flame kernel is assumed to be spherical and is represented with particle markers identified with an index searching algorithm. One of the benefits of the DPIK model is that the flame

kernel size is not restricted to the grid size during the very early stage of the ignition process. Therefore, the use of a very fine numerical mesh is not necessary. The marked particles move radially at velocities that are determined from turbulence level, equivalence ratio, pressure and temperature in the spark region, and the increase in flame kernel diameter is calculated subsequently, and the fuel burn rate can be computed by the adopted chemical scheme [97]. Transition to the main combustion model takes place when the kernel size reaches the order of the integral turbulence length scale of the flow field [96].

Another Lagrangian-based method is the arc and kernel tracking ignition model (AKTIM) proposed by Colin et al. [98]. In this model, the spark plug is identified by a set of discrete particles to include the heat losses of the kernel [98]. More importantly, a wrinkling factor Ξ is introduced to account for the influence of turbulence at the early stage of the kernel development. The evolution of Ξ is formulated via the production and destruction terms in the transport equation of the flame surface density. The AKTIM model was later adapted to the Eulerian framework and extended to LES [59, 99].

Similar to the DPIK and AKTIM models, Dahms et al. [100] introduced a spark-ignition model (called SparkCIMM) to better account for localised spark plasma channel. More recently, a model was constructed by Lucchini et al. [101] with the inclusion of an electrical circuit model and real properties of the high-temperature gas.

Most of the Lagrangian models are developed in the RANS context, and the exchange of information between the CFD and ignition codes are required. Flow field properties such as burning velocity, unburned gas temperature and density are passed to the Lagrangian ignition model. Out of the ignition model, the Lagrangian flame kernel is usually reconstructed as a distribution of the corresponding Σ field used in the main CFD code.

2.4.3 Autoignition models

In contrast to spark or laser assisted ignition, autoignition is generally encountered where the combustible mixture is in contact with a very hot surface, and it also takes place in compression ignition machines. The complex physics (e.g. high-temperature plasma, electrical circuit, etc.) and the sudden thermal expansion associated with the spark are typically not relevant in an autoignition event. In terms of modelling, general chemical kinetics at the ignition stage are of great importance in order to predict the autoignition process. Therefore, the emphasis has been put on incorporating appropriate ignition kinetics in order to capture properties such as the ignition delay time [102, 103].

2.4.4 Energy deposition approach

Ignition may also be modelled by depositing energy into a selected number of computational cells which approximately represents the spark channel size. An early attempt was made to incorporate a spark power profile in the energy equation by Bradley and Lung [104], where the simulation started just after the breakdown phase. The initial channel temperature was set to $10,000\ K$ according to the experimental data, neglecting the plasma physics. A simpler method is to completely neglect the electric-spark physics and only deposit energy leading to autoignition-like behaviours [105]. The deposition may end when a cut-off temperature limit is reached during which the reaction rate is evaluated using an Arrhenius type model [105].

More recently, an energy deposition (ED) model in LES was investigated for both laser and electrical spark ignition in a turbulent jet [106] and a rocket-like burner [107]. The advantage of this approach is that no separate models are required. Instead, a temporal and spatial varying source term is added to the energy equation, and the formation of the initial kernel is explicitly computed by the LES solver. A volumetric source term $\dot{Q}$ was parametrised by the energy transmitted to the gas as well as the duration and characteristic size of the spark defined as a Gaussian distribution [107]. The LES grid size is reduced at the ignition point, and the distinction between the laser and electrical spark is mainly the amount of transmitted energy described in the ED model [107]. Evidently, the ED model gives the energy profile that reproduces the effect of the real spark when the kernel temperature has decreased below the ionization temperature, thus ignoring the plasma phase. Note that using the ED approach benefits from the coupled TFLES combustion model [41, 43], while the implementation may be less straightforward in FSD based combustion models as the heat release term is typically not driven by the temperature. A thickened flame based model expresses the chemical source term using Arrhenius law via a global one-step or multi-step chemical scheme. This means that the temperature rise resulting from the initial energy deposition can directly trigger the finite-rate chemistry [107]. It is necessary to ensure the combustion model only works on a fully established kernel. Hence, flame thickening is employed after the mass fraction of a burned product species reaches a threshold (e.g. 90%) of that at chemical equilibrium [107].

2.4.5 Flame initiation for LES-FSD

With more refined meshes and smaller time steps in LES compared with RANS, the Lagrangian particle tracking techniques may be less attractive due to their computational inefficiency [95]. There are several points to consider when initialising combustion in the LES-FSD context: (i)

during the initial flame development, the calculation of Σ from the main combustion formalism is not theoretically valid as the flame front is not fully established, (*ii*) it is often convenient to work with the flame surface density during the very early stage of the kernel formation, and (*iii*) an LES simulation cannot resolve a too small flame kernel (less than the filter width Δ), and a flame kernel model must account for the total reaction rate separately when the volume of burned gases is too small.

It is worth mentioning that here the term 'ignition' is used more loosely in the sense of a numerical (thickened or filtered) flame, representing the period before a flame is established numerically (e.g. $\widetilde{c} = 1$ in the computational domain). For the present study, flame initiation has been investigated comparatively using a flame kernel model and a filtered burned kernel.

2.4.5.1 Flame kernel models

Flame kernel models are used to take into account the initial stage of kernel development, which corresponds to the increase of $\widetilde{c}$ from zero to unity. Richard et al. [59] proposed a spark ignition model (AKTIM) coupled with a coherent flame model in LES. It was then extended by Colin and Truffin [108] to incorporate multi-ignition description, and the model is known as ISSIM-LES. The phases of using such a flame kernel model are generalised as follows [59, 99]: (*i*) an initial profile of progress variable or FSD matching the imposed small burned volume, (*ii*) an FSD expression during the ignition period with flame wrinkling taken into account, and (*iii*) transition to main combustion model when the flame is fully established. Practically, using a flame kernel model requires replacing the FSD in the source term of the $\widetilde{c}$ equation.

2.4.5.2 Initialisation of burned flame kernel

As an alternative to modelling ignition, a simulation may also be initialised by imposing a sufficiently large flame kernel. Thus, the very early stage of the kernel formation is not included. Initialising combustion with a burned flame kernel is often used due to the simplicity, and it can be realised by setting a region of burned gases ($\widetilde{c} = 1$). In the majority of FSD combustion formulations, the profile of $\nabla\widetilde{c}$ affects the initial period of computation. Di Sarli et al. [72] investigated the sensitivity of the LES results to the initial burned flame kernel including the size and SGS turbulent velocity fluctuations, and they found that a minimum kernel size is needed to initiate the flame propagation. Wang et al. [47] provide a profile for $\nabla\widetilde{c}$ by filtering the solution from the 1-D computation of a laminar premixed propagating flame at filter width Δ. As this method [47] is robust and computationally efficient, it is applied in most of the simulations performed in this thesis.

2.5 Flame propagation with obstructions

Combustion and flame propagation in the presence of obstacles are of particular interest for the current study. Geometric factors including spatial confinement and obstructions significantly affect the flame behaviours. A variety of physical phenomena have been found in the flame propagation including (*i*) turbulent shear layers from obstacles and their interactions with flame, (*ii*) flame instabilities [109] such as Landau-Darrieus (LD) instability [110, 111] due to thermal expansion of the gas, (*iii*) flow instabilities [112] such as Rayleigh-Taylor (RT) instability resulting from flame acceleration towards the unburned gas and Kelvin-Helmholtz (KH) instability triggered by the velocity shear, (*iv*) pressure wave generation and flame-acoustic interactions due to the confinement [113, 114], (*v*) deflagration-to-detonation transition (DDT) under certain conditions [115], and (*vi*) external combustion as a result of venting [116, 117]. These phenomena determine the behaviours of the propagating flames and the strength of each mechanism depends on the geometric configuration and the stage of flame propagation. For example, in a vented deflagration with obstacles, the LD instability controls the initial quasi-laminar phase, while the effect becomes relatively weak once the flame transits to turbulent.

2.5.1 Experimental studies

The effects of obstacles in vented deflagrations have been experimentally studied by many researchers in lab-scale combustion chambers. Fairweather et al. [118] investigated the effects of turbulence-inducing rings in cylindrical vessels and found that large overpressure is only generated in the later stages of the deflagration due to the turbulent combustion induced by the obstacles. Ibrahim and Masri [119] studied the influence of a single central obstruction of various cross-sectional shapes (cylinder, square, triangle, etc.) and dimensions. They pointed out that the maximum overpressure generally increases with the blockage ratio, but the rate of increase depends on the obstruction geometry. A similar study has also been conducted by Park et al. [120] with more statistics on the flame front obtained from the experiment. Another series of experiments have been performed by Ibrahim et al. [121] to investigate the flame/solid interactions in turbulent premixed flame propagation and highlighted the transient recirculating flow formed behind the solid obstacle. The unburned gas flow field ahead of a propagating flame has also been visualised by Johansen and Ciccarelli [122] using a schlieren based photographic technique. The KH instability, laminar vortex roll-up and multiple scales of turbulence have been observed within the fresh gas in the presence of repeated obstacles [122]. The effects of cross-wise obstacle position have been studied by Wen et al. [123], and

they found that the rate of flame acceleration is the highest when three obstacles are centrally located while it is the lowest when mounted on the same side of the chamber. Wen et al. [124] also conducted experiments with varying angles for a single side-mounted obstacle. The collected sequential flame images [124] show that the gap between the obstacle and the chamber wall affects the flame shape and acceleration. The impact of obstacle separation distance has been explored by Na et al. [125], and they pointed out that the overpressure, flame speed and turbulence level can be higher even with obstacles of lower blockage but spaced optimally. A series of experimental tests have been performed by [65, 126, 127] where baffle plates are used to promote the generation of turbulence, and the smaller-scale (50×50×250 mm) combustion chamber made detailed measurement feasible. There are also a few papers [127–131] providing data for the flame propagation of hydrogen and H_2 enriched fuels.

2.5.2 Numerical studies

Numerical study of transient flame propagation has been performed in the context of RANS [11, 118, 132–134] for both lab and industrial scale cases. Catlin et al. [132] predicted the premixed flame propagation in a large-scale cylindrical vessel consisting of turbulence-inducing rings using the RANS approach. In their mathematical model, turbulence ahead of the flame modelled using a standard $k-\epsilon$ closure, and combustion was described with a modified power-law eddy breakup formalism. A similar numerical study has been conducted by Fairweather et al. [118] where the predicted flame shape and position were in good agreement with experiments. In the studies of Fairweather et al. [118] and Catlin et al. [132], the combustion model was considered semi-empirical since the turbulent diffusion and source terms in the energy and progress variable equations were modified to give a specified turbulent burning velocity. Patel et al. [133] applied a transport FSD approach to simulate lab-scale deflagration with three central rectangular obstacles. Their numerical results highlighted the impact of using a linear or non-linear eddy viscosity turbulence model. Given that the computations performed in these studies [118, 132, 133] were two-dimensional with semi-empirical parameters, the RANS results provided adequate information such as flame shape and acceleration.

In the past few years, LES has been extensively used in the research of propagating turbulent flames [65, 72–74, 76, 77, 88, 99, 135–138]. Kirkpatrick et al. [76] conducted LES computations for a combustion chamber with a single rectangular obstacle using the original Boger's FSD formulation Eq. (2.23b) with an additional molecular diffusion term in the $\widetilde{c}$ equation. The model parameter β in Eq. (2.23b) was set to a value to give a correct turbulent flame speed as

in the experiments [76]. The importance of the velocity boundary condition at the far-field (i.e. outside the vent) is also discussed in the study [76]. Masri et al. [65] applied a similar FSD model to a combustion chamber with one baffle and a central obstruction and commented on the following: (*i*) flame propagation can be divided into quasi-laminar, turbulent and blow-down regions, and the mesh size may be specified based on them; (*ii*) the difference between the coarse and fine meshes lies in the quasi-laminar stage of flame propagation, while both grids have similar results for the rate of change in pressure and the flame propagation speed downstream of this region. However, peak overpressures were found out to be different; (*iii*) grid independence in LES for reacting flows was not a matured consideration compared to RANS, and the filter width plays an important role in the simulation. It was also suggested by Masri et al. [65] that a smaller scale chamber would be of greater significance and practice in terms of forming a thorough analysis of the numerical accuracy in LES.

The use of the gradient form of the Boger's expression [45], i.e. Eq. (2.20), has been found in the work of Di Sarli et al. [72] and Di Sarli et al. [73, 74] with the wrinkling factor closed using the Charlette's formalism [56]. Their study has shown that the magnitude of the flame wrinkling factor has a substantial influence on the peak overpressure, considering the same experiments presented in [133]. Gubba et al. [77] applied the Boger's algebraic model [45] to investigate flame propagation in a small-scale combustion chamber with removable baffle plates and a square central obstacle, and the work has then been extended by Gubba et al. [88] using the Knikker's [87] dynamic FSD model. It has been demonstrated by Gubba [139] that the overpressure prediction is improved with the dynamic model, and Abdel-Raheem et al. [140] subsequently applied it to simulate the hydrogen deflagration with satisfactory results. The same combustion chamber has also been studied by Quillatre et al. [137], Volpiani et al. [138], and Vermorel et al. [141] using the thickened flame model. Vermorel et al. [141] investigated the performance of the two formalisms for the sub-grid wrinkling factor, namely Colin's [41] and Charlette's [56] expressions in combustion chambers of three scales. It was concluded that LES agreed well with experiments at a given chamber scale and a fixed model constant for the wrinkling factor, while the performance was not the same for the larger-scale cases. Hence, a priori fitting of the model parameters may be required for such algebraic models to be applied in various scales of problems [141]. Volpiani et al. [138] combined the thickened flame model with a dynamic formalism for the wrinkling factor. They first conducted a few preliminary 2-D DNS tests and pointed out that the accurate prediction of flow and turbulence structures ahead

of the flame are crucial for the overall flame propagation. They commented that the inner cut-off length scale also plays an important role in the prediction of the maximum overpressure. The 3-D LES tests [138] successfully predicted the essential flame behaviours, and the evolution of the model parameter also helped to illustrate the combustion characteristics for different obstacle arrangements. Volpiani et al. [138] also commented on the peak overpressure affected by using an iso-thermal or adiabatic boundary condition on the chamber walls.

2.6 Summary

A comprehensive review of the literature and the relevant modelling considerations is given in this chapter. Turbulent premixed combustion manifests itself as propagating flame fronts towards the fresh gas, subjected to interactions with the turbulent flow field. The influence of turbulence on the flame is wrinkling and stretching present in most of the practical cases, and the characteristics of interaction can be described using a regime diagram. The difficulty of using LES for turbulent premixed combustion is that the real flame front is generally thinner than the computational grid size. Thus, the filtered chemical source term in the transport equation has to be modelled completely. Out of the available combustion models in the literature, the FSD approach addresses this issue by resolving the filtered flame front which usually crosses a few grid points. The conventional algebraic FSD models are popular due to their simplicity and robustness, but a drawback is that the model parameter needs to be predefined prior to a simulation according to similar experimental data. The highlight of the present work is the incorporation of a dynamic formalism in the renowned algebraic FSD expression of Boger et al. [45] to automatically adjust the model coefficient (the sub-grid wrinkling factor Ξ) in the simulation. After a thorough review of various aspects of the dynamic combustion modelling in the literature, the model of Wang et al. [47] has been adapted and implemented in the present work. It is expected that the flame initiation in LES may affect the early and overall flame propagation. Thus, various methods for initialising combustion are reviewed. In the context of the LES-FSD approach, initialising a flame kernel is generally related to the way of giving the $\widetilde{c}$ profile, and the effect will later be discussed in the later chapters. The process of flame propagation with the presence of obstacles constitutes abundant flow and flame phenomena ranging from turbulence generation to flow instabilities. Compared to experiments, numerically studying the process is significant to reveal the underlying physics and to predict the essential flame characteristics. The present study will provide insights and modelling considerations into the physical problem.

Chapter 3

Governing Equations and Models

This chapter serves to present the essential mathematical elements of the LES computations performed in this work. The instantaneous conservation equations of mass, momentum and scalars for reacting flows are listed first. Section 3.2 provides a brief introduction to LES filtering, and a complete set of filtered governing equations for the current study is given. Section 3.3 includes the mathematical description of the combustion model which forms the core of this work. Finally, the methods for flame initiation investigated in this study are explained in Section 3.4.

3.1 Conservation equations for reactive flows

The starting point for a computational study is a series of governing equations for the phenomena under investigation. Reactive flows are governed by a set of balance equations including mass, momentum, species and energy [55]. Under various assumptions and simplifications, they are appropriate to be solved numerically.

3.1.1 Conservation of mass and momentum

The conservation of mass in a Cartesian coordinate (x_i with i = 1, 2 and 3) can be written using the index notation as

$$\frac{\partial \rho}{\partial t} + \frac{\partial \rho u_i}{\partial x_i} = 0 \tag{3.1}$$

where ρ is the density, and u_i is the velocity in the i-direction. The equations of momentum are

$$\frac{\partial \rho u_i}{\partial t} + \frac{\partial (\rho u_i u_j)}{\partial x_j} = -\frac{\partial p}{\partial x_i} + \frac{\partial}{\partial x_j}\left[2\mu\left(S_{ij} - \frac{1}{3}\delta_{ij}S_{kk}\right)\right] + b_i \tag{3.2}$$

where $\partial p/\partial x_i$ is the pressure gradient, and b_i is the body force. The Kronecker delta $\delta_{ij} = 1$ if $i = j$, otherwise $\delta_{ij} = 0$. The strain-rate tensor

$$S_{ij} = \frac{1}{2}\left(\frac{\partial u_i}{\partial x_j} + \frac{\partial u_j}{\partial x_i}\right) \tag{3.3}$$

in Eq. (3.2) relates the stress tensor τ_{ij} to the velocity gradients for a Newtonian fluid.

3.1.2 Conservation of scalars

To describe a chemically reactive flow requires solving for transport equations of scalars in addition to those of mass and momentum. For a general scalar ϕ, the transport equation is of the form

$$\frac{\partial \rho\phi}{\partial t} + \frac{\partial(\rho u_i \phi)}{\partial x_i} = \frac{\partial}{\partial x_i}\left(\rho D \frac{\partial \phi}{\partial x_i}\right) + \dot{\omega}_\phi \tag{3.4}$$

where D is the molecular diffusivity (using Fick's law), and $\dot{\omega}_\phi$ is the source term.

Primitive variables such as mass fraction Y_k or mole fraction X_k have to be solved for each species k to represent the chemical processes involved in combustion. Directly solving the scalar transport equations for all the species with an appropriate chemical kinetic mechanism is not yet applicable in turbulent combustion. The difficulty with the direct method is the dramatic computational time requirement due to a large number of species and reactions involved in a detailed fuel chemical mechanism. Stiffness caused by the wide range of chemical and turbulence time scales could be significant without a substantial mechanism reduction. In the case of premixed combustion, it is a common practice to solve for only one scalar: the progress variable c. It can be defined as a normalised quantity, e.g. temperature (T), product mass fraction (Y_P) or fuel mass fraction (Y_F), which increases monotonically from zero in the unburned gases to unity in the burned gases:

$$c = \frac{T - T_u}{T_b - T_u}, \qquad c = \frac{Y_P - Y_P^u}{Y_P^b - Y_P^u} \qquad or \qquad c = 1 - \frac{Y_F}{Y_F^u} \tag{3.5}$$

where the super- or sub-scripts u and b represent the unburned and burned status of the gas mixture, respectively. The transport equation of c can be derived from Eqs. (3.4) and (3.5) as

$$\frac{\partial \rho c}{\partial t} + \frac{\partial(\rho u_i c)}{\partial x_i} = \frac{\partial}{\partial x_i}\left(\rho D \frac{\partial c}{\partial x_i}\right) + \dot{\omega}_c \tag{3.6}$$

under the assumption of low Mach number and unity Lewis number.

Obtaining the temperature field usually requires solving an energy equation. Various forms may be used in a CFD code considering the primary variable, e.g. total energy, sensible energy, total enthalpy or temperature. For the present work, an equation using the specific sensible enthalpy is

$$\frac{\partial \rho h}{\partial t} + \frac{\partial (\rho u_i h)}{\partial x_i} = \frac{\partial p}{\partial t} + 2\mu \left(S_{ij} - \frac{1}{3}\delta_{ij} S_{kk} \right) : \frac{\partial u_i}{\partial x_j} + \frac{\partial}{\partial x_i} \left(\frac{\mu}{Pr} \frac{\partial h}{\partial x_i} \right) + \dot{q}''' \tag{3.7}$$

The first three terms on the right-hand side are contributions from pressure work, viscous dissipation and flow dilatation. Surface heat conduction is written with a Prandtl number Pr, and the last term $\dot{q}'''$ is the heat release rate per unit volume representing the enthalpy generated to the fluid as a result of chemical reaction. Note that the enthalpy h in Eq. (3.7) is defined with respect to the reference point $h(298K) = 0$. In addition, temperature and enthalpy are related by the following polynomial

$$h = a_0 + a_1 T + a_2 T^2 \tag{3.8}$$

where a_0, a_1 and a_2 are mixture dependent constants.

An equation of state is necessary to relate pressure, density and temperature. For an ideal gas, it is

$$p = \frac{\rho R_0 T}{M} \tag{3.9}$$

where $R_0 = 8.314\ (J/mol \cdot K)$ is the universal gas constant, and M is the molecular weight of the mixture. For gases, the molecular viscosity also varies significantly with temperature and is calculated using a linear relation between the two properties.

3.2 Filtered governing equations

The instantaneous Navier-Stokes equations (Eq. (3.2)) are valid for both laminar and turbulent flows. However, unless a numerical grid is sufficiently fine (i.e. towards DNS), most turbulence motions cannot be captured for a flow with a moderate Reynolds number. It is known that the large scales of turbulence generally control the behaviour of a flow, and they tend to be dependent on the flow and geometry. In contrast, the small turbulent eddies are more universal and may be modelled with fewer efforts. The idea of LES is to only numerically resolve the large and flow-controlling turbulent motions, while the effect of the small and unresolved scales

is modelled.

3.2.1 LES filtering

Spatial filtering is generally used to partition the solution space into resolved and unresolved scales in LES. The application of a spatial filter G to a field variable $\phi(x', t)$ is defined as

$$\overline{\phi}(x) = \int_{\Omega} G(x - x'; \overline{\Delta}(x))\phi(x', t)dx' \tag{3.10}$$

Typical filters used in LES are the box filters and Gaussian filters [142]. Applying an explicitly defined filter function is also known as 'explicit' filtering. In contrast, common LES solvers realise the filtering procedure implicitly by the applied computational grid and discretisation. Hence, an 'implicit' filter function is not needed nor can be determined [143]. The cut-off width $\overline{\Delta}$ is generally of the order of the grid size, which is set to

$$\overline{\Delta} = 2(\delta x \delta y \delta z)^{1/3} \tag{3.11}$$

where δx, δy and δz are the grid spacing in x, y and z directions, respectively.

In LES, an instantaneous field variable ϕ is decomposed into large-scale, resolved part $\overline{\phi}$ and sub-grid-scale, fluctuating part ϕ' as

$$\phi = \overline{\phi} + \phi' \tag{3.12}$$

Typically, for problems in which there are large changes in density, it is convenient to use a Favre filtered (density weighted) form of decomposition,

$$\phi = \widetilde{\phi} + \phi'' \tag{3.13}$$

where

$$\widetilde{\phi} = \overline{\rho\phi}/\overline{\rho} \tag{3.14}$$

3.2.2 Filtered mass and momentum equations

The Favre filtered governing equations of mass and momentum are

$$\frac{\partial \overline{\rho}}{\partial t} + \frac{\partial \overline{\rho}\widetilde{u}_i}{\partial x_i} = 0 \tag{3.15}$$

$$\frac{\partial \overline{\rho}\widetilde{u}_i}{\partial t} + \frac{\partial(\overline{\rho}\widetilde{u}_i\widetilde{u}_j)}{\partial x_j} = -\frac{\partial \overline{p}}{\partial x_i} + \frac{\partial}{\partial x_j}\left[2\overline{\mu}\left(\widetilde{S}_{ij} - \frac{1}{3}\delta_{ij}\widetilde{S}_{kk}\right)\right] + \widetilde{b}_i - \frac{\partial \tau_{ij}^{sgs}}{\partial x_j} \tag{3.16}$$

with the filtered rate of strain tensor as

$$\widetilde{S}_{ij} = \frac{1}{2}\left(\frac{\partial \widetilde{u}_i}{\partial x_j} + \frac{\partial \widetilde{u}_j}{\partial x_i}\right) \tag{3.17}$$

The unclosed sub-grid stress tensor τ_{ij}^{sgs} arises from the advection term

$$\tau_{ij}^{sgs} = \overline{\rho}(\widetilde{u_i u_j} - \widetilde{u}_i\widetilde{u}_j) \tag{3.18}$$

and most of the closure methods for the SGS stress tensor are based on locally resolved velocities.

3.2.2.1 Closure of SGS stress tensor: Smagorinsky model

The Smagorinsky model is a widely-used eddy viscosity model, and it assumes that the anisotropic part of the SGS stress tensor is proportional to the large-scale strain-rate tensor:

$$\tau_{ij}^{sgs} - \frac{1}{3}\delta_{ij}\tau_{kk}^{sgs} = -2\mu_t\left(\widetilde{S}_{ij} - \frac{1}{3}\delta_{ij}\widetilde{S}_{kk}\right), \tag{3.19}$$

In Eq. (3.19), the eddy viscosity μ_t is a function of the filter size and the strain rate

$$\mu_t = \overline{\rho}C\overline{\Delta}^2\left|\widetilde{S}\right| \tag{3.20}$$

where $\left|\widetilde{S}\right| = \sqrt{2\widetilde{S}_{ij}\widetilde{S}_{ij}}$, and C is a dimensionless coefficient. In the classical model, it is specified a priori and is often written as the Smagorinsky coefficient $C_s = \sqrt{C}$. The isotropic part of the SGS stress tensor, τ_{kk}^{sgs}, is modelled using the relation [76]

$$\tau_{kk}^{sgs} = 2\overline{\rho}C_I\Delta^2\left|\widetilde{S}\right|^2 \tag{3.21}$$

with C_I of the order 0.01. For incompressible flows, the isotropic part of the SGS stress is absorbed into the pressure. However, this term may be significant for compressible flows.

A dynamic procedure proposed by Germano et al. [86] uses local instantaneous flow conditions to calculate the Smagorinsky model coefficient (C_s) dynamically. The dynamic Smagorinsky (DS) model involves the application of a test filter to the velocity field to extract

information from the smallest resolved scales which is then used to calculate the coefficient. The DS model has been predominantly used in the present study, and more details of the model are provided in Appendix A.

3.2.3 Filtered equation for progress variable

The Favre-filtered equation for the progress variable is written as

$$\frac{\partial \overline{\rho}\widetilde{c}}{\partial t} + \frac{\partial(\overline{\rho}\widetilde{u}_i\widetilde{c})}{\partial x_i} + \frac{\partial}{\partial x_i}\left[\overline{\rho}\left(\widetilde{u_i c} - \widetilde{u}_i\widetilde{c}\right)\right] = \overline{\frac{\partial}{\partial x_i}\left(\rho D \frac{\partial c}{\partial x_i}\right)} + \overline{\dot{\omega}}_c \tag{3.22}$$

The filtered molecular diffusion term can be divided into resolved and unresolved parts as [52]

$$\overline{\frac{\partial}{\partial x_i}\left(\rho D \frac{\partial c}{\partial x_i}\right)} = \frac{\partial}{\partial x_i}\left(\overline{\rho}\overline{D}\frac{\partial \widetilde{c}}{\partial x_i}\right) + \left[\overline{\frac{\partial}{\partial x_i}\left(\rho D \frac{\partial c}{\partial x_i}\right)} - \frac{\partial}{\partial x_i}\left(\overline{\rho}\overline{D}\frac{\partial \widetilde{c}}{\partial x_i}\right)\right] \tag{3.23}$$

and the unresolved part in Eq. (3.23) is often not explicitly modelled [52], resulting in

$$\overline{\frac{\partial}{\partial x_i}\left(\rho D \frac{\partial c}{\partial x_i}\right)} = \frac{\partial}{\partial x_i}\left(\frac{\overline{\mu}}{Sc}\frac{\partial \widetilde{c}}{\partial x_i}\right) \tag{3.24}$$

using a Schmidt (Sc) number to relate momentum and molecular transports. The sub-grid scalar flux in Eq. (3.22) arises from the filtered convection term and is typically closed using the simple gradient approach [26]

$$\overline{\rho}\left(\widetilde{u_i c} - \widetilde{u}_i\widetilde{c}\right) = -\frac{\mu_t}{Sc_t}\frac{\partial \widetilde{c}}{\partial x_i} \tag{3.25}$$

where Sc_t is a turbulent Schmidt number. Then, the filtered $\widetilde{c}$-equation can be expressed as

$$\frac{\partial \overline{\rho}\widetilde{c}}{\partial t} + \frac{\partial(\overline{\rho}\widetilde{u}_i\widetilde{c})}{\partial x_i} = \frac{\partial}{\partial x_i}\left[\left(\frac{\overline{\mu}}{Sc} + \frac{\mu_t}{Sc_t}\right)\frac{\partial \widetilde{c}}{\partial x_i}\right] + \overline{\dot{\omega}}_c \tag{3.26}$$

The final form of Eq. (3.26) will be shown in Section 3.3 to account for the counter-gradient transport [26, 45] and the filtered reaction rate $\overline{\dot{\omega}}_c$

3.2.4 Filtered energy equation

The filtered enthalpy equation takes the form

$$\begin{aligned}\frac{\partial \overline{\rho}\widetilde{h}}{\partial t} + \frac{\partial(\overline{\rho}\widetilde{u}_i\widetilde{h})}{\partial x_i} + \frac{\partial}{\partial x_i}\left[\overline{\rho}\left(\widetilde{u_i h} - \widetilde{u}_i\widetilde{h}\right)\right] = \frac{\partial \overline{p}}{\partial t} + 2\overline{\mu}\left(\widetilde{S}_{ij} - \frac{1}{3}\delta_{ij}\widetilde{S}_{kk}\right) : \frac{\partial \widetilde{u}_i}{\partial x_j} \\ + \frac{\partial}{\partial x_i}\left(\frac{\overline{\mu}}{Pr}\frac{\partial \widetilde{h}}{\partial x_i}\right) + \overline{\dot{q}'''}\end{aligned} \tag{3.27}$$

where the sub-grid heat flux term is approximated using a gradient model similar to Eq. (3.25)

$$\overline{\rho}\left(\widetilde{u_i h} - \widetilde{u}_i \widetilde{h}\right) = -\frac{\mu_t}{Pr_t}\frac{\partial \widetilde{h}}{\partial x_i} \tag{3.28}$$

and the filtered heat release term for premixed combustion is expressed as

$$\overline{\dot{q}'''} = \overline{\dot{\omega}}_c (Y_F^u - Y_F^b)\Delta H_F \tag{3.29}$$

where the Y_F^u and Y_F^b are the mass fraction of the fuel in the unburned and burned gases, respectively, and ΔH_F is the respective heat of combustion of the fuel. The Favre-filtered equation of state

$$\overline{p} = \frac{\overline{\rho} R_0 \widetilde{T}}{M} \tag{3.30}$$

is used to obtain the filtered density. In the LES solver, Eqs. (3.16), (3.22) and (3.27) are solved numerically, and the mass conservation (Eq. (3.15)) is realised by deriving a Poisson's equation for the pressure correction, as will be described in Chapter 4.

3.3 The dynamic flame surface density model

While a typical premixed flame front cannot be resolved on an LES computational mesh, the filtered flame (can be seen as $\nabla\widetilde{c}$) can be discretised on an appropriate grid. It avoids the numerical difficulty in computing the sharp jump of temperature or progress variable within one computational cell. The filtered transport equations of mass and momentum have been shown in Section 3.2.2, and the modelling effort for combustion lies in the $\widetilde{c}$ equation (Eq. (3.22)). As has been reviewed in Section 2.3, the present work applies a dynamic FSD formalism to account for the flame wrinkling based on the resolved flame information. Thus, following [47, 81, 82], the $\widetilde{c}$ equation is of the form

$$\frac{\partial \overline{\rho}\widetilde{c}}{\partial t} + \frac{\partial}{\partial x_i}\left(\overline{\rho}\widetilde{u}_i\widetilde{c}\right) = \frac{\partial}{\partial x_i}\left(\frac{\rho_u \Xi s_L^0 \Delta}{16\sqrt{6/\pi}}\frac{\partial \widetilde{c}}{\partial x_i}\right) + 4\rho_u s_L^0 \sqrt{\frac{6}{\pi}}\Xi\frac{\widetilde{c}\,(1-\widetilde{c})}{\Delta} \tag{3.31}$$

where Ξ is the sub-grid wrinkling factor; s_L^0 denotes the unstrained laminar burning velocity and $\Delta = n_{res}\Delta x$ is the LES combustion filter size. Note that the model implicitly assumes that Δ is larger than the mesh size Δx in order to resolve the filtered progress variable gradient

by around $\Delta/\Delta x$ grid points. The evaluation of Ξ is based on a fractal-like expression [47]:

$$\Xi = \left(\frac{\Delta}{\delta_c}\right)^{\beta} \tag{3.32}$$

A dynamic procedure is applied to compute the model parameter β, and the formalism [81, 89] is

$$\beta \approx \frac{\ln\left(\left\langle|\widehat{\nabla\widetilde{c}}|\right\rangle / \langle|\nabla\widehat{\widetilde{c}}|\rangle\right)}{\ln(\gamma)} \tag{3.33}$$

where test filtering is denoted by the operator $\widehat{...}$ at filter size $\widehat{\Delta}$, and the $\langle ... \rangle$ operation represents the volume averaging. The constant

$$\gamma = \sqrt{1 + \left(\widehat{\Delta}/\Delta\right)^2} \tag{3.34}$$

corresponds to the effective filter size, considering the combination of the two filters of widths Δ and $\widehat{\Delta}$. In this study, testing filtering is realised by a spatial three-dimensional Gaussian filter $G(\mathbf{x})$ of the form [45, 53, 144]

$$G(x,y,z) = \left(\frac{6}{\pi\widehat{\Delta}^2}\right)^{3/2} \exp\left[-\frac{6}{\widehat{\Delta}^2}\left(x^2+y^2+z^2\right)\right] \tag{3.35}$$

Note that the test-filter size $\widehat{\Delta}$ specified in Eq. (3.35) is with respect to the physical coordinates and is independent of the local mesh size. It needs to be sufficiently large compared to the resolved flame for the dynamic model to capture the wrinkling of the resolved flame front (typically $\widehat{\Delta} \geq \Delta$). Volume averaging $\langle ... \rangle$ in Eq. (3.33) is also performed by using the Gaussian filter of size Δ_m over the computational domain. Finally, the corrections for calculating β close to the computational boundaries are considered [79]. It is important to note that the use of Eq. (3.31) includes a modified diffusion term to control the resolved flame thickness (gradient of $\widetilde{c}$). The same treatment has also been applied in the diffusion term of the energy equation [41] to ensure that thermal and mass transports are consistent.

3.4 Methods for flame kernel initiation

The FSD computed from Eq. (3.31) is theoretically valid only when a fully established flame front is present, and the flame kernel is sufficiently large (typically compared with Δ) to be resolved on the LES grid. For the present study, four methods (described below as I1-I4) have

been investigated for initialising the combustion.

I1: use a flame kernel model to account for the very early stage of the kernel formation and switch to the main combustion model when the kernel is established

I2: impose a filtered flame kernel larger than the filter width Δ from the solution of 1-D laminar flame calculation

I3: impose a kernel of burned gases larger than the filter width Δ and apply a Gaussian filter on it

I4: set progress variable $\widetilde{c} = 0.5$ in an ignition region

These methods will be described in the following sections.

3.4.1 I1: Flame kernel model

The flame kernel model is based on the work of Richard et al. [59] and Colin and Truffin [108]. In their studies [59, 108], a coherent flame model for LES is used where Σ is obtained from a transport equation. Note that the $\widetilde{c}$ equation [see 59, Equation 8] is of the similar form as the present work where the resolved flame thickness is controlled by the diffusion term. The method starts with defining a sufficiently small amount of burned gases (compared with the combustion chamber) of the mass m_{ign} at the ignition location. Following Colin and Truffin [108], it is defined with a cylinder of radius $2\delta_L^0$: $m_{ign} = 4\pi\rho_u d_0 \delta_L^0$, where d_0 is the estimated size of the initial spark. Then, this burned gas volume is filtered at scale Δ using a Gaussian function and is imposed on the computational domain:

$$\widetilde{c} = c_0 \exp\left[\frac{-|\mathbf{x} - \mathbf{x}_{ign}|^2}{(0.6\Delta)^2}\right] \tag{3.36}$$

where $\mathbf{x}_{ign}$ is the location of the ignition point. The constant c_0 is evaluated to ensure that Eq. (3.36) satisfies the integral

$$\int_\Omega \rho_b \overline{c} dV = m_{ign} \tag{3.37}$$

where Ω denotes the computational domain. The initialisation weakly depends on the value of c_0 providing that it is small, meaning that the mass of the initial burned gases is negligible compared with that in the whole combustion chamber. Assuming that the initial kernel grows spherically, the volume can be approximated as the total volume occupied by the burned gases:

$$V_b = \int_\Omega \overline{c} dV \tag{3.38}$$

Consequently, the corresponding kernel radius and the mean flame area are

$$r_b = [3V_b/(4\pi)]^{1/3} \qquad \text{and} \qquad A_m = 4\pi r_b^2 \tag{3.39}$$

Taking into account the possible flame front wrinkling by small-scale turbulence, the total flame area is

$$A_t = \Xi_{ker} A_m \tag{3.40}$$

where Ξ_{ker} is a single wrinkling factor at the stage of kernel development. Finally, the local flame surface density Σ_{ker} is computed using the Boger et al. [45] algebraic expression:

$$\Sigma_{ker} = k_s \widetilde{c}(1 - \widetilde{c}) \tag{3.41}$$

The parameter k_s should be evaluated so that the total flame surface is distributed spatially over the computational grid

$$k_s = \frac{A_t}{\int_\Omega \widetilde{c}(1 - \widetilde{c})} \tag{3.42}$$

The resulting filtered reaction rate during ignition is modified to

$$\overline{\dot{\omega}}_c = \rho_u s_L^0 \Sigma_{ker} \tag{3.43}$$

Eq. (3.43) is used until the maximum value of $\widetilde{c}$ reaches unity somewhere in the computational domain, and the kernel radius is not smaller than Δ. This means that a fully resolvable flame kernel has been established. Thereafter, $\overline{\dot{\omega}}_c$ is evaluated with the expression of the main combustion model in Eq. (3.31).

During the initial flame propagation, the wrinkling factor Ξ_{ker} is set to unity. Different from a fully resolved flame front, a rigorous mathematical expression for Ξ_{ker} would be more complicated for a very small flame kernel in the SGS range. This treatment has been confirmed by Colin and Truffin [108] for the relatively low turbulence intensities in an engine environment

during the kernel formation. Considering the reasonably low initial turbulence level in the experimental test cases for the present study, $\Xi_{ker} \approx 1$ is expected to be physically valid.

3.4.2 I2: Filtered flame kernel from a 1-D solution

The primary purpose of this approach is to impose a sufficiently large burned flame kernel at the ignition point of the domain so that there is no need to consider the flame formation process. Simulation is initiated by imposing a flame kernel of burned gases at the position of the ignition source. The initial profile of filtered progress variable $\widetilde{c}$ across the flame front is given by filtering the steady solution of one-dimensional propagating laminar flame under the LES filter scale Δ.

The procedure practically includes a 1-D calculation of laminar flame with detailed chemistry, filtering the flame profile according to the LES filter size and imposing a filtered burned flame kernel on the LES grid. First, a one-dimensional calculation of stoichiometric propane/air mixture is performed using a detailed chemical reaction mechanism, GRI 3.0 [145] in the specialised software, FlameMaster [146]. Note that the resulting flame profile from the 1-D computation is still thinner than the mesh size of LES. Hence, a one-dimensional Gaussian filter [144] described by Eq. (3.44) is employed to obtain the Favre-filtered progress variable $\widetilde{c}$ under specified LES filter size Δ. Finally, a burned kernel with a specified size is superimposed in the computational domain.

$$G(x) = \left(\frac{6}{\pi\Delta^2}\right)^{1/2} \exp\left(-\frac{6x^2}{\Delta^2}\right) \tag{3.44}$$

3.4.3 I3: Pre-filtered burned flame kernel approach

In this approach, a burned flame kernel with a unit step function ($\widetilde{c} = 1$ within the burned gas) is first imposed in the numerical domain. Then, the Gaussian filter expressed by Eq. (3.44) is applied to the kernel to obtain a filtered profile of $\widetilde{c}$. Note that this treatment of burned flame kernel is very similar to that by filtering the 1-D laminar solution, but it does not require a prior 1-D computation. The approach aims to investigate the influence of $\nabla\widetilde{c}$ profile on the early flame propagation since it is essentially $\nabla\widetilde{c}$ that drives the reaction rate for the present combustion model.

3.4.4 I4: Setting a region of "burning" cells

This model sets $\widetilde{c} = c_{ign}$ in a region where $0 < c_{ign} < 1$ and computes the kernel growth using the main FSD model. It is a comparatively crude treatment of ignition compared to the flame

kernel model considering that the value of c_{ign} and the size of the ignition region may decide the formation of the flame.

3.5 Summary

This chapter details the mathematical models used for the present work. The filtered governing equations of mass, momentum, progress variable and energy are solved numerically in LES. A turbulence model is required to close the sub-grid stress term in the momentum equations, and a combustion model is needed to close the filtered chemical source term in the $\widetilde{c}$ equation. The core of this study is the dynamic FSD model where the sub-grid wrinkling factor is evaluated dynamically based on the $\widetilde{c}$ profile of the resolved flame front. The present work also investigates the impact of flame kernel initiation with four different approaches. An LES simulation may be initialised by using an ignition model for the initial kernel growth, or by imposing a sufficiently large burned kernel so that LES is able to resolve it.

Chapter 4

Numerical Approach

The conservation equations of mass, momentum and scalars (e.g. progress variable) are discretised and solved numerically on a computational grid. An in-house LES code PUFFIN [66] written in FORTRAN 90/95 has been used in this work. The code has been applied to study a range of premixed [76, 135], non-premixed [91, 147] and partially-premixed [148] combustion and also non-reactive [149] flow problems. This chapter provides an overview of various numerical aspects and solution methodologies implemented in the LES code PUFFIN. One-dimensional test cases (Section 4.9) have also been conducted in order to verify the capability of the combustion model in recovering the laminar flame behaviour.

4.1 Discretisation of transport equations

PUFFIN uses finite volume spatial discretisation methodology, on a forward staggered, non-uniform, Cartesian grid, as shown in Figure 4.1. The conservation equations for momentum and scalar variables presented in Section 3.1 are all in a similar form and can be represented by a generic transport equation:

$$\frac{\partial \rho\phi}{\partial t} = -\frac{\partial(\rho u_i \phi)}{\partial x_i} + \frac{\partial}{\partial x_i}\left(\Gamma \frac{\partial \phi}{\partial x_i}\right) + S_\phi \tag{4.1}$$

where ϕ is a generic variable (velocities, specific enthalpy, etc.), Γ is a kinematic diffusion coefficient and S_ϕ is a general source term.

Integrating Eq. (4.1) over a volume V bounded by a surface A and using the Divergence Theorem yields the integral form of the equation:

$$\underbrace{\frac{\partial}{\partial t}\int_V \rho\phi dV}_{\text{unsteady}} = \underbrace{-\int_A \rho u_i \phi dA_i}_{\text{advection}} + \underbrace{\int_A \Gamma \frac{\partial \phi}{\partial x_i} dA_i}_{\text{diffusion}} + \underbrace{\int_V S_\phi dV}_{\text{source}} \tag{4.2}$$

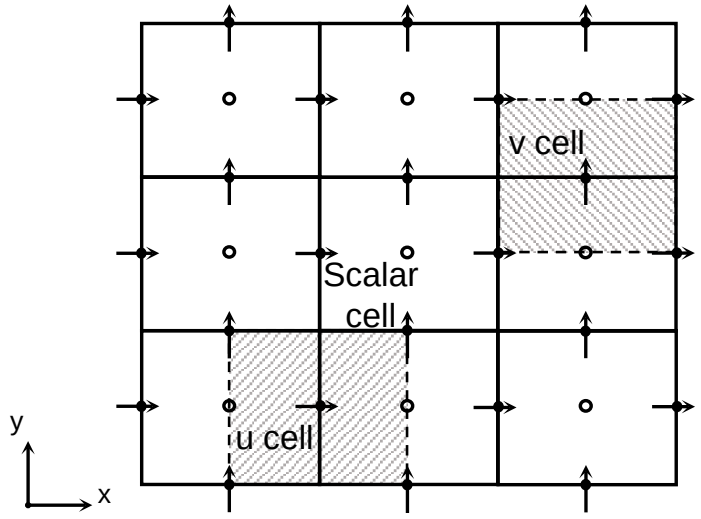

Figure 4.1: Staggered grid and node placement in two dimensions. Circles are scalar nodes; horizontal arrows are nodes of u velocity component and vertical arrows are the nodes of v velocity component. Examples of u, v and scalar cells are highlighted.

The term on the LHS is the unsteady term, while the terms on the RHS are the advection, diffusion and sources terms.

Figure 4.2 displays a cell and its neighbours in two dimensions. The subscript P refers to the cell for which the integrals in Eq. (4.2) are to be computed. East (E), North (N), West (W) and South (S) correspond to the locations of cell centres. Lower letters (e.g. e, s, etc.) represent the centroids of respective cell faces. The notation of a three-dimensional cell would include Up (U) and Down (D) as cell centres and u and d for the cell faces.

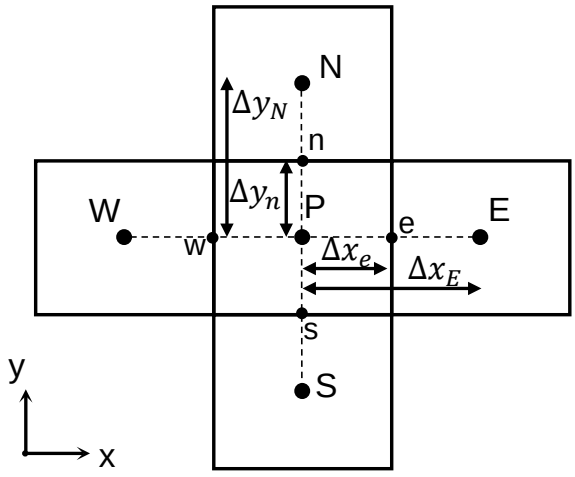

Figure 4.2: A finite volume cell and its neighbours in the xy-plane.

4.1.1 Unsteady term

The unsteady term is discretised by assuming ϕ at the node is representative throughout the cell. Using a central-difference approximation for the time derivative at $n + 1/2$ gives

$$\frac{\partial}{\partial t}\int_V \rho\phi dV \approx \frac{(\rho\phi)^{n+1} - (\rho\phi)^n}{\Delta t}\Delta V \tag{4.3}$$

where the superscript n is the time level.

4.1.2 Advection term

The advective flux across the cell face e is given by

$$F_{A,e} = (\rho u \Delta A)_e \phi_e = C_e \phi_e \tag{4.4}$$

where $C_e = (\rho u \Delta A)_e$. Interpolation with a linear profile can be used to evaluate ϕ_e at the face centre:

$$\phi_e = (1 - \theta)\phi_P + \theta\phi_E \tag{4.5}$$

where the weighting factor for the interpolation is $\theta = \Delta x_e / \Delta x_E$. Δx_e and Δx_E are the distances from the node P to the face centroid e and the east neighbour node E, as shown in Figure 4.2. The evaluation of $(\rho u)_e$ depends on whether the variable ϕ is a scalar or velocity component due to the use of a staggered grid. When ϕ is a scalar, u_e is found directly, but ρ_e has to be interpolated using Eq. (4.5). In contrast, when ϕ is a velocity component, linear interpolation is required to find u_e while ρ is obtained directly.

Summing the advective fluxes across all faces gives a formula for the discrete advection operator:

$$\int_A \rho u_i \phi dA_i \approx \sum C_f \left[(1 - \theta_f)\phi_P + \theta_f \phi_{nb} + \sum S_{QUICK_f}\right] \tag{4.6}$$

where nb is a generic subscript for neighbour cells and f is for a quantity evaluated at a cell face. The source term S_{QUICK} is to account for the curvature of the field for when the QUICK scheme is applied.

4.1.3 Diffusion term

Using the central difference approximation to the gradient, the diffusive flux of ϕ across a cell face is given by

$$F_{D,e} = (\Gamma \Delta A)_e \frac{\phi_E - \phi_P}{\Delta x_E} = D_e(\phi_E - \phi_P) \tag{4.7}$$

where $D_e = (\Gamma \Delta A)_e / \Delta x_E$. The diffusion coefficient at the face centre Γ_e is calculated by linear interpolation.

Summing the diffusive fluxes across all the faces gives a formula for the discrete diffusion operator:

$$\int_A \Gamma \frac{\partial \phi}{\partial x_i} dA_i \approx \sum D_f(\phi_{nb} - \phi_P) \tag{4.8}$$

4.1.4 Source term

Source terms vary for each variable. In the momentum equations (Eq. (3.2)), these include terms of pressure gradient and the force due to gravity and compressibility. For the enthalpy equation (Eq. (3.7)), source terms include contributions from pressure work, viscous dissipation and flow dilatation as well as a chemical source term in the case of reactive flows. The reaction rate is also a source term in the equation for the reaction progress variable. All source terms are treated by evaluating the function representing the source term S_ϕ at the node and multiplying by the volume of the cell:

$$\int_V S_\phi dV \approx S_{\phi_P} \Delta V \tag{4.9}$$

A general expression is written as

$$S_{\phi_P} \Delta V = S_{imp} \phi_P + S_{exp} \tag{4.10}$$

where the "implicit" and "explicit" refer to the manner in which the components of the source term are integrated in time. The implicit component is integrated using an implicit time-stepping scheme, while integration of the explicit component uses an explicit scheme.

4.1.5 Complete discretised equation

The resulting discretised transport equation for a general variable ϕ is [66]

$$\begin{aligned}\frac{(\rho\phi)^{n+1}-(\rho\phi)^{n}}{\Delta t}\Delta V = &\left\{\sum C_f[(1-\theta_f)\phi_P+\theta_f\phi_{nb}]\right\}^{(n-2,n-1,n,n+1)}\\ &+\left\{\sum D_f[\phi_{nb}-\phi_P]\right\}^{(n-1,n,n,n+1)}\\ &+\{S_{imp}\phi_P\}^{(n-1,n,n+1)}+\{S_{exp}\}^{(n-2,n-1,n,n+1)}\end{aligned} \tag{4.11}$$

where the curly brackets $\{\}$ with superscripts $(n-2, n-1, \cdots)$ represent a weighted average of the term evaluated at the listed time levels, which gives an estimate of the term at the $(n+1/2)$ time level, as discussed in Section 4.2. After collecting coefficients, Eq. (4.11) becomes

$$\begin{aligned}A_P^{n+1}\phi_P^{n+1} = &\sum_{nb}(A_{nb}^{n+1}\phi_{nb}^{n+1})+S_{imp}\phi_P^{n+1}+S_{exp}^{n+1}\\ &+\left[\sum_{nb}(A_{nb}^{n}\phi_{nb}^{n})-A_P^n\phi_P^n+S_{imp}\phi_P^n+S_{exp}^n\right]\\ &+\left[\sum_{nb}(A_{nb}^{n-1}\phi_{nb}^{n-1})-A_P^{n-1}\phi_P^{n-1}+S_{imp}\phi_P^{n-1}+S_{exp}^{n-1}\right]\\ &+\left[\sum_{nb}(A_{nb}^{n-2}\phi_{nb}^{n-2})-A_P^{n-2}\phi_P^{n-2}+S_{exp}^{n-2}\right]\end{aligned} \tag{4.12}$$

where the coefficients corresponding to the node A_P and its neighbours A_{nb} are formed from the C_f's and D_f's representing advective and diffusive contributions.

4.2 Time advancement

The spatially discretised governing equations need to be advanced in time to obtain solutions to time-accurate, unsteady simulations. The conservation equation for a scalar ϕ integrated in time using the Crank-Nicolson scheme is

$$\begin{aligned}\frac{(\rho\phi)^{n+1}-(\rho\phi)^{n}}{\Delta t}\Delta V = &-\frac{1}{2}\left[H^{n+1}(\phi^{n+1})+H^n(\phi^n)\right]\\ &+\frac{1}{2}\left[L^{n+1}(\phi^{n+1})+L^n(\phi^n)\right]\\ &+\frac{1}{2}\left[S_{imp}^{n+1}\phi^{n+1}+S_{imp}^n\phi^n\right]\\ &+\frac{1}{2}\left[S_{exp}^{n+1}(\phi^{n+1})+S_{exp}^n(\phi^n)\right]\end{aligned} \tag{4.13}$$

where $H(\phi)$ is the discrete advection operator $\sum C_f[(1-\theta_f)\phi_P+\theta_f\phi_{nb}]$ and $L(\phi)$ is the discrete diffusion operator $\sum D_f[\phi_{nb}-\phi_P]$.

Time integration of the momentum equations uses either Crank-Nicolson or the second and third order hybrid Adams schemes. In the hybrid schemes, advection terms are treated explicitly using an Adams-Bashforth scheme while diffusion terms are treated implicitly using Adams-Moulton [66]. As an example, the momentum equations integrated using the Crank-Nicolson scheme can be expressed as:

$$\begin{aligned}\frac{\rho^{n+1}u^* - \rho^n u^n}{\Delta t}\Delta V = &-\frac{1}{2}\left[H^{n+1}(u^*) + H^n(u^n)\right] \\ &+\frac{1}{2}\left[L^{n+1}(u^*) + L^n(u^n)\right] \\ &+\frac{1}{2}\left[S^{n+1}_{imp}u^* + S^n_{imp}u^n\right] \\ &+\frac{1}{2}\left[S^{n+1}_{exp}u^* + S^n_{exp}u^n\right] - Gp^{n-1/2}\end{aligned} \tag{4.14}$$

Compared with Eq. (4.13), the additional pressure gradient term $Gp^{n-1/2}$ is evaluated at $n-1/2$ time level. The approximate velocities calculated at $n+1$ time level before the pressure correction step are denoted with superscripts $*$. The advection terms in the momentum equations are non-linear and hence require an iterative procedure with the Crank-Nicolson scheme to retain second order accuracy. It should be noted that for reactive flows where density and viscosity vary significantly, iteration of the overall solution procedure is necessary to obtain the correct value of ρ^{n+1} in the unsteady term and μ^{n+1} in the diffusion term.

4.3 Pressure correction method

The pressure correction in PUFFIN is based on a fractional step method for compressible flows. The algorithm is briefly described in the following paragraph, and a detailed illustration can be found elsewhere [see 66]. For reactive flows, both the velocity and density fields must be corrected simultaneously to ensure mass conservation. Since density depends on both pressure and temperature, an iterative method is required. The m^{th} iteration of the time step from $t = n$ to $t = n + 1$ is considered, and the superscript $n + 1$ is left off for clarity. Any terms with superscripts m, $m - 1$ or $*$ refer to steps in the iterations towards the solution at $n + 1$.

First, the equations for the progress variable and the enthalpy are solved giving the temperature field for the m^{th} iteration T^m. An approximate density field ρ^* for the m^{th} iteration is then found using the equation of state with the temperature T^m and the pressure from the previous iteration P^{m-1}:

$$\rho^* = \frac{RT^m}{p^{m-1}} \tag{4.15}$$

where R is the specific gas constant. The momentum equations are integrated using ρ^* and p^{m-1} to find an approximate solution u_i^*:

$$\frac{(\rho^* u_i^*)^{n+1} - (\rho u_i)^n}{\Delta t} = \Upsilon(u_i^*, u_i^*) - \frac{1}{2}\left[\frac{\partial p^n}{\partial x_i} + \frac{\partial p^{m-1}}{\partial x_i}\right] \tag{4.16}$$

where Υ is an operator representing the remaining terms in the momentum equation. An equation for the pressure correction can be derived as [66]

$$\frac{1}{RT^m}\frac{p'}{\Delta t} - \frac{\Delta t}{2}\frac{\partial^2 p'}{\partial x_i^2} = -\left[\frac{\rho^* - \rho^n}{\Delta t} + \frac{\partial(\rho^* u_i^*)}{\partial x_i}\right] \tag{4.17}$$

where the pressure correction is defined as $p' = p^m - p^{m-1}$. Once p' is found, it is used to correct pressure, velocity and density:

$$p^m = p^{m-1} + p' \tag{4.18a}$$

$$\rho^m = \rho^* + \frac{p'}{RT^m} \tag{4.18b}$$

$$u_i^* = \frac{1}{\rho^*}\left[\rho^m u_i^m + \frac{\Delta t}{2}\frac{\partial p'}{\partial x_i}\right] \tag{4.18c}$$

The pressure correction equation (Eq. (4.17)) is discretised in space in a similar manner to the transport equations for other variables. Integrating Eq. (4.17) yields

$$\frac{1}{RT^m}\frac{p'}{\Delta t}\Delta V - \frac{\Delta t}{2}\sum\left(\frac{\partial p'}{\partial x_i}\Delta A\right)_f = -\left[\frac{\rho^* - \rho^n}{\Delta t}\Delta V + \sum(\rho^* u_i^* \Delta A)_f\right] \tag{4.19}$$

Second-order central differences are used to calculate the gradients $\partial p'/\partial x_i$. It is important to use the same discretisation for the pressure gradient in the momentum and pressure correction equations. This minimises the projection error and ensures convergence if an iterative scheme is used.

4.4 Solution of algebraic equations

The system of algebraic equations, obtained through numerical discretisation, is generally solved using linear equation solvers. PUFFIN has two solvers, namely Alternating-Direction-Implicit (ADI) solver and Bi-Conjugate Gradient Stabilized (BiCGStab) solver with a Modified Strongly Implicit (MSI) pre-conditioner. The present study has been carried out using BiCGStab to solve the momentum, scalar and pressure correction equations, which is more efficient and requires ten-times less number of iterations to achieve the same level of convergence by ADI

[66].

4.5 Boundary conditions

Boundary conditions give additional constraints to the partial differential equations. These may include solid, inflow and outflow boundaries. In the present investigation, the problem considered is the propagation of turbulent premixed flames, evolved from stagnant condition in a chamber with multiple solid obstacles. Outflow boundary conditions are imposed outside the chamber, while solid boundaries are used to represent walls and obstacles along the borders and within the domain (e.g. the rectangular obstruction in the experimental test cases for the present study). The details of these boundary conditions are described in the following sections.

4.5.1 Solid boundaries

At solid wall boundaries, the normal and tangential velocity components are set to zero, corresponding to the impermeable and the no-slip conditions at the wall. For turbulent boundary layers in which it is not possible to resolve the viscous sub-layer, a wall function is used in order to apply the correct shear force to the fluid. The power-law wall function of Werner and Wengle [150] is used in this work.

4.5.2 Outflow boundaries

The outflow boundary conditions generally use a zero normal gradient

$$\frac{\partial \phi}{\partial \mathbf{n}} = 0 \tag{4.20}$$

or a convective outlet boundary condition

$$\frac{\partial \phi}{\partial t} + U_b \frac{\partial \phi}{\partial \mathbf{n}} = 0 \tag{4.21}$$

where U_b is the bulk velocity across the boundary. It is very important in the case of compressible flows that the pressure wave generated within the chamber must be allowed to leave smoothly without reflection. Since the pressure field is dependent on the velocity field, the boundary conditions applied for the velocity will determine the pressure wave behaviour. Boundary conditions of Eqs. (4.20) and (4.21) work well when the dominant force on the fluid flow is due to advection and diffusion. However, in the present case (Chapter 5), due to the compressible nature of the propagating flame, the dominant force is the pressure gradient resulting from

pressure waves radiating from the chamber. Consequently, both of the boundary conditions would result in significant pressure reflections. Hence, to overcome this problem, Kirkpatrick [66] developed a new non-reflecting boundary condition for velocity, analogous to commonly used convective boundary conditions in incompressible LES

$$v_i = \left(v_{i-1} - \frac{\Delta x_i}{a} \frac{\partial v_{i-1}}{\partial t} \right) \frac{R_{i-1}^3}{R_i^3} \tag{4.22}$$

where v_i is the velocity on the boundary, v_{i-1} is the velocity in the adjacent cell within the domain, Δx_i is the distance between the two nodes, R_i and R_{i-1} are the distances from the two nodes to the centre of the open end of the chamber and a is the speed of sound, which is the "convective" velocity. The numerical domain has to be extended sufficiently from the outlet of the cavity to ensure that this boundary condition is accurate.

4.6 Solution procedure

The overall solution procedure for each time step follows similar to that of Kirkpatrick [66] for compressible flows. The following steps are performed in a timing loop

Step 1: Solve scalar transport equations (e.g. Eq. (4.13)) including the progress variable and enthalpy.

Step 2: Compute fluid properties such as temperature, molecular viscosity and density based on provided thermodynamic relations.

Step 3: Solve momentum equations for the velocity components (e.g. Eq. (4.14)).

Step 4: Solve the pressure correction equation (Eq. (4.17)).

Step 5: Correct pressure, velocity and density fields (Eq. (4.18)).

Step 6: Check mass conservation error and repeat steps 4 and 5 as required.

Step 7: Calculate eddy viscosity μ_t.

Step 8: Compute other terms such as the pressure gradient ($\partial p/\partial t$) and S_{kk} (Eq. (3.19)).

Typically, about eight outer iterations of this procedure are required to obtain satisfactory convergence at each time step. For the present test cases of strong transient nature, the time step is varied to ensure that the Courant number, $CFL = u_i \Delta t / \Delta x_i$ remains less than 0.5.

4.7 Implementation of the DFSD model

The implementation of the dynamic FSD model described in Section 3.3 uses Eqs. (3.31) to (3.33). To illustrate the motivation of flame filtering approach, Figure 4.3 gives an example of a 1-D Gaussian-filtered (Eq. (3.44)) progress variable of unit step function representing a 1-D flame. It is apparent that more grid points are present in the $\overline{c}$ gradient when the filter width increases. Similar to the turbulence modelling, the present flame filtering is implicit considering the filter width Δ as a function of the grid size in Eq. (3.31), so that no explicit filtering is needed.

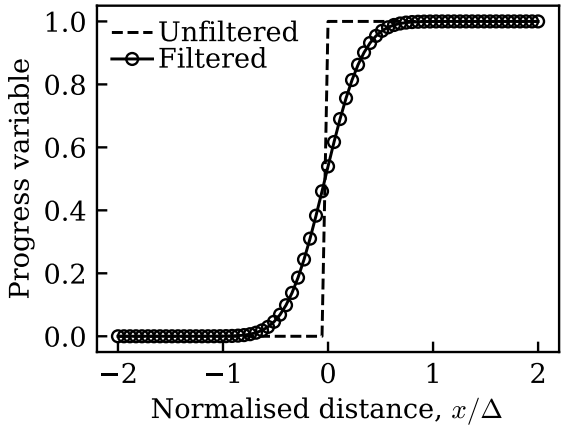

Figure 4.3: Effect of a spatial Gaussian filter (Eq. (3.35)) having a size Δ larger than the mesh size Δx.

The expression for the model parameter β (Eq. (3.33)) requires the determination of test-filtered gradient of the resolved progress variable $\langle|\widehat{\nabla\widetilde{c}}|\rangle$. Note that in practice β may be a local (evolving in space and time) or global (a single value for the entire flow field, only evolving with time) parameter [53, 82]. When the volume-averaging operation $\langle ... \rangle$ is the overall computational domain, it corresponds to a global parameter, while a small volume refers to a local parameter β [82]. However, the global formalism is designed for reducing the computational cost for homogeneous flows and is not considered suitable for the present highly unsteady cases.

A Gaussian filter (Eq. (3.35)) is used for the test-filtering operation. It is different from the usual three- or five-point discrete filters [151, 152] as the test-filter for the DFSD model should be large enough to contain the wrinkling of the filtered flame [53]. Unlike in unstructured mesh where calculating the gradient $\nabla\widetilde{c}$, range searching for the filter domain [153] and storing the Gaussian weights may be a significant computational overhead [53, 95], the present imple-

mentation in the *structured* code is much more straightforward. Practically, the test-filtering operation has been constructed by using a combination of three 1-D Gaussian filters in the x, y and z directions, respectively, and each direction is filtered independently [152]. The simplicity also lies in the computation of the discrete Gaussian-filter weights, which would need to be pre-stored in a 1-D table for an unstructured solver [53, 95]. The test-filtered quantities are obtained based on the definition of a convolution filter over the computational domain Ω as

$$\widehat{\widetilde{\phi}}(\mathbf{x}) = \int_{\Omega} G(\mathbf{x}-\mathbf{x}')\widetilde{\phi}(\mathbf{x}')d\mathbf{x}' \tag{4.23}$$

The filtered field at the ith grid point is obtained by applying a discrete (2M+1)-point filter to the variable ϕ as

$$\widehat{\widetilde{\phi}}_i = \sum_{l=-M}^{M} g_l \widetilde{\phi}_{i+l} \tag{4.24}$$

where the filter coefficients g_l are the Gaussian weights taking into account the grid spacing, and by definition, they satisfy

$$\sum_{l=-M}^{M} g_l = 1 \tag{4.25}$$

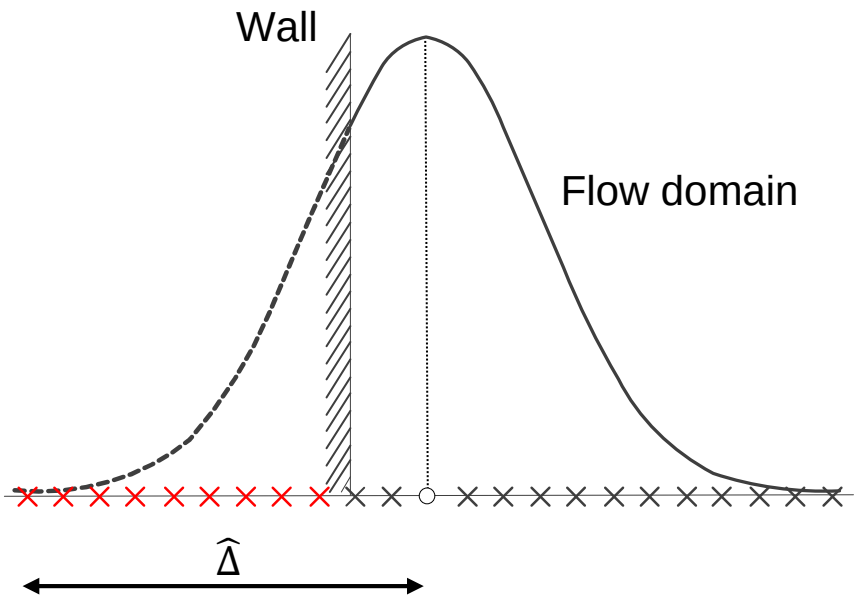

Figure 4.4: Test filter near the computational boundary.

For a structured CFD solver, the number of points M within half of the Gaussian filter

($\widehat{\Delta}$) is specified by the 1-D filter function. Note that the filtering operation (Eq. (4.24) is performed sequentially in the x, y and z-direction of the domain of the combustion chamber. Test-filtering near solid boundaries requires special treatments since the Gaussian function would be spatially incomplete. It typically occurs when the distance between the point to be filtered and the boundary is smaller than the test filter size, as shown in Figure 4.4. In such a case, the test-filtering domain is extended to at least the size of $\widetilde{\Delta}$ to ensure that the Gaussian filtering (Eq. (4.25)) is complete. Another necessary treatment is to replace $|\nabla\widehat{\widetilde{c}}|$ by $|\widehat{\nabla\widetilde{c}}|$ near the boundary to avoid the non-realistic values of β [79]. Finally, the wrinkling parameter β is calculated within the effective flame region (defined here as $0.02 < \widetilde{c} < 0.98$).

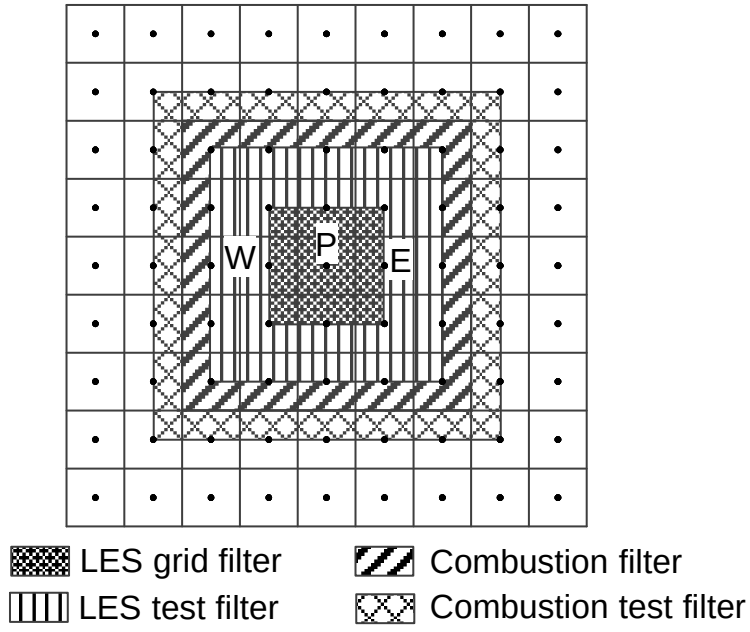

Figure 4.5: Filters for momentum equation and combustion.

Figure 4.5 illustrates the size of the filters involved implicitly or explicitly in the LES solver. The present LES grid filter $\overline{\Delta} = 2\Delta x$ specifying the cut-off width for the turbulence modelling. An LES test filter would be present if the dynamic Smagorinsky model was applied, and the size is set to twice the grid filter [66]. Regarding combustion, the filtered flame is implicitly defined by the filter width Δ, typically larger than four times the grid size. The dynamic FSD model applies a Gaussian test filter $\widehat{\Delta}$ of at least the size of Δ. In addition, the volume average also uses a Gaussian filter of the size $1.5\widehat{\Delta} \geq \Delta_m \leq 3\widehat{\Delta}$.

4.8 Implementation of the flame kernel model

Implementing the flame kernel model (i.e. method I1 in Section 3.4.1) is straightforward, and the mesh size around the ignition point has been found to have a minimal effect on the resulting $\widetilde{c}$ profile. Note that the DFSD model is not applied when the flame kernel model is in control, as the flame front is not established or resolvable at this stage. It means that the sub-grid wrinkling of the flame font is only computed when the kernel is sufficiently large. For simulations starting with burned flame kernels, the dynamic FSD model would initially predict a low wrinkling in some regions of the laminar flame front, and this is typical for small spherical laminar flame kernels [79].

4.9 1-D planar flame tests

The aim of this section is to discuss the performance of the implemented combustion model in simple cases corresponding to laminar flame propagation. The significance of these tests is reflected in the fact that in almost all the practical deflagration processes the flame starts as a laminar flame and transits to turbulent depending on the flow conditions. It is thus necessary to validate the model in the absence of turbulence to ensure: (i) $\beta = 0$ (Eq. (3.33)) or $\Xi = 1$ (Eq. (3.32)) for a planar laminar flame [47], and (ii) the laminar flame speed is recovered, and the numerical flame thickness is controlled.

The test corresponds to a one-dimensional, plane, laminar premixed flame, subject to no sub-grid scale turbulence or flame wrinkling. Since the present combustion model requires the unstrained laminar burning velocity s_L^0 as an input, it is essential to reproduce this speed in a simulation when turbulence vanishes. This 1-D analysis serves to provide a clear interpretation of the model behaviours.

4.9.1 Theoretical analysis

The test case considered here is a tunnel-shape configuration as illustrated in Figure 4.6 [48]. In this configuration, the gas velocities in the unburned and burned gases are u_u and u_b, respectively. The flame is initiated near the open side of the tunnel, and it travels into quiescent gas towards the closed end. The apparent flame propagation velocity, denoted by u_p, represents the speed at which the flame propagates relative to the walls, and it will be used as the diagnostic to interpret the numerical results. Based on the definition of s_L^0, u_p can be

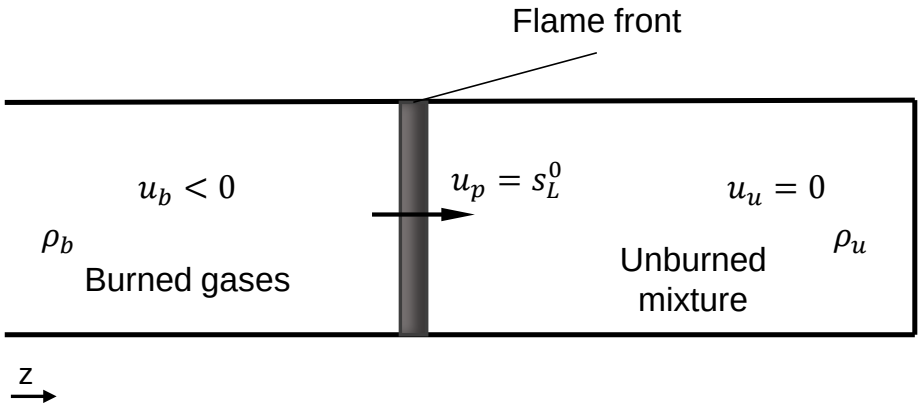

Figure 4.6: Tunnel configuration where a flame travels in the positive z-direction towards the closed end of the domain.

expressed as

$$u_p = s_L^0 - u_u \tag{4.26}$$

Given that $u_u = 0$ because of the wall at the closed end, $u_p = s_L^0$ when the flame is not too close to the end wall. It is worth mentioning that if the flame travels towards the open end, the apparent velocity will increase due to the thermal expansion such that $u_u < 0$. Note that from the continuity at the flame front

$$\rho_u s_L^0 = \rho_b (u_p - u_b) \tag{4.27}$$

Eq. (4.27) may be rewritten to obtain u_b as

$$u_b = s_L^0 \left(1 - \frac{\rho_u}{\rho_b}\right) \qquad or \qquad u_b = s_L^0 \left(1 - \frac{T_b}{T_u}\right) \tag{4.28}$$

where the relation of ideal gases is used.

4.9.2 Numerical consideration

A schematic of the computational domain for the test case is shown in Figure 4.7, where the flame travels in the positive z-direction. Note that 1-D simulations may be performed using a separate code solving for 1-D equations, with the assumption that the momentum equations reduce to a 1-D Euler equation without pressure gradient [62]. Realising that the in-house code PUFFIN is not able to solve for 1-D governing equations, pseudo 1-D simulations have

been performed where only 2 cells (limited by the discretisation) are placed in the x- and y-directions. This corresponds to a uniform cubic mesh of size $\Delta x = 0.5\ mm$, similar to that used in the 3-D turbulent simulations. The results confirmed that the flame and flow structures have negligible y and z variations, while the configuration is still treated as three dimensional. Since numerics are expected to play a minimal role in this case, the 1-D analysis may serve to obtain the desired laminar burning velocity and adiabatic flame temperature prior to the 3-D turbulent cases. Constant pressure at atmosphere is given at the open end of the chamber, and all the solid boundaries are treated as slipped walls to avoid shear forces on the flame front. Initially, the flame may be initiated by setting $\widetilde{c}$ in a few layers of cells at the open end, and the influence of flame initiation will be discussed.

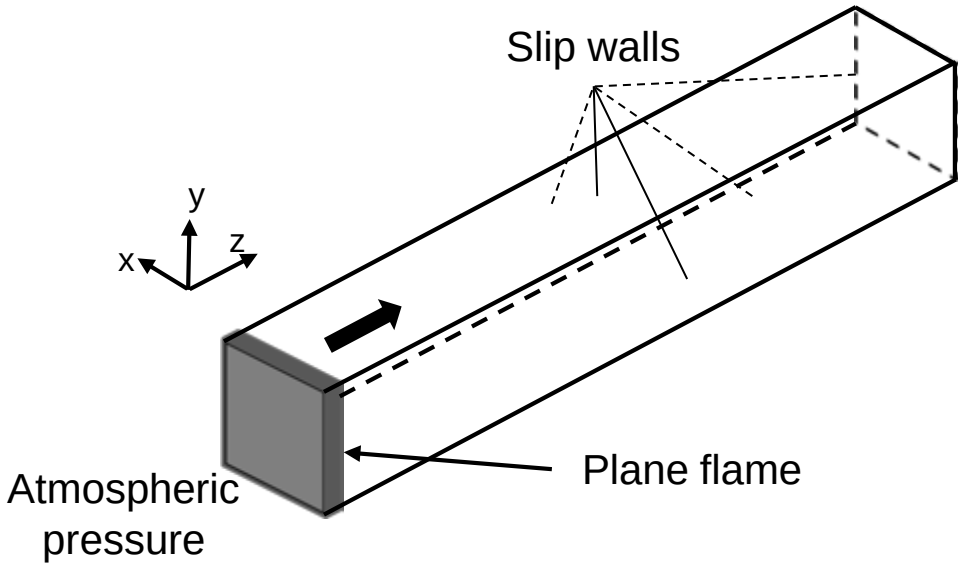

Figure 4.7: Schematic of computational domain and boundary conditions for the 1-D laminar deflagration.

In the simulation, the propagation velocity u_p can be related to the burned volume V_b as

$$u_p = \frac{dV_b}{dt}\frac{1}{A} \tag{4.29}$$

where A is the cross-section area of the domain. The volume occupied by the burned gas may be obtained from the simulation according to

$$V_b(t) = \int_\Omega \overline{c}(t) dV \tag{4.30}$$

where the spatial integration of the progress variable is performed over the computational domain of volume Ω.

A series of runs have been conducted to investigate the trends of u_p as well as the filtered flame thickness against the filter width Δ. In the simulation, $s_L^0 = 40\ cm/s$ is specified in the FSD model, which is a typical burning velocity for a stoichiometric propane/air mixture. The calculated u_p can be compared against the exact s_L^0 to discuss the model performance.

4.9.3 Results

Figure 4.8 displays the computed flame speed u_p and the filtered flame thickness with a range of filter widths $\Delta = n_{res}\Delta x$ where $2 \leq n_{res} \leq 15$. The flame speed is overestimated by $\sim 40\%$ when $\Delta = 2\Delta x$, but the error reduces with the increase in Δ as the computed flame speed (u_p) approaches to the pre-specified exact value s_L^0. Another observation is that when Δ is small, the estimated u_p tends to fluctuate with time, meaning that the numerical solution is less stable. The present code requires a filter width of $\Delta \geq 5\Delta x$ for the error between u_p and s_L^0 to be less than 10%, which agrees with the literature using similar models [59, 78, 99, 154].

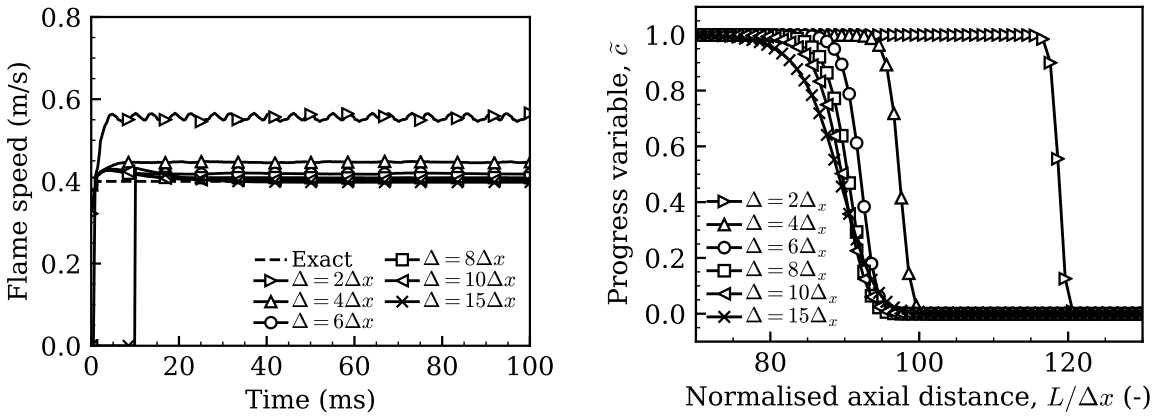

Figure 4.8: Effect of filter width. *Left*: comparison of calculated and exact flame speeds. *Right*: flame thickness.

The instantaneous $\widetilde{c}$ profiles across the flame front are displayed in Figure 4.8 at the same instant of time. The spatial deviation of $\widetilde{c}$ with $\Delta = 2\Delta x$ is due to the largely over-predicted flame speed. As the computed wrinkling factor is unity in all the cases considered here, Figure 4.8 essentially illustrates the effect of numerical flame resolution. When the flame filter size is small ($n_{res} < 4$) so that the $\widetilde{c}$-gradient is numerically stiff, there will be a tendency to develop numerical oscillations and the inaccuracy of flame propagation speeds. While a too thick filtered flame may induce a change in its interaction with turbulence, these results emphasise the importance of ensuring a well-resolved flame front in a simulation so

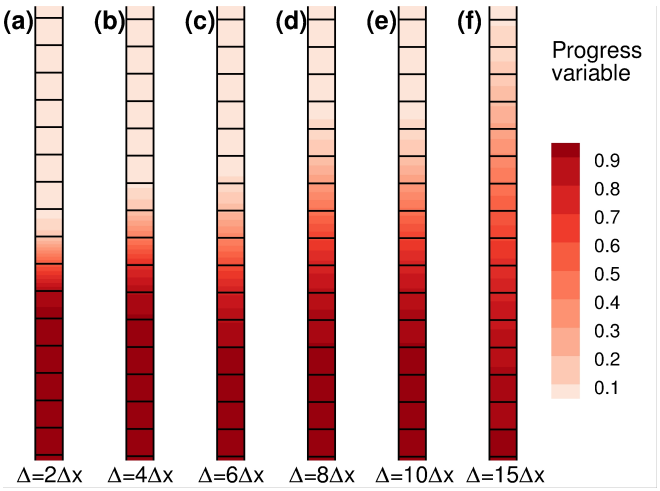

Figure 4.9: Instantaneous flame contoured by the progress variable.

that the flame behaviours are controlled by the combustion model instead of other numerics. Figure 4.9 shows the direct consequence of the filter-to-grid ratio as the numerical flame tends to be smeared. It is found out that the effective $\widetilde{c}$-gradient developing at the flame location is approximately resolved by n_{res} grid points, indicating the control of flame thickness by the model.

Figure 4.10 presents the influence of the flame initiation and mesh resolution on the predicted laminar flame propagation speed. The initial plane flame has been initialised by imposing various $\widetilde{c}$ profiles in the first 8 cells at the open end of the domain, denoted by $\widetilde{c}_0$. As shown in Figure 4.10, there is no observable difference in the predicted flame speed after a short early transient. On the other hand, the grid size has an impact on the flame speed at the same filter to grid ratio. Figure 4.10 shows that the computed speed increases by about 4% when the grid size doubles. Figure 4.11 presents the temperature variation across the flame using various filter width, and it is clear that the burned gas temperature approaches to the adiabatic flame temperature ($T_{ad} \approx 2250\ K$ for a stoichiometric propane/air mixture) as the $\Delta/\Delta x$ increases.

It should be noted that the heat of combustion ΔH_F in the code is specified by the user to obtain the desired burned gas temperature. This is primarily due to the fact that the specific heats may not be realistic for the composition in the burned mixture. The same treatment has also been found in an earlier version of the open-source code FDS [154]. The discussions made in the 1-D analysis provided insights into the behaviours of the combustion model, especially the significance of the flame resolution controlled by Δ. On the other hand, both unity wrinkling factor (not shown here) and correct laminar flame propagation are proved to be recovered using

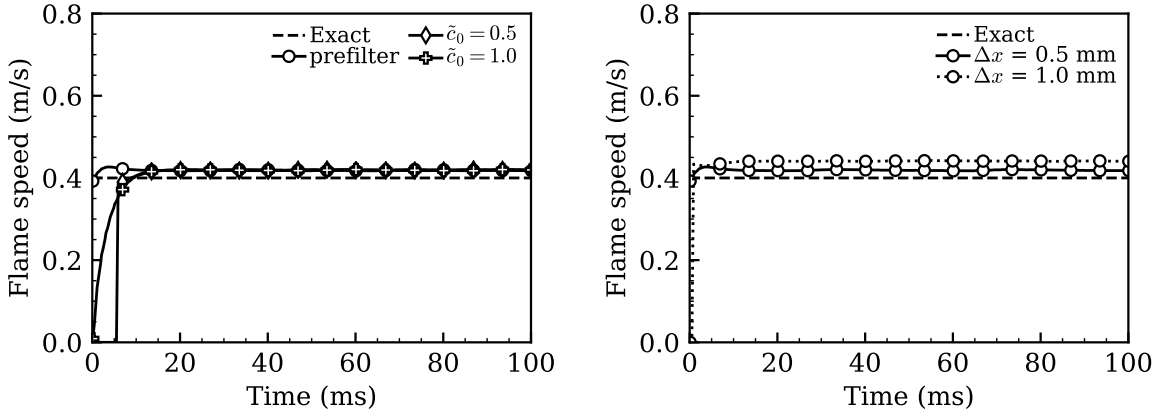

Figure 4.10: *Left*: influence of the flame initialisation; $\widetilde{c}_0$ is the initial $\widetilde{c}$ profile in the first 8 cells at the open end of the computational domain. *Right*: sensitivity of mesh resolution; $\Delta/\Delta x = 6$.

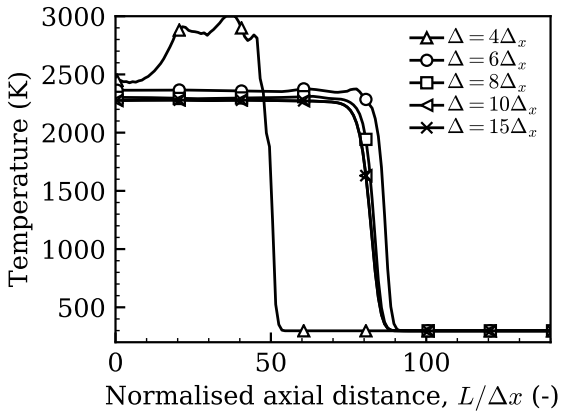

Figure 4.11: Computed temperature profiles using different filter width.

the present dynamic FSD formalism when turbulence effects vanish.

4.10 Summary

This chapter presents various aspects of the numerical techniques adopted for the present study. The simulations performed in this work use the structured LES solver PUFFIN [66], and the discretisation of equations and other numerical treatments are included in the chapter. Implementation of the DFSD model in PUFFIN requires considering the size of the flame test filter, especially at the solid boundaries. Methods of flame initiation in the context of FSD are described and will be investigated in Chapter 6. The code with the implemented models is first tested in a 1-D laminar configuration, and the analysis serves to illustrate the behaviours of the combustion model. It is verified that the current model is able to reproduce the correct laminar flame speed and unity wrinkling factor with the absence of turbulence, and

this is considered important in describing the early quasi-laminar stage of a typical deflagration. The consequence of the filter to grid ratio for the flame is highlighted, and a sufficient flame resolution is required for the numerical accuracy.

Chapter 5

Test Cases and Numerical Setup

This chapter describes the experimental test cases considered for the present study. The combustion research group at the University of Sydney performed experiments [126, 127, 155, 156] to investigate the critical issue of transient premixed flame propagation and the influence of turbulence and solid obstacles on the burning rate. These experiments are used in the present numerical study. The highlight of the combustion chamber is the ability to produce various turbulence environment using obstructions. Section 5.1 gives the specifications of the combustion chamber, flow configurations based on the obstacle arrangements, and some issues and uncertainties involved in the experiments. A brief introduction and some technical details of the various measuring techniques and laser ignition system are provided. Section 5.2 provides an example of the averaging of the experimental pressure signals for the validation of the numerical results. The computational domain and settings of simulations are illustrated in Section 5.3.

5.1 Experimental considerations

An important factor influencing the design of the experimental rig is that it should be readily applicable to numerical simulations. It requires appropriately defined initial and boundary conditions, less complex geometry and appropriate physical size for LES [65]. In the earlier studies of Ibrahim et al. [121] and Masri et al. [157], a sizeable experimental chamber with a volume of about 20 litres was used to study premixed flames propagating past one turbulence generator and a solid obstacle. This configuration posed two main issues: (i) the turbulence generated was not sufficiently high; (ii) LES conducted for the experiments were time-consuming.

Taking into account the suitability for both the model validation for CFD and the desired

optical accessibility, the experimental rig was developed by Kent et al. [158] with a volume of only 0.625 litres. Compared with the earlier chambers [121, 157], this alternative design allows for

(*i*) the use of multiple turbulence-generating grids without running the risk of deflagration to detonation transition.

(*ii*) broad optical access.

(*iii*) improved control including laser ignition (compared to spark ignition) and hinged flap (compared to plastic film) for sealing the vent.

(*iv*) a substantial reduction in the computational time for sensible LES.

It is important to note that the physical size of the problem is by no means a limitation on applying reliable LES in real-world scenarios. However, the present LES study aims to resolve sufficient length scales at an affordable cost in these test cases. Kent et al. [158] studied the flame wrinkling scale by measuring the length and the linear distance between two points on a contorted flame front from the OH images. Hall et al. [126] performed experiments using the vessel to investigate the effects of position and frequency of obstacles. The latest version of the combustion chamber has been reported by Alharbi et al. [127] including the tests of hydrogen and two other hydrocarbon fuels, and its reconfigurable capability to generate a range of configurations facilitates the validation of the present computational setup.

5.1.1 Combustion chamber specification

The combustion chamber is a Perspex square prism, with internal dimensions of width $W = 50\ mm$ and length $L = 250\ mm$, which gives an overall volume of 0.625 L and a ratio $L/W = 5$. The external prism is constructed from 20 mm thick Perspex walls, encapsulating the inner combustion chamber. The chamber can accommodate three removable baffle plates (also referred to as grids or obstacles in the rest of the thesis) with a schematic shown in Figure 5.1b. Each baffle consists of five 4-mm wide and 3-mm thick strips evenly separated by six 5-mm gaps, producing an area blockage ratio (ABR) of 40% in the flow direction. A single baffle also creates a volume blockage ratio (VBR), i.e. the ratio of blocked volume to the total volume of the chamber, of 0.48%. These may be located at any of the three locations: 19 mm (B1), 49 mm (B2) and 79 mm (B3) from the base. A further solid obstruction with a square cross-section can be placed such that its lower surface is 96 mm away from the base plate.

Two solid obstacles may be used, a small one with a cross-section of 12×12 mm or a large one with a size of 25×25 mm. They create ABRs of 24% and 50% (VBRs of 1.152% and 5%), respectively.

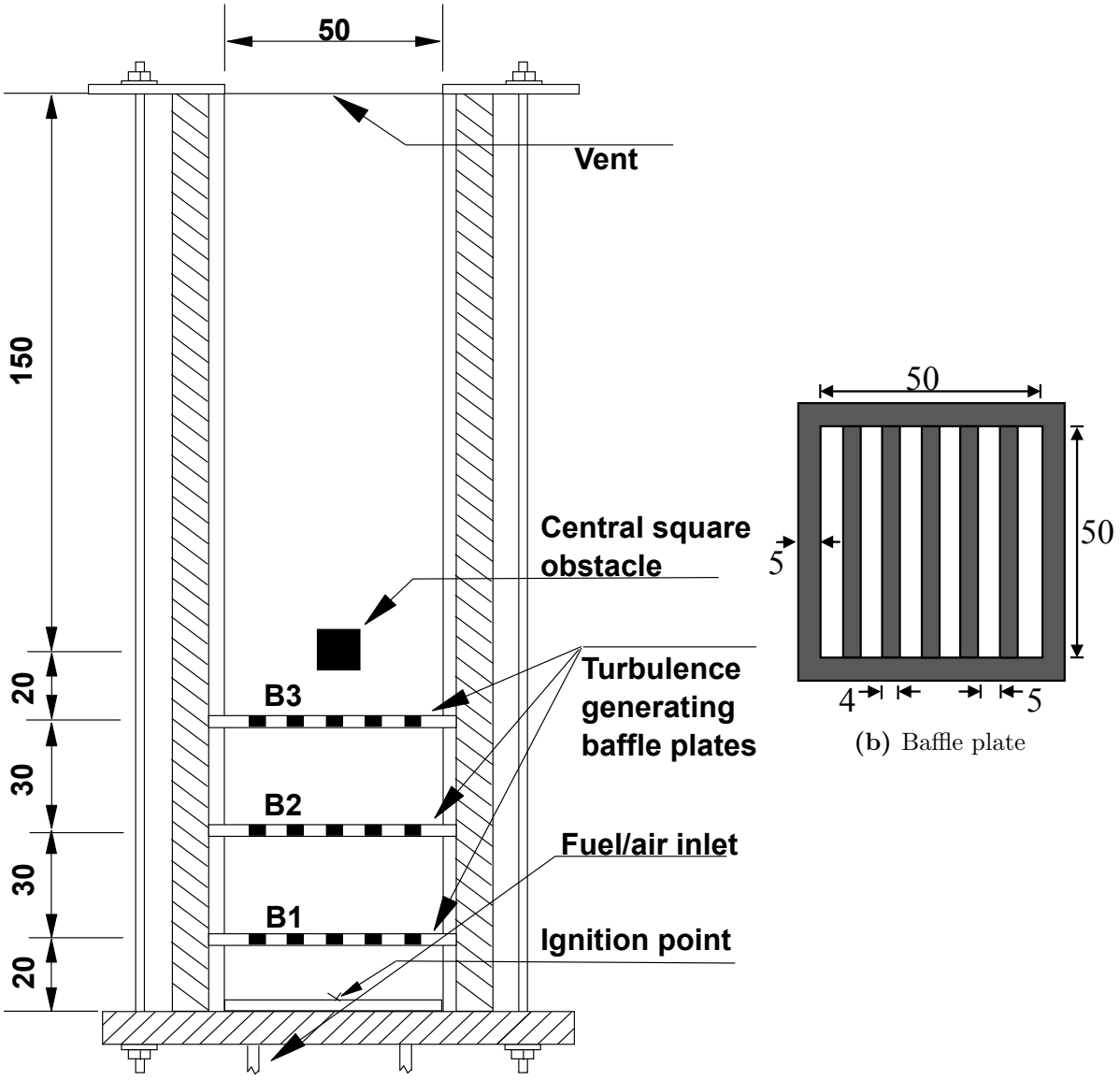

(a) Chamber

(b) Baffle plate

Figure 5.1: Specifications of the explosion chamber used in the experiment [156] (not to scale, dimensions are in mm).

5.1.2 Experimental procedures

Experiments are conducted with three different fuels, hydrogen, compressed natural gas, CNG, liquefied petroleum gas, LPG (95% C_3H_8, 4% C_4H_{10} and 1% C_5 + hydrocarbons by vol.), each with two equivalence ratios Φ. For CNG and LPG, $\Phi = 0.8$ and 1.0 are examined while only lean hydrogen-air mixtures of $\Phi = 0.7$ and 0.8 are used. This is due to the excessive overpressure generated by stoichiometric mixtures of hydrogen, potentially exceeding the 100

kPa of pressure transducers.

In the experiment, the fuel-air mixture enters the atmospheric pressure chamber through a non-return valve, and it is allowed to rest before each ignition event. The stagnant fuel-air mixture is then ignited by focusing the infrared output from an Nd:YAG laser 2 mm above the base, and it sets the time zero for each experimental run. Simultaneously, the laser imaging system is trigged to start collecting images. The hinged flap at the chamber exit rises 1 second before ignition to allow venting throughout the explosion.

5.1.2.1 Pressure measurement

Pressure is recorded at 25 kHz using two Keller type PR21-SR piezo-electric pressure transducers. One of them located diagonally on the base plate, with 10 mm distance from two adjacent walls, and the other one was mounted in the wall just downstream from the main obstacle (186 mm from the base, equidistant from two walls).

5.1.2.2 High-speed imaging of the flame front

The chamber is constructed with a rectangular viewing window and extended optical access area to all of the baffles and square obstacle positions. Therefore, High-speed imaging of laser-induced fluorescence from OH (LIF-OH) is able to include the propagation of the flame over all of the obstructions. Flame structure and position are captured as spatially resolved images of chemical species concentrations by laser-induced fluorescence (LIF). It excites chemical species by absorbing photons, making them emit light that can be monitored. Heat release in a combustion process produces H atoms, and they are reacting with oxygen subsequently to produce more OH radicals. Evidently, OH is a major species and is only created within the thin reaction zone. Therefore, images of OH species are collected as a sensible indication of the flame front.

High-speed imaging of LIF-OH with a repetition rate of 5 kHz is performed providing an excellent representation of the evolution of the reaction zones. As reported by Al-Harbi [156], a full experimental cycle takes 35 s for LPG, 30 s for CNG and 25 s for hydrogen.

This well-devised experiment setup is of specific interest for modelling hydrogen explosion using LES. Experimentally, the compact size of this combustion chamber makes accurate measurement and repeated experimental runs more feasible. In addition, as LES for combustion is often grid-dependent to an extent, modelling the small-scale chamber makes it affordable to resolve a range of flow length scales in order to reveal the underlying physics of vented deflagration. Using obstacles with rectangular cross-sections is not only physically efficient in

generating turbulence but also simplifies the mesh generation for LES. Finally, a variety of possible obstacle arrangements provides a wide range of excellent test cases for the validation of the dynamic combustion model.

5.1.3 Flow configurations

Various combinations of obstacles in the test chamber make it possible to conduct a detailed study of the effects of obstacles on vented deflagration. Figure 5.2 displays 11 configurations using different permutations of baffles and obstacles investigated numerically for the present study, while a total of 18 configurations were tested in the experiments for each of the three fuels (LPG, CNG, and H_2) [156]. A code is used to identify each configuration in order to specify the obstruction locations and size of the solid obstacle. For example, 0B0S stands for the case where one baffle plate is at B2 and the small central obstacle (S) are placed downstream of the ignition point, and BBBL represents the configuration where three baffle plates B1, B2 and B3, as well as the large central obstacle (L), are positioned in the same order away from the chamber bottom.

The chamber height and configurations were specified so that the combustion process started as a slow laminar deflagration and transformed to a fast turbulent deflagration mainly by the turbulence generation by obstacles. It should be noted that the flame acceleration would not trigger detonation (i.e. DDT) even for hydrogen under the experimental conditions. Thus, it has been ensured that the current mathematical models and numerical framework are sufficient to describe the whole deflagration.

5.1.4 Other considerations

Since the experiment is highly transient, optimal initial conditions have been determined to reduce sources that could affect the repeatability of the runs [155]. Each experiment starts with filling fuel-air mixture while the venting flap at the chamber exit is closed, which is 10 s for all the fuels. The filling time has been carefully monitored to make sure the chamber is filled with enough mixture. Then, the mixture needs to settle throughout the chamber in order to be ignited from rest. The settlement needs to be throughout the chamber to ensure that the mixture is ignited from rest. After the settling period (15 s for LPG, 10 s for CNG and 5 s for hydrogen), the flap opens and lasts for one second. Right after that, the flammable mixture is ignited by the Nd:YAG laser, and the time between the flap opening and ignition was examined and monitored. At the end of each experiment, the chamber is given time to expel the exhaust gases after the run and before refilling takes place. The exhaust fan may

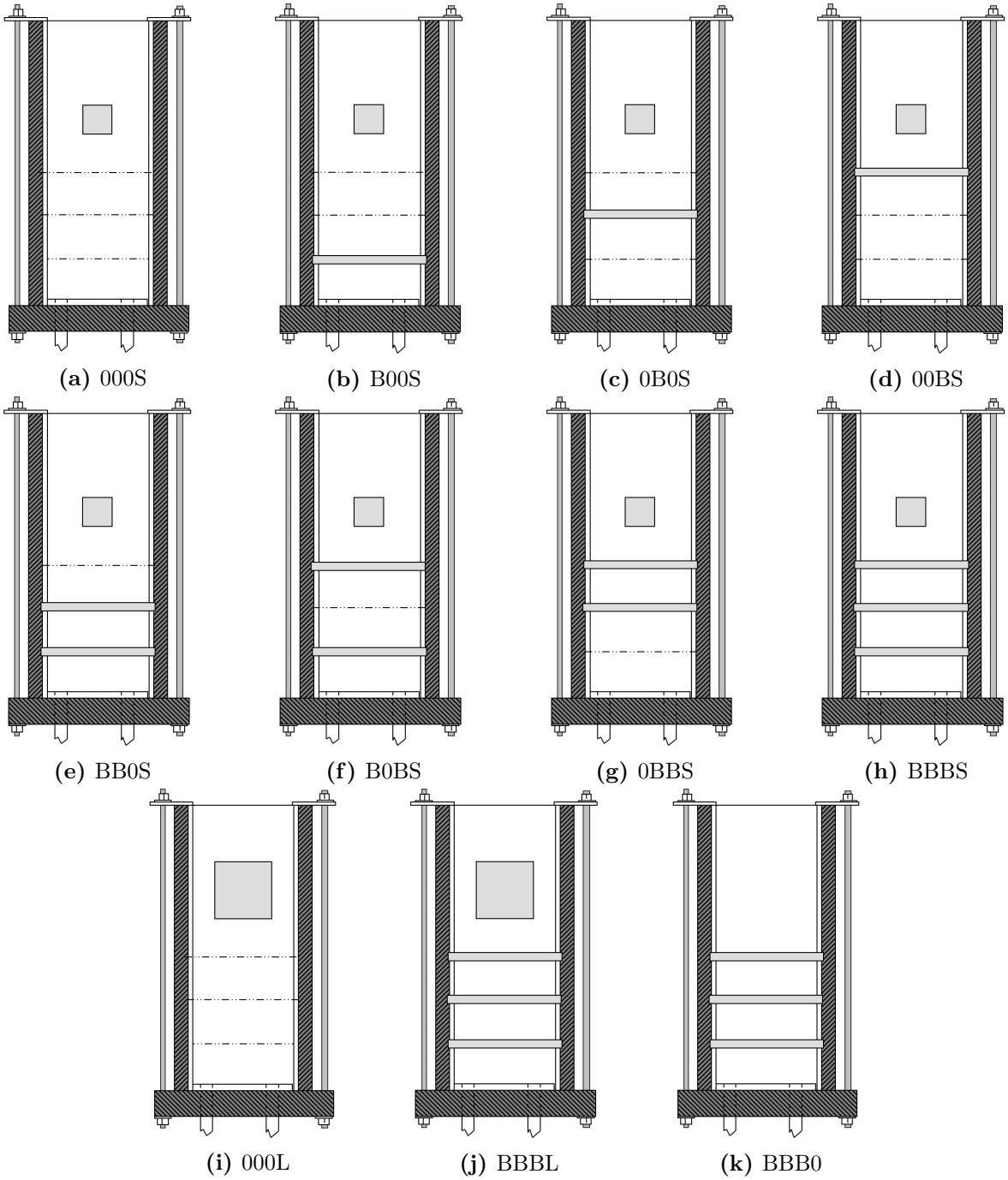

(a) 000S **(b)** B00S **(c)** 0B0S **(d)** 00BS

(e) BB0S **(f)** B0BS **(g)** 0BBS **(h)** BBBS

(i) 000L **(j)** BBBL **(k)** BBB0

Figure 5.2: A list of configurations studied in this thesis with a code indicating if a baffle is present (B) or not (0) and whether a small (S) or a large (L) central obstacle is used [127].

affect the chamber pressure due to its closeness to the open side of the chamber. Thus, the fan speed and the distance between the exhaust and the chamber open end have been optimised.

Another factor to consider is that the temperature of the ignition mixture is influenced by that of the chamber which stores a certain amount of heat. During the two-hour test, the initial temperature prior to each ignition event increases, while the maximum chamber temperature only changes slightly. To reduce the effect of this error on overpressure and the time taken to reach peak pressure, the chamber is preheated for thirty minutes before the experiment starts. In the earlier experimental work [126], the top venting flap rises to about 45° from the chamber lid. Al-Harbi [156] concerned that the flap position could obstruct the gas venting, and a small effect on the pressure record has been found using different opening angles. Thus, a modification was made to fully open the flap, i.e. 90°.

The pressure data collected is subject to variations caused by variability in mixture composition, the power of the laser igniter, pressure transducer voltage, high-speed imaging signals, system vibration, etc. The experiment was repeated at least 30 times for each configuration, resulting in multiple pressure-time traces from the pressure transducer. It was considered sufficient to obtain a reliable and representative value for the mean peak pressure, its rate of change, and the time taken to reach the peak.

5.2 Averaging of pressure signals

The pressure inside the chamber is a primary parameter to investigate in both the combustion experiment and numerical simulation. Since a particular interest of using the experimental data is to obtain the maximum overpressure and the time taken to reach it, the raw pressure signals have been appropriately averaged for the purpose of model validation.

Figure 5.3 illustrates the averaging process of the raw experimental pressure signals, with an example of the configuration B0BS using a lean H_2/air mixture at $\Phi = 0.7$. Note that the mean overpressure for each case presented in this thesis is averaged from at least 30 individual experimental realisations. A representative average of the experimental data is required for the verification of the developed computational model. Even though uncertainties exist in the experimental process including the ignition energy, the opening of the venting flap, system vibration, etc. [156], the repeatability is very high, and the pressure trends in each experiment are very similar [156]. It can be seen from Figure 5.3 that generally the internal pressure maintains a low value in the early stages of the explosion and almost monotonically increases up to its peak from $t \approx 4\ ms$. Therefore, the averaging procedure is performed after shifting

all the pressure traces in time to match the maximum overpressure of each one. The range of the overpressure magnitude and the time taken to reach the peak pressure ($t_{p,exp}$) are also shown in the processed data to facilitate the comparison with the numerical results.

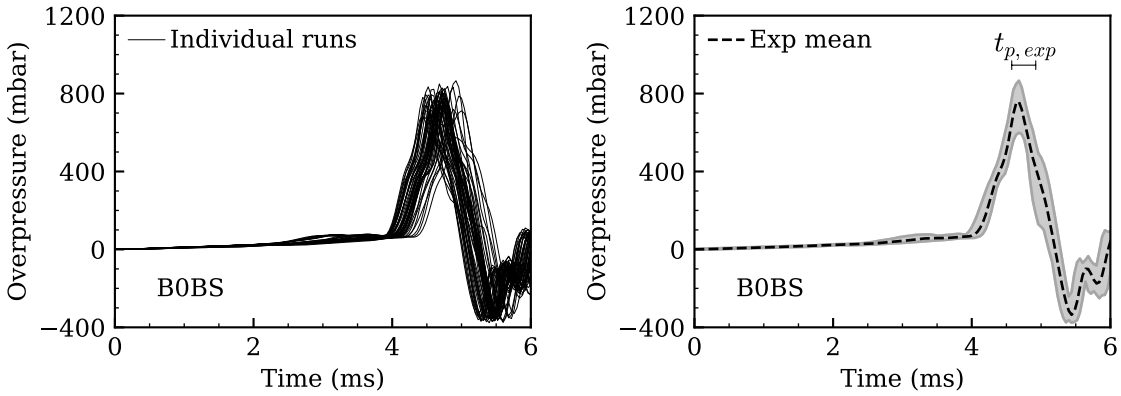

Figure 5.3: Processing of the overpressure data at the chamber base from the experiments for configuration B0BS (H_2, $\Phi = 0.7$). *Left*: original pressure signals. *Right*: averaged pressure data. Statistical envelope (grey background). The range of time taken to the peak overpressure in the experiment ($t_{p,exp}$ with $\vdash\dashv$).

5.3 Computational setup

Numerical simulations of the test cases have been conducted using the in-house code PUFFIN [66]. The spatial discretisation of the momentum equations applies QUICK for the advection terms and second-order central differences for the others. Second-order central differences are also used for the pressure correction equation. Conservation equations for scalars use second-order central difference scheme for diffusion terms. SHARP [159] is applied for advection terms of the scalar equations to avoid problems associated with oscillations in the solution. The equations are advanced in time using a fractional step method. A Crank-Nicolson scheme is used for the time advancing of momentum and scalar equations. Mass conservation is enforced using an iterative projection method for compressible flow in which pressure, velocity and density fields are corrected simultaneously. Sub-grid-scale turbulence is typically modelled using the dynamic Smagorinsky eddy viscosity model [86].

The computational domain includes the venting combustion chamber and the surrounding atmosphere. Figure 5.4 shows a schematic of the generated mesh along the midplane of the chamber for the configuration BBBS. The domain of the explosion chamber has dimensions of $50 \times 50 \times 250$ mm, and the size of the whole computational domain is $325 \times 325 \times 500$ mm. A typical numerical grid has $120 \times 120 \times 476$ cells in the x, y and z directions, respectively, with $85 \times 85 \times 423$ cells within the chamber. The cells are distributed uniformly in the chamber,

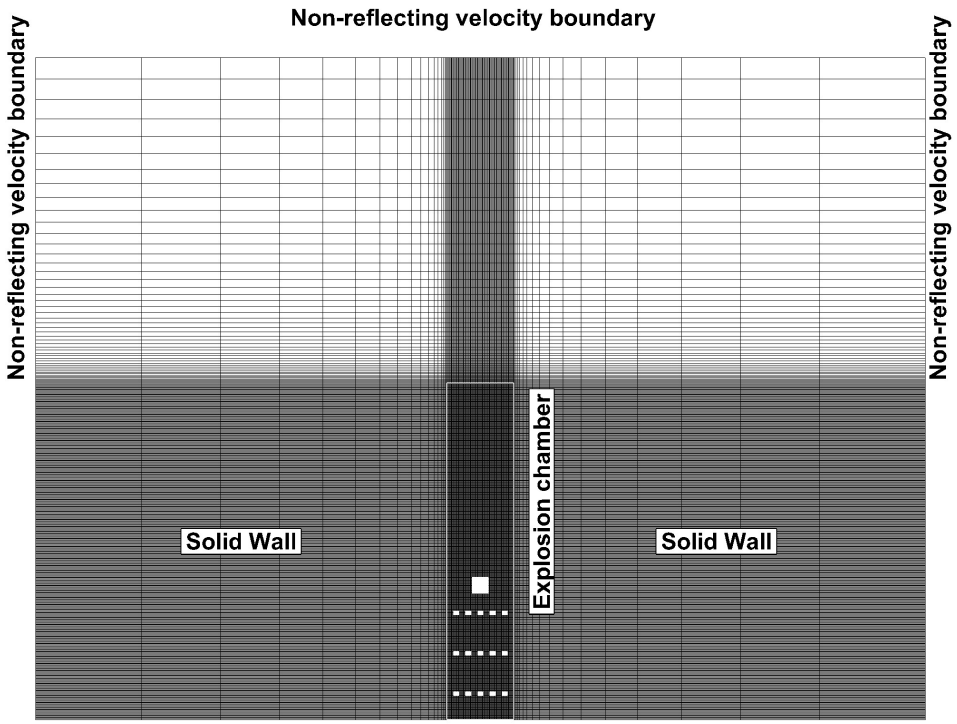

Figure 5.4: Vertical section through the computational domain and grid in the yz-plane for configuration BBBS.

giving a grid size of $\Delta x \approx 0.59\ mm$. The mesh size is chosen to ensure that the filtered flame thickness ($\approx \Delta$) is smaller than the gaps between the strips of the baffle plates. While applying uniform mesh within the chamber is not necessarily a rule of thumb, it is preferred here considering: (i) same local filter and test-filter width; (ii) capture turbulent motions at the same resolution within the chamber. The grid is expanded with an expansion ratio (in the z-direction) of $r_z \approx 1.07$ from the chamber towards the far-field boundaries to save the computational time. The dynamic procedure for turbulence is not used in the external domain to eliminate the possible commutation errors in this region.

Within the chamber, adiabatic and no-slip boundary conditions are employed on the solid walls of the chamber, and the $1/7th$ power law wall function of Werner and Wengle [150] is used to calculate the shear stress at the solid wall. Due to the excessive axial inertial force generated from the flame propagation, solutions are insensitive to the wall-function models [66]. Non-reflecting boundary conditions [76] are applied to the boundaries of the far fields. From the preliminary investigation, they should be applied with a sufficiently large (in the axial direction) external plenum to minimise the effect of reflected pressure waves on the internal pressure field of the chamber.

Initial conditions have energy and reaction progress variable set to zero everywhere and the

fuel mass fraction stoichiometric in accordance with the experiment. The initial velocity field is quiescent, with a random perturbation to allow the development of turbulence. Simulation is typically initiated by imposing a filtered burned flame kernel at the ignition point of the chamber.

The discretised equations are solved using a Bi-Conjugate Gradient solver with an MSI preconditioner. The time step is limited to ensure the Courant–Friedrichs–Lewy (CFL) condition such that $CFL < 0.51$ with the extra limitation that $\Delta t < 0.1\ ms$. The solution for each time step requires around eight iterations to converge, with residuals for the momentum equations less than 2.5×10^{-5} and scalar equations less than 2.0×10^{-3}. In addition, the mass conservation error is less than 5.0×10^{-8}. The computation for propane and methane has been performed on an HP Z420 workstation with an Intel Xeon 3.5 GHz processor, while hydrogen simulations are on an HP Z840 workstation with the same processor. A typical LES run for the case BBBS (the most turbulent and time-consuming) requires about 408 and 312 CPU hours for propane and hydrogen, respectively, until the leading edge of the flame exits the explosion chamber.

5.4 Summary

The experimental test cases are small-scale vented deflagrations with a series of in-built obstructions. The size, geometry and design of the combustion chamber take into account various aspects of experiments and modelling. An apparent feature of the experimental setup is the capability to create a range of obstacle configurations. The overpressure signals approximately averaged from the original pressure signals facilitates the comparison between the numerical and experimental results. The computational setup is detailed including the domain, boundary and initial conditions and various numerical schemes.

Chapter 6

Results and Discussion: Propane

This chapter presents LES results using propane as the fuel. Section 6.1 provides an in-depth parametric analysis of the sensitivity of the LES calculation regarding the influential factors including flame initiation, Smagorinsky constant, filter width and mesh size. Section 6.2 illustrates the development of the propagating flame and the mechanisms driving the pressure build-up inside the combustion chamber using the LES data. Characteristics of flame-turbulence interactions are studied in Section 6.3 including the LES regime of combustion for the present simulations. Results of several selected flow configurations are presented in Section 6.4.

6.1 Parametric study

Recall that Section 4.9 presents the impact of filter width Δ and the correct behaviour of the DFSD model with the absence of turbulence in the steady-state 1-D laminar cases. Since the current research interest is mainly three-dimensional transient flame propagation ranging from initially laminar to fully turbulent, the results may be influenced by a range of factors such as coefficients in the turbulence and combustion models. This section examines the sensitivity of simulation results to some of the numerical parameters. Note that the effect of numerical schemes is not within the scope of this thesis but can be found in [66]. The parametric investigation does not intend to select the optimised set of coefficients but to realise and assess the sensitivity of the current computational setup to a range of typical modelling parameters. As a complete parametric investigation would be exhaustive, the present work focuses on (i) initialisation of combustion, (ii) Smagorinsky constant C_s, (iii) mesh size and (iv) combustion filter width Δ. In the dynamic wrinkling formalism, the test filter size is set to $\widehat{\Delta} = 1.1\Delta$ [81], and the inner cut-off scale is $\delta_c = 4\delta_L^0$ [61]. The fuel properties are set as: $s_L^0 = 39.0\ cm/s$ [160, 161] and $\delta_L^0 = 0.37\ mm$ [47] for the stoichiometric propane/air mixture at atmospheric

conditions ($T = 298\ K$ and $p = p_{atm}$). The basic computational set-up has been illustrated in Section 5.3.

6.1.1 Effect of combustion initialisation

Models for flame initiation may be divided into two categories: (i) using an ignition model for the development of the initial flame kernel; (ii) start the simulation with an already established burned flame kernel. Table 6.1 presents the four approaches (labelled as I01-I04) investigated in the present work, and they have been described in Chapter 3.

Table 6.1: List of methods investigated for initialising combustion

Method	Description	Initial $\widetilde{c}$ profile
I01	Ignition by flame kernel model	$\widetilde{c}$ defined by Eq. (3.36), only ignition point specified
I02	Start with a burned flame kernel	Filtered from 1-D solution, hemisphere with $4 - mm$ radius
I03	Start with a burned flame kernel	Filtered from a unit step function, hemisphere with $4 - mm$ radius
I04	Ignition by setting a region	$\widetilde{c} = 0.5$, hemisphere with $4 - mm$ radius

When applied to the present test cases, the flame is initiated at the bottom of the combustion chamber, near the closed end. Figure 6.1 shows the computed flame kernels (iso-lines of $\widetilde{c}$) in the configuration 000S using the four approaches at various time instants when the kernels are sufficiently large. It can be seen that small differences in $\widetilde{c}$ exist at the intersection between the kernel and the bottom wall. When the ignition is taken into account (i.e. I01 and I04), the wall shear takes into effect as the kernel establishes close to the chamber bottom wall, while this influence will not be seen if starting from burned kernels (i.e. I02 and I03). The difference in the $\widetilde{c}$ distribution across the flame front is considered small given that the early turbulence intensity around the ignition point is sufficiently low.

The influence of the flame initiation methods on the pressure trace and flame propagation are investigated using the configuration 000S and BBBS representing the least and most turbulent cases, respectively. Figure 6.2 displays the overpressure and the flame front position from the four approaches and the experiments for the configuration 000S. It can be noticed that the timing ($t_{p,LES}$) and magnitude ($P_{p,LES}$) of the pressure peak varies using different flame initiation approaches. The calculation using the flame kernel model gives a later $t_{p,LES}$, while starting from a burned kernel generally leads to early $t_{p,LES}$, and the discrepancy can be about 3.5 ms. One may expect this consequence as the burned kernel models simply neglected

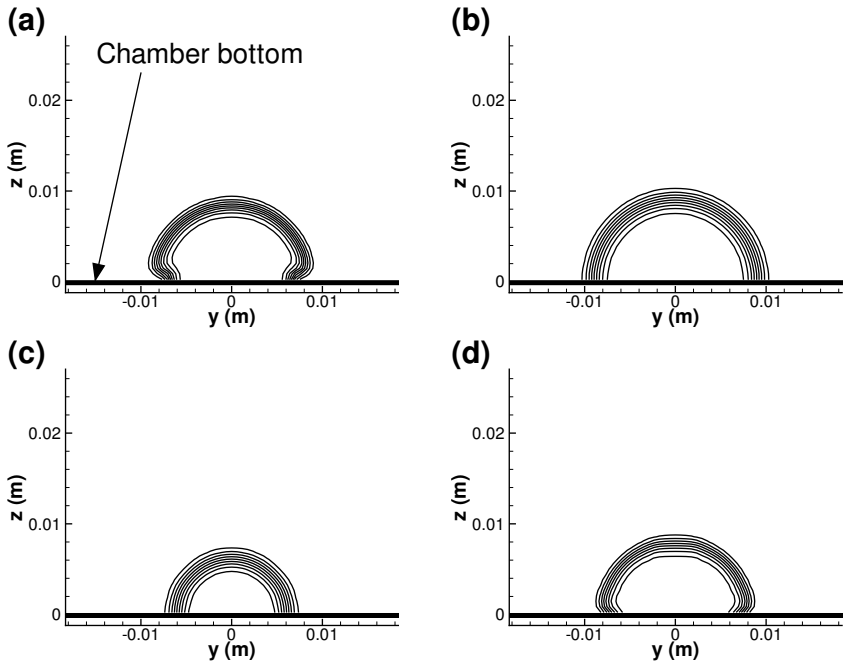

Figure 6.1: The structure of fully established flame kernels denoted by the iso-lines between $\widetilde{c} = 0.1$ and $\widetilde{c} = 0.9$ in the configuration 000S: (a) flame kernel model (I01), $t = 3.1\ ms$, (b) $\widetilde{c}$ from 1-D solution (I02), $t = 0.1\ ms$, (c) pre-filtered burned kernel using a Gaussian filter (I03), $t = 0.1\ ms$ and (d) ignition using the main combustion model (I04), $t = 1.4\ ms$.

the initial flame development. It can be seen that the initial treatment of the flame kernel has a non-trivial impact on the time taken to reach the pressure peak. Applying the same methods in the case BBBS results in similar effects. As can also be seen from Figure 6.3, the variation in $t_{p,LES}$ is about 3.3 ms for the configuration BBBS, and this is similar between the two configurations. On the other hand, the influence on the pressure peak magnitude is found to be small, with the deviation less than 3 mbar for the configuration 000S. The flame kernel treatment affects the early pressure fluctuations but has limited effect on the overpressure trend once it increases sharply.

The flame position profiles shown in Figure 6.2 illustrates that even with the same combustion model, the early-stage propagation speed is affected by the flame kernel modelling. The flame propagates faster when initialised using a filtered c profile from the 1-D laminar solution, while applying the flame kernel model leads to a slower propagation. Interestingly, as the flame becomes turbulent interacting with the central obstacle, the difference in flame speed tends to vanish. This is also seen for the configuration BBBS (Figure 6.3(right)) as the flame propagates roughly at the same speed after passing the second baffle plate. It may be concluded that the flame initiation has an impact on the quasi-laminar phase of the flame propagation, but the effect becomes much less significant in the turbulent stage. Since the

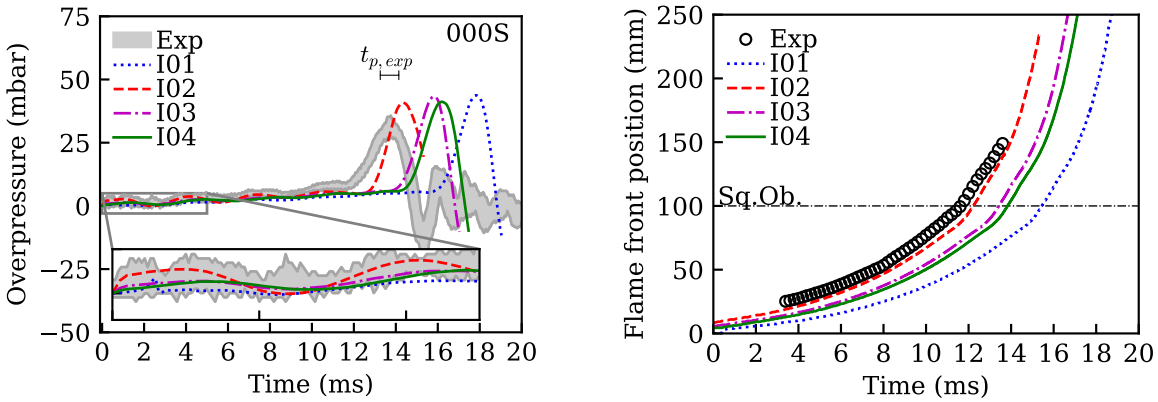

Figure 6.2: LES results with four flame initialisation methods: configuration 000S. *Left*: overpressure. *Right*: flame front position (leading edge of $\widetilde{c} = 0.5$).

primary contribution to the peak pressure is the turbulent phase of combustion, initial flame kernel treatment has a limited influence on the magnitude of the peak overpressure.

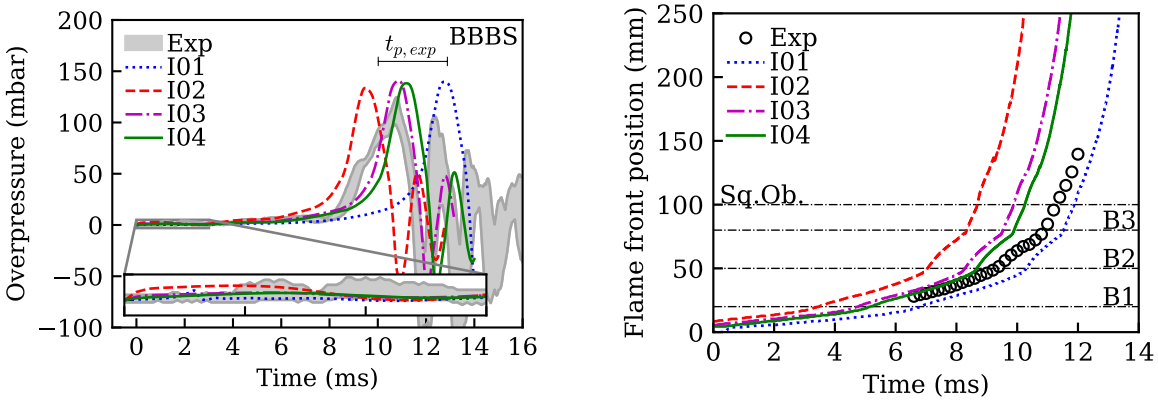

Figure 6.3: LES results with four flame initialisation methods - configuration BBBS. *Left*: overpressure. *Right*: flame front position (leading edge of $\widetilde{c} = 0.5$).

Table 6.2 summaries the practical considerations regarding flame initiation in the LES-FSD context. When using the flame kernel model (I01), one does not need to specify an ignition region, and the early flame development is calculated by the model. By contrast, the other three models require the specification of an appropriate kernel radius. Note that if the imposed flame kernel is too small in terms of the number of computational cells, the flame may just dissipate instead of propagating downstream. Therefore, a sufficient and reasonable kernel size is essential for using such models. Since the initial velocity field in the present test cases is quiescent, the turbulence effect is only dominant in the later phases of the flame propagation when the turbulence and vortex are sufficiently developed. The advantage of using a realistic ignition model would be more apparent in a case of more turbulent and chaotic

environment such as engine cylinders where the early flame kernel may be stretched, wrinkled or even convected away [108]. However, as the measurements, theory and modelling technique regarding ignition and early kernel formation in the SGS range are not yet matured, such ignition models still require further development [108]. For the rest of the study presented in this thesis, simulations are initiated with a burned flame kernel.

Table 6.2: Summary of advantages and disadvantages of each method for combustion initialisation.

Method	Advantage	Disadvantage
I01	No ignition radius specified Very early stage described	Extra computational time Very early stage may be insignificant
I02	Realistic c profile	1-D flame results in advance Specify kernel radius
I03	Profile directly available	Specify kernel radius Profile may not be realistic
I04	Make use of main combustion model	Ignition region large enough Initial $\widetilde{c}$ value has an effect

6.1.2 Grid sensitivity study

The motivation to study the grid sensitivity is twofold: (*i*) to investigate the dependence of results on the mesh resolution; (*ii*) to verify the quality of LES regarding the resolution. In most steady RANS simulations, the grid-independent solution may be found by refining the mesh. However, it is a much more complicated issue for transient cases using LES. As the filter width is generally linked to the grid spacing in the implicit LES approach, an LES would eventually tend to reach DNS when the grid size is progressively reduced [162]. For reacting LES, additional SGS models for combustion on top of modelling turbulence lead to other difficulties of assessing LES quality [163]. Thus, LES results are generally dependent on mesh resolution to an extent [164].

Table 6.3 displays the three grids used for the present investigation with the mesh refined from grid A to C, and all of them have cubic cells uniformly distributed within the chamber domain. The most turbulent case (BBBS) is selected for the verification since the sub-grid models are expected to be more influential compared with the other less turbulent ones.

Figure 6.4 shows that as the mesh is refined from grid A to B, the peak pressure increases by around 26%, with a further increase of 3.8% seen by changing from grid B to C. The calculated values of $t_{p,LES}$ appear to be very close using the three mesh sizes, but the relationship between the two is not monotonous. As expected, the early pressure development, as well as the flame

Table 6.3: Specification of the three grids studied

Grid	Δx (mm) within the chamber	No. of cells (million) within the chamber
A	1	1.4
B	0.75	3.0
C	0.59	6.9

propagation speed is much less dependent on the mesh or filter size. A noticeable variation on the pressure trace is only found after $t \approx 7$ ms. Flame speed computed by grid C becomes slightly higher after the second baffle, while the early propagation is not sensitive to the grid size. While the earlier work of Masri et al. [65] using the original Boger's FSD formalism [45] shows that the initial quasi-laminar phase is grid-dependent to an extent, the present model formulation ensures the mesh resolution has a minimal influence on the flame propagation speed at the early stage.

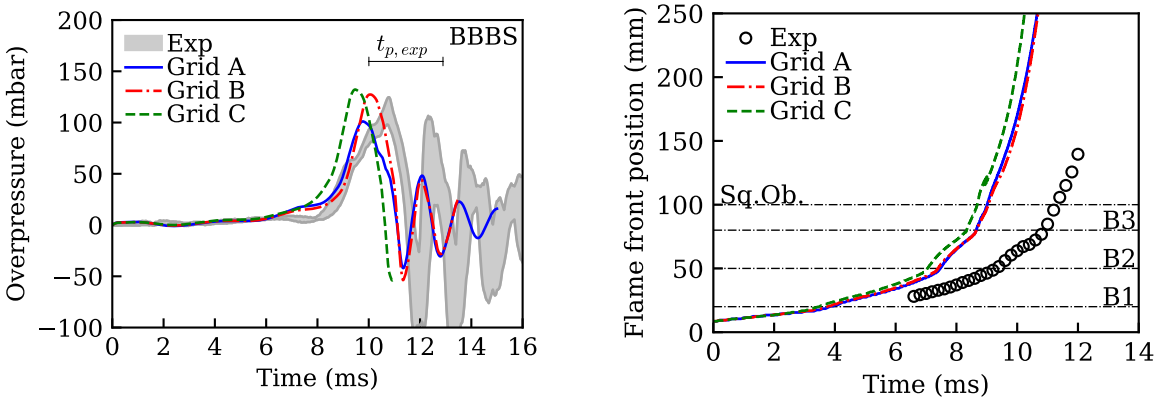

Figure 6.4: Sensitivity to mesh resolution as the number of cells increases from Grid A to C: configuration BBBS. *Left*: overpressure. *Right*: flame front position.

A quantitative method to assess the quality of the grid in terms of turbulence resolution is known as the Pope's criterion [165]. It states that the resolved portion of the total turbulent kinetic energy (TKE), η_{tke} should be typically greater than 80% for a good grid resolution.

$$\eta_{tke} = \frac{k_{res}}{k_{tot}} = 1 - \frac{k_{sgs}}{k_{tot}} \tag{6.1}$$

where k_{res} and k_{sgs} are the resolved and SGS parts of the total kinetic energy, k_{tot}, respectively. The resolved part is defined as

$$k_{res} = \frac{1}{2}(u_1'^2 + u_2'^2 + u_3'^2) \tag{6.2}$$

where u_i' ($i = 1, 2$ and 3) represents the RMS velocity fluctuations in the x, y and z directions, respectively, with respect to the Favre-filtered mean quantities from LES [164]. Note that the Favre notation $\widetilde{u}_i$ for velocities is dropped here for convenience. The mean velocity U_i is calculated using a common time average defined by

$$U_i(\mathbf{x}, t) = \frac{1}{t_{av}} \int_t^{t+t_{av}} u_i(\mathbf{x}, t) dt \tag{6.3}$$

where t_{av} is the time interval used for temporal integration. Given the transient nature of the problem, the average has been performed on a rolling basis throughout the simulation with a $t_{av} = 0.1\ ms$ [74]. The choice of the averaging time interval takes into account a sufficient sample of data points and the need to capture the transient velocity signal. The SGS part of the total TKE may be estimated as

$$k_{sgs} = \frac{\nu_t^2}{(C_s \overline{\Delta})^2} \tag{6.4}$$

where $\nu_t = \mu_t / \overline{\rho}$ is the turbulent kinematic viscosity given by the Smagorinsky model with C_s being the Smagorinsky constant. The grid filter scale $\overline{\Delta}$ used in the LES solver is twice the characteristic grid size $\overline{\Delta} = 2(\delta x \delta y \delta z)^{1/3}$ [66].

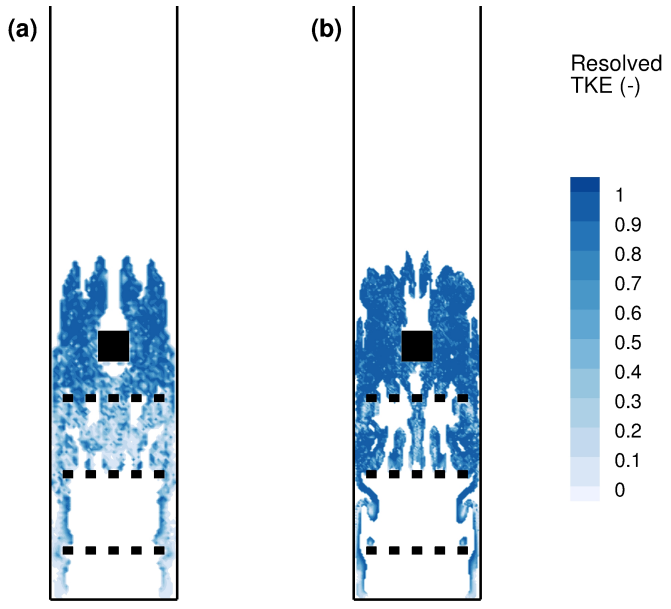

Figure 6.5: Resolved portion of turbulent kinetic energy conditioned in the flame front zone ($0.05 < \widetilde{c} < 0.95$): (a) grid A with $\Delta x \approx 1$ mm and (b) grid C with $\Delta x \approx 0.59$ mm.

Figure 6.5 shows the contribution of the resolved TKE in the flame front ($0.05 < \widetilde{c} < 0.95$) in the fully turbulent stage using grid A and C. The percentage of resolved kinetic energy is

generally lower on grid A with a typical value less than 40% before the third baffle. For grid C, k_{res} reaches $> 95\%$ in the regions downstream of the second baffle plate, while it considerably decreases closer to the ignition end of the chamber. The reason is that the turbulent intensity is substantially lower in these areas where the flame is quasi-laminar. Consequently, Pope's criterion [165] is reasonably satisfied for both grids as the $\eta_{tke} > 80\%$ in the majority of the flame, and grid C has a comparatively smaller under-resolved region. The variation in the overall flame structure between the two grids indicates the importance of mesh resolution in determining the resolved flame shape. Thus, the rest of the study uses grid C considering that it resolves a sufficient percentage of flow length scales to capture the essential flame dynamics.

6.1.3 Influence of Smagorinsky constant

A sensitivity study is performed with the three Smagorinsky constants C_s: 0.05, 0.1 and dynamic evaluation. For the classical Smagorinsky model, C_s between 0 and 0.2 are typically found in the literature for the reactive LES. Using a $C_s \to 0$ would be equivalent to not applying a turbulence model, meaning there is no contribution from the sub-grid scales to the turbulent momentum and scalar fluxes. Figure 6.6(left) shows that using a $C_s = 0.1$ tends to give a lower overpressure once the rate of pressure rise significantly goes up at around 8 ms, while the dynamic Smagorinsky model would give a moderate peak pressure. In contrast, the early stage of pressure build-up ($t < 8$ ms) has a very weak dependence on the C_s value. The flame-front locations shown in Figure 6.6(right) indicate a relatively weak correlation between the flame front speed and the Smagorinsky constant throughout the deflagration.

Figure 6.7(left) displays the evolution of the sub-grid wrinkling factor. The spatially averaged $\langle \Xi \rangle_f$ is defined as

$$\langle \Xi \rangle_f(t) = \frac{\int_{V_f} \Xi(\mathbf{x}, t) dV}{\int_{V_f} dV} \tag{6.5}$$

where V_f denotes the volume occupied by the flame ($0.05 < \widetilde{c} < 0.95$). While the calculation of C_s does not affect the SGS wrinkling in the early stage, it has a substantial influence after passing the second baffle plate. Using the DS model apparently leads to a higher Ξ, followed by the cases with $C_s = 0.05$ and $C_s = 0.1$, and it reflects the relative difference in the overpressure magnitude between $t = 8$ ms and $t = 10$ ms (Figure 6.6(left)). However, a considerable drop in Ξ using the dynamic Smagorinsky model is seen after passing the central obstruction, and the sub-grid wrinkling is highest with $C_s = 0.05$ compared with the other two cases. This

study shows that the relative magnitudes of the Ξ throughout the deflagration determine the peak overpressure as a large Ξ generally delivers greater heat release. Setting $C_s = 0.1$ gives a consistently low sub-grid flame wrinkling, leading to the lowest pressure peak. Comparing the DS model and $C_s = 0.05$, one can see that similar magnitudes of the pressure peaks are caused by the alternating wrinkling factors.

Based on the assumption and the derivation of the present dynamic combustion model [47, 81], the computation of Ξ depends solely on the wrinkling level of the resolved flame front as a result of test-filtering. Hence, different values of C_s modify the turbulence structures that interact with the resolved flame fronts. As the DFSD model evaluates Ξ based on the resolved flame structure, C_s is not directly associated with the combustion model (e.g. through the calculation of u'_Δ). Therefore, the C_s values indirectly link to the Ξ by the varying shapes of the resolved flame fronts.

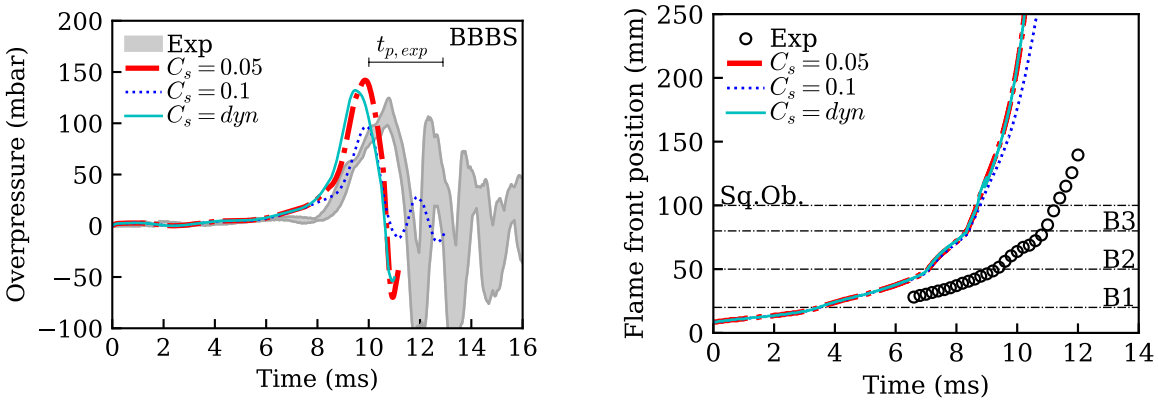

Figure 6.6: Influence of C_s using classical and dynamic Smagorinsky turbulence models: configuration BBBS. *Left*: with dynamic combustion model. *Right*: flame position.

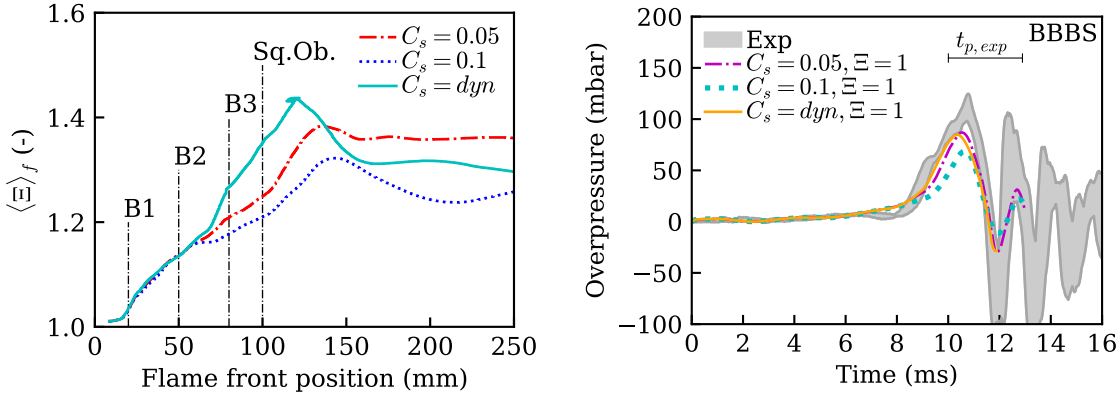

Figure 6.7: *Left:* Effect of C_s on the sub-grid wrinkling factor. *Right:* simulations neglecting the sub-grid reaction rate ($\Xi = 1$) - configuration BBBS.

To further illustrate the link between the C_s and the combustion model, Figure 6.7(right) presents the overpressure traces from the simulations in which Ξ is set to unity. Due to the neglect of the SGS reaction rate, the contribution from the sub-grid flame-turbulence interactions is not taken into account. Thus, it lowers the overpressure magnitude substantially compared with Figure 6.6(left). Figure 6.7(right) shows that the pressure is much less sensitive in this case. Despite the small variation in the pressure peaks, using $C_s = 0.1$ still leads to a lower pressure peak, and $C_s = 0.05$ gives the highest one. It is likely to be caused by the various levels of interactions between the resolved flame and turbulence.

It is important to notice that neglecting SGS contribution of the filtered reaction rate ($\Xi = 1$) would normally lead to insufficient overpressure build-up and slow flame propagation. As will be illustrated in the subsequent sections, the contribution of the sub-grid wrinkling varies depending on the factors such as the mesh resolution, fuel type and obstacle configurations. Figures 6.6 and 6.7 reveal that the influence of the turbulence parameters such as C_s is mainly to alter the wrinkling of the resolved flame front. Consequently, the dynamic FSD model would evaluate the sub-grid flame/turbulence interactions based on the resolved flame wrinkling. It also highlights the significance of accurately resolving the turbulent motions for the reliable application of the DFSD model.

6.1.4 Impact of the filter width

Flame filter width Δ is a critical parameter determining the filtered flame thickness. As first discussed in Section 4.9 using a range of 1-D laminar tests, the flame or the $\widetilde{c}$ gradient is typically resolved on about n_{res} grid points where $\Delta = n_{res}\Delta x$. Another finding from the 1-D test is that the laminar behaviours of the flame can be reproduced given that the flame is well-resolved, i.e. Δ is sufficiently large. The 3-D study considers four filter widths where $n_{res} = 4, 6, 8$ and 10. Figure 6.8 shows that as Δ increases the overpressure and flame position traces tend to converge. A minimum Δ threshold is present when $n_{res} \approx 4$, below which the simulation would considerably over-estimate the overpressure and the flame speed.

Figure 6.9 presents the evolution of the wrinkling factor using various filter widths. It is apparent that the flame wrinkling factor is close to unity and subsequently evolves to take into account the unresolved flame surface. As the computational domain has uniform mesh inside the combustion chamber, the local filter and test filter widths for the flame do not vary during the propagation. The formalism of the DFSD model (Eq. (3.31)) implies that the computed Ξ should compensate the increase of the filtered flame thickness due to Δ as $\overline{\dot{\omega}}_c \sim \Xi/\Delta$. Figure 6.9

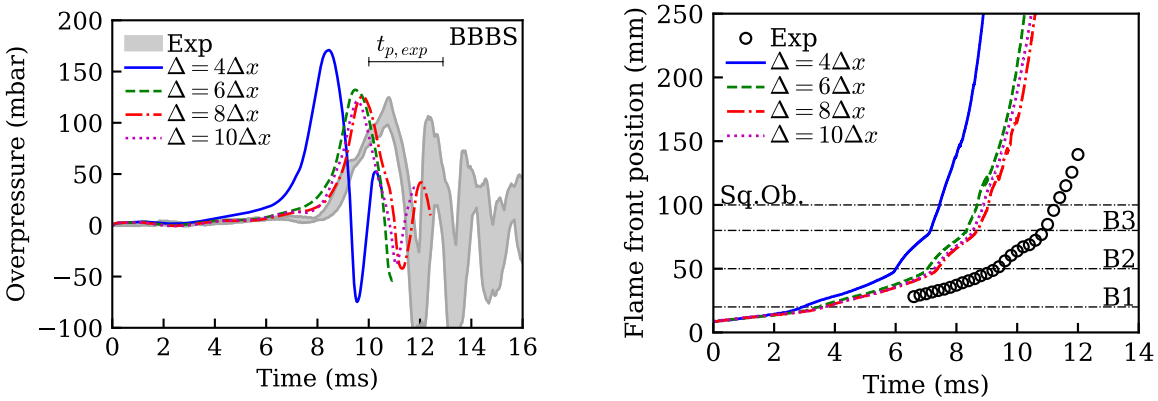

Figure 6.8: Sensitivity to filter width: configuration BBBS. *Left*: overpressure. *Right*: flame front position.

confirms that the sub-grid wrinkling level increases to account for the thicker resolved flame due to the use of a larger filter width. It is also worth pointing out that $\langle \Xi \rangle_f$ tends to be more sensitive to obstructions when a larger filter width is chosen, e.g. between B1 and B2. Thus, this study also shows the essential capability of the DFSD model to evaluate the sub-grid flame wrinkling at different filter scales.

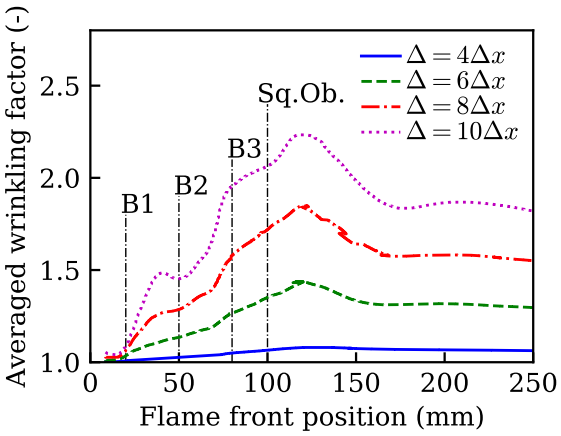

Figure 6.9: Evolution of the spatially averaged wrinkling factor $\langle \Xi \rangle_f$ using different filter widths.

6.1.5 Other considerations

Apart from the numerical schemes, there are other parameters and coefficients that can alter the overall calculation. The thermochemical properties, namely the laminar burning velocity s_L^0 and thermal flame thickness δ_L^0, would have an influence on the overall results as they are part of the combustion model. The role of s_L^0 is in the evaluation of the reaction rate $\overline{\dot{\omega}}_c$. A larger s_L^0 would generally lead to higher overpressure and faster flame propagation, but the

value of s_L^0 varies in the literature. For stoichiometric propane/air mixture at $T = 298\ K$ and $p = p_{atm}$, measured laminar burning velocity may range from 35.0 cm/s to 45.0 cm/s [161], and the variation is also substantial for the lean hydrogen/air mixture [166]. Regarding the laminar flame thickness, the present study adopts the concept of the thermal flame thickness defined using the maximum temperature gradient [167]. While the value is assumed to be constant, δ_L^0 may vary slightly if the chamber pressure is excessively high. The influence of δ_L^0 mainly comes from its relation to the inner cut-off scale δ_c in the DFSD model.

Another factor to consider is the parameters in the dynamic wrinkling formulation, namely the test filter size $\widehat{\Delta}$, the averaging filter size Δ_m and the inner cut-off scale δ_c. As illustrated by Veynante and Moureau [81], the inner cut-off scale should be prescribed by the user and cannot be determined by the dynamic procedure. Knikker et al. [61] found that δ_c varies from 3 to 4 times the thermal flame thickness from an experimental study, and Wang et al. [47] used $\delta_c = 3\delta_L^0$ for the simulation of turbulent flame kernels. While the inner cut-off scale should be of the order of the laminar flame thickness [81], uncertainties of this parameter still exist for the current model. The present work uses $\delta_c = 4\delta_L^0$ following Knikker et al. [61]. The test filter size $\widehat{\Delta}$ should be slightly larger than the filter size Δ, typically $1 < \widehat{\Delta}/\Delta < 2$ [81] to capture the resolved flame wrinkling. The averaging volume or filter width Δ_m is typically larger than the test-filtered flame thickness [81] and has been found to have a fairly limited influence for the present study.

Table 6.4: List of simulations and their parameter settings for the configuration BBBS. The time taken to reach the peak pressure (t_p) and the maximum overpressure (p_{max}). The text of the base simulation is in italic.

Simulation	Initialisation method	C_s	Grid	$\Delta/\Delta x$	Deviation t_p, %	Deviation p_{max}, %
I01-dynCs-gC-f6	I01	*dyn*	*C*	*6*	34.5	4.5
I02-dynCs-gC-f6					*0*	*0*
I02-Cs005-gC-f6		0.05			4.1	6.3
I02-Cs01-gC-f6		0.1			4.5	-27.4
I02-dynCs-gA-f6	*I02*	dyn	A		3.1	24.4
I02-dynCs-gB-f6			B		6.2	-4.7
I02-dynCs-gC-f4			C	4	-10.9	27.9
I02-dynCs-gC-f8				8	3.1	5.7
I02-dynCs-gC-f10				10	0.8	-9.5
I03-dynCs-gC-f6	I03			6	14.7	5.3
I04-dynCs-gC-f6	I04				17.9	3.5

Table 6.4 summarises the simulations performed to investigate the effect of numerical parameters in the configuration BBBS. The time taken to reach the peak pressure (t_p) and

the maximum overpressure (p_{max}) for each case are displayed with the deviation from the base simulation *I02-dynCs-gC-f6*. In general, flame kernel initiation has a profound role in determining the computed t_p, but it has a much weaker influence ($< 5\%$) on p_{max}. The impact of the flame filter width Δ remains weak (with a variation $< 10\%$) on both t_p and p_{max} as long as the filtered flame is sufficiently resolved on the LES mesh (i.e. $\Delta > 4\Delta x$). The Smagorinsky constant affects the evaluation of the dynamic combustion model since it alters the structure of the resolved flame front. Note that the behaviours of the results also rely on other factors such as the thermochemical properties and the dynamic model parameters. In the following sections, simulations have been performed according to the parameters of the base simulation *I02-dynCs-gC-f6*.

6.2 Phenomenological study

This section studies the phenomenon of the deflagration using LES, with the focus on the dynamic behaviours of the propagating flames and the mechanisms driving the pressure rise in the vented chamber. It also aims to show how LES can be used to help understand the complex transient combustion process leading to pressure build-up.

6.2.1 Development of propagating flames

Figure 6.10 displays a sequence of high-speed images of laser-induced fluorescence from OH (LIF-OH) from the experiment (Figure 6.10a) and calculated resolved FSD contours from LES (Figure 6.10b) in the configuration 000S. Note that the LIF-OH images only mark the reaction zone qualitatively, and large values of resolved FSD indicates the numerical reaction zone calculated from LES. Due to some difficulties in the experiments, two imaging tiers were used to capture the maximum viewable height but not the whole explosion chamber [156]. The right-hand side of the LIF-OH images appears blank since the laser sheet is blocked in the corresponding region [156]. These high-speed images are compared with the contours of resolved FSD from LES to demonstrate the flame shape and to validate the global degree of contortion of the flame at various stages. As there is a slight time variation in flame position for each experimental run, the starting time t_0 of the first flame image from LES is chosen so that the furthest flame leading edge matches that of the high-speed image. The time intervals between successive LES images are kept the same as in the high-speed images. The LES images (Figure 6.10b) shows that after ignition, the flame is quasi-laminar until it reaches the square obstruction. Then, the flame becomes corrugated behind the obstacle, as also confirmed by

the LIF-OH images (Figure 6.10a). The resolved flame front on LES follows the same trend as experiments, where it is only subjected to a strong stretch at a distance downstream of the central obstacle.

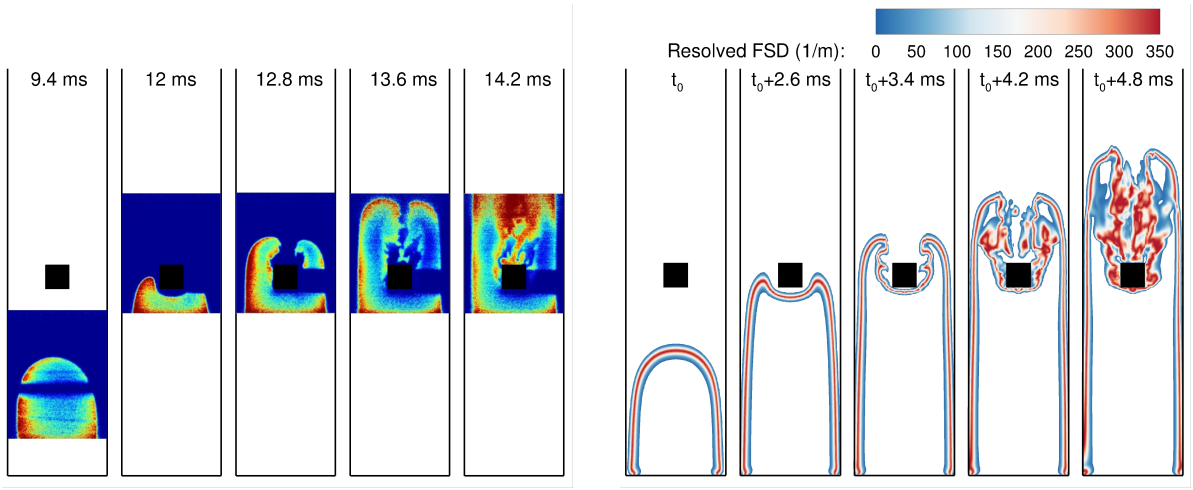

(a) LIF-OH images (false colourised) from experiments [156].

(b) LES images coloured by the resolved part of the FSD.

Figure 6.10: Time sequence of flame propagation: configuration 000S. Physical times after ignition are indicated at the top of each image. Time instant when the position of flame leading edge from LES matches the corresponding LIF-OH image (t_0).

Figure 6.11 gives a comparison of the propagating flame between the experiments (Figure 6.11a) and LES (Figure 6.11b) for the configuration BBBS. It can be seen from Figure 6.11 that the leading edge of the flame hits the first baffle plate and starts protruding through the narrow vents. As a result, the flame separates into finger-like shapes. However, at this early stage, the flame is not much wrinkled because the turbulence level is low behind the first baffle. Between the first and the second baffle plates, the four finger-shape flame humps merge and are also seen to propagate laterally towards the walls of the chamber. Note that the flame forms four fingers again when it hits the second baffle plate. It is then subjected to noticeable stretch due to higher local turbulence. After jetting out of the third baffle, the flame becomes significantly stretched and wrinkled. It encounters the central square obstacle at a very high speed and subsequently wraps around it. The highly wrinkled flame front propagates past the last obstruction and gets reconnected quickly in the recirculation zone. After that, the flame propagates toward the chamber exit.

Note that the 'geometrical' effect of obstacles with a sharp-edged cross-section in the direction of flame propagation can be identified from the flame images. It can be seen from the successive LES images that there are small packets of unburned mixture trapped in the

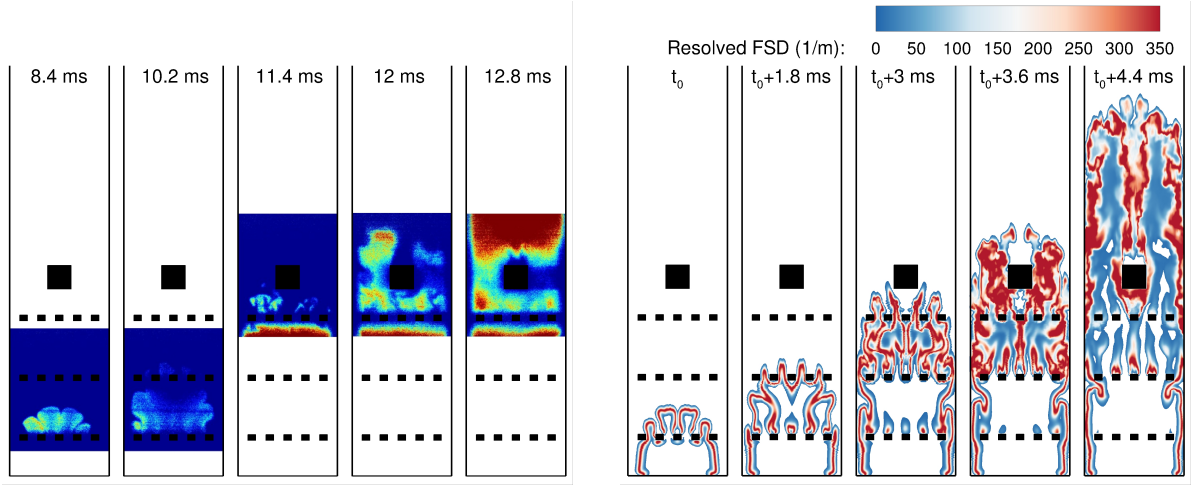

(a) LIF-OH images (false colourised) from experiments [156].

(b) LES images coloured by the resolved part of the FSD.

Figure 6.11: Time sequence of flame propagation: configuration BBBS. Physical times after ignition are indicated at the top of each image. Time instant when the position of flame leading edge from LES matches the corresponding LIF-OH image (t_0).

burned gases on the faces of some obstructions (e.g. strips of the baffle plates), left by the distorted flame front wrapping around them. For instance, the last images of both LES and experiments clearly show the trapped fresh gases in the recirculation zone downstream of the square obstacle. As a matter of fact, the trapped fresh mixture is typically present in the upstream and downstream regions of the baffle bars and the square obstacle and they will be consumed subsequently and contribute to the internal pressure rise of the chamber at later stages of the explosion. Comparison between the LIF-OH images (Figure 6.11a) at 12 *ms* and 12.8 *ms* and also between their corresponding LES images (Figure 6.11b) confirms that the trapped mixture in the area upstream of the central obstacle has been burned. Overall, the numerical and experimental images (Figures 6.10 and 6.11) for both configurations demonstrate the capability of reproducing flame structure, propagation rates and the entrapment of the unburned gases at various stages of the deflagration using LES.

6.2.2 Mechanisms of pressure rise

This section aims to explicate the mechanisms associated with the accumulation and release of the chamber internal pressure. The goal is to illustrate the link between the overpressure history and the flame propagation for explosions in a vented enclosure using LES. Configuration BBBS is used here as a demonstration and the analysis can also be extended to all other cases. Figure 6.12 presents the spatial distribution of the internal overpressure at five instants from the LES. As pressure is found to be nearly homogeneous in the cross-section of the explosion

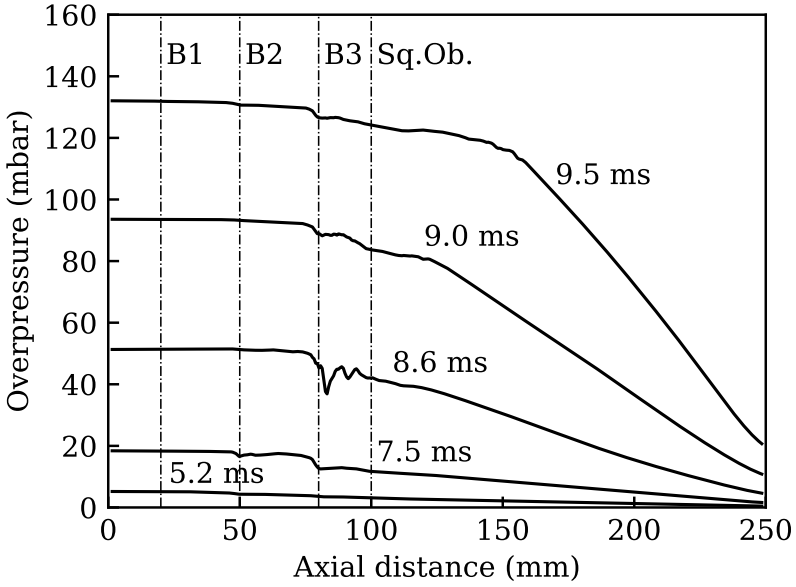

Figure 6.12: Spatial distribution of overpressure along the axial direction from the ignition end and between the first two baffle strips for configuration BBBS. Pressure profiles are extracted from the LES and the physical times are indicated.

chamber, only the axial profiles are given. It can be seen from Figure 6.12 that the pressure remains nearly uniform in the region of obstacles while there is a negative gradient from the most downstream obstruction towards the chamber exit (250 mm). As expected, the maximum internal pressure is located near the closed end of the chamber where ignition takes place. Hence, the overpressure monitored on the chamber base is considered for the analysis and discussion in the rest of the section.

The increase and decrease of overpressure within the explosion chamber can be directly explained by the competition between the two phenomena: expansion of the gases and venting at the chamber exit. The rate of gas expansion can be represented by the rate of volume change of the fresh unburned gases with the burned gases. In LES, this may be calculated from

$$\dot{V}_{expa} = \frac{\partial}{\partial t} V_b \left(1 - \frac{\rho_b}{\rho_u}\right) \tag{6.6}$$

where ρ_u and ρ_b are the densities of unburned and burned mixtures, respectively. The volume occupied by the burned gases, V_b, can be evaluated by integrating $\overline{c}$ over the entire computational domain Ω: $V_b = \int_\Omega \overline{c}\, dV$ [47]. The venting rate is computed as the volume flow rate across the chamber exit:

$$\dot{V}_{vent} = \int_{A_{exit}} \tilde{\mathbf{u}} \cdot \tilde{\mathbf{n}}\, dA \tag{6.7}$$

where $\tilde{\mathbf{u}}$ and $\tilde{\mathbf{n}}$ are the velocity and its normal direction, respectively.

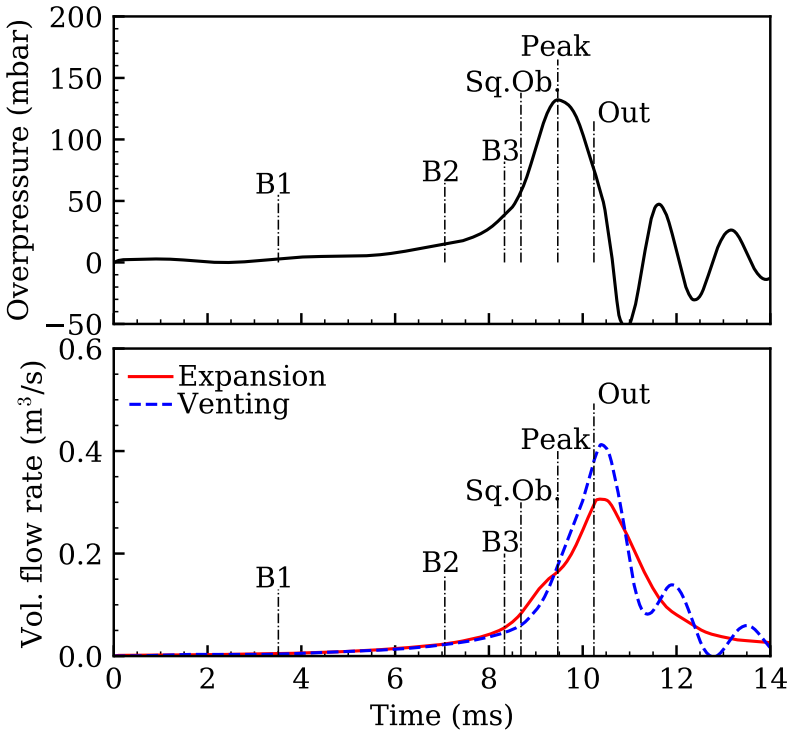

Figure 6.13: Pressure rise and oscillations of configuration BBBS illustrated by expansion and venting of gases. *Top*: Overpressure time trace from LES. *Bottom*: Expansion and venting rates evaluated by LES. Time instants of flame reaching the three baffle plates (B1, B2, B3), the central square obstacle (Sq.Ob.) and chamber outlet ('Out'). Time of the first peak overpressure ('Peak').

Figure 6.13 displays the rates of expansion and venting and their relation to the evolution of overpressure in the explosion for case BBBS. Times of flame moving through the midpoints of all the obstructions are also identified as B1, B2, B3, and Sq.Ob. The figure also indicates the time taken to reach the peak overpressure and the time when the flame exits the chamber. When $\dot{V}_{expa} > \dot{V}_{vent}$, pressure builds up inside the chamber. In contrast, $\dot{V}_{expa} > \dot{V}_{vent}$ will lead to a decrease in overpressure.

It is clear from Figure 6.13 that the overpressure history is closely related to the competition between gas expansion and venting. Before the flame reaches the second baffle, pressure increases gradually in a fluctuating way. A similar pattern can also be observed from the experimental pressure signals in other configurations. The fluctuation is represented by the alternative evolution of both expansion and venting rates. When the flame is at the upstream position of B2, the explosion chamber is efficiently vented, given that the expansion and venting rates grow at very close values and the pressure remains relatively low. At this early stage of the explosion, the expanded volume created by the burned gas from the combustion process

can be properly exhausted through the venting from the chamber outlet. Overpressure begins to rise sharply between B2 and B3 where the flame starts to transit from quasi-laminar to fully turbulent. This is reflected by the significant growth in the expansion rate at almost the same time. Meanwhile, rapid burning also pushes more unburned mixture towards the chamber exit, inducing a corresponding enhancement in explosion venting. However, a lag between the two phenomena means that the flow is not sufficiently expelled from the chamber and it gives rise to the pressure rise. Maximum overpressure is reached when the venting rate takes over the expansion rate. It takes place between the square obstacle and the chamber open end as it is the furthest obstruction downstream encountered by the flame. Beyond this point, overpressure drops because venting is relatively more efficient than combustion for the rest of the fresh gases within the chamber. At about 10.2 ms, the leading edge of the flame exits the chamber and the expansion rate stops rising. The combustion rate is only maintained for a very short period before decreasing, as a result of the burning of the remaining fresh gases at the corners of the chamber and in the wake area of the obstructions. In the meantime, the venting rate is adjusted by the acoustic reflection, and consequently, pressure drops and oscillates towards the atmospheric level. As shown in Figure 6.13, both venting and expansion rates decrease in an alternative manner after the flame leaves the chamber, generating weak peaks observed in the pressure history from LES. The oscillations of overpressure after the first peak reproduced by LES agree with the frequency observed in the experiments (not shown in this thesis) [156]. The computation of these oscillations is closely related to the size and the velocity boundary condition of the extended computational domain which resembles the external atmosphere. However, reliable prediction of pressure oscillations due to acoustics is outside the scope of this study. The discussion here primarily intends to demonstrate the identification and quantification of venting and expansion processes related to the whole overpressure history in an explosion event.

6.3 Flame-turbulence interactions

An essential feature of these cases is the interaction between the flame front and the obstacle-generated turbulence. The flame surface evolution and the flame propagation mechanism are predominantly governed by the unburned gas flows such as turbulent eddies and shear layers generated downstream of solid obstacles. Johansen and Ciccarelli [122] provided a visualisation of the unburned gas flow field ahead of an accelerating flame in an obstructed channel. They found that the initially formed vortices are laminar with a defined structure, and unstable and

fully turbulent shear layers grow with time due to the upstream flame propagation [122]. It is thus useful to characterise the role of obstructions in the path of the flame travelling. The two cases with distinct turbulent environments, configurations 000S and BBBS, are considered in this section.

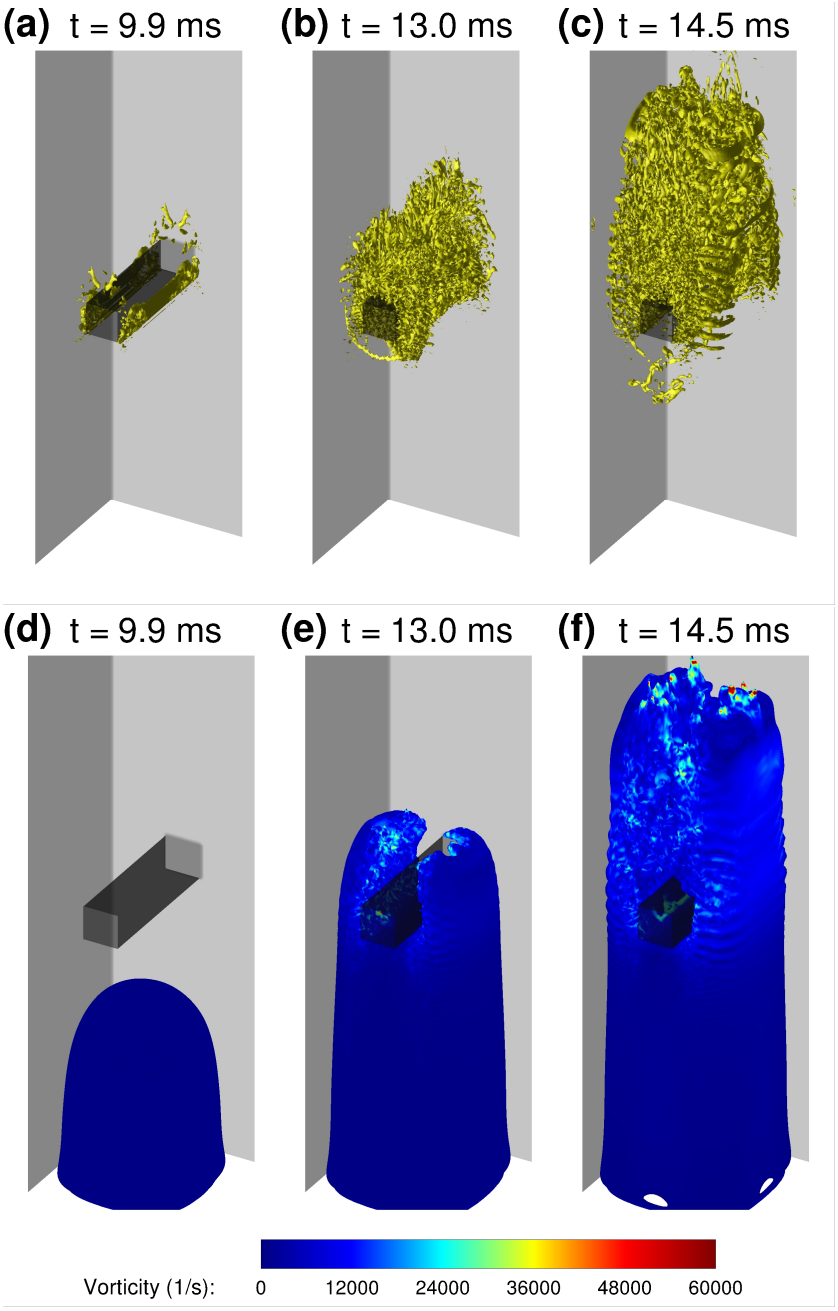

Figure 6.14: Vortex structure and flame-turbulence interaction: configuration 000S. (a)-(c): iso-surface of $Q = 5 \times 10^6\ s^{-1}$ at various time instants. (d)-(f): flame front ($\widetilde{c} = 0.5$) coloured by the vorticity magnitude at corresponding time instants.

Figure 6.14 captures the sequential vortex structure and its interactions with the flame front for the case 000S. Q-criterion [168] is an indicator of turbulent flow and has been used in visualising vortical structures in reacting flows [169, 170]. The unburned gas flow ahead of

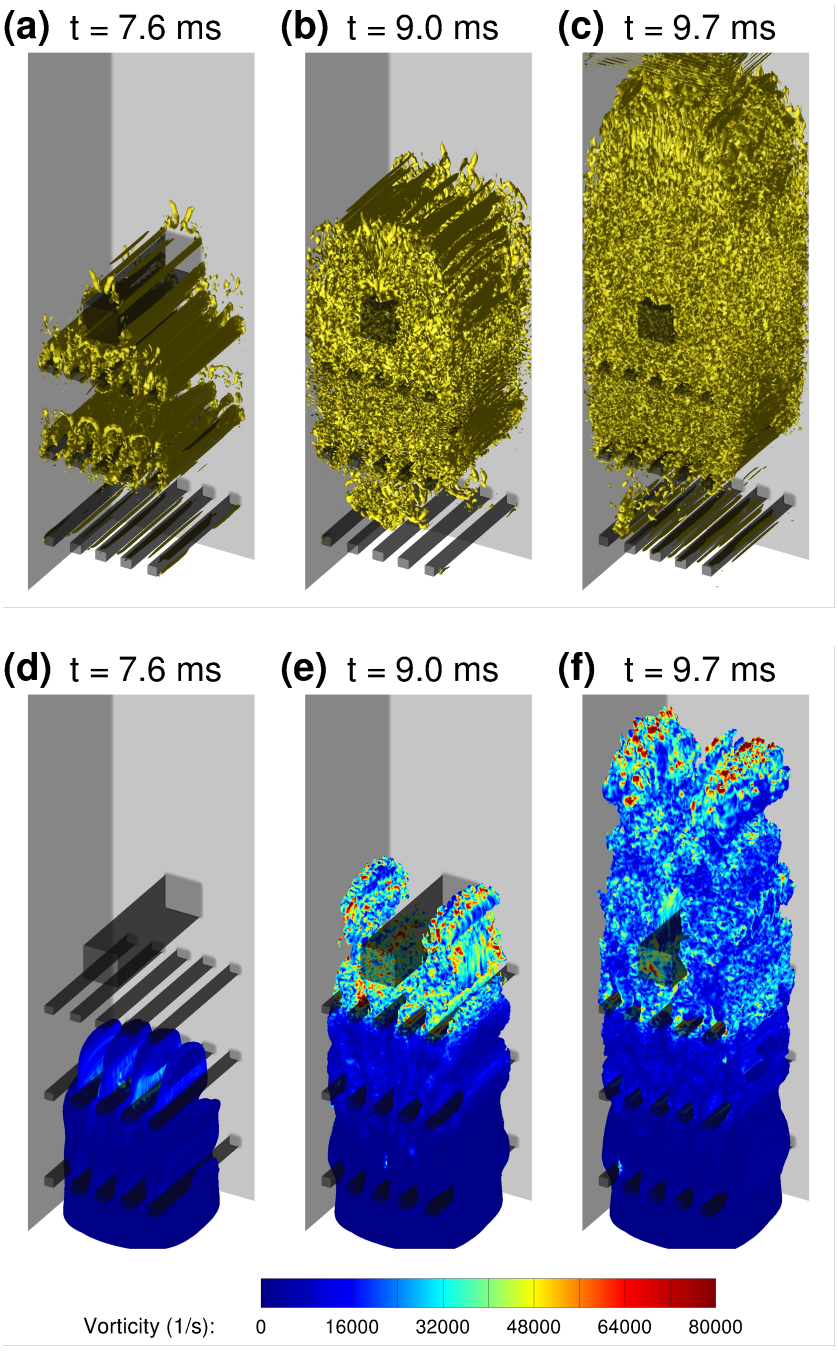

Figure 6.15: Vortex structure and flame-vortex interaction: configuration BBBS. (a)-(c): iso-surface of $Q = 5 \times 10^6\ s^{-1}$ at various time instants. (d)-(f): flame front ($\widetilde{c} = 0.5$) coloured by the vorticity magnitude at corresponding time instants.

the flame starts from quiescent and gradually develops in the wake of the central obstruction as a result of the gas expansion, confinement and blockage. Another factor influencing the flow development is the passage between the obstacle and the chamber side walls dictated by the area blockage ratio ($ABR = 0.24$ in this case). From Figure 6.14d-f, the vorticity magnitude contoured on the flame implies the strength of interaction between the turbulence and the resolved flame font. As turbulent structures are predominantly located behind the obstacle, the flame front remains quasi-laminar before reaching it. It is also clear that the vortical structure in the wake area grows as the flame approaches the central obstacle, but the flame-flow interactions only begin after the flame passes the obstacle. As the deflagration is a highly transient process, it is expected that the location of the central obstacle governs the turbulence generation in the case of the single obstruction. The obstacle-generated turbulence would not have sufficient time to develop if its location is too close to the initial flame kernel, and consequently, the flame-turbulence interactions would be relatively weak. In contrast, if the obstacle was placed very close to the chamber exit, most of the fresh mixture would have been consumed before interacting with it.

Figure 6.15 gives the turbulence and flame snapshots for the case BBBS at three locations same as that in Figure 6.14. Figure 6.15a shows that the sharp-edged rectangular grids are particularly effective in creating turbulence. As the iso-surfaces of the Q-criterion are at the same values between the two configurations, it indicates the much more substantial turbulence generation. It is clear that the relatively short separation between the third baffle and the central obstacle makes the region full of turbulent eddies, and it gives rises to a considerable flame wrinkling as shown in Figure 6.15e. On the other hand, turbulence has not developed much behind the first baffle plate due to its short distance away from the ignition end. At the early stage, the patterns of the turbulent vortex shedding resulting from the baffle plates are more coherent (Figure 6.15). However, the propagating flame front breaks these patterns by producing eddies of smaller scales. Comparing the snapshots when the flame has just passed the central obstacle (Figure 6.14e and Figure 6.15e) for the two configurations, it can be seen that the flame front has already been substantially wrinkled by propagating through the three successive baffle plates. Despite the considerable turbulence effect at the later phase, interactions do not occur on the entire flame. Figure 6.15e and f confirm that in the region before the third baffle the flame only subjects to a weak turbulence influence.

Figure 6.16 presents the overpressure traces from the experiments and LES for the two

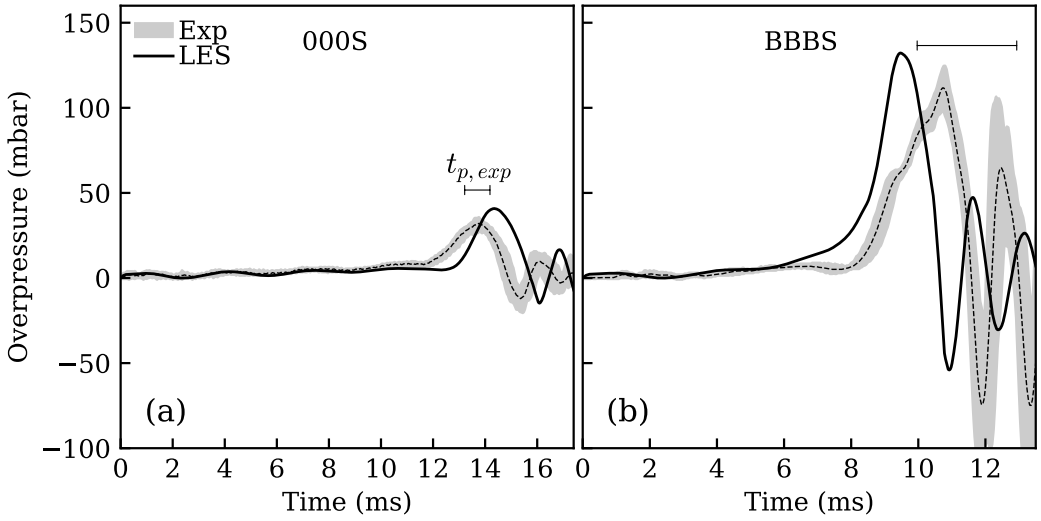

Figure 6.16: Overpressure traces between LES and experiments. Configuration: (a) 000S and (b) BBBS. mean experimental pressure signal (- - - -). The range of time taken to the first peak overpressure in the experiment, $t_{p,exp}$ (⊢⊣).

configurations. Evidently, the overpressure remains low at the early stage of combustion for both cases. In spite of the slight over-estimation, LES captures the overpressure trends correctly for both configurations. Based on LES, the pressure magnitude is low before a sharp increase is seen at $t = 13\ ms$ and $t = 6\ ms$ for the two configurations, respectively. The peak pressure of the configuration BBBS is nearly four times higher than the other, and it is primarily due to the strong turbulent intensity generated using the three baffle plates. For the filtered flame front, the flame-turbulence interactions are divided into the resolved and the sub-grid parts. The former is directly taken into account by the resolved portion of the filtered reaction rate, while the latter is estimated using the sub-grid wrinkling factor. Figures 6.14 and 6.15 also illustrate that the resolved part of the interactions is related to the turbulence motions resolved on the LES grid, and it is substantially higher for the configuration BBBS. The effect of the smaller-scale turbulence on the filtered flame front is compensated by the sub-grid wrinkling factor Ξ.

Figure 6.17 shows the evolution of the mean wrinkling factor $\langle\Xi\rangle_f$ over the flame propagation for the two configurations. In general, the sub-grid wrinkling factor calculated for the case BBBS is greater than that in 000S due to the presence of the baffle plates. Under the same numerical condition, $\langle\Xi\rangle_f$ can reach up to 1.45 with the case BBBS, while that of the other remains less than 1.2. The initial wrinkling factor is close to unity as the turbulence influence on the imposed flame kernel is negligible. For the case 000S, $\langle\Xi\rangle_f$ remains to be unity before passing the square obstacle due to the relatively long quasi-laminar phase. By contrast, in

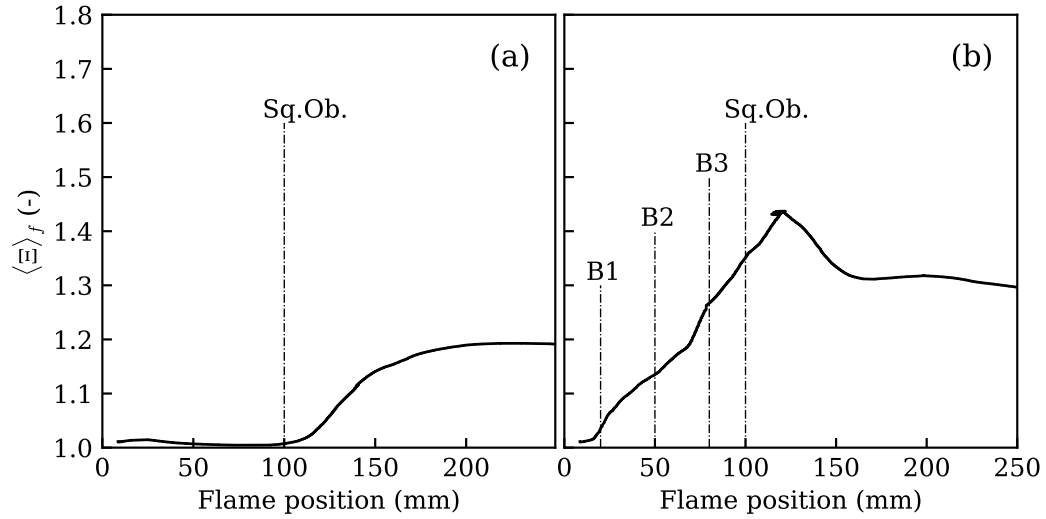

Figure 6.17: Evolution of flame wrinkling factor. Configuration: (a) 000S and (b) BBBS.

the case BBBS, the flame is continuously wrinkled and the SGS part of the contribution to the reaction rate increases when passing through successive obstructions. In the blow-down region downstream of the last obstacle, fast flame propagation is still maintained by the local turbulence, and $\langle \Xi \rangle_f$ has a tendency to stabilise. LES reproduces the essential physical process for the deflagration and the impact of the obstructions.

Figure 6.18 gives the sequential flame images contoured by the sub-grid wrinkling factor Ξ for both configurations. It also indicates the dynamic nature of the combustion model in evaluating the flame wrinkling for various turbulent environments. For the configuration 000S, the entire flame remains quasi-laminar until hitting the central obstruction ($t = 11.8\ ms$), and $\Xi \approx 1$ for the flame region during this period. Sub-grid flame wrinkling is only significant after passing the obstacle where Ξ is high around the leading edge of the flame and behind the obstacle (e.g. at $t = 14.5\ ms$). It contributes to the main pressure peak as shown in Figure 6.16a. Comparatively, for the configuration BBBS, the sub-grid flame wrinkling evolves with time but remains relatively low before the third baffle plate ($t = 7.6\ ms$). Due to the short distance between the third grid and the central obstacle, a strong turbulent flow field is generated in the region where the Ξ reaches up to 1.7 (e.g. at $t = 8.6\ ms$ and $t = 9.0\ ms$). It leads to the sharp rise in the overpressure trace as shown in Figure 6.16b. Evidently, the presence of the baffle plates enhances the contribution of the sub-grid reaction rate, resulting in faster local flame propagation in areas of high Ξ. Downstream of the square obstacle ($t = 9.7\ ms$), the overall Ξ decreases but is still considerably maintained by the flame-turbulence interactions in the second half of the chamber. Note that even in the turbulent phase, the sub-grid contribution of the

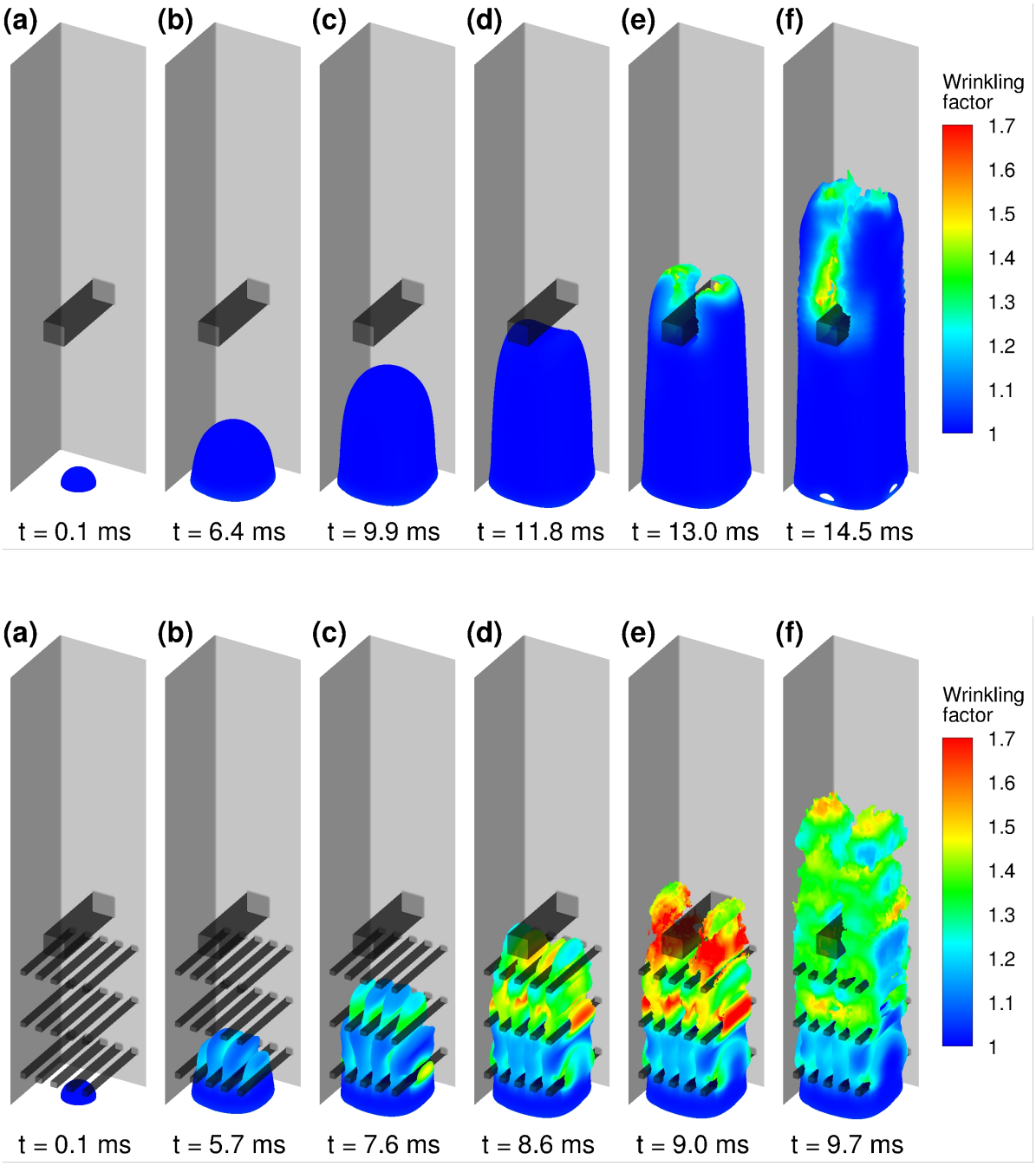

Figure 6.18: Three-dimensional flame images (iso-surface of $\widetilde{c} = 0.5$) contoured by Ξ at various time instants. (a) to (f) correspond to the flame leading edge ($\widetilde{c} = 0.5$) at $35, 65, 90, 120, 170\ mm$ away from the ignition end. *Top:* configuration 000S. *Bottom:* configuration BBBS.

flame wrinkling remains low for the entire deflagration in areas where the flame is quasi-laminar (near the ignition end). Figure 6.18 also illustrates the capability of the dynamic FSD model in accounting for both the temporal and spatial sub-grid flame wrinkling for the least and most turbulent cases. It can also be concluded from Figures 6.15 and 6.17 that the higher peak overpressure generated by configuration BBBS is a consequence of both the greater resolved and sub-grid parts of the flame-turbulence interactions. As a matter of fact, the application of a combustion test filter means the intrinsic link between the resolved and the sub-grid flame surfaces.

6.3.1 LES regime of combustion

The Pitsch LES regime [35, 39] for turbulent premixed combustion is used here to characterise flame-turbulence interactions in a deflagration event. Regime diagrams for RANS proposed by Borghi [30] and Peters [34] generally use the physical quantities such as u'/s_L and ℓ_0/δ_L to indicate different regimes. The LES regime proposed by Pitsch and De La Geneste [35] is constructed introducing the modelling parameters including the filter width Δ and sub-grid velocity fluctuation u'_Δ. Thus, it characterises the sub-grid turbulence-flame interactions and provides insights into the modelling aspects.

As demonstrated in Section 2.1.2, the Karlovitz number may be evaluated using the laminar flame scales and sub-grid velocity fluctuations u'_Δ as

$$Ka = \sqrt{\frac{\delta_L}{s_L^3}\epsilon} = \sqrt{\left(\frac{u'_\Delta}{s_L}\right)^3 \frac{\delta_L}{\Delta}} \tag{6.8}$$

where ϵ is the viscous dissipation rate, and u'_Δ corresponds to the sub-grid velocity fluctuations at the flame filter scale. Following Wang et al. [53] and Vermorel et al. [99], it may be scaled from the LES grid filter scale $\overline{\Delta}$ as

$$u'_\Delta = u'_{\overline{\Delta}} \left(\Delta/\overline{\Delta}\right)^{1/3} \tag{6.9}$$

using the fluctuations at the flow filter scale $u'_{\overline{\Delta}}$. It may be computed as [99]

$$u'_{\overline{\Delta}} = \frac{\nu_t}{C_s \overline{\Delta}} \tag{6.10}$$

where the eddy viscosity ν_t is estimated from the Smagorinsky model [42, 60]

$$\nu_t = (C_s\overline{\Delta})^2\sqrt{2\widetilde{S}_{ij}\widetilde{S}_{ij}} = (C_s\overline{\Delta})^2\sqrt{\frac{1}{2}\left(\frac{\partial\tilde{u}_i}{\partial x_j}+\frac{\partial\tilde{u}_j}{\partial x_i}\right)^2} \tag{6.11}$$

Combining Eqs. (6.10) and (6.11) results in

$$u'_{\overline{\Delta}} = C_s\overline{\Delta}\sqrt{\frac{1}{2}\left(\frac{\partial\tilde{u}_i}{\partial x_j}+\frac{\partial\tilde{u}_j}{\partial x_i}\right)^2} \tag{6.12}$$

It should be noted that the C_s and u'_{Δ} in Eqs. (6.9) and (6.12) must be positive to ensure the validity of evaluating Ka using Eq. (6.8). However, the application of the dynamic Smagorinsky model may result in negative C_s caused by the negative eddy viscosity μ_t in certain regions of the flame. As a matter of fact, negative eddy viscosity is associated with backscatter where energy from the sub-grid scales transfers to the resolved scales of motions. On the other hand, negative eddy diffusivity for scalars is related to counter-gradient turbulent diffusion. According to Veynante et al. [171], high heat release rates at the flame front lead to significant dilatation and pressure gradients, promoting the counter-gradient diffusion. It is expected in the present test cases from the numerical point of view [66]. Thus, simulations of constant $C_s = 0.07$ are performed here for evaluating the LES regime diagram to avoid the issue of negative μ_t.

Figure 6.19 shows the location of the present simulations in the LES regime diagram (constructed based on [144]) throughout the deflagration. Due to the nature of the transient flame propagation, an averaged Karlovitz number is extracted from the computational nodes in the filtered flame front ($0.05 < \widetilde{c} < 0.95$) at each time step. The regime plot ranges horizontally resulting from the uniform grid (hence the filter width) within the chamber. Sub-grid combustion takes places in the thin reaction zone when $Ka > 1$, and it lies in the corrugated flame regime for $Ka < 1$. Further increase in Karlovitz number ($Ka > 100$ or $Ka_\delta > 1$) would bring the flame into the broken reaction zones (not shown in Figure 6.19), and some numerical methods designed for thin fronts may become inappropriate [39]. Another critical length scale corresponding to the smallest size of an eddy that can cause flame front wrinkling is the Gibson scale [36]:

$$\ell_G = \frac{s_L^3}{\epsilon} = \frac{s_L^3\Delta}{{u'_{\Delta}}^3} \tag{6.13}$$

Combining Eqs. (6.8) and (6.13) with the condition of $\Delta = \ell_G$ gives the line of $Ka^{-2} = \Delta/\delta_L$

in the LES regime diagram (Figure 6.19). Under the constant filter width, flame wrinkling is controlled by the Karlovitz number. The thin reaction zone regime is of the particular interest in which most practical premixed combustion devices are operated [39]. As illustrated by Pitsch [39] and Fiorina et al. [144], on the left-hand side of the $\Delta = \ell_G$ line, the flame front wrinkling is fully resolved on the filter scale, while the right-hand-side of the $\Delta = \ell_G$ line indicates the existence of the sub-grid scale wrinkling. Note that even when the flame wrinkling is resolved on the grid, the current simulations will not enter the zone of resolved turbulence as the filter width is still much larger than the Kolmogorov scale.

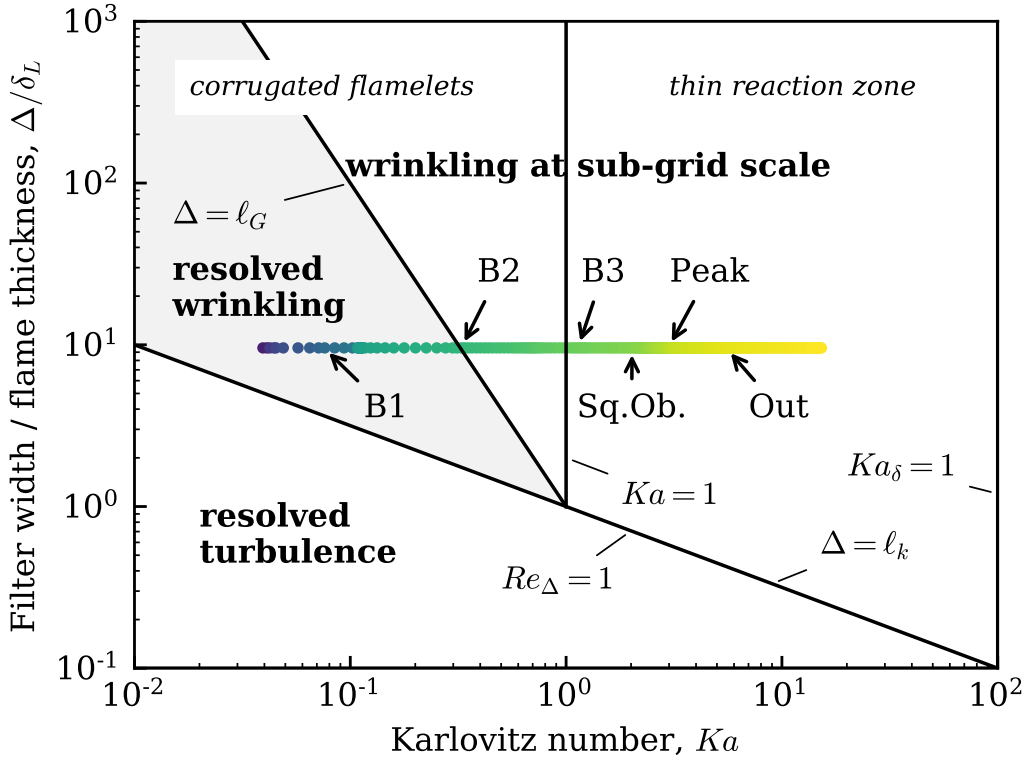

Figure 6.19: LES regime diagram [144] for turbulent premixed combustion considering the filtered flame front ($0.05 < \widetilde{c} < 0.95$) at various time instants - configuration BBBS. The colour from dark blue to light yellow indicates the time advancement during the flame propagation.

Figure 6.19 also indicates the locations of the flame leading edge in the regime diagram. Since the filter width is constant in the simulation, obstacles induce a continuous growth in the flame Karlovitz number, causing its positive movement in the diagram. It is evident that the flame wrinkling is fully resolved at the LES filter before reaching the second baffle B2 due to the low turbulence intensity. This indication in the regime diagram reasonably agrees with the computed low sub-grid wrinkling factor ($\Xi \leq 1.15$) prior to B2, as shown in Figure 6.17b. However, the computed mean Ξ value is not exactly zero at the flame front during the period,

as shown in Figure 6.18(bottom)b considering (*i*) there are uncertainties in the estimation of u'_Δ for the regime diagram; (*ii*) the test-filtering operation captures non-zero wrinkling of the resolved progress variable field stretch. Nevertheless, since u'_Δ is not directly related to the model formulation of combustion, both the DFSD model and the regime diagram confirm the weak contribution from the sub-grid scale reaction rate during the initial flame propagation. As the flame propagates further, the sub-grid contribution of the flame wrinkling begins to grow, and it impacts the propagation speed of the filtered flame front. The flame enters the thin reaction zone regime from the corrugated flamelets after passing the third baffle. Evidently, the main pressure peak is reached when the flame is within the thin reaction zone regime, and the substantial Karlovitz number indicates the intensive interaction of flow and combustion on the smallest turbulent scales. Figure 6.19 also confirms that the deflagrating flame will not transit to the broken reaction zone for the entire deflagration so that the filtered flame front retains its flamelets-like structure. While the sub-grid scale wrinkling dominates in the turbulent stage of the deflagration, the overall flame wrinkling is expected to be resolved to a larger extent with the future increase in computational power. Hence, it highlights the importance of correctly predicting the laminar flame propagation and the turbulence generated in the path of the deflagration.

6.4 Comparative study of flow configurations

Detailed analysis of pressure trends and flame behaviours are only given for five configurations, clustered into two families as shown in Figure 6.20. Each configuration has an associated code representing the number and position of obstructions. For example, configuration BB0S indicates baffles at the first two locations near the ignition end and a small solid square obstacle. Family 1 intends to investigate the effects of increasing the number of baffle plates starting from one baffle furthest from the ignition point (configuration 00BS, 0BBS and BBBS), while family 2 is to study the impact of increasing baffle plates starting from one plate closest to the ignition point (configuration B00S, BB0S and BBBS).

6.4.1 Combustion characteristics: family 1

Family 1 (Figure 6.20a) consists of configurations 00BS, 0BBS and BBBS with a progressively increasing number of baffle plates that are positioned furthest from the ignition bottom. Figure 6.21 presents the histories of overpressure at the base of the chamber from LES and experiments for the configurations in family 1. Some data processing of raw experimental

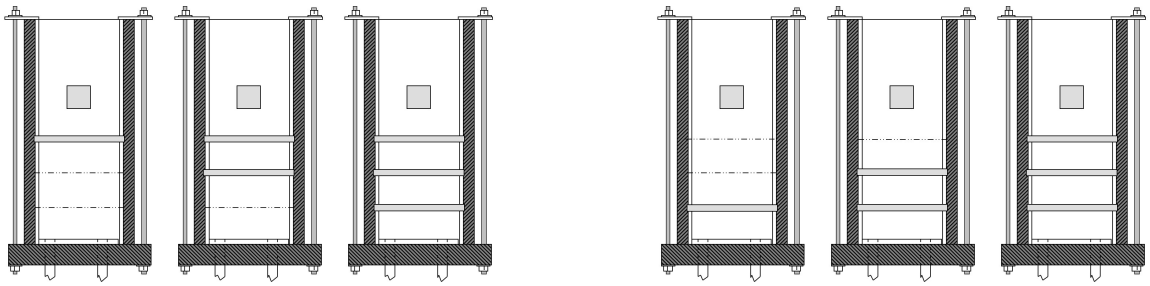

(a) Family 1 **(b)** Family 2

Figure 6.20: Configurations classified into two families.

pressure signals was conducted to facilitate the comparison against the numerical results. First, pressure signals are aligned based on the peak overpressure for each realisation and are then grouped in a statistical envelope, in order to perform averaging and to visualise the variation in overpressure magnitudes for all the signals. Next, the mean pressure trace is plotted within the envelope to view the pressure trend and mean peak overpressure from experiments. Lastly, as there is a slight shift in time due to the variability in the ignition for each run, the variation in the time to reach the peak (referred to as "time-to-peak") is indicated in Figure 6.21. Experimental mean pressure trace is placed according to the averaged times taken to reach the peak. Predicted LES pressure is also plotted to compare with the experimental data.

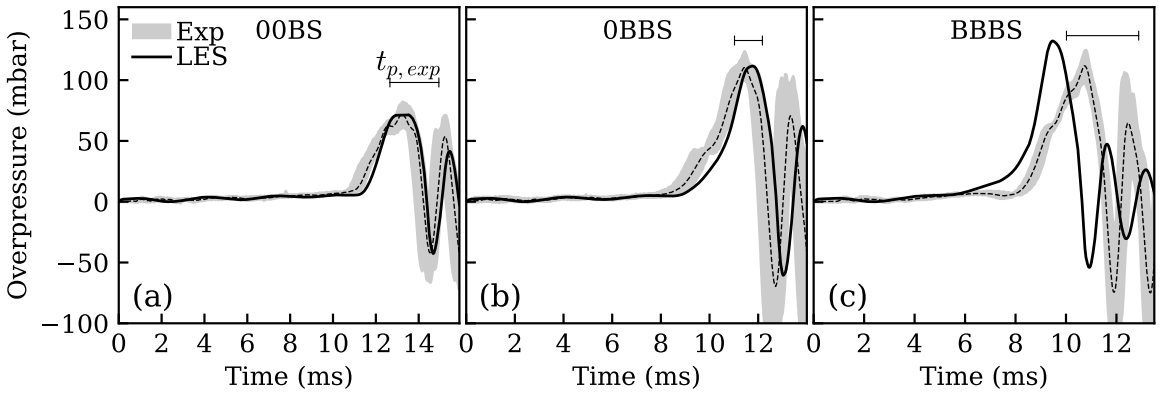

Figure 6.21: Comparison of predicted and measured pressure-time traces for configurations in family 1: (a) 00BS, (b) 0BBS and (c) BBBS. Mean experimental pressure signal (- - - -). The range of time taken to the first peak overpressure in the experiment, $t_{p,exp}$ (⊢⊣).

It can be seen from Figure 6.21 that LES with the DFSD model is able to correctly predict the trend and magnitude of overpressure compared with experiments. The calculated time instant for the peak overpressure also matches the experiments well. Furthermore, the predicted maximum overpressure is in good agreement with experiments. This is encouraging because the peak pressure is one of the most important parameters used in the safe design

of buildings and equipment. It can be observed that the trend of overpressure rise is similar for all the three configurations in family 1. It is apparent that following ignition, the pressure grows in a fluctuating manner but remains relatively low (less than 10 mbar) in the initial period of the explosion. Then, it increases sharply up to the peak pressure and the process is almost monotonic. Thereafter, the overpressure begins to drop, and it oscillates towards the atmospheric pressure due to acoustics. It should be noted that considering the computational time and practical importance, calculated magnitudes of subsequent weak pressure peaks are not validated in the present study.

Figure 6.21 also shows the impact of the number of baffle plates and their positions with respect to distance from the ignition bottom. Evidently from both LES and experiments, increasing the number of baffles gives rise to increased turbulence, faster flames and shortens the time to reach the peak pressure. Generally, the maximum overpressure also increases when extra baffle plates are added from 00BS to BBBS. From experiments, the magnitude of the peak pressure increases by about 52% when an additional baffle is added upstream of the third one, i.e. from 00BS to 0BBS, which is also excellently reproduced by LES. Interestingly, although configuration BBBS gives the highest overpressure level as expected, the relative growth is considered small when the first baffle is added in configuration 0BBS. Changing from 0BBS to BBBS, LES predicts an increase in peak pressure by around 18% while it is only 1.4% in the experiments. It may reveal that the effect of the first baffle is not as significant as predicted numerically. One possible interpretation is that the DFSD model tends to overestimate the level of flame wrinkling in this case, while the influence of turbulence on the flame is practically not that strong when the flame passes the first baffle. It also explains the slight advance in the calculated time-to-peak for configuration BBBS compared with experiments. Nevertheless, LES is able to mimic the pressure rise and fluctuation in the early stage of the explosion. It is also satisfactory in predicting the peak overpressure, its time of incidence as well as pressure gradient in all three configurations.

Flame acceleration is responsible for the rapid burning of the fresh mixture and the subsequent rise in internal pressure in an explosion enclosure. It is known that the flow around the obstacles results in an increase of flame surface and it can lead to flame acceleration. In addition to the 'geometrical' factor, turbulence and eddies may also wrinkle the flame front at the same time.

Locations of the midpoints of the three baffle plates (B1, B2, B3) and the central square

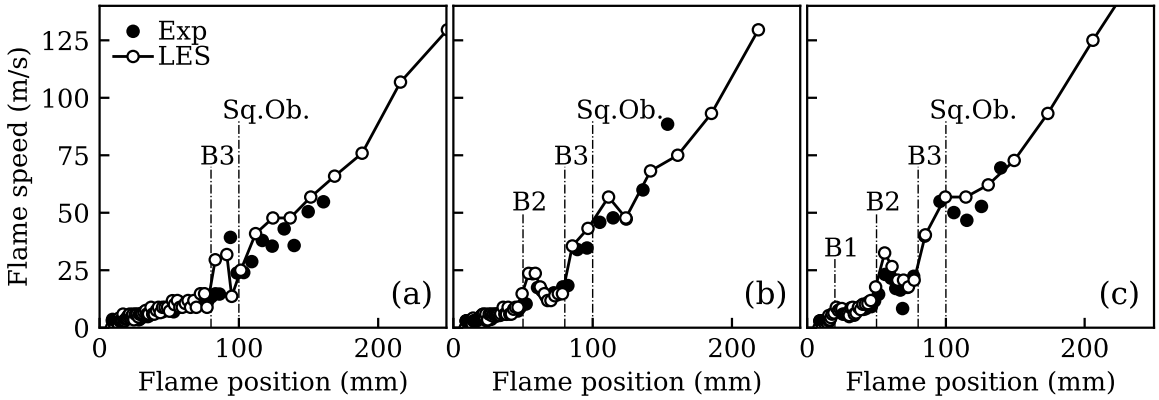

Figure 6.22: Propagation speed of the flame's leading edge from LES and experiments. Configurations in family 1: (a) 00BS, (b) 0BBS and (c) BBBS.

obstacle (Sq.Ob.) are also annotated in the figure. Experimentally, flame displacements are derived from the measured LIF-OH flame images. The speed of the flame leading point is then computed knowing that the high-speed imaging system has a repetition rate of 5 kHz. Numerically, it is calculated from the flame position identified by $\tilde{c} = 0.5$.

Figure 6.22 displays the speed of flame leading point from LES and experimental measurements. To understand the phenomenon and mechanism of flame acceleration, configuration BBBS is taken here for the illustration. Throughout the explosion event, the flame front speed increases significantly from ~ 5 m/s close to the bottom end of the chamber to ~ 140 m/s near the top exit. Initially, the flame is laminar and expands hemispherically before touching the side walls. Consequently, the flame front moves relatively slowly within the chamber until turbulence develops. The leading-edge speed in the early stage is mainly determined by two factors: (i) the laminar burning velocity of the fuel/air mixture, and (ii) thermal expansion caused by the density difference between the unburned and burned gases. A slight increase in flame speed can be observed as the flame propagates through the first baffle, B1. Flame acceleration across B1 seems to be a more of a weak 'geometrical' impact on the flame surface, compared to the effect of flame stretch due to turbulence. Flame speed remains relatively low (less than 20 m/s) between B1 and B2 and starts to rise again when the flame moves through B2. Interestingly, a noticeable decrease in flame speed can be observed right after the second baffle from both LES and experiments. Around B3, flame starts to accelerate remarkably due to the high turbulence level. A sudden drop in speed is then predicted by LES after wrapping around the central obstacle and a similar trend is also present in the experimental measurements. This is likely to be caused by the unavoidable lateral movement when interacting

with the eddies and wake around the central obstacle. Thereafter, flame speed increases in a quasi-steady manner towards the chamber exit, as predicted by LES. However, comparison with experiments is not applicable in the region close to the open end. Notice that in spite of the high congestion of obstructions, the flame front tends to decelerate after propagating through each baffle plate mainly due to the lateral movement and interference from vortices and eddies.

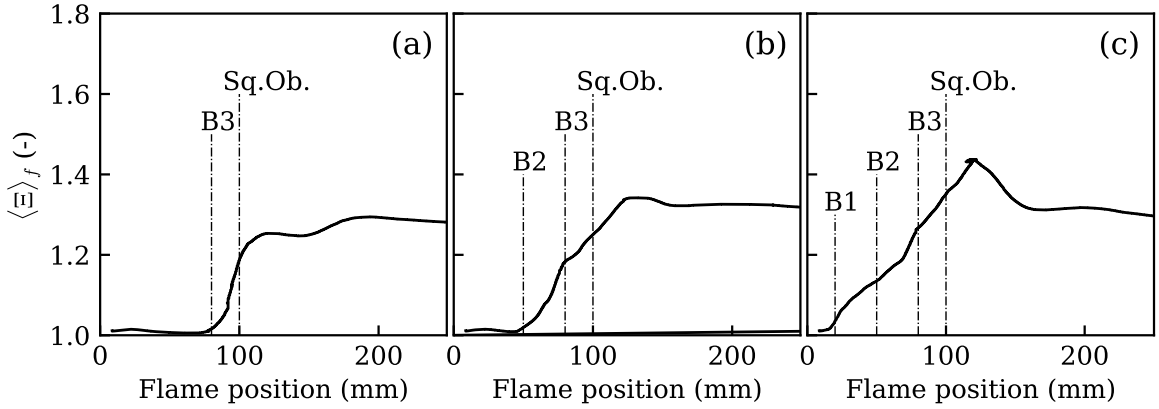

Figure 6.23: Evolution of the mean sub-grid wrinkling factor $\langle \Xi \rangle_f$ from LES. Configurations in family 1: (a) 00BS, (b) 0BBS and (c) BBBS.

Figure 6.22 also reveals the effects of baffle plates in this series of configurations. Comparing configuration 0BBS and BBBS with the case of the single baffle, 00BS, it is noticeable that increasing the obstruction frequency leads to greater flame propagation speed in the blow-down region after the last obstruction. The kinks in the speed profiles are because of the temporary slowdown of the flame front right before it encounters an obstacle. Globally, LES reproduces the essential dynamic behaviours of the explosion such as flame acceleration and deceleration in all three configurations very well. Slight deviations from the experimental measurements can be noticed when the flame is downstream of the square obstacle in the blow-down region. This may be partially due to the limited time resolution of high-speed images considering the high turbulence and flame front speeds within the region.

Figure 6.23 gives the evolution of the flame wrinkling factor with respect to the flame front position. It shows the close relationship between the obstructions and the sub-grid wrinkling factor, and the increase in the obstacle frequency in this order promotes the continuous rise of Ξ. Evidently, the sub-grid flame wrinkling only becomes significant when the flame passes an obstacle. Downstream of the square obstruction, the wrinkling factor tends to stabilise for the three configurations.

6.4.2 Combustion characteristics: family 2

Family 2 consists of configuration B00S, BB0S and BBBS where baffles increase from 1 to 3 from the ignition end. The explosion characteristics of configurations in this family and comparison with family 1 are discussed in this section.

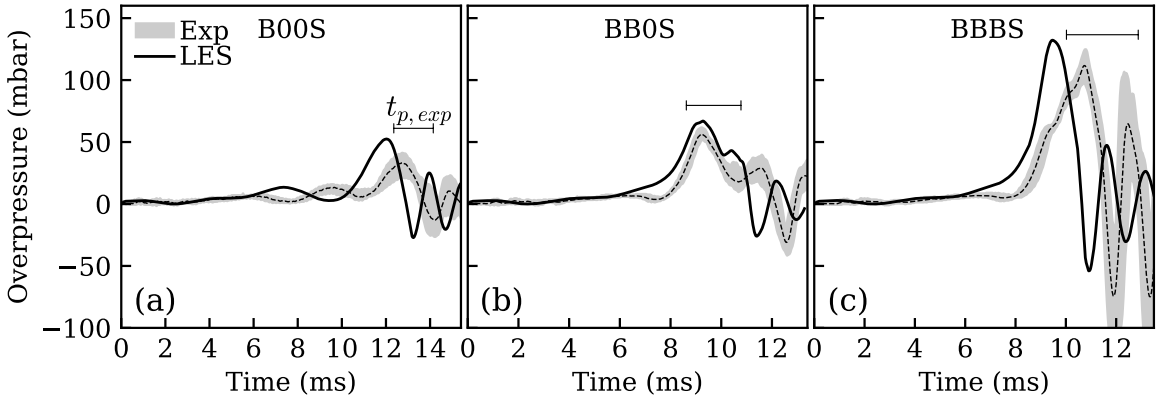

Figure 6.24: Comparison of predicted and measured pressure-time traces for configurations in family 2: (a) B00S, (b) BB0S and (c) BBBS. Mean experimental pressure signal (----). The range of time taken to the first peak overpressure in the experiment, $t_{p,exp}$ (⊢⊣).

Figures 6.24 and 6.25 present the pressure history and flame front speed, respectively for this family. Within the family, peak pressure increases with respect to the number of baffles and its incidence time also advances. This is expected as additional baffles increase the turbulence level and the interaction with the flame front, enhancing the burning rate as a result. Compared to family 1, configurations B00S and BB0S have lower peak pressures than their counterparts 00BS and 0BBS where the same number of baffles are applied. It can be observed that for the cases of a single baffle plate and a square obstacle, moving the baffle from B3 to B1 leads to a $\sim$ 50% reduction in peak overpressure. This is reflected from both experiments and LES although the peak pressure is somewhat overestimated in LES for case B00S. It reveals the influence of the baffle position with respect to the square obstacle and ignition end.

Figure 6.25 proves that for the case B00S, the relatively large distance between the baffle and square obstacle allows the flame to relaminarise before it reaches the central obstacle. This results in a noticeable small increase in the pressure history after the flame passes the first baffle. Encouragingly, LES is able to reproduce the first pressure peak in this case though there is a slight time difference compared to the experiments. Similarly, for the configuration BB0S, the separation between the second baffle and the obstacle allows the flame to relaminarise. Therefore, it can be concluded that the distance between the baffle plate and the ignition source controls the pressure level and the global flame propagation. It is worth mentioning

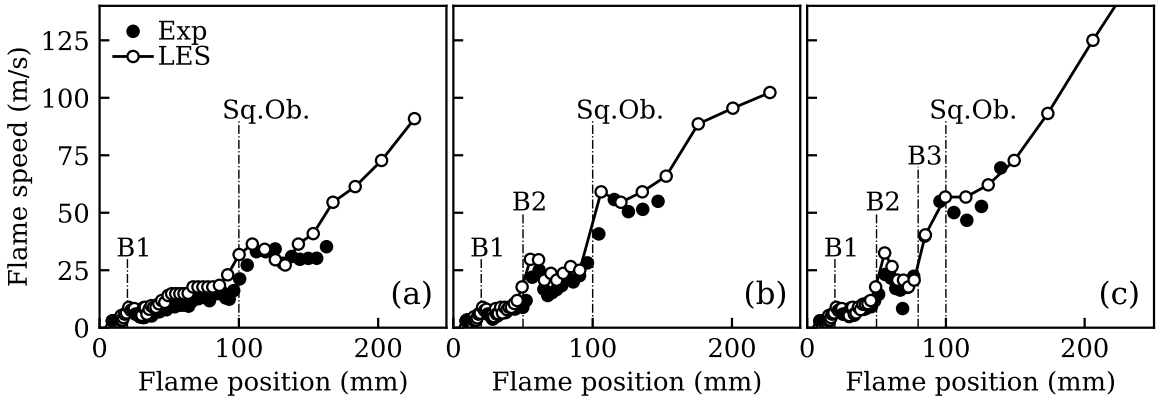

Figure 6.25: Propagation speed of the flame's leading edge from LES and experiments. Configurations in family 2: (a) B00S, (b) BB0S and (c) BBBS.

that relaminarisation can occur in a deflagration if the distance between adjacent obstructions is sufficiently large.

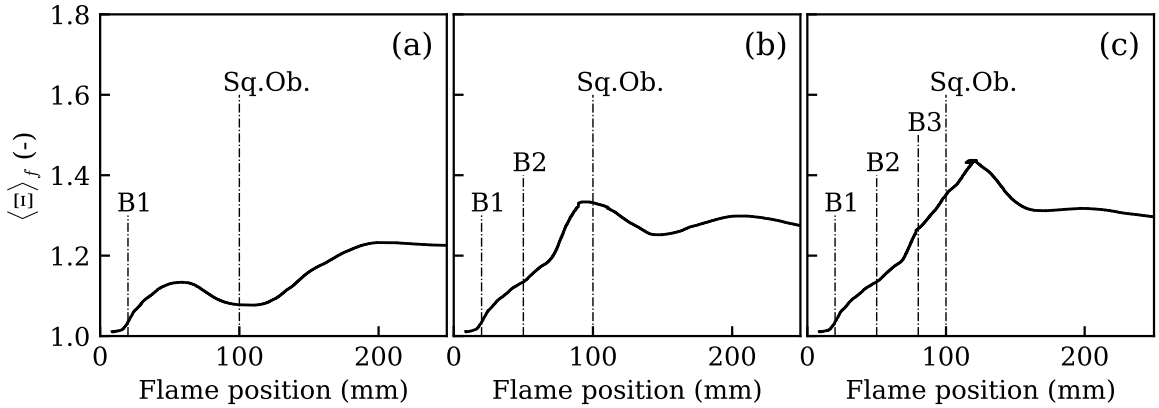

Figure 6.26: Evolution of the mean sub-grid wrinkling factor $\langle \Xi \rangle_f$ from LES. Configurations in family 2: (a) B00S, (b) BB0S and (c) BBBS.

Another interesting observation is that for the case BB0S only, there is a noticeable small pressure peak when it is dropping following the main peak, at around 10 ms (Figure 6.24b). The weak peak has been found to occur when the flame is located between the central obstacle and the chamber exit, which is also reproduced by LES. From the numerical perspective, the instantaneous increase in overpressure can be reflected by the sudden rise in the flame wrinkling factor or global burning rate within the chamber. On the other hand, there could be trapped unconsumed fresh gases upstream and downstream of the obstructions after propagating past them, and the combustion of these may be a contributory source of turbulence depending on the configuration. Therefore, the subsequent consumption of a relatively large amount of trapped unburned mixture may contribute to the weak overpressure rise after the main pressure

peak in configuration BB0S. However, further experimental and numerical investigations of flow and flame structures around this weak peak are needed for a complete explanation.

Figure 6.26 shows the averaged sub-grid wrinkling factor as a function of the flame front location, indicating the dynamic nature of flame/turbulence interactions. The level of wrinkling generally increases when the flame leading edge encounters a solid obstruction. Figure 6.26a illustrates the phenomenon of flame relaminarisation associated with the configuration B00S as the sub-grid wrinkling drops between the separate obstacles, revealing a decrease in the contribution of the SGS turbulence on the total reaction rate. The peak values of the wrinkling factor (typically after the square obstacle) reflect the relative magnitudes of the maximum overpressure for the three cases.

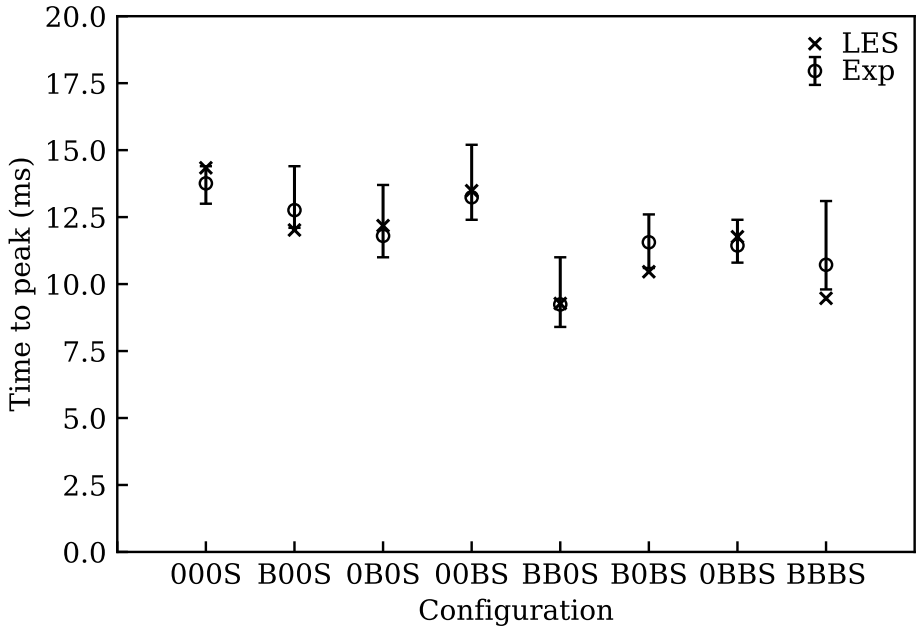

Figure 6.27: Summary of the time taken to reach the main pressure peak from experiments and LES for 8 configurations.

The performance of the current computational model in a range of obstacle scenarios may be evaluated by a critical parameter, namely the main peak overpressure. Figure 6.27 shows the time taken to reach the main peak overpressure extracted from the experimental and LES results. The calculated times to peak are within the range of experimental errors, and the largest deviation occurs for the configuration BBBS where the prediction is ∼11% ahead of the experimental average. Figure 6.28 shows the magnitude of the pressure peaks from LES and experiments. The predictions of configuration 00BS, B0BS and 0BBS are most consistent with the experiments and the relative error is less than 7%. The trend of maximum pressure

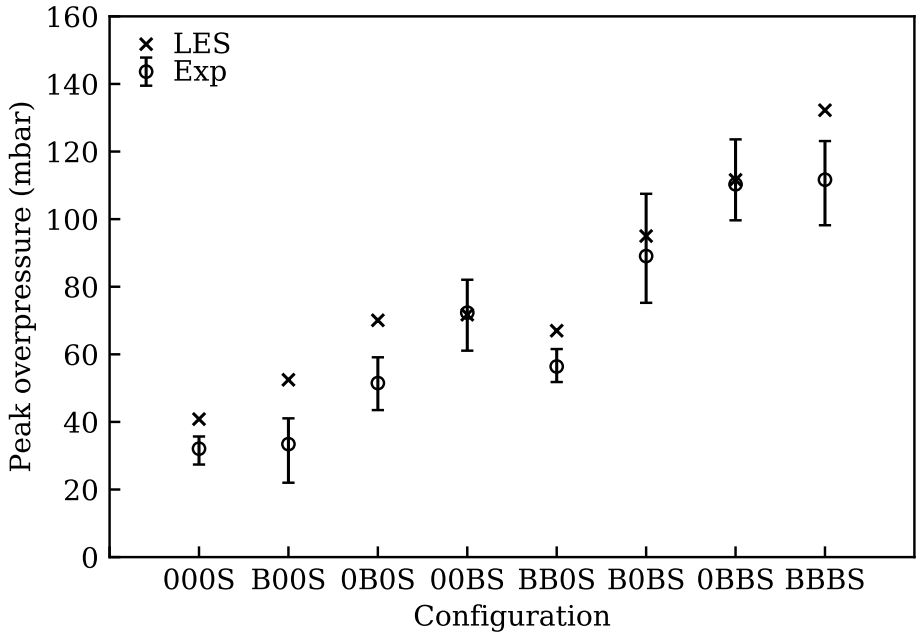

Figure 6.28: Summary of the magnitude of the main pressure peak at the base of the chamber from experiments and LES for 8 configurations.

corresponding with configurations is also correctly captured by LES. Notable discrepancies are found in cases B00S and 0B0S where they are overestimated by ~ 20 *mbar*. It is noted that slightly over-predicted pressure peaks are also present in several other configurations (e.g. 000S and BB0S). This may be partly due to the non-inclusion of the chamber heat loss as a result of the adiabatic boundary condition on the walls of the chamber. However, as the flame/wall interactions and heat transfer in a highly unsteady explosion event are not well understood, the present treatment is thought to be effective.

Comparing Figures 6.27 and 6.28 reveals that the time to peak and the magnitude of the pressure peak are not always negatively correlated. For instance, the maximum pressure of the case 0BBS is almost twice that of BB0S, but the incidence time for the latter is more than 2 *ms* faster, as indicated by both LES and the experiment. This may be explained by the difference in the flame front location where the main pressure peak is reached. The study of obstacle arrangement within the chamber (Figure 6.28) also shows that the optimal case for producing internal pressure is the BBBS configuration which has three baffles and a square obstacle. In this case, the flame stretches to a very high level as it passes the three successive baffles, which is a result of the high level of turbulence caused by the baffle plates. The progressive increase in burning rate leads to continuous flame acceleration and considerable pressure build-up.

Chapter 7

Results and Discussion: Hydrogen

This chapter mainly presents the results using hydrogen as the fuel considering its speciality as a fuel and the growing need of evaluating hazards in accidental hydrogen explosions. The study focuses on the influence of obstacle number, location and size on the critical combustion parameters and flame characteristics. Another investigation is the impact of fuel type where the results of methane, propane and hydrogen are compared.

Table 7.1 displays a total number of eleven configurations classified into 6 groups to facilitate the analysis of the impact of obstructions. Groups 1-4 are used to investigate the influence of the turbulence-generating baffle plates, while groups 5 and 6 intend to examine the impact made by changing the size of the central obstacle. This classification of flow configurations is made to represent various means of blockage including the number and location of the baffles as well as the size of the solid central obstacle. Computational settings for the lean hydrogen/air deflagration ($\Phi = 0.7$) are same as the base simulation for propane (see Table 6.4) with the different thermochemical properties. The laminar burning velocity and flame thickness are set to $s_L^0 = 125\ cm/s$ [166] and $\delta_L^0 = 0.12\ mm$ [141], respectively.

7.1 Qualitative study

The physical phenomena and the typical flame behaviours behind the hydrogen-air deflagration are discussed in this section using configuration B0BS as an example. Figure 7.1 shows the shape of the typical hydrogen-air explosion flame extracted experimentally and numerically for configuration B0BS. The reaction zone is marked using a sequence of high-speed images of LIF-OH in the experiment [127], which is indicated using the contour of $\widetilde{c}$ numerically from LES. Evidently from Figure 7.1, LES is able to reproduce both the flame structure and the global propagation speed. It can be noticed that the flame shape continuously changes during

Table 7.1: Configurations classified into groups to study the influence of obstructions

Group	Description	Configuration
1	Baffles are progressively increased and kept furthest from ignition end	00BS, 0BBS, BBBS
2	Baffles are progressively increased from ignition end	B00S, BB0S, BBBS
3	Two baffles are positioned at different stations of the chamber	BB0S, B0BS, BBBS
4	One baffle is positioned at a different station of the chamber	B00S, 0B0S, 00BS
5	Central obstacle size increases with all three baffle plates present	BBB0, BBBS, BBBL
6	Small or large central obstacle without any baffle plates	000S, 000L

the explosion. Initially, the flame is laminar and expands hemispherically before impinging on the first baffle plate. It penetrates the grid and separates into four fingers primarily resulting from the 'geometric' stretch caused by the strips of the baffle plate. Then, they quickly merge with each other due to the lateral spread of the flame. Meanwhile, the surface area of the flame tends to decrease before reaching the next grid. The flame then jets through the gaps of B3 and immediately strikes the square obstacle. It can be seen that the flame front is very much corrugated when interacting with the obstacle. After passing the last obstruction (square obstacle), the flame is significantly wrinkled ($t = 4.4\ ms$ of the LIF-OH images) and propagates towards the chamber outlet. The blockage introduced by the central obstruction also leaves a small amount of unburned mixture behind it when wrapped by the flame front. It is then consumed when the leading flame point is further downstream, as indicated by both high-speed and LES images. It can be noticed that the flame spreads faster in the upper part of the combustion chamber. This is due to the increased flame distortion caused by the interaction with the upstream obstacles.

Figure 7.2 shows the calculated overpressure distribution along the axial direction on the mid-plane of the chamber for the configuration B0BS. The pressure has been found to be nearly uniform on the xy-plane (i.e. cross-section) of the chamber. During the explosion process, the magnitude of the internal pressure rises as well as its spatial range of influence, which is approximately the region of the burned gases. Note that the wall pressure (downstream of the central obstacle) measured in the experiments is consistently lower than the base and it may suggest that a pressure gradient exists within the chamber [156]. This is further confirmed by LES with a negative pressure gradient vertically along the chamber, which drives the explosion

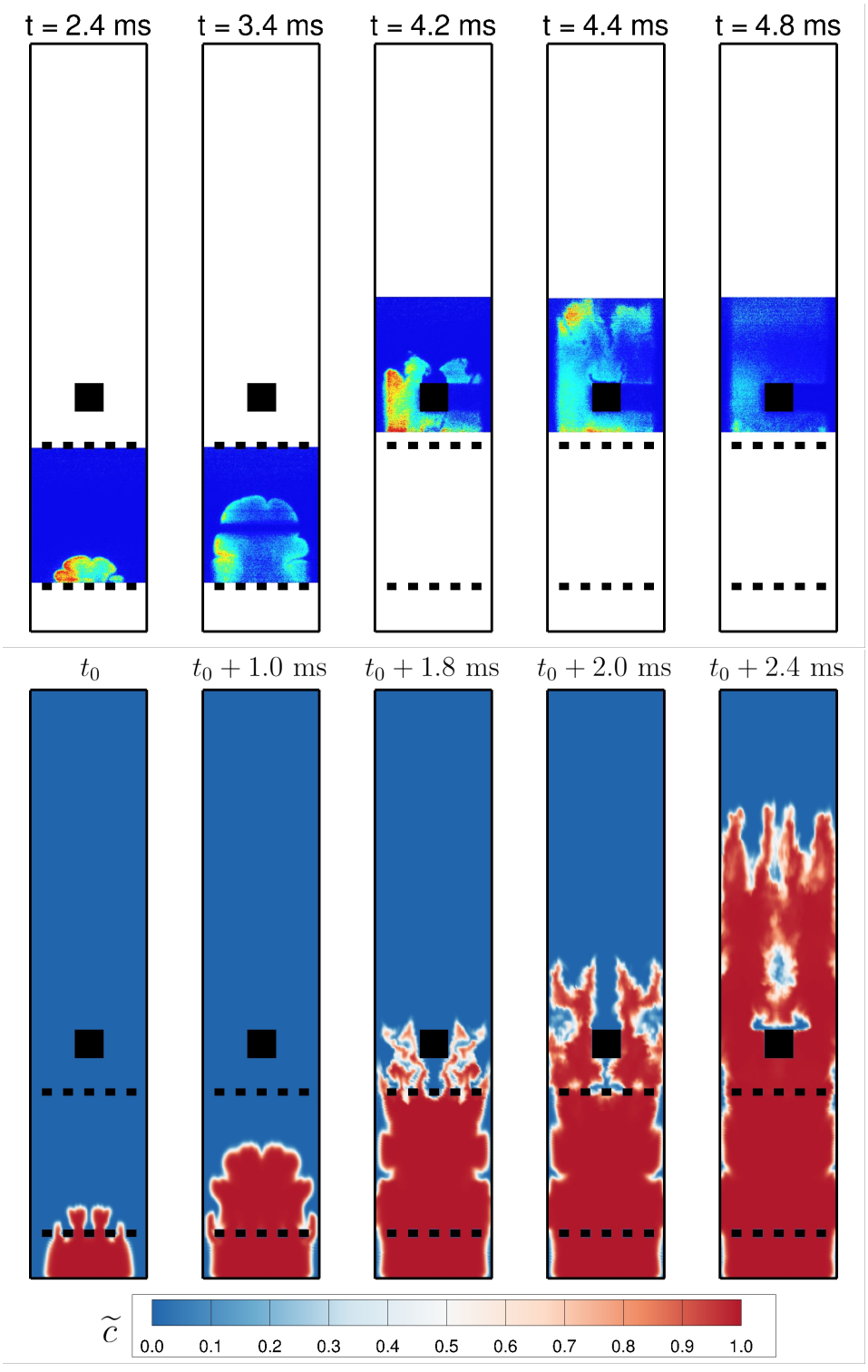

Figure 7.1: Comparison of H_2 flame propagation between simulations and experiments for configuration B0BS. *Top*: LIF-OH high-speed images from the experiments [156]. *Bottom*: LES flame images contoured by $\widetilde{c}$. t_0 is set to match the position of the flame leading point with the high-speed image. Time intervals between successive LES images are kept the same as the experiment.

gases out across the outlet. A large pressure drop to atmospheric level due to venting can be found near the exit of the combustion chamber. Furthermore, both the numerical (not shown here) and the experimental results [156] confirm that the two pressure probes on the chamber base and on the wall downstream of the central obstacle have given similar pressure patterns in all the test cases. Therefore, the analysis and discussion of the rest of this paper will focus on the pressure at the bottom of the vessel.

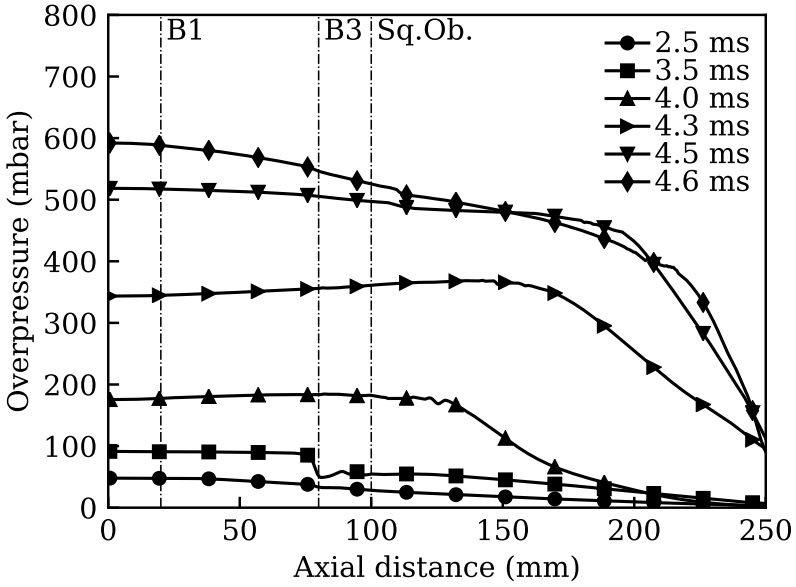

Figure 7.2: Overpressure distribution along the axial direction on the mid-plane of the chamber ($y = 14\ mm$ from the centre) for configuration B0BS at various times. Positions of the first and the third baffle plates (B1 and B3) and the central square obstacle (Sq.Ob.).

Figure 7.3 shows the flow dynamics and flame-flow interactions in the hydrogen explosion for the configuration B0BS extracted from LES. The evolution of the flame is plotted by the iso-line of $\widetilde{c} = 0.5$, and the turbulence level may be seen by the vorticity contour. The recirculation zones and the turbulence level may be seen from the vorticity contour and the flame front is defined using the iso-line of $\widetilde{c}$. As demonstrated earlier, the presence of obstacles may greatly promote the combustion rate and significantly increase the explosion overpressure. The obstacles can induce vortices and turbulence of various length scales and strength. For instance, at $t = 2.2\ ms$, weak recirculation regions behind the downstream obstacles can be observed even if the flame front is only interacting with the first grid. The degree of turbulence in the wake area of B3 and Sq.Ob. gradually becomes stronger with the rapid approach of the flame front. Intense flame-turbulence interactions make the flame surface wrinkle. As can be seen from $t = 3.8\ ms$ in Figure 7.3, it not only speeds up the flame but also creates

more turbulence. Note that even in the downstream area of the last obstruction, the fast explosion is sustained by the continuous interactions between the propagating flame front and the generated turbulence in this region. As hydrogen explosions are usually rapid and highly unsteady, LES proves itself as a valuable tool in visualising the entire explosion process and in helping to understand its underlying physics.

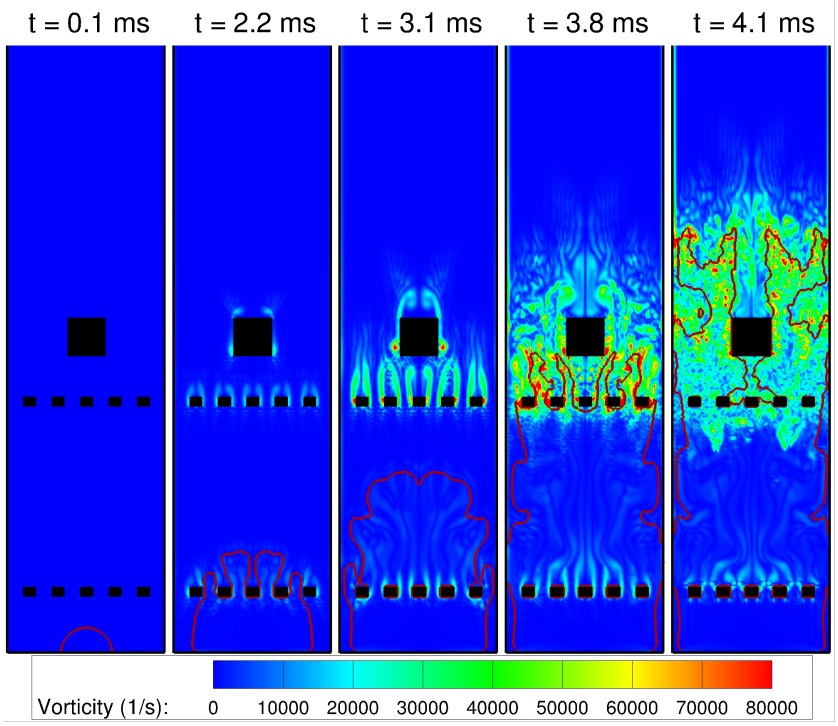

Figure 7.3: Numerical snapshots of the flame front represented by the iso-line of $\widetilde{c} = 0.5$ with vorticity contours for configuration B0BS. Time instants correspond to $t = 0.1, 2.2, 3.1, 3.8$ and 4.1 ms (from left to right).

7.2 Overview of overpressure prediction

Figure 7.4 shows the comparison of the maximum overpressure and its time of incidence between LES and the experiments for all the configurations studied in this paper. It is clear that the magnitude and timing of the peak pressure are strongly related to the configuration of the explosion chamber. Maximum pressure can increase by up to 400% from less than 200 to ~ 1000 $mbar$ changing from the configuration 000S to BBBL when the VBR increases from 1.15% to 6.44%. It is important to realise that a real explosion in hydrogen process plants is likely to occur in much larger scales. Thus, the generated maximum overpressure can be much higher in larger-scale scenarios. As can be seen from groups 1 and 2, the more congested the obstacles, the higher the overpressure peak it can reach. The position of the baffle plates also plays a vital role in determining the maximum pressure, e.g. group 3 and 4. Generally, the

peak pressure decreases when the grids are closer to the ignition source or large separation distance is present between two successive obstacles. Results of groups 5 and 6 reveal that the size or the blockage level of the central square obstacle significantly affects the pressure magnitude.

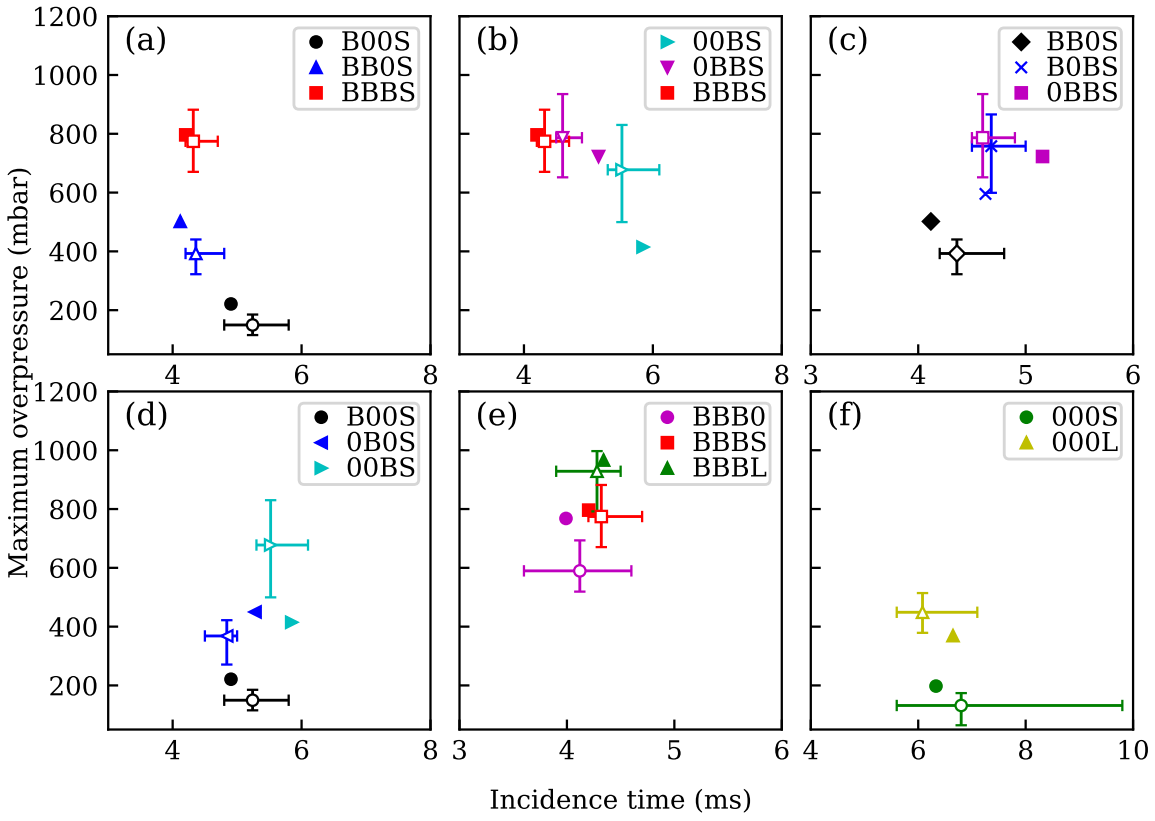

Figure 7.4: Comparison of the peak overpressure and its incidence time between the experiments and LES for all studied configurations: (a) Group 1, (b) Group 2, (c) Group 3, (d) Group 4, (e) Group 5 and (f) Group 6. Experimental mean values and variations (hollow symbols with error bars of time to peak and maximum overpressure).

Overall, LES gives satisfactory results compared with experiments in terms of both the timing and magnitude of the maximum overpressure. This implies that the applied DFSD model successfully accounts for the flame wrinkling in a range of flow configurations with various turbulence level. In terms of the overpressure magnitude, the numerical calculations give excellent predictions for cases such as 0BBS, BBBS and BBBL. A small degree of overestimation can be seen on configuration BB0S, 0B0S and BBB0. The largest discrepancy (absolute error) lies in the case 00BS where it is under-predicted by ~ 250 *mbar*. Calculated time taken to reach the peak pressure, $t_{p,LES}$, is generally within or close to the range of the experimental measurement for all the test cases. Experimentally, the mean time taken to reach the peak overpressure varies approximately from 4 to 7 *ms* depending on the configuration. In

general, one may expect that the greater the pressure peak, the shorter the time of occurrence. It is true when the number of grids increases, i.e. group 1 and 2, and this effect can be explained by the increased rate of flame propagation. However, there are some exceptions where the relationship between the two is more complicated. For example, in group 3, the maximum pressure of BB0S is only half of 0BBS, but its time of incidence is obviously shorter than the latter. As it can be seen, LES also shows a correct prediction behaviour consistent with the experimental results. Note that the variation in the timing and magnitude of the peak overpressure does exist in the experimental measurements, e.g. a comparatively wide range of $t_{p,exp}$ for the configuration 000S. Considering that LES results are from a single realisation, factors including the initial turbulence level, numerical schemes and thermochemical properties of the fuel can affect the results to an extent. Thus, with the current modelling setup, the discrepancies shown in Figure 7.4 are thought to be acceptable. In general, all trends seen in experiments for key parameters such as peak pressure and time to peak are predicted reasonably well. This study, therefore, reveals the capability of the developed computational setup in capturing crucial explosion characteristics and calculating these critical design-related factors for a range of obstacle arrangement.

7.3 Effect of obstruction arrangements and size

This section focuses on presenting and analysing the impact of the number and location of obstacles on the hydrogen-air explosion characteristics. Results of group 1 to 4 are discussed here with a different arrangement of turbulence-generating baffle plates (or grids). All configurations in these groups have a small square obstacle downstream of the grids.

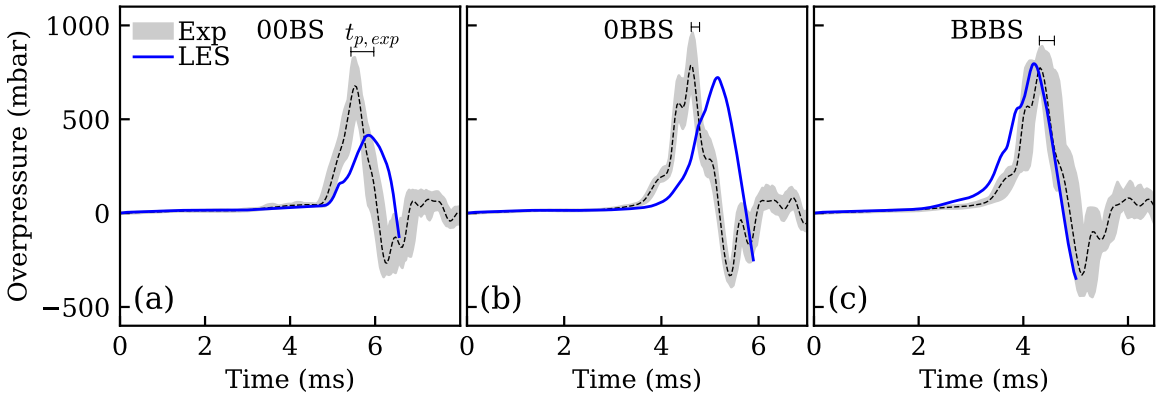

Figure 7.5: Comparison of overpressure between LES and experiments. Mean experimental signal (----). The variation in $t_{p,exp}$ (⊢⊣). Configurations in group 1: (a) 00BS, (b) 0BBS and (c) BBBS.

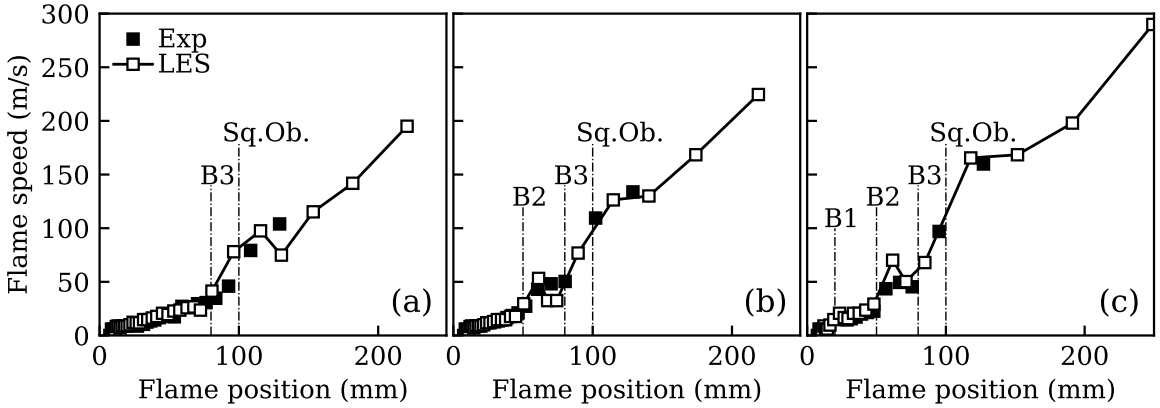

Figure 7.6: Comparison of flame propagation speed between LES and experiments. Configurations in group 1: (a) 00BS, (b) 0BBS and (c) BBBS.

Figures 7.5 and 7.6 show the numerical and experimental overpressure-time traces and flame front speeds for the configurations in group 1. It is apparent that the introduction of more obstructions in the path of the flame propagation increases the overall turbulence level generated within the chamber. Note that the addition of baffle plates increases the VBR of the chamber. Therefore, the cause for the increased overpressure is expected from the more intensive interactions between the propagating flame front and the extra obstructions. Both LES and experiments indicate that adding another grid to the case 0BBS (i.e. changing from 0BBS to BBBS) does not significantly increase the overpressure peak. This may reflect the weak effect of having the lower grid compared to the other two. Figure 7.6 indicates that adding additional grids also contributes to the higher flame speed in the region downstream of the central obstruction.

Computed maximum pressures are consistent with the experimental results for most of the cases. However, an apparent underestimation has been found for configuration 00BS, where it is ~ 250 *mbar* less than the mean experimental value. A closer look at the pressure trace reveals that the early-stage overpressure matches well with the experiment despite the under-prediction of the peak. Further investigation shows that the flame wrinkling factor in the turbulent stage of the deflagration is apparently lower than configurations such as 0BBS considering that their peak pressures are of similar values. The lack of predicted flame wrinkling is responsible for the under-prediction in this case.

Figures 7.7 and 7.8 present the pressure and flame speed evolutions for group 2 configurations. Compared with group 1, here obstruction grids are added starting closest to the ignition end. In this order, maximum pressure almost doubles when an additional grid is

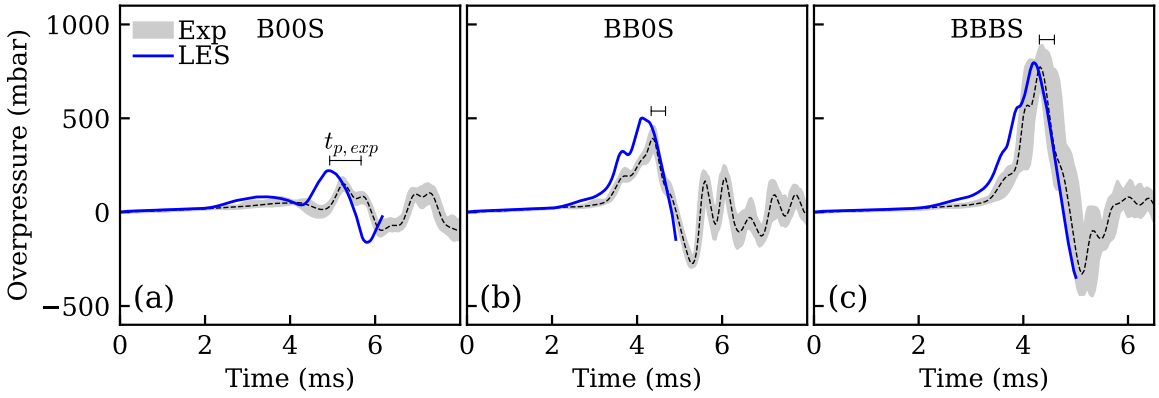

Figure 7.7: Comparison of overpressure between LES and experiments. Mean experimental signal (----). The variation in $t_{p,exp}$ (⊢⊣). Configurations in group 2: (a) B00S, (b) BB0S and (c) BBBS.

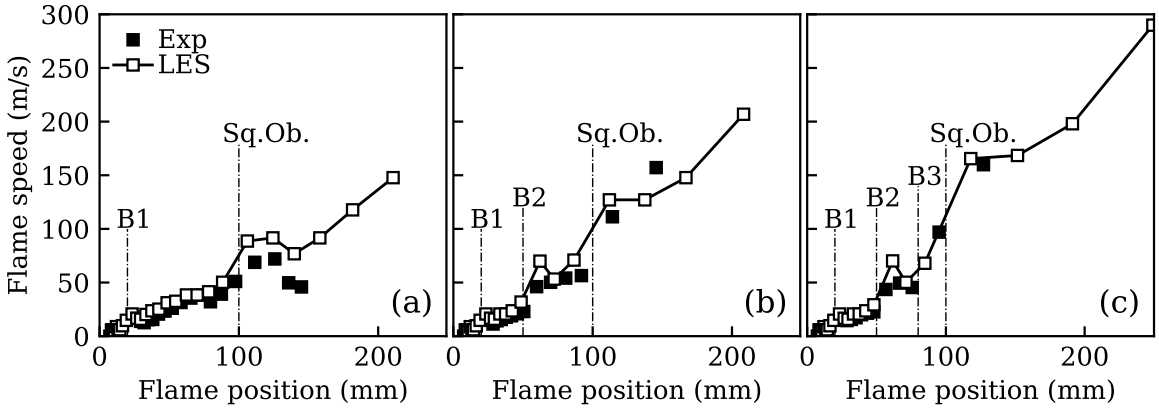

Figure 7.8: Comparison of flame propagation speed between LES and experiments. Configurations in group 2: (a) B00S, (b) BB0S and (c) BBBS.

placed. Comparison between the overpressure history and the corresponding flame speed (e.g. Figures 7.7 and 7.8) indicate that high overpressure is commonly accompanied by a large flame propagation speed. Both numerical and experimental flame speed results have shown that the flame front is generally accelerating during the explosion process and it is responsible for fast burning rate and subsequent rise in the internal pressure.

The exact mechanism of flame acceleration due to obstacles and confinement is complex. It may involve several types of flow instabilities such as the well-known RT instability [112]. Furthermore, self-acceleration resulting from the intrinsic wrinkling of expanding laminar flame [112] may be present in the early development and quasi-laminar stage of the explosion. It is noted that LES mesh does not resolve the real flame front and no models are currently available for these instabilities [134] of the laminar flame, as they are physically not well understood. However, for all the test cases considered here, the effect of obstacle-generated turbulence is

so dominant that the influence of the flame surface growth due to these instabilities may be neglected.

Overall, the prediction of flame velocity by large eddy simulations is in good agreement with the experimental results. Resulted from the blockage and the high reactivity of hydrogen, the flame acceleration is significant in the explosion. The velocity reaches $\sim 160\ m/s$ for case BBBS just downstream of the square obstacle, and the flame can accelerate up to about $300\ m/s$ close to the exit as predicted by LES. Note that the maximum viewable distance of the LIF-OH system is about $150\ mm$ in the experiment where measurements are available. The kinks in the speed profiles due to the temporary slowdown of the flame front right before it encounters an obstacle are also properly reproduced numerically. It indicates that the dynamic behaviour of flame propagation is correctly captured by the developed model. Slight deviations from the experimental measurements can be noticed when the flame is downstream of the square obstacle in the blow-down region. This may be partially due to the limited time resolution of high-speed images considering the high turbulence and flame front speeds within the region.

LES also has excellent performance in reproducing the overpressure trends and magnitudes. It can be noticed (e.g. from Figure 7.7) that even details such as small turning points in the pressure curves due to sudden changes in the burning rate are properly computed. This reflects the main advantage of using the DFSD model as the model coefficient accounting for the SGS flame wrinkling adjusts automatically in the simulation. It is particularly useful in the present test cases since the level of the flame front wrinkling can vary significantly for various configurations of obstacles. In addition, the flame wrinkling also evolves gradually in a single case where the deflagrating flame may grow from early quasi-laminar to fully turbulent.

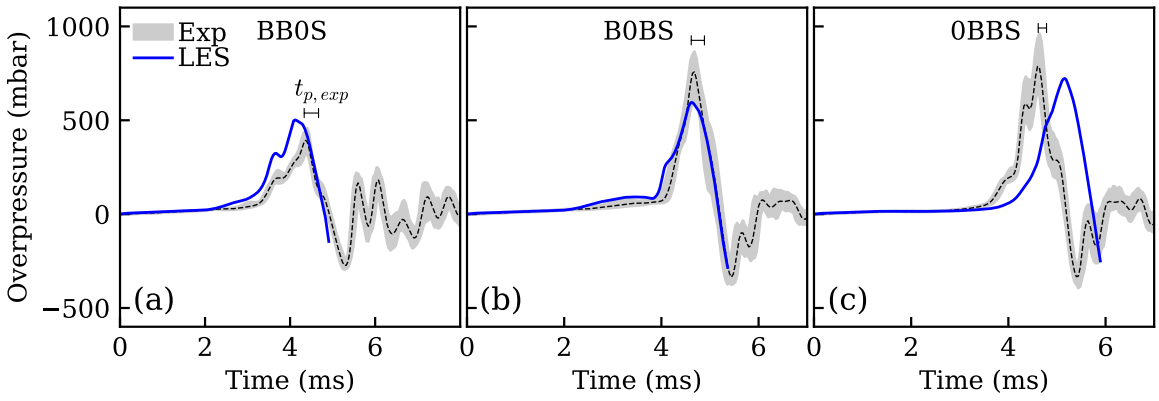

Figure 7.9: Comparison of overpressure between LES and experiments. Mean experimental signal (- - - -). The variation in $t_{p,exp}$ (⊢⊣). Configurations in group 3: (a) BB0S, (b) B0BS and (c) 0BBS.

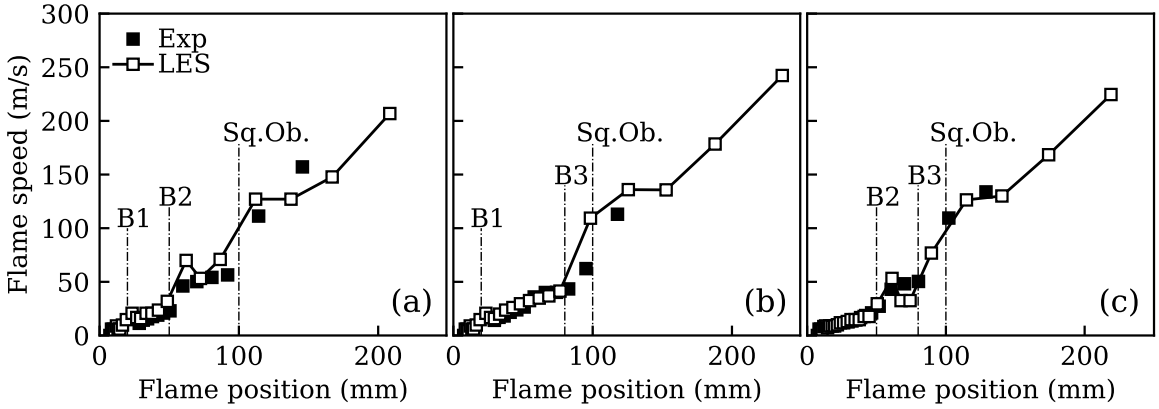

Figure 7.10: Comparison of flame propagation speed between LES and experiments. Configurations in group 3: (a) BB0S, (b) B0BS and (c) 0BBS.

Figures 7.9 and 7.10 demonstrate the effect of alternating the position of two baffle plates. Note that all the cases in group 3 have the same blockage ratio (i.e. VBR), only the position of the grids varies. It clearly shows that higher overpressure is generated when the two grids are closer to the central obstruction. Comparatively, for configuration BB0S, the separation between the second baffle and the obstacle allows the flame to relaminarise. This is also the case for B0BS where the flame decelerates before contacting B3 as also illustrated in Figure 7.3. It can be identified by the lower flame speed just before the Sq.Ob. compared to the other two configurations.

Figures 7.11 and 7.12 shows that the position of a single grid inside the chamber increases the pressure to different degrees. For configuration B00S, due to the closeness of the lower baffle plate to the ignition source and the small thickness of the grid (3 mm), the flame front is only slightly stretched by B1 and then relaminarises as it passes. This is identified by a noticeable bump in the pressure trace at ~ 4 ms from both LES and experiments. It is also interesting to see that adding B1 to case 000S does not alter the peak overpressure very much (see Figure 7.4) even though the blockage ratio increases.

Figure 7.13 illustrates the effect of the single grid on the flame front structure just before contacting the square obstacle. For both cases of 000S and B00S, the flame front essentially travels to the square obstacle in a quasi-laminar manner. Although the greater vertical flow velocity of the latter indicates that the flame does propagate faster, it also promotes the venting from the top of the chamber. The lack of generated overpressure by adding the first grid may also be explained by the efficient venting after the flame passes B1 because of the relatively long separation distance between B1 and Sq.Ob. Accordingly, LES predicts a maximum overpressure

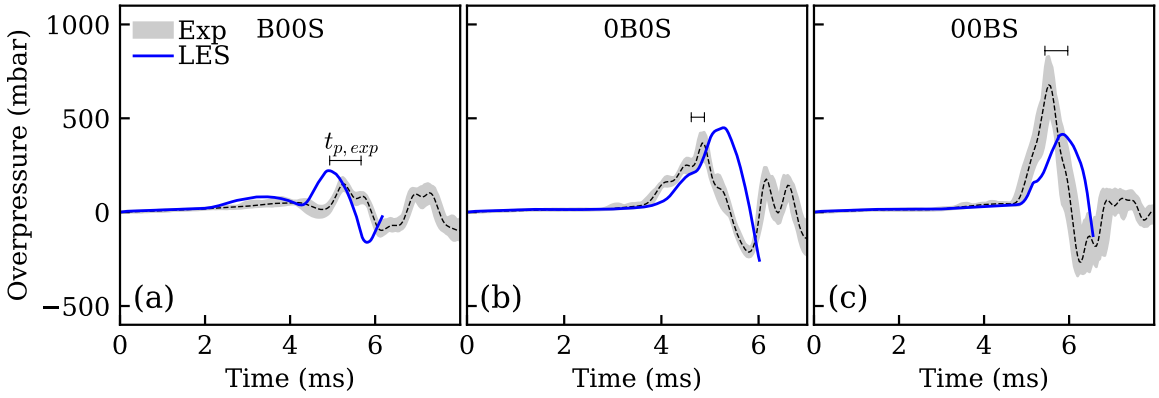

Figure 7.11: Comparison of overpressure between LES and experiments. Mean experimental signal (- - - -). The variation in $t_{p,exp}$ (⊢⊣). Configurations in group 4: (a) B00S, (b) 0B0S and (c) 00BS.

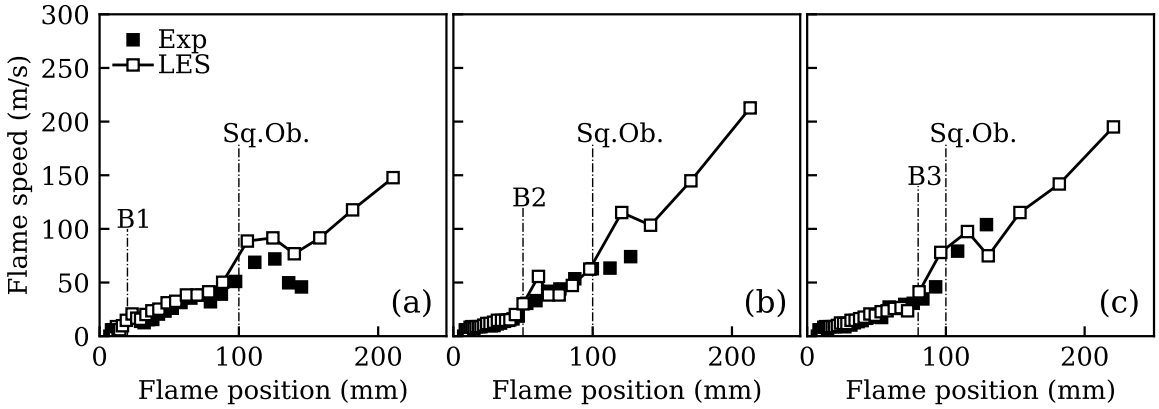

Figure 7.12: Comparison of flame propagation speed between LES and experiments. Configurations in group 4: (a) B00S, (b) 0B0S and (c) 00BS.

of ~ 200 *mbar* for both 000S and B00S despite that the experimental values are slightly lower.

A closer look at Figure 7.13 reveals that the flame structure substantially changes when moving the grid from the lower (B1) to the middle position (B2). Since the axial velocity (~ 40 m/s .vs. ~ 10 m/s) at the baffle openings increases in time, the Reynolds number of the fresh gases based on the scale of the grid is higher. Furthermore, the formation of a few disconnected flame islands behind the baffle strips confirms the presence of stronger recirculation zone when flame-baffle interactions occur. This explains the more wrinkled and corrugated flame front for case 0B0S. The significant growth of the flame surface area before reaching the central obstacle also enhances their subsequent interactions, and the subgrid wrinkling automatically detected by the DFSD model will be higher. Consequently, the computed maximum overpressure of the case 0B0S is more than twice of that in the case B00S (~ 400 *mbar* .vs. ~ 200 *mbar*), as also proved by the experiments. Therefore, it may be

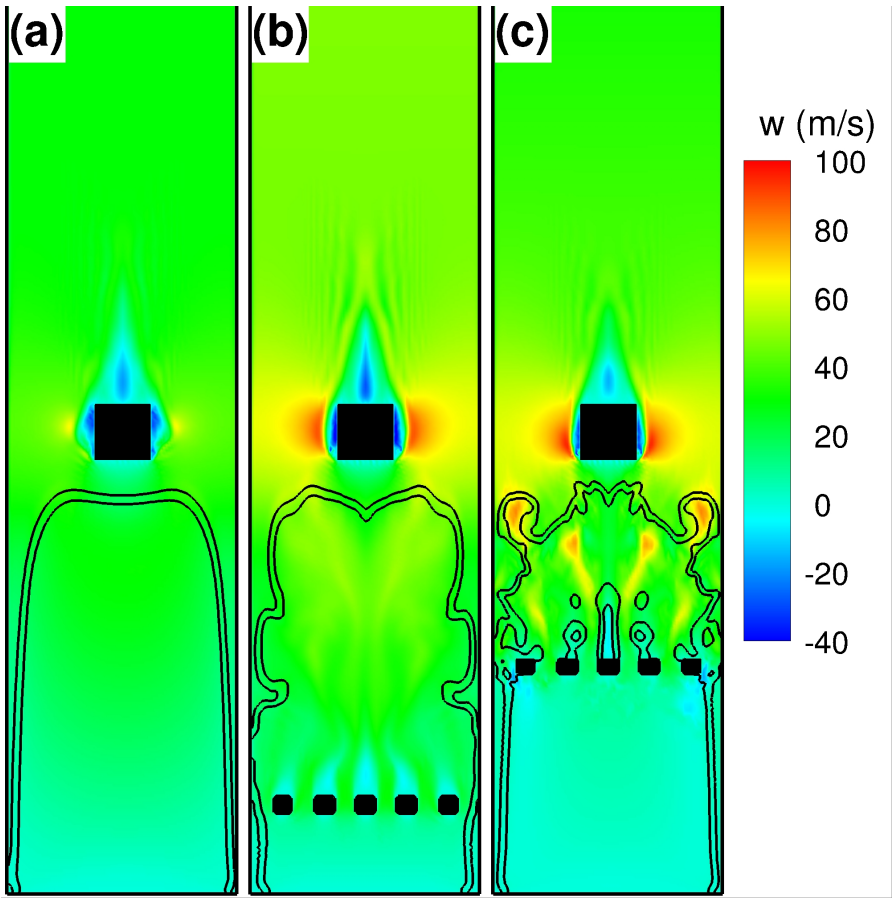

Figure 7.13: Effect of the single grid (baffle plate) as illustrated by the flame front structure (iso-lines of $\widetilde{c} = 0.2$ and $\widetilde{c} = 0.8$) before reaching the square obstacle for configurations: (a) 000S, (b) B00S and (c) 0B0S. Contours of negative axial velocity (w) indicate recirculation regions in the flow.

concluded that the distance between the grid and the ignition source serves as a controller and the generated overpressure is higher as the grid moves further downstream.

Figures 7.14 and 7.15 present the overpressure history for the configurations in groups 5 and 6. It is recalled that group 5 consists of the configurations BBB0, BBBS and BBBL in which central obstacle starts from none to large. Group 6 constitutes configuration 000S and 000L where no baffles are present. As expected, increasing the size of the obstruction enhances the peak pressure. For instance, Figure 7.15 shows that when the central obstacle is the only obstruction in the chamber, the maximum overpressure is nearly doubled by using a large one. In this case, the ABR almost doubled by changing from 000S to 000L and the VBR of the latter (5%) is about four times of the former (∼1.2%).

Comparison between Figures 7.14 and 7.15 reveals that with the presence of the three baffle plates, the maximum pressure is generally higher than the configurations with only the central obstruction. It shows the effectiveness of the baffles plates in creating turbulence and

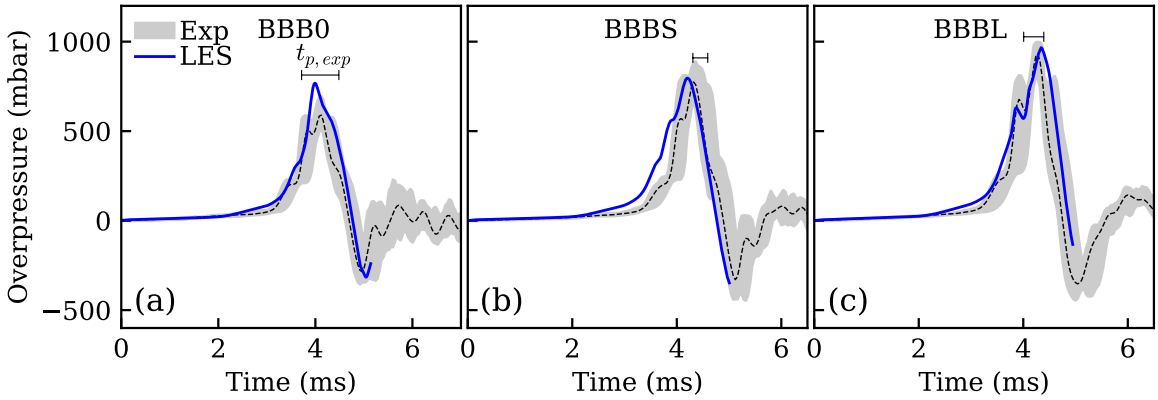

Figure 7.14: Comparison of overpressure signals between LES and experiments for group 5 cases. Mean experimental signal (----). The range of $t_{p,exp}$ (⊢⊣).

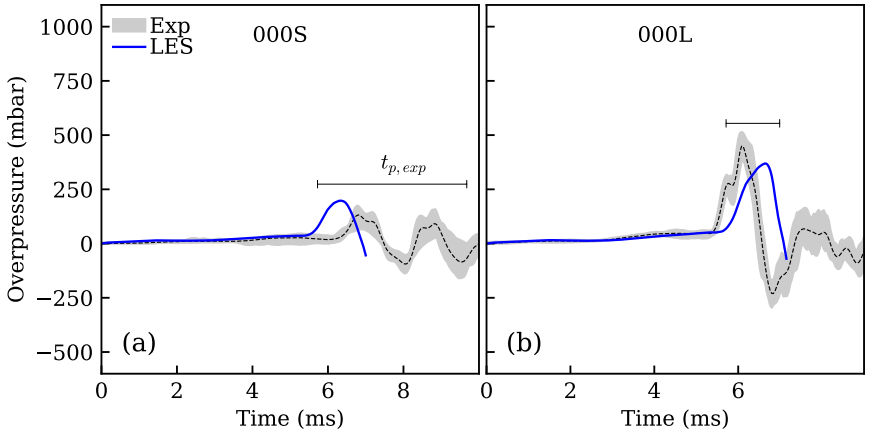

Figure 7.15: Comparison of overpressure signals between LES and experiments for group 6 configurations. Mean experimental signal (----). The range of $t_{p,exp}$ (⊢⊣).

the contribution of continuous flame-turbulence interactions towards the internal pressure of the explosion chamber. The high turbulence intensity in the shear layer of the sharp-edged baffle strips leads to the largely wrinkled flame front when reaching the central obstruction. Figure 7.14 also shows that the maximum pressure increases by ∼30% when a small obstacle is added to configuration BBB0. A further rise of ∼20% is seen when it is replaced by the large one. Note that the overpressure generated by configuration BBBL is the highest among all the cases and it can reach nearly 1000 *mbar* (1 *bar*). Again, LES successfully captures the details on the pressure trace such as the sudden decrease in the overpressure at about 4 *ms*.

It is worth mentioning that both ABR and VBR are critical explosion-related parameters [7]. However, as has been demonstrated, the explosion overpressure is also influenced by the arrangement of obstacles in a multi-obstruction environment. Hence, LES is potentially a useful tool in complex obstructed process areas where simple correlations using parameters

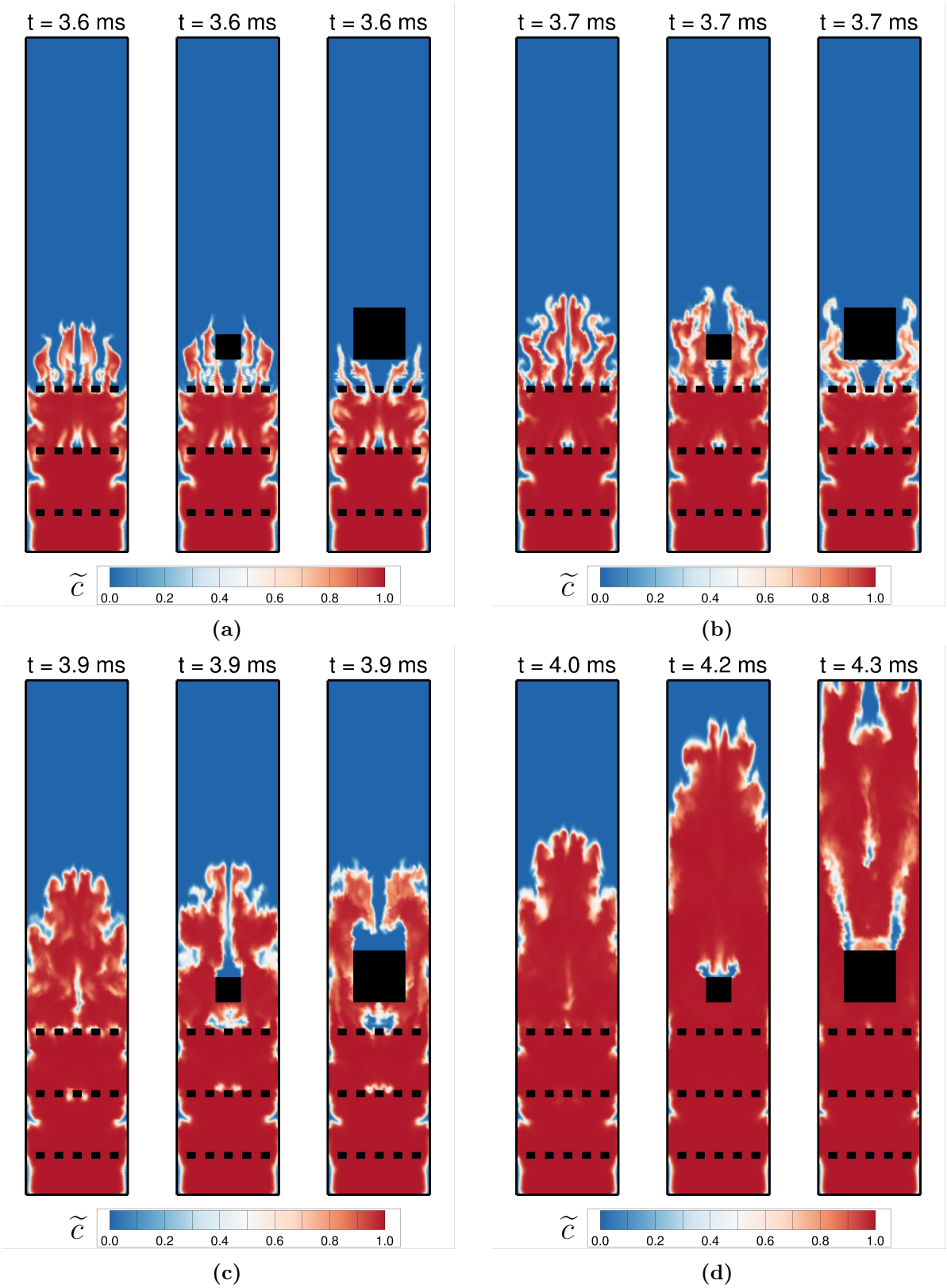

Figure 7.16: Flame snapshots (contoured by $\widetilde{c}$) of group 5 configurations (BBB0, BBBS and BBBL) showing the effect of the size of the central obstacle on the flame propagation. (a) $t = 3.6\ ms$. (b) $t = 3.7\ ms$. (c) $t = 3.9\ ms$. (d) $t \approx t_{p,LES}$.

such as the blockage ratio are not sufficient.

Figure 7.16 shows the later stage of the explosion extracted from LES for the configurations BBB0, BBBS and BBBL at various time instants. It can be seen that the deflagrating flame behaves differently based on the size of the obstacle at the central position. Without the central obstacle (i.e. the configuration BBB0), the fingers-like flame fronts induced by B3 merge and it propagates towards the outlet. When an obstacle is placed, the flame tends to wrap around it and get further distorted. Note that the size of the obstacle plays an important role in the flame front structure. The passage between the side of the obstacle and the wall of the combustion chamber becomes narrower when the size is larger, causing the flame to be ejected from there at high speed. Furthermore, the large obstacle introduces a wider turbulent wake behind it where the flame is significantly wrinkled. On the other hand, some unburned hydrogen-air mixture is trapped when passing it, as shown at $t = 3.9\ ms$ from Figure 7.16.

The last snapshot of Figure 7.16 displays the flame location where the overpressure peaks ($t \approx t_{p,LES}$) for each configuration in the simulation. It can be seen that when the maximum pressure is reached, the flame is at a position closer to the outlet if the degree of obstruction is increased. This may be due to the higher propagation speed of the flame front. For the case BBBL, the peak pressure is reached when the leading edge of the flame is nearly at the exit of the chamber. This is also confirmed in the experiments [156] that the flame location where the maximum overpressure is reached depends on the obstacle arrangement, and it may be more downstream when the overall turbulent intensity of the chamber is higher.

7.4 Comparison of three fuels

This section compares the combustion behaviours of individual fuels regarding the pressure build-up within the chamber as well as the flame characteristics. The present study considers three fuel/air mixtures: CNG ($\Phi = 1$), LPG ($\Phi = 1$) and hydrogen ($\Phi = 0.7$), and the first two are treated using their primary components, namely propane and methane in the numerical simulation. Table 7.2 lists the laminar burning velocity and flame thickness used for the combustion model, and all other numerical settings are identical for the three fuels.

Table 7.2: List of input laminar flame properties for the three fuel/air mixtures.

Fuel type	$s_L^0\ (cm/s)$	$\delta_L^0\ (mm)$
CH_4	36.0 [172]	0.41 [141]
C_3H_8	38.5 [160]	0.37 [47]
H_2	125 [166]	0.12 [137, 141]

While the actual deflagration depends on a range of conditions, the magnitude of peak pressure may be ranked qualitatively for common fuels. Bjerketvedt et al. [7] carried out experiments using stoichiometric hydrogen/air and several hydrocarbon/air mixtures and reported that the explosion pressure is highest using hydrogen and lowest with methane under the same experimental configuration. Considering that the rate of gas expansion predominantly determines the pressure rise in the deflagration, the influential factors of fuels mainly lie in the intrinsic laminar burning velocity and the adiabatic flame temperature. Typically, under the constant atmospheric condition ($p = 1\ atm$ and $T = 298\ K$), the stoichiometric CH_4/air mixture has an adiabatic flame temperature of $T_{ad} \approx 2225\ K$, and C_3H_8 has a similar value of $\sim 2266\ K$, calculated numerically using the GRI 3.0 mechanism [173]. For a lean H_2/air ($\Phi = 0.7$) mixture, $T_{ad} \approx 2000\ K$ [174, 175]. Note that the measured laminar burning velocities have a noticeable margin in the literature. At standard atmosphere, stoichiometric propane/air mixture can have s_L^0 ranging approximately from 35 to 45 cm/s [160, 161]. For CH_4/air mixtures, it may range from 32 to 40 cm/s [172], and the variation for the lean H_2/air mixture is even larger (100 to 150 cm/s) [166, 176]. However, qualitatively the flame velocity for hydrogen is the highest followed by propane and methane, and the latter two have similar magnitudes. The thickness of a flame has multiple definitions [167], and there are also uncertainties in the measurement. In this study, the thermal flame thickness is used based on the maximum temperature gradient in a planar laminar flame.

Results of six configurations with one and two baffle plates are presented here to reveal the role of the fuel type in various flow scenarios. Figures 7.17 to 7.19 display the numerical and experimental overpressure time traces for methane, propane and hydrogen, respectively. It can be seen that LES appropriately estimates the overpressure trend and magnitude and reproduces the influence of the obstacles for the three fuel/air mixtures. The maximum pressure of H_2 is an almost an order of magnitude higher than that of CH_4 and C_3H_8 even at a lower equivalence ratio of $\Phi = 0.7$. For instance, overpressure rises to a maximum of $\sim 50\ mbar$ and $\sim 80\ mbar$ for methane and propane, respectively for the configuration B0BS, while it reaches more than 700 $mbar$ with hydrogen. Given that the burned gas temperature is, in fact, lower for hydrogen compared with the other two fuels, the excessive generated pressure is mainly due to its higher laminar flame speed. The higher gas velocity ahead of the flame enhances the venting rate, however, the much more rapid consumption rate of the fresh mixture gives rises to the large pressure rise.

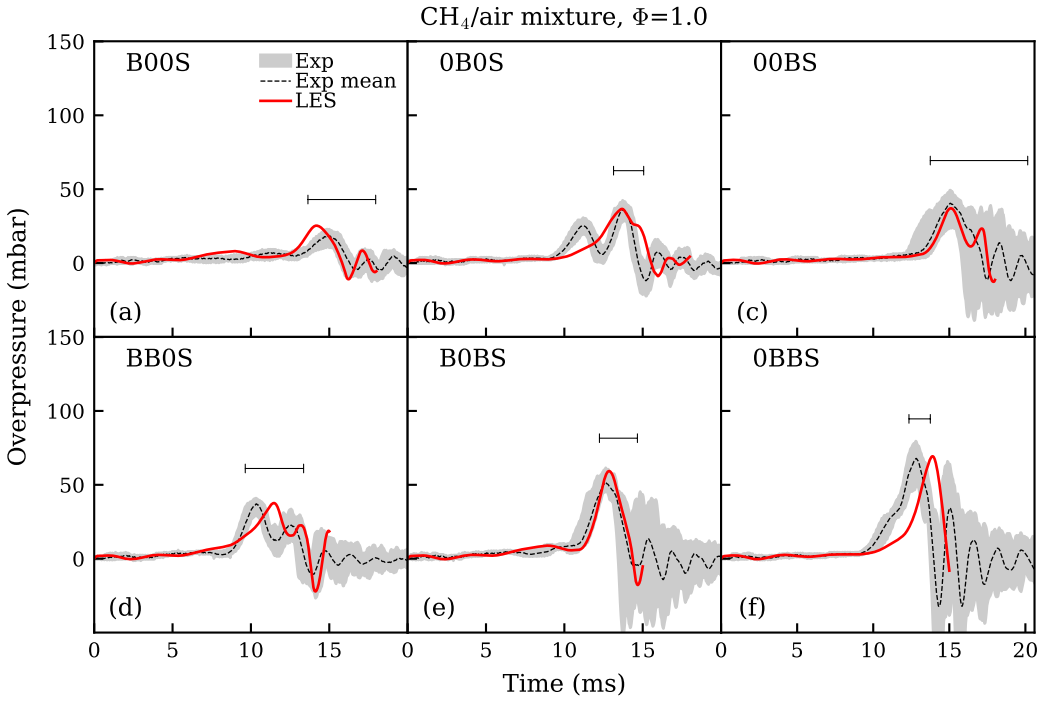

Figure 7.17: Computed and experimental overpressure traces using methane ($\Phi = 1.0$) for six configurations from (a) to (f).

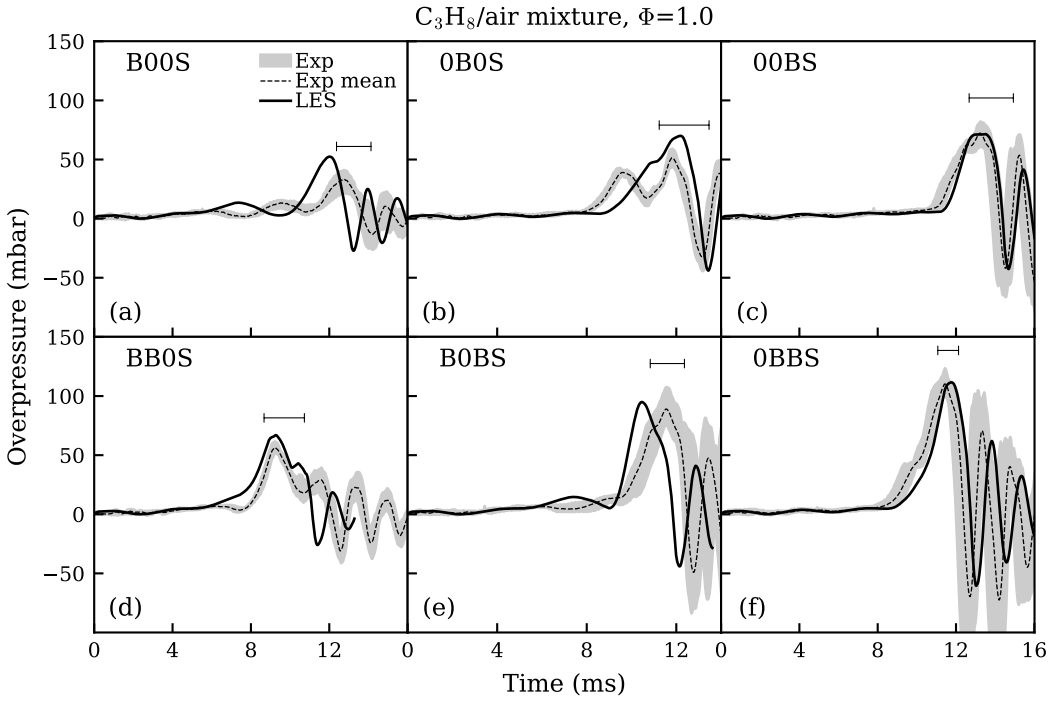

Figure 7.18: Computed and experimental overpressure traces using propane ($\Phi = 1.0$) for six configurations from (a) to (f).

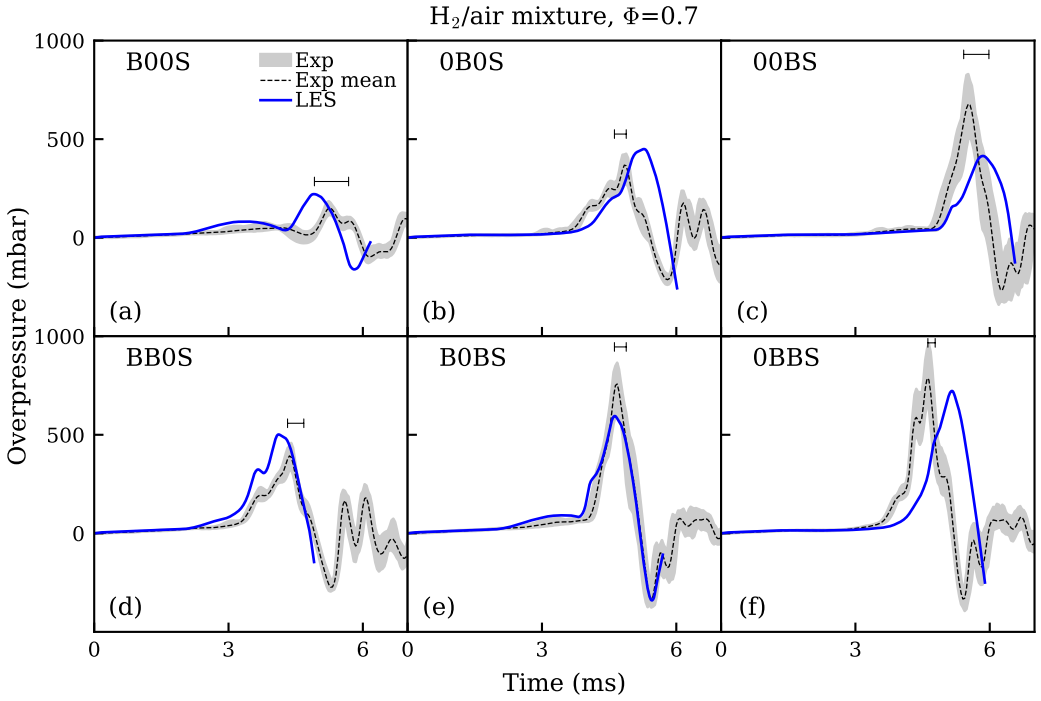

Figure 7.19: Computed and experimental overpressure traces using hydrogen ($\Phi = 0.7$) for six configurations from (a) to (f).

Also, the time taken to reach the main pressure peak depends on the fuel type. For the studied configurations, the variation in computed $t_{p,LES}$ is $10-15$ ms (Figure 7.17) for methane, $8-13$ ms (Figure 7.18) for propane and $4-5$ ms for hydrogen. Similar values of $t_{p,exp}$ can also be found from the experiments, and it takes roughly two times longer for methane and propane to attain the major pressure peak compared to the hydrogen cases. The LES-DFSD approach also makes a reasonable prediction in the details of the pressure evolution. Take the configuration BB0S, for example, there is a tiny pressure peak before the maxima at around 4 ms for hydrogen (Figure 7.19d), while it is not present for methane (Figure 7.17d) or propane (Figure 7.18d). In contrast, a small peak after the maxima can be found at about 10 ms for propane (Figure 7.18d) in the experiment, and it is also predicted numerically.

Figure 7.20 illustrates the flame structure when interacting with obstacles using the $\widetilde{c}$ field extracted from LES. The cases of methane and hydrogen are considered here since the propane/air flame behaves in a fairly similar manner as methane. Also shown in Figure 7.20 are the LIF-OH images for the flame front in the experiments, assuming that OH radical adequately indicates the reaction zone. Due to the numerical filtering effect, the comparison between the flame shapes from LES and experiments may not be straightforward. Thus, only a qualitative investigation has been made to reveal the essential flame characteristics. Note that the leading edges of the two flames have proceeded at the same distance from the square

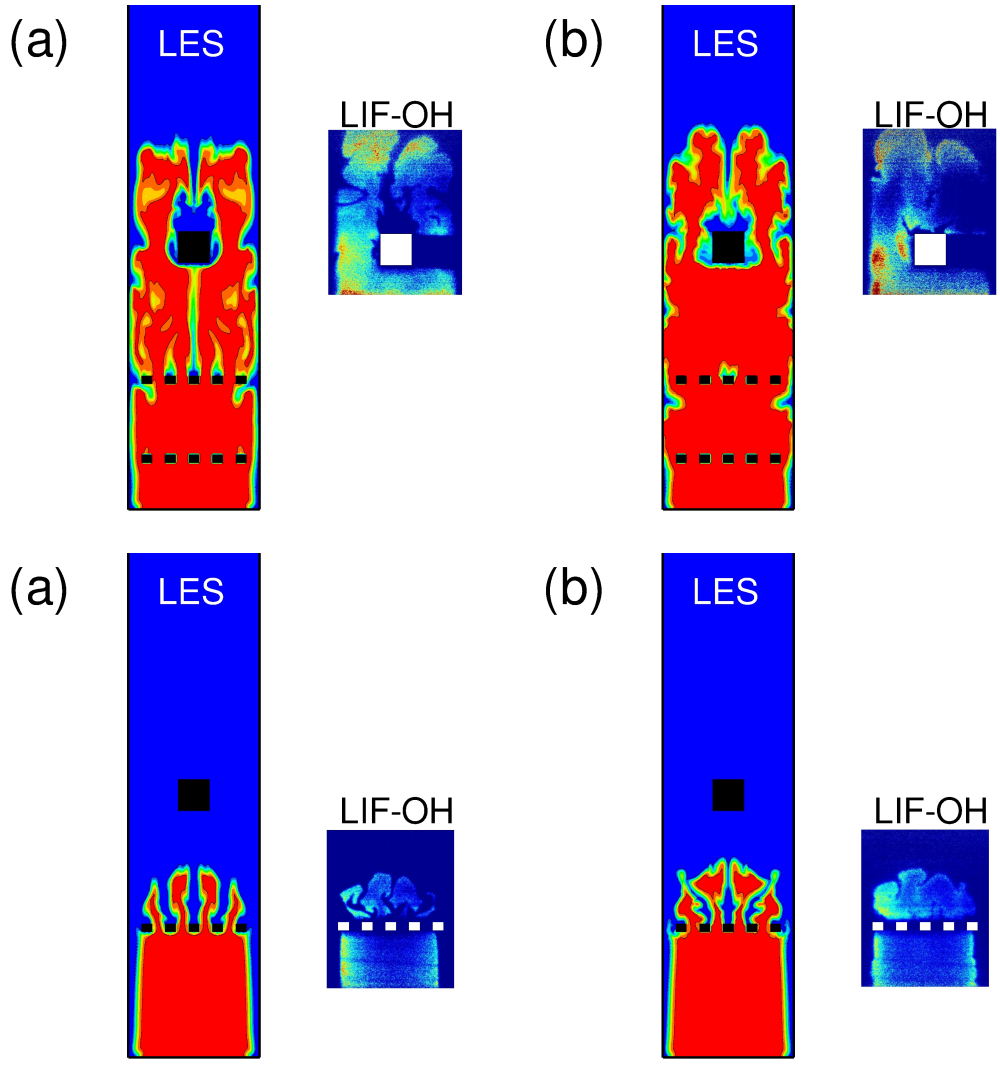

Figure 7.20: Comparison of numerical and experimental flames showing the effect of the obstacle on the flame. *Top:* Configuration BB0S. *Bottom:* Configuration 0B0S. (a) methane and (b) hydrogen. Contour lines in LES indicate the regions of $0.05 < \widetilde{c} < 0.95$.

obstacle as shown in Figure 7.20(top), however, the hydrogen/air flame (Figure 7.20(top)b) seems to have consumed more of the unburned gases in the recirculation area compared with methane (Figure 7.20(top)a). Although the hydrogen flame has a much higher inertia in the axial direction due to the considerable propagation speed, the stronger turbulence motions in the wake of the central obstruction enhance the flow-induced lateral movement of the flame. The two separated flame fronts resulting from the blockage of the central obstacle tend to merge faster in the hydrogen case (Figure 7.20(top)b). The LIF-OH images (Figure 7.20(top)a and b) also confirm the more rapid consumption of the trapped unburned mixture when hydrogen is used as the fuel. It is an indication of the more intensive vortex structures behind the central obstacle. Figure 7.20(bottom)a and b further demonstrate that for the configuration with a single baffle (i.e. 0B0S), the methane/air flame fingers merge at a slower rate than that of hydrogen due to the less turbulent environment behind the baffle strips. The contours of progress variable in Figure 7.20(top)a and b show isolated pockets of reactants trapped in the burned gases behind the second baffle plate, and they contribute to the burning rate in the later stage of the deflagration. There are considerably more reactant pockets in the case of methane (Figure 7.20(top)a) compared with that of hydrogen (Figure 7.20(top)b). It is again due to the more recirculating turbulent flows generated behind the baffle enhancing the consumption of this trapped fresh mixture in the case of hydrogen.

Figure 7.21(left) shows the flame position computed by LES and that extracted from the LIF-OH images. It can be seen that the overall prediction is satisfactory, but after the second baffle plate, the LES overestimates the flame position to a small extent. The deviation between the numerical and experimental results also comes from the initial condition in LES such as the initial flame kernel size. Throughout the deflagration process, the hydrogen flame travels much faster than methane and propane and reaches the chamber exit in about 4 ms. From the slope of the position curves, the flames of methane and propane have almost the same velocity after ignition, but the speed of the latter increases beyond the former after passing the first obstacle. Interestingly, after passing the second baffle, the difference in the axial velocity of the two flame leading edges is not obvious. It may result from the strong flame-turbulence interaction in the lateral direction. The speed-up locations in Figure 7.21(left) reveals that the hydrogen deflagrating flame not only propagates at a higher rate but also responds more to the obstructions. It is due to the positive feedback loop regarding the obstacle-enhanced flame propagation. A more rapid flame velocity of hydrogen would create stronger turbulent flows

behind the obstruction where the interaction would also be more intensive.

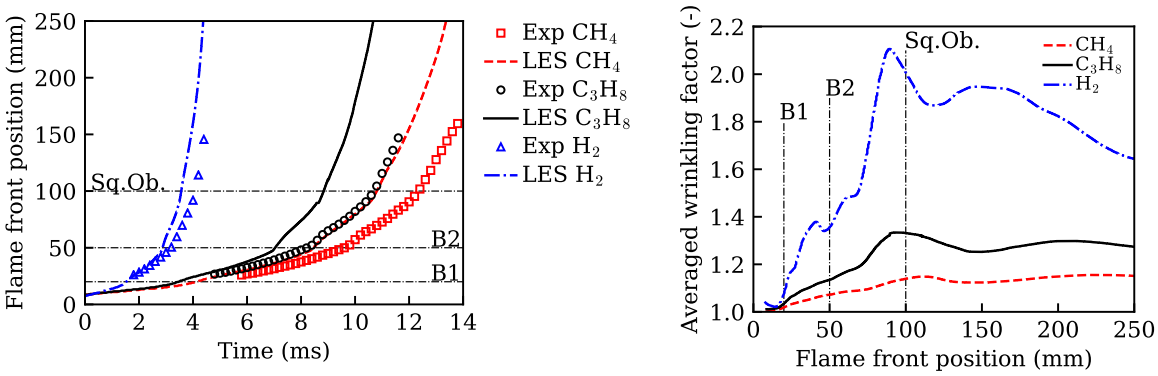

Figure 7.21: The influence of fuel type on the flame position (left) and sub-grid wrinkling factor (right) for the configuration BB0S. Numerical flame leading edge is located at $\widetilde{c} = 0.5$ furthest from the ignition end. Averaged wrinkling factor $\langle \Xi \rangle_f$ evaluated within $0.05 < \widetilde{c} < 0.95$.

Figure 7.21(right) presents the computed sub-grid wrinkling factor $\langle \Xi \rangle_f$ in the path of the flame propagation. It is important to reiterate that in the LES-DFSD approach, Ξ represents the level of flame-turbulence interaction at sub-grid scale, while the effect of large-scale turbulence on the filtered flame is resolved on the mesh. The overall sub-grid wrinkling evolves following a similar trend for the three fuels. As the flame is not yet wrinkled by turbulence motions before encountering the first baffle, $\langle \Xi \rangle_f \approx 1$, and it grows between adjacent obstacles to account for the unresolved flame surfaces. Passing the square obstacle, the mean sub-grid wrinkling factors of CH_4/air and C_3H_8/air flames tend to stabilise, while that of the H_2/air flame drops towards the chamber exit. The absolute value and the rate of change of $\langle \Xi \rangle_f$ are considerably larger for the hydrogen/air flame at all phases of the deflagration. Especially in the later turbulent stage, the hydrogen flame has a significantly higher mean Ξ of about 1.8, compared with 1.3 for propane and 1.1 for methane. Based on the definition of Ξ, one can relate the resolved ($\dot{\omega}_{res}$) and the total ($\dot{\omega}_{tot}$) reaction rates as $\dot{\omega}_{tot} = \Xi \dot{\omega}_{res}$. Thus, it is useful to examine the contribution of the resolved part of the combustion rate η_{res} as

$$\eta_{res} = \frac{\dot{\omega}_{res}}{\dot{\omega}_{tot}} = \frac{1}{\Xi} \tag{7.1}$$

From Figure 7.21, it is clear that for the filtered hydrogen flame, a significant portion of the reaction rate results from the sub-grid scale. It shows that only half of the reaction rate is resolved on the grid when $\langle \Xi \rangle_f$ reaches 2.0. In contrast, most of the combustion rate ($\eta_{res} \approx$91% for $\langle \Xi \rangle_f = 1.1$) is resolved for methane even in the later turbulent stage. Furthermore, the evolution of mean wrinkling factor reflects the higher sensitivity to the obstructions for the

H_2/air flame, indicating the stronger turbulence influence at the sub-grid scale.

For the present study, lean hydrogen/air flames produce significantly higher (more than six times) maximum overpressure compared with that of stoichiometric methane and propane. The hydrogen flame is also found to induce stronger turbulence in the recirculation areas behind the baffle strips and central obstruction. It is due to the more intensive flame/turbulence interactions at both the resolved and sub-grid scales when hydrogen is used as the fuel. The LES-DFSD approach correctly captured the characteristics of flame and flow when using different fuels, and it also achieved satisfactory predictions of pressure and flame position.

Chapter 8

Conclusions and Future Perspectives

8.1 Conclusions and present contributions

The present research work focuses on simulating transient turbulent premixed flames using the LES-DFSD approach. The study is motivated by the fact that deflagrating flames typically start being laminar and develop to fully turbulent. The level of flame-turbulence interactions is strongly dependent on the surrounding obstructions and confinement. While applying algebraic FSD models in LES is attractive, its satisfaction is often prohibited by the uncertainty of determining the model parameters in the model. Hence, a more robust approach to evaluate the model parameter is necessary for the successful modelling of a range of combustion scenarios. The present research has implemented, tested and evaluated a dynamic FSD model for studying propagating flames in the presence of solid obstacles.

The first investigation was to demonstrate the correct behaviours of the present FSD model in terms of the flame propagation speed and the filtered flame thickness. For this purpose, a series of 1-D laminar flame tests have been conducted where the effect of turbulence is absent. The tests have shown that the present model formulation is able to recover the correct laminar burning velocity. On the other hand, the filter width has been found to be a critical parameter controlling the thickness of the numerical flame. The calculated laminar propagation speed converged to the exact value as the filter size increases. It was also confirmed that the effective filtered flame front described by the progress variable generally crosses n_{res} grid points where $\Delta = n_{res}\Delta x$. The 1-D test cases also revealed that the successful use of the FSD model requires a sufficient flame resolution. For a typical LES grid, one should ensure that $n_{res} > 4$, otherwise, the filtered flame would be under-resolved, and consequently, the laminar flame propagation cannot be recovered in the absence of turbulence.

The LES-DFSD approach has then been applied to study the unsteady flame propagation in a small-scale vented combustion chamber. The experiments have been performed at the University of Sydney using three fuels, namely CNG, LPG and hydrogen, with the first two treated as methane and propane numerically. Abundant and high-quality data of pressure signals and LIF-OH flame images are also available from the experiment. The combustion chamber contains three removable baffle plates and a central obstacle with a square cross-section. A distinct advantage of the test set-up is the ability to provide various level of turbulence by altering the obstacle frequency, location and size. LES results of overpressure and flame front position have been compared with the experimental measurements to assess the capability of the modelling approach and to give insights into the flame propagation process.

To lay the foundation for the subsequent numerical tests, a sensitivity study was conducted using the stoichiometric propane/air deflagration in the configuration BBBS. It aims to examine the influence of modelling factors including flame initiation, Smagorinsky constant, mesh size and filter width on the LES results. The fact that LES cannot resolve a very small flame kernel made it necessary to consider the appropriate approaches to initialising the simulation. Four methods of combustion initialisation have been tested in the context of LES-DFSD: (*i*) using a separate ignition model, (*ii*) start with a burned flame kernel with a filtered 1-D flame solution as the $\widetilde{c}$ profile, (*iii*) initiate a burned flame kernel with a unit step function as the $\widetilde{c}$ profile, and (*iv*) numerically ignite the gas by setting a region of $\widetilde{c} = 0.5$. It has been found that the effect of ignition modelling mainly lies in the early quasi-laminar phase of the deflagration. Furthermore, the timing of the main pressure peak is strongly linked to the flame initiation, while its magnitude remains insensitive to an extent. In the early quasi-laminar stage, the leading edge of the flame travels faster when starting with a burned flame kernel than computing using an ignition model. However, the difference in predicted flame propagation speeds is negligible when the turbulence effect becomes significant. The Smagorinsky constant was found to have a moderate influence on the overpressure magnitude especially in the later stage, although the propagation speed was fairly insensitive to the parameter. On the other hand, the filter width of the flame should be chosen to ensure that the filtered flame is sufficiently resolved. An under-resolved flame gives a much faster flame propagation and higher peak overpressure, while they tend to converge when the filter width increases.

After the sensitivity study, a qualitative comparison has been made between the LES

and LIF-OH flame images for the stoichiometric propane/air flame. It showed the ability of the present modelling approach in predicting the flame structure throughout the deflagration. Clearly, LES results also helped to understand the mechanism of pressure build-up inside the chamber by monitoring the evolution of both gas expansion and venting rates. It has been demonstrated that flame-turbulence interactions due to obstacles play a critical role in the deflagration, noting that the rectangular baffle plates are efficient turbulence generators. Comparing the configurations 000S and BBBS, there was a strong flame wrinkling downstream of the central obstacle for the latter case, resulting from the smaller and more intensive turbulent structures in the second half of the chamber. Also, the DFSD model automatically captured the evolution of the sub-grid wrinkling factor, and consequently a much higher pressure peak is computed in the configuration BBBS. By constructing an LES regime diagram of turbulent premixed combustion for the case BBBS, it was confirmed that the flame wrinkling is largely resolved before reaching the second baffle. Furthermore, the overpressure peak was reached when the flame front is within the thin reaction zone of the regime. Promising results such as the peak overpressure and flame speed have been obtained for a range of obstacle configurations using stoichiometric propane/air mixture. It proved the capability of the present numerical set-up in reproducing essential features for transient flame propagation such as the flame relaminarisation for certain configurations. The sub-grid wrinkling factor was seen as an excellent indicator of the dynamic behaviours of the flame propagation.

The LES-DFSD approach has then been applied to study the hydrogen deflagration with a total number of eleven flow configurations. Satisfactory agreements have been seen between the LES and experiments regarding the timing and magnitude of the maximum overpressure. The position of the baffle plates largely controls the level of flame-turbulence interaction. For the configurations with the same number of baffles, the smaller separation distance between obstacles leads to more intensive flame front wrinkling. One should note that a flame may relaminarise in the cases where the distance between two adjacent obstacles is sufficiently large. The first baffle plate has been found to have a relatively weak influence on the overall pressure development. It is due to the closeness between the ignition point and the grid, leading to an insufficient time for the turbulence to be created. A further investigation was carried out to study the effect of the obstacle size. It showed that a larger square obstacle typically induces higher peak pressure resulting from a greater level of blockage. It has also been demonstrated that when the pressure peak is reached, the flame leading edge would be more downstream if

a larger central obstacle was used.

Finally, the impact of the fuel type has been investigated using the three fuels, namely methane, propane and hydrogen. In general, the effects of obstacle arrangement were similar for all the fuels considered in this study. While the pressure traces and flame behaviours were to be similar between methane and propane, hydrogen generated an order-of-magnitude higher maximum pressure even with a lean mixture. The calculated sub-grid wrinkling factor and the flame position tracking also revealed the higher sensitivity to obstructions when using hydrogen. Both the LES and LIF-OH images illustrated the difference in flame structure between the hydrogen/air and methane or propane/air deflagrations. In the test cases using hydrogen as the fuel, the more rapid flame propagation was found to induce a stronger turbulence field in the wake of the obstructions. Also, the individual flame fingers caused by the obstacle tended to merge at a faster speed. LES results also confirmed the quicker consumption of the trapped reactant pockets behind the obstructions in the hydrogen deflagration. Under the same mesh resolution, the calculated sub-grid wrinkling factor for hydrogen was substantially higher than that of propane and methane, indicating a considerable portion of the reaction rate at sub-grid scale. Encouragingly, LES also captured the dynamics shown on the pressure curves for the three fuels such as the sudden changes before or after the main peak for some flow cases.

One of the main contributions of the present research work is the implementation, testing and validation of a dynamic FSD combustion model to evaluate the model coefficient on-the-fly. Compared to the conventional algebraic closures where model coefficients are empirical and constant, it has increased the capability of capturing the dynamic nature of flame-turbulence interactions and the early quasi-laminar stage of the deflagration. The present study has also helped to establish a good level of confidence in using the large eddy simulation technique for transient turbulent premixed propagating flames in a series of flow configurations. It has also identified the influence of a wide range of numerical factors such as methods for flame initiation and turbulence parameters. The validated LES computation has enhanced the understanding of the mechanisms of turbulence generation by obstacles and pressure build-up in vented flame deflagrations. For the first time, a systematic study of a series of obstacle configurations and fuel types has been carried out using the novel LES-DFSD approach for testing and performance assessment. The satisfactory results indicate the advantage of using the present LES-DFSD framework to understand and predict such unsteady combustion phenomena.

8.2 Recommendations for future work

The present work is only considered preliminary to describe and predict more complex reacting flows in practical engineering systems. Future validation work on the LES-DFSD approach can involve the study of stratified combustion where a premixed flame occurs in a spatially non-uniform mixture distribution. Stratification aims to reduce soot and fuel consumption in practical combustion processes and is often encountered in real gas explosion scenarios. Another validation could be larger-scale deflagrations where the scaling effect and model behaviours are of the practical interest [141]. To achieve that, the in-house code needs to be extended to include the capability of accounting for reaction at various mixture concentrations. It may be realised through tabulated chemistry [144], or a simpler approach to relate the burning velocity in the equation of progress variable with the local mixture equivalence ratio under the laminar flamelet assumption [48]. In addition, the role of intrinsic flame instabilities [112, 177] could be identified as they may be dominant in obstacle-free deflagrations where flame wrinkling due to turbulence is considerably weak. While the exact contribution and mechanism of the intrinsic instabilities remain unclear, they are very likely to be a sub-grid phenomenon in LES. A first attempt could be to introduce a quasi-laminar burning velocity or to include a corresponding wrinkling factor to take into account the resulting increase in the flame surface [177].

Bibliography

[1] IEA., *World Energy Outlook 2017* (Organisation for Economic Co-operation and Development, OECD, 2017).

[2] J. Heywood, *Internal combustion engine fundamentals* (McGraw-Hill Education, 1988).

[3] P. G. Aleiferis, A. M. Taylor, K. Ishii, and Y. Urata, The nature of early flame development in a lean-burn stratified-charge spark-ignition engine, Combustion and Flame **136**, 283–302 (2004).

[4] J. Bohbot, F. A. Lafossas, A. Albrecht, M. Miche, M. Chraibi, and P. Menegazzi, A New Coupling Approach Using a 1D System Simulation Software and a 3D Combustion Code Applied to Transient Engine Operation, in 2004 powertrain & fluid systems conference & exhibition (Oct. 2004).

[5] D. J. Torres and M. F. Trujillo, KIVA-4: An unstructured ALE code for compressible gas flow with sprays, Journal of Computational Physics **219**, 943–975 (2006).

[6] STAR-CD, Version 3.20 user manual, 2004.

[7] D. Bjerketvedt, J. R. Bakke, and K. Van Wingerden, Gas explosion handbook, Journal of Hazardous Materials **52**, 1–150 (1997).

[8] Buncefield Major Incident Investigation Board, *The Buncefield incident, 11 December 2005: the final report of the Major Incident Investigation Board* (Health and Safety Executive, 2008).

[9] A. S. GexCon, FLACS v10. 0 User's Manual, 2013.

[10] K. McGrattan, S. Hostikka, R. McDermott, J. Floyd, C. Weinschenk, and K. Overholt, *Fire Dynamics Simulator technical reference guide*, tech. rep. (2017), pp. 1–147.

[11] S. S. Vianna and R. S. Cant, Explosion pressure prediction via polynomial mathematical correlation based on advanced CFD Modelling, Journal of Loss Prevention in the Process Industries **25**, 81–89 (2012).

[12] J. Li, F. Hernandez, H. Hao, Q. Fang, H. Xiang, Z. Li, X. Zhang, and L. Chen, Vented Methane-air Explosion Overpressure Calculation-A simplified approach based on CFD, Process Safety and Environmental Protection **109**, 489–508 (2017).

[13] G. Marbán and T. Valdés-Solís, Towards the hydrogen economy?, International Journal of Hydrogen Energy **32**, 1625–1637 (2007).

[14] A. Veziroglu and R. MacArio, Fuel cell vehicles: State of the art with economic and environmental concerns, International Journal of Hydrogen Energy **36**, 25–43 (2011).

[15] T. E. Lipman, M. Elke, and J. Lidicker, Hydrogen fuel cell electric vehicle performance and user-response assessment: Results of an extended driver study, International Journal of Hydrogen Energy **43**, 12442–12454 (2018).

[16] C. M. White, R. R. Steeper, and A. E. Lutz, The hydrogen-fueled internal combustion engine: a technical review, International Journal of Hydrogen Energy **31**, 1292–1305 (2006).

[17] P. E. Dodds, I. Staffell, A. D. Hawkes, F. Li, P. Grünewald, W. McDowall, and P. Ekins, Hydrogen and fuel cell technologies for heating: A review, International Journal of Hydrogen Energy **40**, 2065–2083 (2015).

[18] Y. Lee, J. Kim, J. Kim, E. J. Kim, Y. G. Kim, and I. Moon, Development of a web-based 3D virtual reality program for hydrogen station, International Journal of Hydrogen Energy **35**, 2112–2118 (2010).

[19] E. Kim, J. Park, J. H. Cho, and I. Moon, Simulation of hydrogen leak and explosion for the safety design of hydrogen fueling station in Korea, International Journal of Hydrogen Energy **38**, 1737–1743 (2013).

[20] B. Angers, A. Hourri, P. Benard, E. Demaël, S. Ruban, and S. Jallais, Modeling of hydrogen explosion on a pressure swing adsorption facility, International Journal of Hydrogen Energy **39**, 6210–6221 (2014).

[21] S. Kikukawa, H. Mitsuhashi, and A. Miyake, Risk assessment for liquid hydrogen fueling stations, International Journal of Hydrogen Energy **34**, 1135–1141 (2009).

[22] Y. F. Khalil, Science-based framework for ensuring safe use of hydrogen as an energy carrier and an emission-free transportation fuel, Process Safety and Environmental Protection **117**, 326–340 (2018).

[23] A. G. Venetsanos, D. Baraldi, P. Adams, P. S. Heggem, and H. Wilkening, CFD modelling of hydrogen release, dispersion and combustion for automotive scenarios, Journal of Loss Prevention in the Process Industries **21**, 162–184 (2008).

[24] J. Yanez, M. Kuznetsov, and A. Souto-Iglesias, An analysis of the hydrogen explosion in the Fukushima-Daiichi accident, International Journal of Hydrogen Energy **40**, 8261–8280 (2015).

[25] K. M. Groth and E. S. Hecht, HyRAM: A methodology and toolkit for quantitative risk assessment of hydrogen systems, International Journal of Hydrogen Energy **42**, 7485–7493 (2017).

[26] T. Poinsot and D. Veynante, *Theoretical and numerical combustion*, 2nd ed. (R.T. Edwards, Inc., 2005), p. 522.

[27] A. Marangon, M. Schiavetti, M. Carcassi, P. Pittiglio, P. Bragatto, and A. Castellano, Turbulent hydrogen deflagration induced by obstacles in real confined environment, International Journal of Hydrogen Energy **34**, 4669–4674 (2009).

[28] A. Maries, M. Abedul Haque, S. L. Yilmaz, M. B. Nik, and G. E. Marai, Interactive exploration of stress tensors used in computational turbulent combustion, in *New developments in the visualization and processing of tensor fields* (Springer, 2012), pp. 137–156.

[29] D. C. Wilcox, *Turbulence Modeling for CFD* (1994).

[30] R. Borghi, On the structure and morphology of turbulent premixed flames, in *Recent advances in the aerospace sciences* (Springer US, Boston, MA, 1985), pp. 117–138.

[31] N. Peters, Laminar flamelet concepts in turbulent combustion, Symposium (International) on Combustion **21**, 1231–1250 (1988).

[32] R. Abdel-Gayed, D. Bradley, and F.-K. Lung, Combustion regimes and the straining of turbulent premixed flames, Combustion and Flame **76**, 213–218 (1989).

[33] T. Poinsot, D. Veynante, and S. Candel, Diagrams of premixed turbulent combustion based on direct simulation, Symposium (International) on Combustion **23**, 613–619 (1991).

[34] N. Peters, The turbulent burning velocity for large-scale and small-scale turbulence, Journal of Fluid Mechanics **384**, 107–132 (1999).

[35] H. Pitsch and L. D. De La Geneste, Large-eddy simulation of premixed turbulent combustion using a level-set approach, Proceedings of the Combustion Institute **29**, 2001–2008 (2002).

[36] N. Peters, *Turbulent Combustion*, Cambridge Monographs on Mechanics (Cambridge University Press, 2000).

[37] H. Pitsch, A consistent level set formulation for large-eddy simulation of premixed turbulent combustion, Combustion and Flame **143**, 587–598 (2005).

[38] D. Veynante and L. Vervisch, Turbulent combustion modeling, Progress in Energy and Combustion Science **28**, 193–266 (2002).

[39] H. Pitsch, Large-Eddy Simulation of Turbulent Combustion, Annual Review of Fluid Mechanics **38**, 453–482 (2005).

[40] V. Moureau, B. Fiorina, and H. Pitsch, A level set formulation for premixed combustion LES considering the turbulent flame structure, Combustion and Flame **156**, 801–812 (2009).

[41] O. Colin, F. Ducros, D. Veynante, and T. Poinsot, A thickened flame model for large eddy simulations of turbulent premixed combustion, Physics of Fluids **12**, 1843–1863 (2000).

[42] B. C. Angelberger, D. Veynante, F. Egolfopoulos, and T. Poinsot, Large eddy simulations of combustion instabilities in premixed flames, Center for Turbulence Research Proceedings of the Summer Programme, 61–82 (1998).

[43] J. P. Legier, T. Poinsot, and D. Veynante, Dynamically thickened flame LES model for premixed and non-premixed turbulent combustion, Proceedings of the Summer Program, Centre for Turbulence Research, 157–168 (2000).

[44] D. Veynante and T. Poinsot, *Large eddy simulation of combustion instabilities in turbulent premixed burners*, tech. rep. (1997), pp. 253–274.

[45] M. Boger, D. Veynante, H. Boughanem, and A. Trouvé, Direct numerical simulation analysis of flame surface density concept for large eddy simulation of turbulent premixed combustion, Symposium (International) on Combustion **27**, 917–925 (1998).

[46] M. Boger and D. Veynante, Large eddy simulations of a turbulent premixed v-shape flame, in Eighth european turbulence conference (2000), pp. 448–452.

[47] G. Wang, M. Boileau, D. Veynante, and K. Truffin, Large eddy simulation of a growing turbulent premixed flame kernel using a dynamic flame surface density model, Combustion and Flame **159**, 2742–2754 (2012).

[48] Z. Hu, Low-pressure explosive combustion in compartment fires, PhD thesis (University of Maryland, 2008), p. 124.

[49] C. Duwig, Study of a filtered flamelet formulation for large eddy simulation of premixed turbulent flames, Flow, Turbulence and Combustion **79**, 433–454 (2007).

[50] F. T. M. Nieuwstadt and J. P. Meeder, Large-eddy simulation of air pollution dispersion: A review, in New tools in turbulence modelling (1997), pp. 265–280.

[51] D. B. Spalding, Mixing and chemical reaction in steady confined turbulent flames, Symposium (International) on Combustion **13**, 649–657 (1971).

[52] T. Ma, Flame surface density modelling for the large eddy dimulation of turbulent premixed flames, PhD thesis (Imperial College London, 2013).

[53] G. Wang, M. Boileau, and D. Veynante, Implementation of a dynamic thickened flame model for large eddy simulations of turbulent premixed combustion, Combustion and Flame **158**, 2199–2213 (2011).

[54] P. Auzillon, B. Fiorina, R. Vicquelin, N. Darabiha, O. Gicquel, and D. Veynante, Modeling chemical flame structure and combustion dynamics in les, Proceedings of the Combustion Institute **33**, 1331–1338 (2011).

[55] F. A. Williams, *Combustion theory* (2018).

[56] F. Charlette, D. Veynante, and C. Meneveau, A power-law wrinkling model for LES of premixed turbulent combustion Part I: non-dynamic formulation and initial tests, Combustion and Flame **131**, 159–180 (2002).

[57] E. R. Hawkes and R. S. Cant, Physical and numerical realizability requirements for flame surface density approaches, Combustion Theory and Modelling **5**, 699–720 (2001).

[58] E. Hawkes and R. Cant, Implications of a flame surface density approach to large eddy simulation of premixed turbulent combustion, Combustion and Flame **126**, 1617–1629 (2001).

[59] S. Richard, O. Colin, O. Vermorel, A. Benkenida, C. Angelberger, and D. Veynante, Towards large eddy simulation of combustion in spark ignition engines, Proceedings of the Combustion Institute **31 II**, 3059–3066 (2007).

[60] T. Ma, O. Stein, N. Chakraborty, and A. Kempf, A posteriori testing of the flame surface density transport equation for LES, Combustion Theory and Modelling **18**, 32–64 (2014).

[61] R. Knikker, D. Veynante, and C. Meneveau, A priori testing of a similarity model for large eddy simulations of turbulent premixed combustion, Proceeding of Combustion Institute **29**, 2105–2111 (2002).

[62] T. Ma, O. Stein, N. Chakraborty, and A. Kempf, A posteriori testing of algebraic flame surface density models for LES, Combustion Theory and Modelling **17**, 431–482 (2013).

[63] H. Weller, G. Tabor, A. Gosman, and C. Fureby, Application of a flame-wrinkling les combustion model to a turbulent mixing layer, Symposium (International) on Combustion **27**, 899–907 (1998).

[64] T. Poinsot, S. Candelt, and A. Trouvé, Applications of Direct Numerical Simulation Premixed Turbulent Combustion, Progress in Energy and Combustion Science **21**, 531–576 (1996).

[65] A. R. Masri, S. S. Ibrahim, and B. J. Cadwallader, Measurements and large eddy simulation of propagating premixed flames, Experimental Thermal and Fluid Science **30**, 687–702 (2006).

[66] M. P. Kirkpatrick, A large eddy simulation code for industrial and environmental flows, PhD thesis (The University of Sydney, 2002), p. 266.

[67] C. Fureby, A fractal flame-wrinkling large eddy simulation model for premixed turbulent combustion, Proceedings of the Combustion Institute **30**, 593–600 (2005).

[68] F. Charlette, C. Meneveau, and D. Veynante, A power-law flame wrinkling model for LES of premixed turbulent combustion Part II: Dynamic formulation, Combustion and Flame **131**, 181–197 (2002).

[69] K. N. C. Bray, P. A. Libby, and J. B. Moss, Unified modeling approach for premixed turbulent combustion-Part I: General formulation, Combustion and Flame **61**, 87–102 (1985).

[70] K. N. C. Bray, M. Champion, and P. A. Libby, The interaction between turbulence and chemistry in premixed turbulent flames, in Turbulent reactive flows, edited by R. Borghi and S. N. B. Murthy (1989), pp. 541–563.

[71] N. Chakraborty and R. S. Cant, A priori analysis of the curvature and propagation terms of the flame surface density transport equation for large eddy simulation, Physics of Fluids **19** (2007) 10.1063/1.2772326.

[72] V. Di Sarli, A. Di Benedetto, G. Russo, S. Jarvis, E. J. Long, and G. K. Hargrave, Large eddy simulation and PIV measurements of unsteady premixed flames accelerated by obstacles, Flow, Turbulence and Combustion **83**, 227–250 (2009).

[73] V. Di Sarli, A. Di Benedetto, and G. Russo, Using Large Eddy Simulation for understanding vented gas explosions in the presence of obstacles, Journal of Hazardous Materials **169**, 435–442 (2009).

[74] V. Di Sarli, A. Di Benedetto, and G. Russo, Large Eddy Simulation of transient premixed flame-vortex interactions in gas explosions, Chemical Engineering Science **71**, 539–551 (2012).

[75] U. Allauddin, M. Klein, M. Pfitzner, and N. Chakraborty, A priori and a posteriori analyses of algebraic flame surface density modeling in the context of Large Eddy Simulation of turbulent premixed combustion, Numerical Heat Transfer; Part A: Applications **71**, 153–171 (2017).

[76] M. P. Kirkpatrick, S. W. Armfield, A. R. Masri, and S. S. Ibrahim, Large eddy simulation of a propagating turbulent premixed flame, Flow, Turbulence and Combustion **70**, 1–19 (2003).

[77] S. R. Gubba, S. S. Ibrahim, W. Malalasekera, and A. Masri, LES modeling of premixed deflagrating flames in a small-scale vented explosion chamber with a series of solid obstructions, Combustion Science and Technology **180**, 1936–1955 (2008).

[78] R. Mercier, V. Moureau, D. Veynante, and B. Fiorina, LES of turbulent combustion: On the consistency between flame and flow filter scales, Proceedings of the Combustion Institute **35**, 1359–1366 (2015).

[79] S. Mouriaux, O. Colin, and D. Veynante, Adaptation of a dynamic wrinkling model to an engine configuration, Proceedings of the Combustion Institute **36**, 3415–3422 (2017).

[80] M. Klein and N. Chakraborty, A-priori analysis of an alternative wrinkling factor definition for flame surface density based Large Eddy Simulation modelling of turbulent premixed combustion, Combustion Science and Technology **00**, 1–14 (2018).

[81] D. Veynante and V. Moureau, Analysis of dynamic models for large eddy simulations of turbulent premixed combustion, Combustion and Flame **162**, 4622–4642 (2015).

[82] T. Schmitt, M. Boileau, and D. Veynante, Flame wrinkling factor dynamic modeling for large eddy simulations of turbulent premixed combustion, Flow, Turbulence and Combustion **94**, 199–217 (2015).

[83] J. Smagorinsky, General circulation experiments with the primitive equations, Monthly Weather Review **91**, 99–164 (1963).

[84] S. B. Pope, Turbulent flows, 2001.

[85] I. Langella, N. Swaminathan, Y. Gao, and N. Chakraborty, Large eddy simulation of premixed combustion: sensitivity to subgrid scale velocity modeling, Combustion Science and Technology **189**, 43–78 (2017).

[86] M. Germano, U. Piomelli, P. Moin, and W. H. Cabot, A dynamic subgrid-scale eddy viscosity model, Physics of Fluids A: Fluid Dynamics **3**, 1760–1765 (1991).

[87] R. Knikker, D. Veynante, and C. Meneveau, A dynamic flame surface density model for large eddy simulation of turbulent premixed combustion, Physics of Fluids **16**, L91 (2004).

[88] S. R. Gubba, S. S. Ibrahim, W. Malalasekera, and A. R. Masri, Measurements and LES calculations of turbulent premixed flame propagation past repeated obstacles, Combustion and Flame **158**, 2465–2481 (2011).

[89] D. Veynante, T. Schmitt, and M. Boileau, Analysis of dynamic models for turbulent premixed combustion, in Center for turbulence research proceedings of the summer program (2012), pp. 387–396.

[90] P. S. Volpiani, T. Schmitt, and D. Veynante, Large eddy simulation of a turbulent swirling premixed flame coupling the TFLES model with a dynamic wrinkling formulation, Combustion and Flame **180**, 124–135 (2017).

[91] W. Malalasekera, K. K. J. Ranga-Dinesh, S. S. Ibrahim, and A. R. Masri, LES of recirculation and vortex breakdown in swirling flames, Combustion Science and Technology **180**, 809–832 (2008).

[92] R. Maly, State of the art and future needs in S.I. engine combustion, Symposium (International) on Combustion **25**, 111–124 (1994).

[93] J. Xu, F. Behrendt, and J. Warnatz, 2D-LIF investigation of the early stages of flame kernel development during spark ignition, in International symposium comodia 94 (1994), pp. 69–73.

[94] J. B. Heywood, Combustion and its Modeling in Spark-Ignition Engines, 1994.

[95] C. P. Ranasinghe, Development of combustion models for RANS and LES applications in SI engines, Ph.D. Thesis (Loughborough University, 2013).

[96] L. Fan, G. Li, Z. Han, and R. D. Reitz, *Modeling fuel preparation and stratified combustion in a gasoline direct injection engine*, tech. rep. (1999).

[97] Z. Tan and R. D. Reitz, An ignition and combustion model based on the level-set method for spark ignition engine multidimensional modeling, Combustion and Flame **145**, 1–15 (2006).

[98] O. Colin, A. Benkenida, and C. Angelberger, 3D modeling of mixing, ignition and combustion phenomena in highly stratified gasoline engines, Oil and Gas Science and Technology **58**, 47–62 (2003).

[99] O. Vermorel, S. Richard, O. Colin, C. Angelberger, A. Benkenida, and D. Veynante, Towards the understanding of cyclic variability in a spark ignited engine using multi-cycle LES, Combustion and Flame **156**, 1525–1541 (2009).

[100] R. N. Dahms, M. C. Drake, T. D. Fansler, T. W. Kuo, and N. Peters, Understanding ignition processes in spray-guided gasoline engines using high-speed imaging and the extended spark-ignition model SparkCIMM. Part A: Spark channel processes and the turbulent flame front propagation, Combustion and Flame **158**, 2229–2244 (2011).

[101] T. Lucchini, L. Cornolti, G. Montenegro, G. D'Errico, M. Fiocco, A. Teraji, and T. Shiraishi, A comprehensive model to predict the initial stage of combustion in SI engines, in Sae 2013 world congress & exhibition (2013).

[102] S. C. Kong and R. D. Reitz, Multidimensional modeling of diesel ignition and combustion using a multistep kinetics model, Journal of Engineering for Gas Turbines and Power-Transactions of the Asme **115**, 781–789 (1993).

[103] S. Singh, L. Liang, S.-C. Kong, and R. D. Reitz, Development of a flame propagation model for dual-fuel partially premixed compression ignition engines, International Journal of Engine Research **7**, 65–75 (2006).

[104] D. Bradley and K. K. Lung, Spark ignition and the early stages of turbulent flame propagation, Combust. Flame **69**, 71–93 (1987).

[105] J. C. Henson, Numerical Simulation of Spark Ignition Engines with special emphasis on Radiative Heat Transfer, PhD thesis (Loughborough University, 1998), p. 318.

[106] G. Lacaze, E. Richardson, and T. Poinsot, Large eddy simulation of spark ignition in a turbulent methane jet, Combustion and Flame **156**, 1993–2009 (2009).

[107] G. Lacaze, B. Cuenot, T. Poinsot, and M. Oschwald, Large eddy simulation of laser ignition and compressible reacting flow in a rocket-like configuration, Combustion and Flame **156**, 1166–1180 (2009).

[108] O. Colin and K. Truffin, A spark ignition model for large eddy simulation based on an FSD transport equation (ISSIM-LES), Proceedings of the Combustion Institute **33**, 3097–3104 (2011).

[109] M. Matalon, Intrinsic Flame Instabilities in Premixed and Nonpremixed Combustion, Annual Review of Fluid Mechanics **39**, 163–191 (2007).

[110] G. Darrieus, Propagation d'un front de flamme, La Technique Moderne **30**, 18 (1938).

[111] L. D. Landau, On the theory of slow combustion, Acta Phys. **19**, 77–85 (1944).

[112] S. B. Dorofeev, Flame acceleration and explosion safety applications, Proceedings of the Combustion Institute **33**, 2161–2175 (2011).

[113] H. Xiao, R. W. Houim, and E. S. Oran, Effects of pressure waves on the stability of flames propagating in tubes, Proceedings of the Combustion Institute **36**, 1577–1583 (2017).

[114] L. Zhou, L. Zhong, J. Zhao, D. Gao, and H. Wei, Flame propagation and combustion modes in end-gas region of confined space, Combustion and Flame **190**, 216–223 (2018).

[115] G. Ciccarelli and S. Dorofeev, Flame acceleration and transition to detonations in ducts, Progress in Energy and Combustion Science **34**, 499–550 (2008).

[116] A. Harrison and J. Eyre, "External Explosions" as a Result of Explosion Venting, Combustion Science and Technology **52**, 91–106 (1987).

[117] C. A. Catlin, Scale effects on the external combustion caused by venting of a confined explosion, Combustion and Flame **83**, 399–411 (1991).

[118] M. Fairweather, G. K. Hargrave, S. S. Ibrahim, and D. G. Walker, Studies of premixed flame propagation in explosion tubes, Combustion and Flame **116**, 504–518 (1999).

[119] S. S. Ibrahim and A. R. Masri, The effects of obstructions on overpressure resulting from premixed flame deflagration, Journal of Loss Prevention in the Process Industries **14**, 213–221 (2001).

[120] D. J. Park, A. R. Green, Y. S. Lee, and Y. C. Chen, Experimental studies on interactions between a freely propagating flame and single obstacles in a rectangular confinement, Combustion and Flame **150**, 27–39 (2007).

[121] S. S. Ibrahim, G. K. Hargrave, and T. C. Williams, Experimental investigation of flame / solid interactions in turbulent premixed combustion, Experimental Thermal and Fluid Science **24**, 99–106 (2001).

[122] C. T. Johansen and G. Ciccarelli, Visualization of the unburned gas flow field ahead of an accelerating flame in an obstructed square channel, Combustion and Flame **156**, 405–416 (2009).

[123] X. Wen, M. Yu, Z. Liu, G. Li, W. Ji, and M. Xie, Effects of cross-wise obstacle position on methane-air deflagration characteristics, Journal of Loss Prevention in the Process Industries **26**, 1335–1340 (2013).

[124] X. Wen, H. Ding, T. Su, F. Wang, H. Deng, and K. Zheng, Effects of obstacle angle on methane–air deflagration characteristics in a semi-confined chamber, Journal of Loss Prevention in the Process Industries **45**, 210–216 (2017).

[125] A. M. Na, H. N. Phylaktou, and G. E. Andrews, Explosion flame acceleration over obstacles : Effects of separation distance for a range of scales, Process Safety and Environmental Protection **107**, 309–316 (2017).

[126] R. Hall, A. R. Masri, P. Yaroshchyk, and S. S. Ibrahim, Effects of position and frequency of obstacles on turbulent premixed propagating flames, Combustion and Flame **156**, 439–446 (2009).

[127] A. Alharbi, A. R. Masri, and S. S. Ibrahim, Turbulent premixed flames of CNG, LPG, and H2 propagating past repeated obstacles, Experimental Thermal and Fluid Science **56**, 2–8 (2014).

[128] X. Rocourt, S. Awamat, I. Sochet, and S. Jallais, Vented hydrogen-air deflagration in a small enclosed volume, International Journal of Hydrogen Energy **39**, 20462–20466 (2014).

[129] M. Yu, K. Zheng, L. Zheng, T. Chu, and P. Guo, Scale effects on premixed flame propagation of hydrogen/methane deflagration, International Journal of Hydrogen Energy **40**, 13121–13133 (2015).

[130] X. Lv, L. Zheng, Y. Zhang, M. Yu, and Y. Su, Combined effects of obstacle position and equivalence ratio on overpressure of premixed hydrogen–air explosion, International Journal of Hydrogen Energy **41**, 17740–17749 (2016).

[131] T. Li, F. Hampp, and R. P. Lindstedt, Experimental study of turbulent explosions in hydrogen enriched syngas related fuels, Process Safety and Environmental Protection **116**, 663–676 (2018).

[132] C. A. Catlin, M. Fairweather, and S. S. Ibraiim, Predictions of turbulent, premixed flame propagation in explosion tubes, Combustion and Flame **102**, 115–128 (1995).

[133] S. Patel, S. Jarvis, S. Ibrahim, and G. Hargrave, An experimental and numerical investigation of premixed flame deflagration in a semiconfined explosion chamber, Proceedings of the Combustion Institute **29**, 1849–1854 (2002).

[134] R. Cant, W. Dawes, and A. Savill, Advanced CFD and modeling of accidental explosions, Annual Review of Fluid Mechanics **36**, 97–119 (2004).

[135] S. R. Gubba, S. S. Ibrahim, W. Malalasekera, and A. R. Masri, An assessment of large eddy simulations of premixed flames propagating past repeated obstacles, Combustion Theory and Modelling **13**, 513–540 (2009).

[136] S. S. Ibrahim, S. R. Gubba, A. R. Masri, and W. Malalasekera, Calculations of explosion deflagrating flames using a dynamic flame surface density model, Journal of Loss Prevention in the Process Industries **22**, 258–264 (2009).

[137] P. Quillatre, O. Vermorel, T. Poinsot, and P. Ricoux, Large eddy simulation of vented deflagration, Industrial and Engineering Chemistry Research **52**, 11414–11423 (2013).

[138] P. S. Volpiani, T. Schmitt, O. Vermorel, P. Quillatre, and D. Veynante, Large eddy simulation of explosion deflagrating flames using a dynamic wrinkling formulation, Combustion and Flame **186**, 17–31 (2017).

[139] S. R. Gubba, Development of a Dynamic LES Model for Premixed Turbulent Flames, PhD thesis (Loughborough University, 2009), p. 253.

[140] M. A. Abdel-Raheem, S. S. Ibrahim, W. Malalasekera, and A. R. Masri, Large Eddy simulation of hydrogen-air premixed flames in a small scale combustion chamber, International Journal of Hydrogen Energy **40**, 3098–3109 (2015).

[141] O. Vermorel, P. Quillatre, and T. Poinsot, LES of explosions in venting chamber: A test case for premixed turbulent combustion models, Combustion and Flame **183**, 207–223 (2017).

[142] H. K. Versteeg and W. Malalasekera, *An Introduction to Computational Fluid Dynamics: The Finite Volume Method*, 2nd ed. (Pearson Education Limited, 2007).

[143] J. Gullbrand and F. K. Chow, The effect of numerical errors and turbulence models in large-eddy simulations of channel flow, with and without explicit filtering, Journal of Fluid Mechanics **495**, 323–341 (2003).

[144] B. Fiorina, R. Vicquelin, P. Auzillon, N. Darabiha, O. Gicquel, and D. Veynante, A filtered tabulated chemistry model for LES of premixed combustion, Combustion and Flame **157**, 465–475 (2010).

[145] G. P. Smith, D. M. Golden, M. Frenklach, N. W. Moriarty, B. Eiteneer, M. Goldenberg, C. T. Bowman, R. K. Hanson, S. Song, W. C. Gardiner Jr, et al., GRI 3.0 Mechanism, Gas Research Institute (http://www. me. berkeley. edu/gri_mech) (1999).

[146] H. Pitsch, FlameMaster: A C++ computer program for 0D combustion and 1D laminar flame calculations, 1998.

[147] A. Kempf, W. Malalasekera, K. K. Ranga-Dinesh, and O. Stein, Large eddy simulations of swirling non-premixed flames with flamelet models: A comparison of numerical methods, Flow, Turbulence and Combustion **81**, 523–561 (2008).

[148] S. M. R. V. V. Venkata, Advanced flamelet modelling of turbulent nonpremixed and partialy premixed combustion, PhD Thesis, 277 (2008).

[149] W. Malalasekera, K. K. J. Ranga Dinesh, S. S. Ibrahim, and M. P. Kirkpatrick, Large eddy simulation of isothermal turbulent swirling jets, Combustion Science and Technology **179**, 1481–1525 (2007).

[150] H. Werner and H. Wengle, Large-eddy simulation of turbulent flow over and around a cube in a plate channel, in Turbulent shear flows 8 (1993), pp. 155–168.

[151] O. V. Vasilyev, T. S. Lund, and P. Moin, A General Class of Commutative Filters for LES in Complex Geometries, Journal of Computational Physics **146**, 82–104 (1998).

[152] P. Sagaut and R. Grohens, Discrete filters for large eddy simulation, International Journal for Numerical Methods in Fluids **31**, 1195–1220 (1999).

[153] J. Bentley and J. Friedman, Data Structures for Range Searching, ACM Computing Surveys **11**, 397–409 (1979).

[154] J. Williamson, J. Mcgill, and A. Trouve, Large Eddy Simulation Modeling of Turbulent Deflagrations, in Fire safety science - proceedings of the eighth international symposium (2005), pp. 1375–1386.

[155] A. R. Masri, A. Alharbi, S. Meares, and S. S. Ibrahim, A comparative study of turbulent premixed flames propagating past repeated obstacles, Industrial and Engineering Chemistry Research **51**, 7690–7703 (2012).

[156] A. Al-Harbi, Turbulent premixed flames propagating past repeated obstacles, PhD thesis (University of Sydney, 2013).

[157] A. R. Masri, S. S. Ibrahim, N. Nehzat, and A. R. Green, Experimental study of premixed flame propagation over various solid obstructions, Experimental Thermal and Fluid Science **21**, 109–116 (2000).

[158] J. E. Kent, A. R. Masri, S. H. Stårner, and S. S. Ibrahim, Wrinkling Scales of Turbulent Premixed Propagating Flame Fronts Obtained From LIF-OH Imaging, Fourth Australian Conference on Laser Diagnostics in Fluid Mechanics and Combustion, 77–80 (2005).

[159] B. P. Leonard, A stable and accurate convective modelling procedure based on quadratic upstream interpolation, Computer methods in applied mechanics and engineering **19**, 59–98 (1979).

[160] M. Metghalchi and J. Keck, Laminar burning velocity of propane-air mixtures at high temperature and pressure, Combustion and Flame **38**, 143–154 (1980).

[161] M. S. Ebaid and K. J. Al-Khishali, Measurements of the laminar burning velocity for propane: Air mixtures, Advances in Mechanical Engineering **8**, 1–17 (2016).

[162] M. Klein, An Attempt to Assess the Quality of Large Eddy Simulation in the Context of Implicit Filtering, Flow, Turbulence and Combustion **75**, 131–147 (2005).

[163] A. M. Kempf, B. J. Geurts, T. Ma, M. W. A. Pettit, and O. T. Stein, Quality Issues in Combustion LES, Journal of Scientific Computing **49**, 51–64 (2011).

[164] G. Boudier, L. Y. M. Gicquel, and T. J. Poinsot, Effects of mesh resolution on large eddy simulation of reacting flows in complex geometry combustors, Combustion and Flame **155**, 196–214 (2008).

[165] S. B. Pope, Ten questions concerning the large-eddy simulation of turbulent flows, New Journal of Physics **6** (2004).

[166] K. T. Aung, M. I. Hassan, and G. M. Faeth, Flame stretch interactions of laminar premixed hydrogen/air flames at normal temperature and pressure, Combustion and Flame **109**, 1–24 (1997).

[167] J. Jarosinski, The thickness of laminar flames, Combustion and Flame **56**, 337–342 (1984).

[168] Y. Dubief and F. Delcayre, On coherent-vortex identification in turbulence, Journal of Turbulence **1** (2000).

[169] S. Nambully, P. Domingo, V. Moureau, and L. Vervisch, A filtered-laminar-flame PDF sub-grid scale closure for LES of premixed turbulent flames. Part I: Formalism and application to a bluff-body burner with differential diffusion, Combustion and Flame **161**, 1756–1774 (2014).

[170] C. Y. Lee and S. Cant, Large-eddy simulation of a bluff-body stabilised turbulent premixed flame using the transported flame surface density approach, Combustion Theory and Modelling **21**, 722–748 (2017).

[171] D. Veynante, A. Trouvé, K. N. C. Bray, and T. Mantel, Gradient and counter-gradient scalar transport in turbulent premixed flames, Journal of Fluid Mechanics **332**, 263–293 (1997).

[172] X. J. Gu, M. Z. Haq, M. Lawes, and R. Woolley, Laminar burning velocity and Markstein lengths of methane-air mixtures, Combustion and Flame **121**, 41–58 (2000).

[173] G. P. Smith et al., GRI-Mech Home Page.

[174] C. E. Frouzakis, N. Fogla, A. G. Tomboulides, C. Altantzis, and M. Matalon, Numerical study of unstable hydrogen/air flames: Shape and propagation speed, Proceedings of the Combustion Institute **35**, 1087–1095 (2015).

[175] C. K. Law, A. Makino, and T. F. Lu, On the off-stoichiometric peaking of adiabatic flame temperature, Combustion and Flame **145**, 808–819 (2006).

[176] C. K. Law, *Combustion Physics* (Cambridge University Press, Cambridge, 2006), p. 722.

[177] H. Hisken, Investigation of instability and turbulence effects on gas explosions : experiments and modelling, PhD thesis (University of Bergen, Norway, 2018).

[178] M. Germano, Turbulence: the filtering approach, Journal of Fluid Mechanics **238** (1992).

[179] D. K. Lilly, A proposed modification of the Germano subgrid-scale closure method, Physics of Fluids A: Fluid Dynamics **4**, 633–635 (1992).

Appendix A

Dynamic Smagorinsky Model

The eddy viscosity μ_t is a function of the filter size and the strain rate

$$\mu_t = \overline{\rho} C \overline{\Delta}^2 \left| \widetilde{S} \right| \tag{A.1}$$

where $\left| \widetilde{S} \right| = \sqrt{2 \widetilde{S}_{ij} \widetilde{S}_{ij}}$ and C is a dimensionless coefficient. In the classical model, C is specified a priori and is often written as the Smagorinsky coefficient $C_s = \sqrt{C}$.

The dynamic procedure [86] uses local instantaneous flow conditions to calculate the Smagorinsky model coefficient dynamically. The procedure involves the application of a test filter to the velocity field to extract information from the smallest resolved scales which is then used to calculate the coefficient. The application of a test filter to the filtered Navier-Stokes equations leads to a test-level SGS stress tensor

$$\mathcal{T}_{ij} = \widehat{\overline{\rho u_i u_j}} - 1/\widehat{\overline{\rho}} \left(\widehat{\overline{\rho u_i}} \, \widehat{\overline{\rho u_j}} \right) \tag{A.2}$$

The resolved turbulent stresses (in the advection term), or Leonard stresses

$$\mathcal{L}_{ij} = \overline{\rho} \widehat{\widetilde{u}_i \widetilde{u}_j} - 1/\widehat{\overline{\rho}} \left(\widehat{\overline{\rho} \widetilde{u}_i} \widehat{\overline{\rho} \widetilde{u}_j} \right) \tag{A.3}$$

can be calculated from the filtered velocity filed. Germano [178] related $\mathcal{L}_{ij}$ to the two SGS stress tensors through the identity

$$\mathcal{L}_{ij} = \mathcal{T}_{ij} - \widehat{\tau}_{ij}^{sgs} \tag{A.4}$$

which can be used to derive an expression for $C\Delta^2$ in Eq. (A.1)

$$C\overline{\Delta}^2 = -\frac{\mathcal{L}_{ij}M_{ij} - 1/3\mathcal{L}_{ll}M_{mm}}{2\left(M_{ij}M_{ij} - 1/3M_{ll}M_{mm}\right)}. \tag{A.5}$$

Here

$$M_{ij} = \alpha^2\widehat{\overline{\rho}}|\widehat{\overline{S}}|\widehat{\overline{S}_{ij}} - \overline{\rho}|\widehat{\overline{S}}|\widehat{\overline{S}_{ij}}, \tag{A.6}$$

where

$$\widehat{\overline{\Delta}} = \alpha\overline{\Delta} \tag{A.7}$$

is the ratio of the test and grid filter widths and is usually taken as 2. The tensors are contracted with M_{ij} rather than S_{ij} as suggested by Lilly [179]. The value for $C\overline{\Delta}^2$ is then substituted into Eq. (A.1) to give the eddy viscosity μ_t.

The Smagorinsky model with the dynamic procedure used to calculate $C\overline{\Delta}^2$ has the correct behaviour near a wall and in laminar flow and allows energy backscatter. Values of the model coefficient tend to fluctuate considerably in space and time, and some form of averaging is usually required to avoid stability problems.